Oleg SIDLETSKIY, Borys GRYNYOV

SCINTILLATION CRYSTALS BASED ON SUBSTITUTIONAL SOLID SOLUTIONS

NATIONAL ACADEMY OF SCIENCES OF UKRAINE
INSTITUTE FOR SCINTILLATION MATERIALS
OF THE NAS OF UKRAINE

НАЦІОНАЛЬНА АКАДЕМІЯ НАУК УКРАЇНИ
ІНСТИТУТ СЦИНТИЛЯЦІЙНИХ МАТЕРІАЛІВ
НАН УКРАЇНИ

Олег СІДЛЕЦЬКИЙ
Борис ГРИНЬОВ

СЦИНТИЛЯЦІЙНІ КРИСТАЛИ НА ОСНОВІ ТВЕРДИХ РОЗЧИНІВ ЗАМІЩЕННЯ

ПРОЄКТ
«УКРАЇНСЬКА НАУКОВА КНИГА
ІНОЗЕМНОЮ МОВОЮ»

КИЇВ
АКАДЕМПЕРІОДИКА
2025

Oleg SIDLETSKIY
Borys GRYNYOV

SCINTILLATION CRYSTALS BASED ON SUBSTITUTIONAL SOLID SOLUTIONS

PROJECT
«UKRAINIAN SCIENTIFIC BOOK
IN A FOREIGN LANGUAGE»

KYIV
AKADEMPERIODYKA
2025

https://doi.org/10.15407/akademperiodyka.559.166
UDC 535.37:548
S57

Rewiewers:

Oleksandr SOROKIN, Dr. Sci., Professor, Deputy Director
of Institute for Scintillation Materials of the NAS of Ukraine

Yuriy ZORENKO, Dr. Hab., Professor of Institute
of Physics of Kazimierz Wielki University in Bydgoszcz, Poland

Approved for publication by the Institute for Scintillation Materials of the National Academy of Sciences of Ukraine (September, 5, 2024, Protocol No. 10)

The publication was funded within the framework of the Targeted Complex Program of the NAS of Ukraine "Scientific Bases of Functioning and Providing for Conditions for the Development of the Scientific and Publishing Complex of the NAS of Ukraine"

Sidletskiy O.Ts.

S57 Scintillation crystals based on substitutional solid solutions / Oleg Sidletskiy, Borys Grynyov; NAS of Ukraine, Institute for Scintillation Materials. — Kyiv: Akademperiodyka, 2025. — 166 p.

ISBN 978-966-360-559-3

The book is devoted to the development of the scientific and technical bases of the development of highly efficient inorganic scintillation crystals based on substitutional solid solutions. The structural, luminescence, and scintillation properties of the obtained oxide crystals were investigated. The conditions for growing large-size oxide crystals of solid solutions by the Czochralski method and crystalline fibers of solid solutions by the micro-pulling-down method (μ-PD) were determined. A general phenomenological approach to the targeted production of crystals with improved light yield, in particular, a tendency towards an increase in the light yield of the solid solution in mixed systems has been determined.

UDC 535.37:548

ISBN 978-966-360-559-3

CONTENTS

LIST OF SYMBOLS, ABBREVIATIONS, AND TERMS

REE — rare earth elements

UV — ultraviolet

VUF — vacuum ultraviolet radiation

TSL — thermally stimulated luminescence

RL — radioluminescence

AES-ICP — atomic emission spectroscopy with inductively coupled plasma

FEM — photoelectric multiplier

HF — high frequency

XRD — X-ray diffraction phase analysis

AAS — atomic absorption spectroscopy

PET — positron emission tomography

μ-PD — Micro Pulling Down (a method of growing fibers by pulling them down)

DTA — differential thermal analysis

SPS — solid phase synthesis

CF — crystallization front

TEC — thermal expansion coefficient

Zef — effective atomic number

LSO — lutetium oxyorthosilicate (Lu_2SiO_5)

GSO — gadolinium oxyorthosilicate (Gd_2SiO_5)

LGSO — lutetium gadolinium oxyorthosilicate $(Lu_{1-x}Gd_x)_2SiO_5$

GYSO — yttrium gadolinium oxyorthosilicate $(Gd_{1-x}Y_x)_2SiO_5$

YSO — yttrium oxyorthosilicate (Y_2SiO_5)

PWO — lead tungstate ($PbWO_4$)

BGO — bismuth germanate ($Bi_3Ge_4O_{12}$)

YTO — yttrium orthotantalate ($YTaO_4$)

YTNO — yttrium tantalo-niobate

GTO — gadolinium tantalite

GTNO — gadolinium tantalum niobate

PREFACE

Scintillation materials capable of detecting ionizing radiation are widely used in many sectors of human activity. High light yield is one of the main parameters of scintillators, along with scintillation decay time, temperature, climate, and radiation stability, chemical inertness, ease of mechanical processing and the cost of the scintillation detector. Energy separation, in particular, depends on the light yield and its proportionality to the excitation energy. In the last decade, a number of highly efficient scintillators with a light yield of 50,000—100,000 photons/MeV and an energy resolution of up to 2—5% at an energy of 662 keV have been developed [1, 2]. Until recently, such indicators were considered unattainable, and the standard scintillator was NaI:Tl with an energy separation of 6—7%. Such progress makes it possible to significantly expand the scope of practical application of scintillators, in particular, in spectrometric instruments for the identification of nuclear isotopes for monitoring the spread of dangerous nuclear materials, where scintillators can compete with semiconductor radiation detectors that have energy separation of about 1%, but also a much higher cost. The diversity of scintillation materials is due to the fact that the ideal scintillator does not exist, and the physical properties of materials can vary not only between classes, but also within each class. Along with physical properties, an important role in the application of scintillation material is played by its cost, which depends both on the cost of raw materials and on the technology of its production. In this regard, the search for efficient scintillators at an acceptable cost is certainly an important task.

Over the past two decades, major progress has been achieved in halide crystals activated by Eu^{2+} and oxide scintillators activated by Ce^{3+}. Materials based on substitutional solid solutions, in which one of the matrix cations or anions that isovalently replaced by another atom, have become one of the main areas of scintillator engineering. In the English-language literature, the term «mixed crystal» is more often used, which is quite equivalent to the term «solid solution crystal». The difference in the ionic radii of substituted atoms in solid solutions is usually insignificant and does not lead to a change in the type of crystal structure. According to the Goldschmidt criterion, the limit of mutual solubility of atoms is at the level of 15% of the difference in their ionic radii for crystals with a perovskite structure, although single crystals are also obtained in systems where this difference is much larger, for example, $Bi_4Ge_{3-x}Si_xO_{12}$, where the ionic radii of Ge^{4+} and Si^{4+} differ by 32%.

It turned out that some crystals of solid solutions can demonstrate qualitatively better scintillation parameters (higher light yield, better energy separation, faster scintillation decay time) compared to their constituents. Among the oxide scintillators, one can mention effective mixed scintillators based on solid solutions: $Lu_{2x}Gd_{2-2x}SiO_5$:Ce (LGSO:Ce), $Lu_3(Al_xGa_{1-x})_5O_{12}$:Ce (LuAGG:Ce), $Y_3(Al_xGa_{1-x})_5O_{12}$:Ce (YAGG:Ce), $Gd_3(Al_xGa_{1-x})_5O_{12}$:Ce (GAGG:Ce). In the GAGG:Ce crystal, a record light yield for oxide scintillators of up to 58,000 photons/MeV was achieved [3]. At the same time, a record energy resolution in oxides (<5% at an energy of 662 keV) was obtained in multicomponent garnet $(Y_xGd_{1-x})_3(Al_xGa_{1-x})_5O_{12}:Ce^{3+}$ [4]. In LYSO:Ce and LGSO:Ce, replacing Lu^{3+} with Y^{3+} or Gd^{3+} improves light yield, energy resolution, and reduces the intensity of afterglow [5, 6]. Among halide scintillators the $BaBr_{1-x}I_x:Eu^{2+}$ (BaBrI:Eu) system stands out with a light yield of up to 97,000 photons/MeV and an energy resolution of 3–4% [7]. Due to the high activator concentration of up to 10% in this and similar systems, $BaBrI:Eu^{2+}$ is, in fact, a solid solution of BaI_2, $BaBr_2$, and EuI_2, where Eu^{2+} replaces Ba^{2+}, and Br^+ replaces I^+.

The above examples demonstrate a tendency to improve the scintillation characteristics in mixed crystals. In addition, the growth of mixed crystals is also advantageous from an economic point when replacing, for example, high-cost lutetium oxide with yttrium or gadolinium oxides. Also, the replacement of Lu^{3+} by Y^{3+} or Gd^{3+} in various complex oxide systems reduces the energy consumption for the production of scintillation materials by lowering their crystallization temperatures. For these reasons, $Lu_{2x}Y_{2-2x}SiO_5$:Ce (LYSO:Ce) crystals have become an alternative to Lu_2SiO_5:Ce (LSO:Ce) as a scintillator for positron emission tomography [8]. A similar replacement of lutetium-aluminum garnet $Lu_3Al_5O_{12}$:Ce (LuAG:Ce) by $Gd_3(Al_{1-x}Ga_x)O12$:Ce (GAGG:Ce) is also reasonable for several applications.

However, on the other hand, the presence of additional components in the system complicates the technological process of crystal growth. During the crystallization of solid solutions from the melt, it is necessary to take into account the difference in the ionic radii of substituted atoms, which leads to their different segregation by the crystallization front in accordance with Pfann's law [9] and uneven distribution in the volume of the crystal. A large difference in the melting temperatures of the components of the solid solution contributes to the formation of macrodefects in crystals [10].

Before the works that became the basis of this monograph, the factors leading to an improvement in the light yield in crystals of solid solutions were studied only in fragments. One of the hypotheses is the heterogeneity of the distribution of matrix cations, which leads to the appearance of regions in the crystal enriched in one of the substituted atoms [11]. At the boundaries of these areas, jumps in the crystal potential should occur, which limit the diffusion of the formalized charge carriers and increase the probability of electron and hole capture at the luminescent center. For crystals based on rare-earth garnets (GAGG:Ce, LuGAGG:Ce), the increase in light yield was explained by the deactivation of small electron traps due to the shift of the the conduction band edge upon cation substitution, which suppresses the slow components of luminescence in favor of fast scintillations [12]. The contribution of the electron-phonon interaction to the scintillation process in mixed crystals was also discussed [13].

Thus, this book is devoted to the processes of obtaining scintillation crystals based on solid substitution solutions, their properties, and searching for mixed scintillators with improved parameters.

CHAPTER 1

CURRENT TRENDS IN THE DEVELOPMENT OF HIGHLY EFFICIENT INORGANIC SCINTILLATORS

As noted in the Preface, major advances in the development of new bright scintillators in recent years have been achieved in Eu^{2+}-activated halide crystals and Ce^{3+}-activated oxide scintillators. Let's take a closer look at each of these types of materials.

1.1. Halide scintillators

The most significant progress has been made in recent years in the engineering of halide scintillators (mainly iodides), in which the alkaline earth cation (Ba^{2+}, Ca^{2+} or Sr^{2+}) is replaced by the activator Eu^{2+}. The impetus for this research was the Homeland Security program launched in 2002 in the United States, which aimed to strengthen control over the movement of dangerous radioactive isotopes, in particular components of «dirty bombs», across the country's land, sea and air borders. A key parameter for the rapid and reliable determination of dangerous isotopes among those used for peaceful purposes, for example, in medicine, is the energy resolution of the scintillator, which is the main element of safety monitoring devices. A large number of vehicles that must be checked in a limited period of time required a qualitatively new level of energy resolution of detectors in the corresponding scanning equipment (Fig. 1.1). These characteristics that have been achieved in some halide materials are listed in Table 1.1. The energy resolution of SrI_2:Eu and some other halides reaches 2—4% at 662 keV, compared to 6—7% in classical scintillators. This increases the scanning speed several times and improves the reliability of identification of radioactive isotopes.

Close values of ionic radii of the matrix cation ($r_i(Sr^{2+}) = 118$ pm and the activator $r_i(Eu^{2+}) = 117$ pm) create conditions for the incorporation of a large amount of Eu^{2+} (up to 10 at.% or more) into the crystal of $SrI_2:Eu^{2+}$ or other Sr^{2+}- or Ba^{2+}-containing halides without significant deformations of the crystal lattice. Due to the high coefficient of activator inclusion, its distribution throughout the crystal volume is uniform. The best values of light yield and energy resolution are usually observed at Eu^{2+} concentrations of 3—5 at.%. Such activator concentrations are unattainable when grown from a melt for the

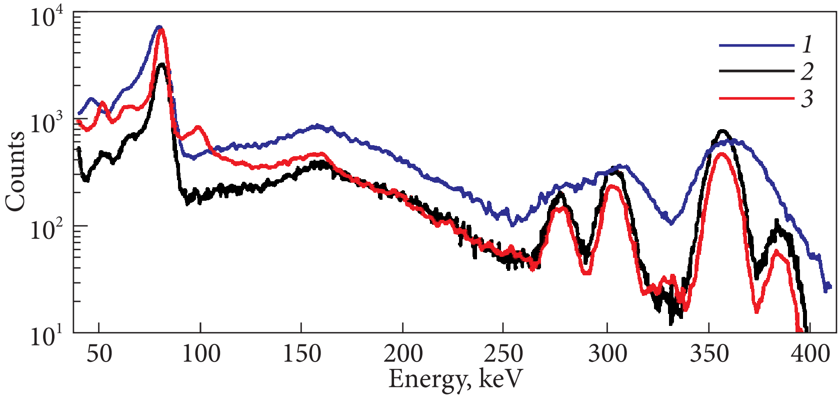

Fig. 1.1. Amplitude spectra of some scintillators when excited by gamma particles of the Ba-133 isotope [14]: *1* — NaI(TI), *2* — LaBr$_3$(Ce), *3* — SrI$_2$(Eu)

Table 1.1. **Scintillation properties of some halides scintillators**

Scintillator	r, g/cm^3	Light yield photons/MeV	Energy resolution at 662 keV,%	Activator concentration, at.%	References
LaBr$_3$:Ce,Sr	5.1	78.000	2.0		[16]
CsBa$_2$I 5:Eu	4.9	80.000	2.3	5% Eu	[17]
KBa$_2$I 5:Eu	4.52	90.000	2.4	4% Eu^{2+}	[18]
SrI$_2$:Eu	4.55	120.000	3.0	5% Eu^{2+}	[15]
K$_2$BaI$_4$:Eu		63.000	2.9	7% Eu^{2+}	[18]
Cs$_2$LiLaBr$_6$:Ce (CLLB)	4.2	50.000	2.9	10% Ce^{3+}	[19]
KCaI$_3$:Eu	3.81	72.000	3	3% Eu$_{2+}$	[20]
LaCl$_3$:Ce	3.8	49.000	3.1	10% Ce	[21]
CeBr$_3$		58.000	3.2	1.9% Ca$^+$	[22]
Cs$_2$HfCl$_6$	3.86	54.000	3.3		[23]
Cs$_2$NaGdBr$_6$:Ce	4.19	48.000	3.3	4% Ce^{3+}	[24]
KSr$_2$Br$_5$:Eu	3.98	75.000	3.5	5% Eu^{2+}	[25]
BaCl$_2$:Eu	3.86	52.000	3.5	5% Eu	[26]
RbGd$_2$Br$_7$:Ce	4.7	55.000	3.8	5% Ce3+	[27]
CsBa$_2$I 5:Eu	5.0	80.000	3.9	3% Eu	[28]
Cs$_2$NaLaBr$_6$:Ce	3.93	46.000	3.9	4% Ce	[29]

vast majority of scintillation crystals activated by Ce^{3+} or Pr^{3+} with large ionic radii, where the latter replaces the trivalent rare earth element (Lu^{3+}, Gd^{3+}, Y^{3+}) with significantly smaller ionic radii. Despite the large number of very efficient scintillators with an energy resolution of 2—4% (Table 1.1) that have been in-

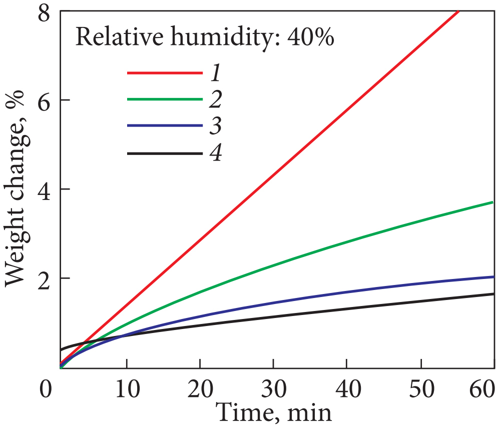

Fig. 1.2. Curves of moisture gain of LaBr3:Ce, KSr_2I_5:Eu 4%, KSr_2Br_5:Eu 2.5%, and NaI:Tl as registered when weighing samples depending on their exposure time [25]: *1* — $LaBr_3$:Ce 5% (8.9%); *2* — KSr_2I_5:Eu 4% (3.8%); *3* — KSr_2Br_5:Eu 2.5% (2.0%); *4* — NaI:Tl (1.6%)

vented, most of the results presented were obtained on samples up to several mm in size, and only for a few of them, methods for obtaining large-size crystals are being developed. Currently, the commercially available halide scintillators are NaI:Tl, CsI:Tl, CsI:Na, CsI, $LaBr_3$:Ce and SrI_2:Eu. Despite reports on obtaining SrI_2:Eu crystals with a diameter of up to 63 mm by the Bridgman method [30], only SrI_2:Eu crystals with a diameter of up to 50 mm [31] produced by C&A (Japan) are commercially available today.The main obstacle to the development of technologies for the production of new large-size halide crystals is their strong hygroscopicity. The relative dynamics of moisture gain [25] (Fig. 1.2) clearly demonstrates that the hygroscopicity of new halide scintillators (KSr_2I_5:Eu 4%, KSr_2Br_5:Eu 2.5%) is significantly higher than the classical NaI:Tl, although it is inferior to $LaBr_3$:Ce. This significantly increases the requirements for the conditions of storage and preparation of raw materials, growing/processing of single crystals to prevent their oxidation. Another limiting factor in the development of new halide scintillators is the extremely high cost of their raw materials due to the lack of large-scale production of these substances. For example, the cost of 99.9% EuI_2 and $EuBr_2$ is about $15,000 per kilo. Subsequent developments of methods for producing large crystals of these compounds are aimed at reducing their cost by optimizing technologies for the production of raw materials for growing single crystals and detectors based on them. It is expected that the raw material costs of these materials can be reduced to the level of classical scintillators (NaI:Tl and CsI:Tl) in large-scale production. The development of potentially inexpensive scintillator technology will provide the opportunity for a new generation of equipment for spectrometric identification of nuclear isotopes to enter the market. Some new scintillation materials, such as SrI_2:Eu, do not require a license for commercial production.

1.2. Oxide scintillators

The key point in the development of activated oxide scintillators in the last decades was the discovery of high-melting-point materials based on complex oxides activated by Ce^{3+} ions: orthosilicates Gd_2SiO_5:Ce (GSO), Lu_2SiO_5:Ce (LSO), Y_2SiO_5:Ce (YSO) $(Lu_{1-x}Y_x)_2SiO_5$:Ce (LYSO), as well as Ce^{3+}- and Pr^{3+}-activated aluminum garnets — $Lu_3Al_5O_{12}$ (LuAG), $Y_3Al_5O_{12}$ (YAG), and perovskites $LuAlO_3$ (LuAP), $YAlO_3$ (YAP). The features of these scintillators are high thermal, chemical and radiation resistance, nanosecond luminescence decay, and significant light yield. Table 1.2 enlists many effective and popular scintillators of this class. Among their disadvantages, one can highlight the moderate density and Z_{ef} of yttrium-containing crystals, the high cost of lutetium-containing crystals, high intrinsic background, and afterglow in LSO:Ce, as well as the difficulty of obtaining large-sized GSO:Ce, LuAP:Ce/Pr, YAP:Ce/Pr crystals. The best achieved energy resolution in these materials was about 7%, so they cannot compete with halide crystals in spectrometric applications.

Another large group of compounds can be summarized by the formula $RE_2Si_2O_7$ (RE = Lu-La, Y, Sc), which comprises pyrosilicates or disilicates of rare earth elements. The structural properties of REE pyrosilicates were quite well studied in the 60s and 70s of the last century. The scintillation properties of pyrosilicates were not studied until the beginning of the XXI century. This is explained by the difficulty of obtaining due to the incongruent melting (except for scandium pyrosilicates and lanthanides with small ionic radii from Lu to Er). Crystals of cerium-activated lutetium pyrosilicate, $Lu_2Si_2O_7$:Ce(LPS:Ce) were shown to exhibit characteristics comparable to LSO:Ce [37]. LPS:Ce has a lower level of afterglow than LSO:Ce and better light yield stability above room

Table 1.2. **Scintillation properties of some oxide scintillators activated by Ce^{3+} [32—36]**

Crystal	Density, g/cm^3	Light yield, Photons/MeV	Energy resolution at 662 KeV,%	Decay time, (ns) at g-excitation	The afterglow after 5 ms,%
Gd_2SiO_5 (GSO)	6.7	8 000	9—11	50	0.02
Lu_2SiO_5 (LSO)	7.4	25 000	7.3—9.7	40	>1
$Lu_2Si_2O_7$ (LPS)	6.2	26 000	9.5	38	~0.02
$Y_3Al_5O_{12}$ (YAG)	4.55	24 000	7.3	85 + slow	ND
$Lu_3Al_5O_{12}$ (LuAG)	6.7	12 500	ND	44	ND
$YAlO_3$ (YAP)	5.35	21 000	6.7	27	ND
$LuAlO_3$ (LuAP)	8.34	11 000	14	16 + slow	ND

ND — no data available.

temperature, which is important for geological exploration applications. The potentially lower production cost of LPS:Ce is due to the lower lutetium content and lower crystallization temperature compared to LSO:Ce.

Another promising scintillator of this chemical class is cerium-activated gadolinium pyrosilicate $Gd_2Si_2O_7$:Ce(GPS:Ce). In terms of light yield, it is similar to LSO:Ce and LPS:Ce, but slightly inferior to the latter in density. The advantages of this scintillator over other rare earth pyrosilicates are the relatively low cost of starting oxides, the crystallization temperature is 100—200 degrees lower compared to orthosilicates, the stability of the light yield at temperatures from room temperature to 100—200 °C [38], the possibility of recording thermal neutrons due to the large cross section of their capture by isotopes ^{155}Gd, ^{157}Gd [39, 40]. The impossibility of crystal growth from the melt due to the incongruent melting was the main obstacle to the practical application of gadolinium pyrosilicate. Due to the addition of La^{3+} cations to GPS:Ce, it was possible to stabilize the orthorhombic pyrosilicate phase [41] and successfully obtain large-sized crack-free crystals up to 2 inches in diameter [42].

High density and effective atomic number Z_{eff} are the most important parameters of scintillators in most applications, in particular, in high-energy physics. These parameters determine the ability to absorb ionizing radiation and, as a result, reduce the required volume of the detector. The highest Z_{eff} in scintillators can be achieved in Pb, W, Bi, Nb, Ta- or lanthanide-containing compounds. Successful examples of the development of dense scintillators include $PbWO_4$ [43, 44], $Bi_4Ge_3O_{12}$ [45—48], Gd_2SiO_5:Ce [49], Lu_2SiO_5:Ce [50], $Lu_{2x}Y_{2-2x}SiO_5$:Ce [5]. Lead tungstate is widely used in electromagnetic calorimeters in high-energy physics experiments. An example is the successful operation of the CMS electromagnetic calorimeter detectors at CERN and the discovery of the Higgs boson [51]. In 2017, a new generation of lead tungstate crystals with improved light yield and high radiation resistance was selected as scintillation detectors in the PANDA project [52]. LYSO:Ce and GSO:Ce were considered as candidates for use in calorimeters for recording muon-to-electron conversion — in the Mu2e experiment at the Fermi Laboratory (USA) [53], and, finally, LYSO:Ce was chosen as a scintillator in the COMET experiment in KEK, Japan [54]. LSO:Ce and LYSO:Ce are also materials used in medical PET scanners [8, 55]. Compounds with the general formula $REAO_4$, where RE is a rare earth element and A is a transition metal, an element of Group 5 (V, Nb, or Ta) of the Periodic Table, have also recently been proposed as effective high-density luminescent materials for recording X-rays and gamma radiation [56—61]. Rare earth vanadates [56, 57] have a light yield of up to 12000 photons/MeV and were proposed as efficient scintillators for recording X-rays and gamma rays. Compounds based on yttrium tantalate [60—62] have attracted attention as materials for use in optoelectronics and X-ray screens. Less attention is paid to non-activated $REAO_4$ compounds (A = Ta,V) because rare-earth vanadates and niobates possess slow luminescence, which makes it impossible to use in applications where fast signal processing is required. It is believed that rare earth tantalates exhibit low luminescence intensity compared to vanadates and niobates [61]. At the same time, tantalates, due to their extremely high density from 7.8 g/cm^3 for $LaTaO_4$ to 9.75 g/cm^3 for $LuTaO_4$ [62], are the most suitable for recording high-energy particles. Luminescence mechanisms in some of them were discussed in [63—65]. It was shown that upon UV and X-ray excitation, orthotantalates and orthoniobates with the fergusonite structure exhibit luminescence of TaO_6 or NbO_6 groups. The scintillation properties of rare-earth tantalates were not systematically studied until the publication [66], where the light yield of 15200 photons/MeV in $YTaO_4$ and 9500 photons/MeV in $LuTaO_4$ were reported, along with the scintillation decay time of several microseconds.

Doped rare-earth tantalates have also been considered as materials for X-ray scanners and medical imaging [67, 68]. Their luminescent properties were studied in [69—71]. Intense luminescence upon activation of Pr^{3+} was recorded in $YTaO_4$ with a fergusonite structure [69]. In this case, Ce^{3+} luminescence is quenched in these matrices [69]. In [71], lanthanum orthotantalate was proposed as a matrix for red luminescence upon activation by rare earth ions, for example, Eu^{3+}. Attempts to obtain fast quenching in orthotanatalates due to 5d-4f transitions in divalent and trivalent lanthanides, by analogy with many other complex oxides, were unsuccessful because in rare earth vanadates, tantalates, and niobates, the excited 5d levels of Ce^{3+} and Pr^{3+} are located within the conduction band [72, 73]. Only in some compounds with $GdTaO_4$ and $YTaO_4$ activated by Sm^{3+}, Tb^{3+} or Dy^{3+}, Eu^{3+}, bright 5d-4f luminescence with microsecond decay was obtained [74]. Thus, the search for new tantaloniobate compositions combining reasonable light output and fast luminescence decay with low contribution of slow components is an urgent task, and oxide materials in general remain popular dense and non-hygroscopic scintillators for a variety of applications.

1.3. Development of scintillators based on substitutional solid solutions

During the development of new scintillation materials of different chemical composition, it was shown that in many crystals based on solid substitution solutions, it is possible to achieve a significant improvement in the basic scintillation parameters — light yield, energy resolution, luminescence decay rate. For example, according to [11, 75], the light yield in Ce activated lutetium-yttrium perovskite increases approximately three times compared to $YAlO_3$:Ce (YAP) and $LuAlO_3$:Ce (LuAP). A similar result was demonstrated for multicomponent garnets $(Lu_{1-x}Gd_x)_3(Al_{1-x}Ga_x)_5O_{12}$:Ce (LuGAGG:Ce) [76]. An earlier but very successful example of mixed rare-earth silicate engineering is LYSO:Ce with improved light yield and homogeneity of characteristics in the crystal volume, as well as a reduced crystallization temperature compared to LSO:Ce

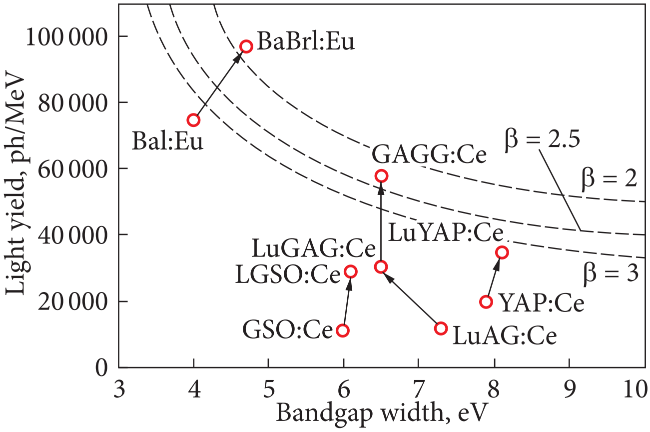

Fig. 1.3. Increase in light yield in some mixed scintillators (shown by arrows) [88], illustrated on the basis of the diagram [87] of the fundamental limitation on light yield depending on the bandgap in scintillators

[5, 77]. The deviation of the light yield from additive values is, as a rule, maximal at a 1:1 ratio of components [13], although there are systems, for example, $BaBr_{2-x}I_x$:Eu^{2+} [78], $La_{3-x}Ce_xF_3$, $La_{3-x}Ce_xPO_4$ [79], $Zn_xCd_{1-x}S$:Ag [80], where the dependence of the light yield or other scintillation parameters is clearly asymmetric with respect to the light yields of the components of the mixed crystal.

New efficient Eu^{2+}-activated halide scintillators with a light yield of up to 112,000 photons/MeV are represented by anion-substituted solid solutions, typically Br^-/I^-, Br^-/Cl^-, Cl^-/I^-, F^-/I^-. In addition to the already mentioned $BaBr_{2-x}I_x$:Eu^{2+} system, we can note $BaBr_{2-x}Cl_x$:Eu^{2+} with a light yield of 52,000 photons/MeV [81], $BaCl_{2-x}I_x$:Eu^{2+} with a light yield of 54,000 photons/MeV [82], $BaF1_xI_x$:Eu^{2+} with a light output of 55,000 photons/MeV [83]. Cation substitution in Eu^{3+}-doped $K(Ca,Sr)I_3$ iodide was explored as well [84]. In oxide scintillators, the best parameters are achieved in $Gd_3(AlyGa_{1-x})_5O_{12}$:$Ce^{3+}$ — 58,000 photons/MeV [3], while the highest energy resolution <5% [85] is registered in the multicomponent crystal $(Y_xGd_{1-x})_3(Al_yGa_{1-x})_5O_{12}$:$Ce^{3+}$, which is a qualitatively new indicator for oxides. A similar energy resolution of 4.4% at 662 keV in oxide scintillators was previously noted only in YAP:Ce [86].

In accordance with the fundamental limitation on the light yield in scintillators [87], the light yield is inversely proportional to the bandgap, E_g, and the number of generated photons in the scintillator is determined by the formula

$$N_{ph} = SQE_g/E_{e\text{-}h} = SQE/2.5E_g, \tag{1.1}$$

where S is the transport coefficient, Q is the quantum efficiency of the luminescent center, E is the energy of the ionizing particle, $E_{e\text{-}h}$ is the number of generated electron-hole pairs.

The multifold increase in light yield in certain mixed crystals can only be attributed to an increase in S due to an improvement in the efficiency of the carrier transport to the luminescent center. According to the diagram of the fundamental limitation of light yield [88], the experimental values of light output in many mixed crystals reach the theoretical limit (i.e. $S = 1$), for $b = E_{e\text{-}h}/E_g =$ = 2—3 (Fig. 1.3). In the most effective scintillation matrices, Q(Ce^{3+}) and Q(Eu^{3+}) are already close to unity [89, 90], E does not depend on the ratio of substituted atoms in a certain matrix, and E_g, as will be shown below, varies by at most 20%, which cannot cause a significant increase in N_{ph}.

Considering the practical value of obtaining scintillators with improved characteristics, studying the concentration dependence of the light yield in mixed scintillators is a new and relevant topic of research. Previously, a relatively small number of such systems were studied. Despite the scintillation mechanisms that lead to an increase in the light yield in mixed crystals having been addressed in some studies, there has been no general approach to predicting the light yield in them. When clarifying the concentration dependence of the light yield in a solid solution, two approaches could be distinguished: modification of the energy structure of the crystal, and the limitation of the thermalization length and/or thermal diffusion of charge carriers.

1.3.1. Engineering of energy structure in solid solutions

According to formula 1.1, the number of electron-hole pairs generated when a certain energy amount is absorbed is inversely proportional to the bandgap of the material. In the case of mixed crystals, this change is not significant and cannot remarkably affect the light yield value. Among the literature analyzed, the largest change in the bandgap is 1.6 eV in the $(Y_xGd_{1-x})_3(Al_yGa_{1-x})_5O_{12}$ system [76, 91], which is about 20% relative to the 7—8 eV bandgap in these crystals. That is, the change in E_g is insufficient to cause an increase in the light output by several times due to a change in the number of generated electron-hole pairs per unit of ionizing radiation energy.

At the same time, the substitution of atoms and the change in the strength of the crystal field also lead to a shift in the energy levels of the activator and traps relative to the bandgap edges. The correlation of these processes with scintillation parameters in $LaBr_{3-x}I_x$:Ce was described in [92]. When Br^+ is substituted for I^+, the 5*d* and 4*f* levels in Ce^{3+} become closer to the edges of the conduction band and valence band, respectively. As a result, the energy interval between the lowest 5*d* level of Ce^{3+} and the bottom of the conduction band gradually changes from ~1 eV in $LaBr_3$:Ce to 0.1—0.2 eV in LaI_3:Ce (Fig. 1.4).

The decrease in light yield with the addition of I^+ occurs due to the quenching of Ce^{3+} luminescence through the autoionization of electrons from the 5*d* level of Ce^{3+} to the conduction band. However, it was not commented why the light yield increases at intermediate concentrations with a maximum for the $LaBr_{1.5}I_{1.5}$:5% Ce^{3+} crystal.

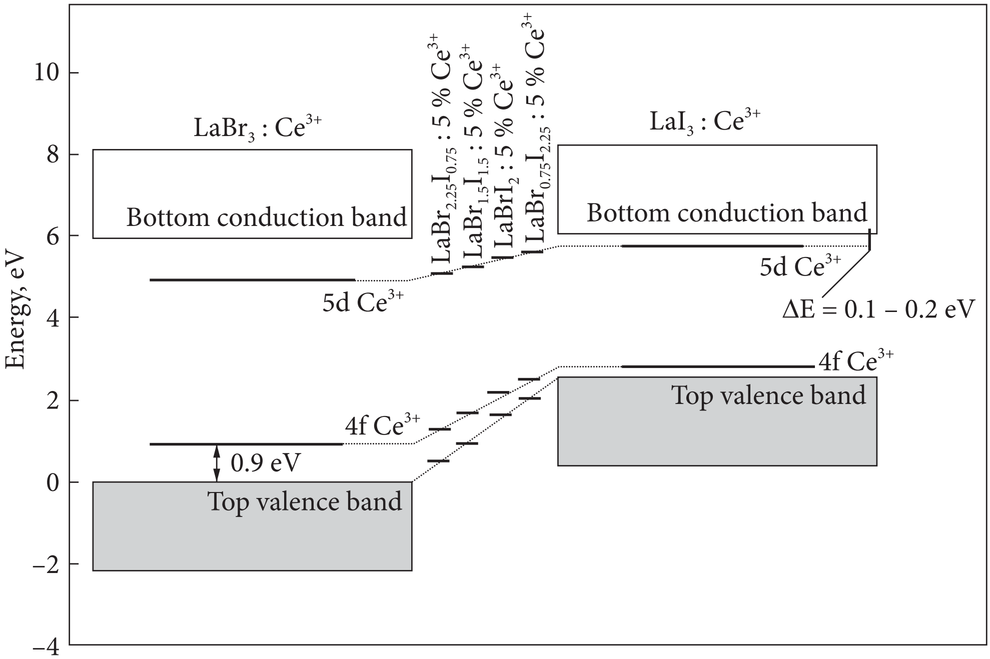

Fig. 1.4. Modification of the energy structure of $LaBr_{3-x}I_x$:Ce when substituting Br^+ for I^+ [92]

This approach (engineering of the energy structure of a mixed crystal, or «bandgap engineering») was developed in [93] when elucidating the reasons for a strong increase in light yield in solid solutions of aluminum-gallium garnets activated by Ce^{3+}. It was shown that, along with the energy levels of cerium, the position of the levels of small traps located under the bottom of the conduction band and competing with cerium for the capture of charge carriers, changes relatively to the conduction band (Fig. 1.5). Substitution by anion should cause similar effects for traps whose energy levels are close to the valence band. At a certain Al^{3+}/Ga^{3+} ratio and the composition of rare earth cations in multi-component garnets, the levels of these traps are completely absorbed by the conduction band and do not capture electrons. At the same time, the light yield of cerium luminescence increases. At a certain concentration of Ga, the lowest $5d_1$ level of cerium shifts too close to the bottom of the conduction band, thermal ionization of electrons to the conduction band occurs, and the light yield rapidly decreases both in lutetium gadolinium garnet [94] and in yttrium-aluminum-gallium garnet YAGG:Ce [95]. Regulation of the cation composition made it possible to obtain the above-mentioned extremely high values of light yield in GAGG:Ce crystals [3, 94, 96]. The concentration dependence of light yield in $Lu_{1-x}Sc_xBO_3$:Ce crystals is explained similarly to garnets [97, 98]. In certain systems, for example, lutetium-yttrium oxyorthosilicate $Lu_{2x}Y_{2-2x}SiO_5$:Ce (LYSO:Ce), shallow traps have little effect on the efficiency of the scintilla-

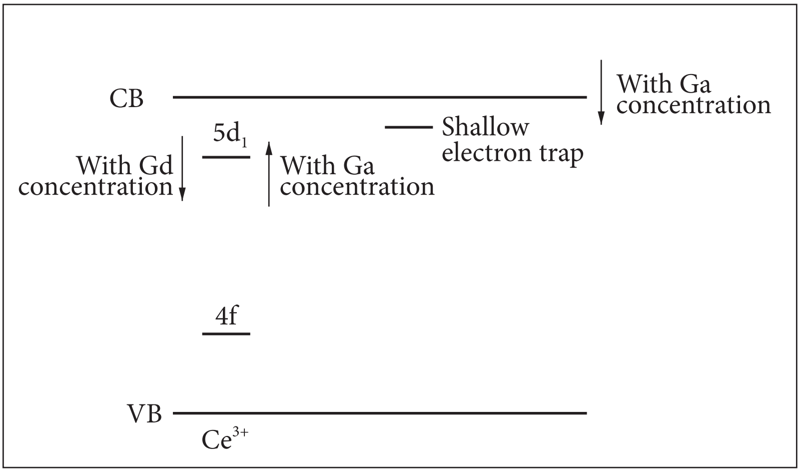

Fig. 1.5. $Lu_yGd_{1-y}(Al_xGa_{1-x})_5O_{12}$:Ce energy structure according to [12]

tion process, and deep traps associated with oxygen vacancies are responsible for electron capture; then the increase in luminous flux can be caused by an increase in the thermal stability of luminescence centers by moving them away from the edge of the conduction band. Such a phenomenon was observed in [99], where the introduction of Y increases the energy interval between the 5*d* level of Ce^{3+} and the bottom of theconduction band.

In general, although the factor of modification of the energy structure in the behavior of the light output in some systems is obvious, its contribution to the scintillation process in most known mixed systems remains unclear.

1.3.2. Limitation of the thermalization length and/or thermal diffusion of charge carriers

Another factor influencing the concentration dependence of the light yield in a mixed crystal is associated with a decrease in the thermalization lengths and thermal diffusion of charge carriers, which increases the probability of radiative recombination of geminate charge carriers (i.e., carriers that formed in one multiplication act) by their capture at the luminescent center. So, let's consider the factors that lead to a decrease in the carrier thermalization length in a solid solution. Data on light yield in several scintillators based on mixed crystals were presented in [13]. It was concluded that the deviation of the light yield in mixed crystals from a linear dependence is systematic, and there should be a general mechanism that explains this phenomenon. Electron-phonon interaction, which affects the efficiency of the primary excitation of the luminescent center, was proposed as such a factor in [13]. In a simple binary crystal, AC or BC (A, B are cations, C is an anion) there is only one type of longitudinal optical phonons. If the energy of optical phonons is higher than the thermal energy $k_B T$, thermalization takes place in two stages [100]: the electron loses energy due to the emission of optical phonons until the kinetic energy of the electron reaches the interval from 0 to the energy of the optical phonon. After this stage, electrons continue to lose energy much more slowly through interactions with acoustic phonons. The higher the energy of the optical phonon is compared to $k_B T$, the longer the thermalization stage of the acoustic phonons, and the longer the average thermalization length of the electron until it reaches the thermal energy. The simulation results indicate that when going from a pure to a mixed crystal, its phonon spectrum is significantly modified. In crystals with two or more types of optical phonons (in particular, in the $A_{1-x}B_xC$ solid solution of two binary crystals), the thermalization process is accelerated due to an increase in the energy relaxation rate. In particular, if the phonon frequencies are significantly different, the rapid relaxation of high-energy phonons is followed by the relaxation stage of optical phonons with lower energy. Thus, the thermalization length becomes shorter than that in a «pure» crystal. Consequently, the appearance of new bands in the phonon spectrum corresponds to the concentration of electron-hole pairs at distances less than the Onsager radius and the minimization of stochastic carrier recombination and nonradioactive losses.

The diffusion length decreases not only due to the increase in inelastic scattering. It is also assumed that another reason for the decrease in the thermalization length in a mixed crystal is the elastic scattering of hot carriers on inhomogeneities in the crystal. Therefore, the diffusion length of thermalized carriers should also depend on the spatial heterogeneity in the mixed crystal. The classification of condensed media into ordered or disordered ones is deeply idealized. A theoretical analysis that takes into account the real arrangement of atoms in space is very complicated and can be carried out only with significant simplifications. The atoms in a crystal are ordered according to the type of crystal lattice, on which compositional fluctuations (alternation of atoms, rows of atoms, or planes) are superimposed when it comes to a substitutional solid solution. These fluctuations in the distribution of atoms and their complexes are associated with the peculiarities of statistical physics, which considers the behavior of atoms and other particles or quasi-particles, as well as with the peculiarities of the formation of ordered structures [101]. The real distribution of atoms in a disordered system cannot be considered chaotic. Fluctuations in the composition and interatomic distances in this case lead to the emergence of atomic complexes (clusters), which is a characteristic feature of the structure of disordered substances. These clusters are local formations in which the short-range part of interatomic interactions plays a special role in the formation of the structure and physical properties [102].

Historically, short-range order refers to the distribution of atoms in amorphous or liquid substances, for example, in liquid crystals. In this case, we are

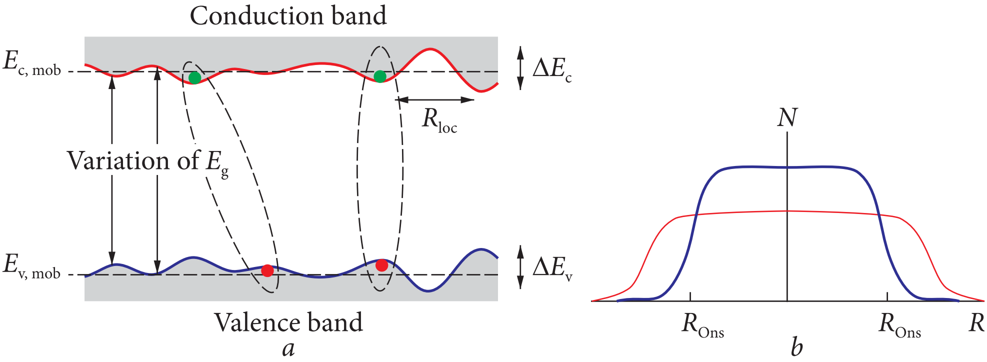

Fig. 1.6. The effect of inhomogeneities on the transport of charge carriers in mixed crystals. With isovalent substitution of atoms, inhomogeneities of the electronic structure and potential barriers are formed that limit the diffusion length of electrons and holes (*a*). This leads to the concentration of electron-hole pairs inside the Onsager sphere (*b*) and minimizes the probability of stochastic recombination [88]

considering the short-range ordering of atoms of different types in a solid. Along with long-range (translational) order in single crystals, short-range order exists at distances of up to several periods of the crystal lattice. Short-range ordering in mixed crystals is the inhomogeneity in the distribution of substituted atoms in a solid solution. At the same time, the type of crystal structure, as a rule, remains unchanged, although the parameters of the crystal lattice must change depending on the size and other properties of substituted atoms. Using the example of metal alloys, it was shown [103, 104] that the size of substituted atoms and their relative concentrations affect the short-range ordering, i.e., their relative distribution in the crystal lattice. There are regions (domains, clusters) enriched with one of the substituted atoms. Such fluctuations in the composition of metal alloys lead to the modulation of the crystal potential and the reduction of the electron diffusion length, which changes many physical characteristics of the alloy, for example, increasing the electrical resistance. Therefore, the short-range ordering factor should also affect the length of thermalization/thermal diffusion of secondary charge carriers. In scintillation crystals, which are mostly dielectrics, the existence of such domains should lead to fluctuations in the value of the crystal potential at the boundaries of such clusters, a decrease in the diffusion length of secondary electrons and holes, and contribute to the localization of electronic excitations inside the Onsager sphere. As was indicated above, the difference in bandgap widths of the mixed crystal components can exceed 1 eV, i.e., on the boundaries of domains enriched in one of the components, the amplitude of the E_g fluctuation is significant.

Electrons with energies $<E_{c,mob}$ and holes with energies $>E_{v,mob}$ (Fig. 1.6) can be localized in the same fluctuation with a lower E_g or in different energy «pits». Genetic recombination is enhanced if the localization radius R_{loc} is ap-

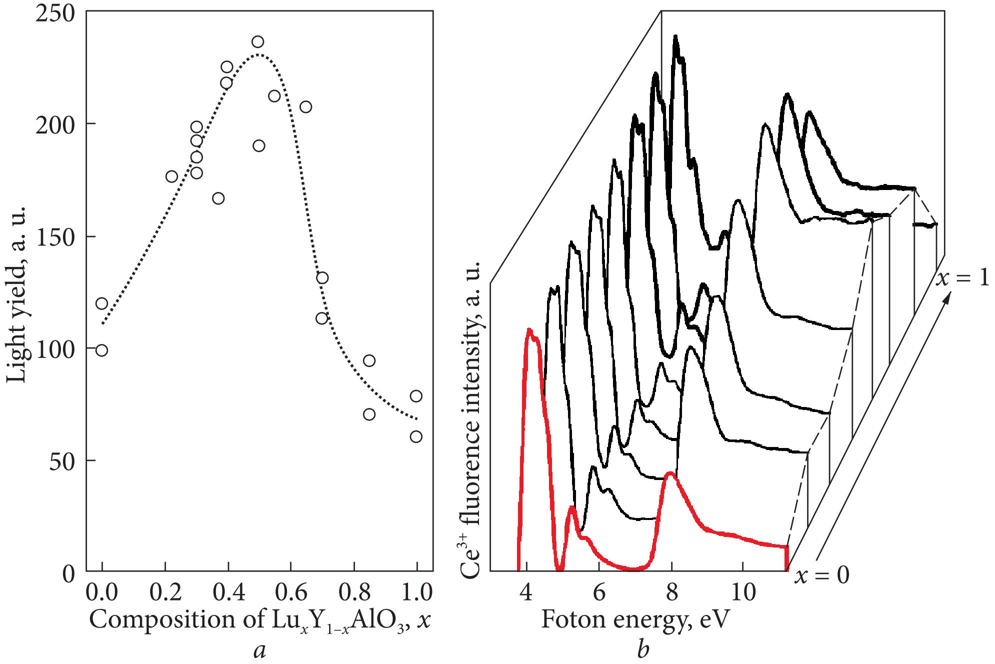

Fig. 1.7. Dependence of light yield of $Lu_{1-x}YAlO_3$:Ce crystals (*a*) luminescence excitation spectra of Ce^{3+} in a series of LuYAP:Ce solid solutions (*b*) [11]

proximately equal to the average distance between an electron and a hole. Efficient recombination does not occur if the localization radius is smaller than the Onsager radius. Too large domains will not affect the thermalization length because R_{loc} will exceed the average distance between electrons and holes.

In [100], an attempt was made to estimate the size of clusters and the amplitude of E_g fluctuations at their boundaries. For this, the effect of statistical disorder on the distribution of substituted ions in the crystal lattice was considered. For the appearance of clusters consisting of atoms of the same type, there must be a certain interaction between them. Without clarifying the nature of these interactions, authors of [100] use the concept of the affinity of atoms AA and BB, or AB in the $A_xB_{1-x}C$ solid solution, which is given by the probability of neighboring crystallographic positions being occupied by atoms of the same or different type. The calculations were performed for a conventional crystal with a cubic structure consisting of components AC and BC, in which $E_{gAC} > E_{gBC}$, $\Delta E_g = E_{gAC} - E_{gBC} = 1$ eV, and substitution occurs in the cationic sublattice.

It turned out that the modulation amplitudes are significantly higher than in the case of a chaotic distribution of atoms and approach ΔE_g. The largest clusters occur at $x = 0.3$ or $x = 0.9$. This indicates the formation of nanoscale

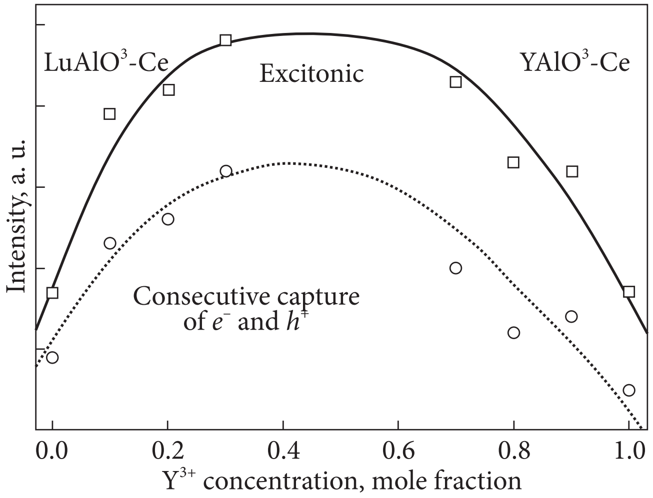

Fig. 1.8. Efficiency of charge transfer to excitons (upper curve) and sequential capture of electron-hole pairs (lower curve) [11]

clusters with sizes up to several lattice parameters in the ranges $0.1 < x < 0.3$ and $0.7 < x < 0.9$. They are enriched with one of the cations and are surrounded by domains enriched with cations of another type. At low affinity, short-range ordering occurs in the solid solution, while at a strong affinity of AA and BB the size of these clusters can increase to 8 lattice parameters. Regarding the situation with AB affinity, as expected, the modulation values ΔE_g are minimal, since in this case the formation probability of the clusters enriched in one of the cations with a size at least on the order of the elementary crystal lattice is low.

That is, if the electron-phonon interaction affects the reduction of the diffusion length of carriers with energies slightly above kT, then spatial inhomogeneities can slow down carriers with significantly higher energies. In addition, if the domain size coincides with the electron-hole interaction radius, the probability of exciton formation and its subsequent transfer to the activator increases. For the first time, this hypothesis was presented in [11] when considering the reasons for the increase in light yield in the LuYAP:Ce mixed crystal in the concentration range of 30—70% (Fig. 1.7).

Indirect evidence of the influence of domain formation on scintillation efficiency at a certain component ratio in a mixed crystal is an increase in the efficiency of carrier transfer to the activator, which is determined by the type of excitation spectrum in vacuum ultraviolet (Fig. 1.7*b*). One pair with energy close to E_g is formed upon excitation near the edge of the fundamental absorption. 2—4 electron–hole pairs can be formed upon excitation by photons with energies of $3–5E_g$, and the average energy of electrons and holes is approximately $1/2E_g$ in relation to the bottom of the conduction band and the upper edge of the valence band. During thermalization, some of them can fly to a distance greater than the radius of capture by the cerium ion and not participate in the scintillation process, but leads to afterglow and other slow processes. Thus, the ratio of luminescence intensities upon excitation at 20—30 eV (~4E_g) and 6—7 eV (~E_g) is an evidence of the participation of electron-hole pairs in the scintillation process. In LuYAP:Ce, the highest efficiency was obtained in the medium concentration range (Fig. 1.8), where the maximum light yield was observed [11]. However, the increase in the efficiency of energy transfer to the activator estimated by the ratio I(~4E_g)/I(~E_g) can also be associated with other factors listed in subsections 1.3.1.—1.3.2, in particular with the minimization of trapping of carriers at these concentrations of lutetium and yttrium.

In Chapter 4 of this monograph, an attempt is made to estimate the contributions of all the listed factors to the scintillation process in solid solution crystals. Other possible reasons for the increase in light yield in mixed crystals are also discussed.

CHAPTER 2

TECHNOLOGICAL CONDITIONS FOR OBTAINING SCINTILLATORS BASED ON SOLID SUBSTITUTION SOLUTIONS

Melt growth methods are most common for solid solution-based scintillation crystals. This is because the size of the crystals in these methods is, in principle, limited only by the size of the crucible and the possibility of growing a crystal with a certain crystallographic orientation on a single-crystalline oriented seed. One of the main requirements for a compound to be obtained from a melt in the form of a single crystal is its ability to melt and crystallize congruently, that is, not to decompose into other compounds.

Therefore, the process of obtaining crystals of solid solutions from the melt is complicated by the presence of many components with different melting temperatures, which can crystallize at different speeds and enter the crystal unevenly, resulting in the appearance of inclusions and even cracks. To obtain high-quality crystals of solid solutions, they are usually crystallized at a slower rate. This effect was studied [10] in the example of $RE_3Ga_5O_{12}$ single crystals (RE is a rare earth element). A correlation was shown between the difference in melting temperatures of the components of the solid solution and the maximum allowable rate of crystal growth, at which no visible inclusions are observed. The growth rate of the $Nd_{1.5}Gd_{1.5}Ga_5O_{12}$ crystal with a difference in melting temperatures of 140 °C between its components $Nd_3Ga_5O_{12}$ and $Gd_3Ga_5O_{12}$ should be ~0.8 mm/h, although specifically for these components of the mixed crystal, the growth rates of 5.6—6.8 mm/h were acceptable.

Another important factor, which will be discussed in detail in later chapters, is the rate of evaporation of melt components in mixed crystals. Different partial pressures of the melt components lead to its nonstoichiometry and the formation of structural defects. This effect is especially significant at a large ratio of the open surface of the melt to its volume, for example, in the micro-pulling (m-PD) method. So, let us dwell in more detail on the main melt growth methods that were used in our work to obtain scintillation crystals based on solid solutions.

The authors of this book obtained several oxide scintillation crystals based on substitutional solid solutions. Melt growing methods (Czochralsky and micro-pulling-down (m-PD)) as well as the ceramic solid-phase synthesis were used (Table 2.1). The latter method is more relevant for obtaining a series of samples of rare earth tantaloniobates with very high melting points.

The most common crucible methods are the Czochralski method, the Kyropoulos method, and the Bridgman-Stockbarger method. Among the above-mentioned methods, the Czochralski is the most suitable because of no contact of the crystal with the crucible surface, unlike the Bridgman-Stockbarger method. Therefore, the Czochralski method was chosen to obtain bulk crystals of LGSO:Ce, GAGG:Ce, YAGG:Ce, YAGP:Ce, GAGP:Ce, and GTNO.

For some new applications of scintillators, for example, new experiments in particle physics with simultaneous registration of scintillation and Cherenkov signals, detectors should be manufactured in the form of single-crystal fibers with a cross section of 1—4 mm^2. One of the effective methods of obtaining such fibers are the micro-pulling method, which allows obtaining fibers of the desired size and shape without further mechanical processing. Crystal fibers of YAGG:Ce and LGSO:Ce were obtained by this method in our work. Taking into account the need to reduce the growth rate in mixed crystals to prevent the formation of defects [10], the optimal growth rates of solid solutions crystals by the Czochralski and micro-pulling methods were lower (Table 2.1) than is usually accepted for their components — 0.5—2 mm/h instead of 2—4 mm/h in the Czochralski method and 6—12 mm/h instead of 12—30 mm/h in the micro-pulling method.

2.1. Obtaining crystals by the Czochralski method

2.1.1. YAGG:Ce and GAGG:Ce

Due to the need to obtain mixed crystals with isovalent substitution by rare earth cation and/or Al^{3+}/Ga^{3+}, the conditions for obtaining single crystals of yttrium-aluminum-gallium garnet $Y_3(Al_{1-x}Ga_x)_5O_{12}$, YAGG, and gadolinium-aluminum-gallium garnet ($Gd_3Al_{5-x}Ga_xO_{12}$, GAGG), activated by cerium were determined. Both mixed crystals containing gallium cannot be grown using W/Mo crucibles Therefore, growth was carried out exclusively from iridium crucibles. Crystals

Table 2.1. **Dimensions and growth rates of solid solutions crystals**

Method for obtaining	Czochralski	Micro-pulling-down (m-PD) method	Solid phase synthesis
Growth rate, mm/hour	0.5—2	3—60	
Grown crystals (their maximum dimensions, mm)	LGSO:Ce (∅45 × 150) YAGG:Ce (∅35 × 150) GAGG:Ce (∅45 × 200) GTNO (∅15 × 50)	LGSO:Ce (2 × 2×100) YAGG:Ce (∅2 × 70)	GTNO YTNO

Fig. 2.1. Thermal insulation element (*a*) and seed holder (*b*) covered with gallium oxide condensate. Gallium oxide condensate on the seed holder after adding oxygen to the growth atmosphere (*c*)

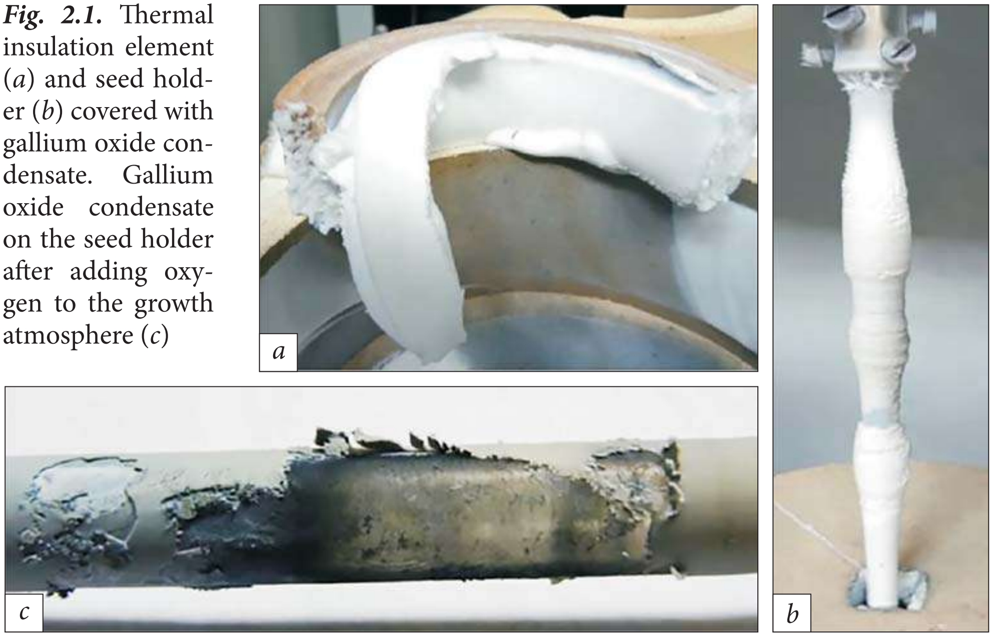

of $Y_3Al_{5-x}Ga_xO_{12}$:Ce (YAGG:Ce), $x = 0, 0.2, 0.4, 0.6, 0.75, 0.85, 1$ (concentrations in the melt) with a diameter of 22—35 mm and up to 150 mm in length were grown on seeds with the orientations [111] and [100] by the Czochralski method using iridium crucibles with a diameter of 40—60 mm and a height of 30—40 mm. Appropriate mixtures of oxide powders of Y_2O_3, Al_2O_3, Ga_2O_3, and CeO_2 with a purity of 99.99% were used as raw materials. The growing atmosphere was Ar + 1% O_2. Oxygen was added to the atmosphere to suppress evaporation of melt components. The concentration of CeO_2 in melts was maintained at the level of 1 mol.%. A crystal with a Ga content of 75 at.% was grown from a melt containing 0.15 at.% Ca^{2+}. The concentration of CeO_2 in melts was maintained at the level of 1 mol.%. A crystal with a Ga content of 75 at.% was grown from a melt containing 0.15 at.% Ca^{2+}. The process of synthesis of the charge as a whole is described by the equation of solid-phase synthesis $3Y_2O_3 + {}$ $+ (5-x)Al_2O_3 + xGa_2O_3 \rightarrow (T) \rightarrow 2Y_3Al_{5-x}Ga_xO_{12}$. Single crystals of YAGG:Ce are characterized by:

- the existence of the garnet phase and congruent melting in the entire range of concentrations of substitution of aluminum by gallium;
- cubic crystal lattice (isotropy of physical properties);
- melting temperature from 1800°C to 1950°C depending on gallium concentration;
- high isomorphic capacity of the crystal lattice.

However, there are several complications in their fabrication technology, in particular:

- the presence of a volatile component of gallium oxide, which begins to evaporate from the melt in the form of $Ga_2O + O_2$ at temperatures >1500 °C, which leads to the non-stoichiometry of the melt;
- the tendency of mixed crystals to crack due to the large difference in the radii of the trivalent ions of gallium and aluminum.

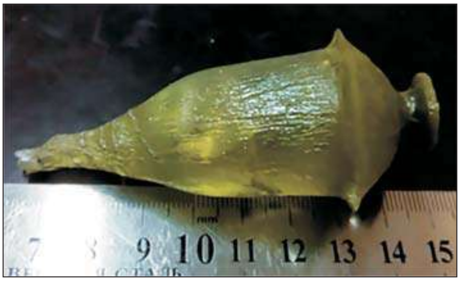

Fig. 2.2. YAGG:Ce crystal (75 at.% Ga) with cracks grown under non-optimal thermal conditions

An excess of gallium oxide in the amount of 1—3 at.% was added to the crucible with the melt to compensate for losses during its evaporation from the melt. However, in practice, this modification only led to stronger evaporation of gallium oxide that can be illustrated by Fig. 2.1. Such intense evaporation could be the reason for the growth of crystals with a large number of inclusions and cracks (Fig. 2.2). In some experiments, due to the condensation of gallium oxide on the seed surface and the reaction between them, the crystal detached from the seed and fell into the crucible with the melt. To reduce the intensity of gallium evaporation, 1 vol.% of oxygen was added to the inert growth atmosphere. This reduced the amount of gallium oxide that deposited on the insulation, but evaporation remained strong. In Figs. 2.1*b*, *c*, one can see a seed holder covered with gallium oxide condensate.

As a result of the implementation of this technological approach, it was possible to obtain single-crystalline YAGG:Ce without cracks and with a small number of inclusions. A feature of this mixed crystal was its uneven surface with numerous grooves, as can be seen, for example, in Figs 2.2, 2.3. Small iridium particles trapped on the YAGG:Ce surface were also observed. The iridium inclusions, probably, arose due to a sufficiently high concentration of oxygen in the growth atmosphere, which was used to prevent gallium oxide from volatilizing.

When crystals are grown in an inert gas atmosphere protected by iridium equipment, color centers associated with oxygen vacancies are formed. The latter negatively affects the optical and scintillation properties. Oxygen deficiency after crystal growth was neutralized by diffusion of oxygen to the crystal lattice during annealing of crystals in an oxygen-containing atmosphere at temperatures of 1300—1500 °C for a long time (depending on the size of the sample). Annealing also significantly reduces the thermoelastic stresses generated in the crystal during growth. The latter manifests themselves in the cracking of crystals during mechanical processing, and sometimes even with the slightest mechanical contact. The crystal coloration weakened after annealing, which indicates compensation for oxygen vacancies formed when growing crystals in an inert atmosphere.

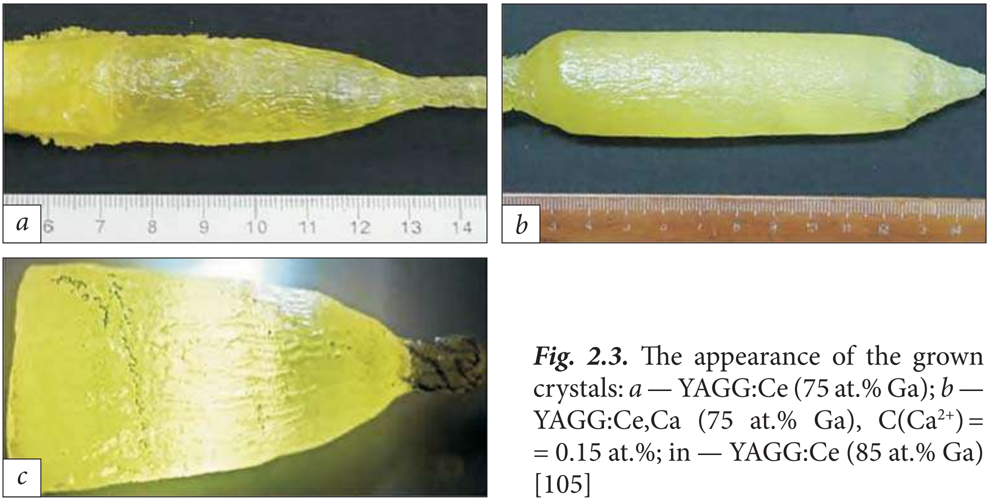

Fig. 2.3. The appearance of the grown crystals: *a* — YAGG:Ce (75 at.% Ga); *b* — YAGG:Ce,Ca (75 at.% Ga), C(Ca^{2+}) = = 0.15 at.%; in — YAGG:Ce (85 at.% Ga) [105]

Table 2.2. **The concentrations of matrix atoms in YAGG:Ce crystals determined by the AES-ICP method [105]. X-ray data (XRD) column is provided for comparison**

Melt composition	Measure	Concentrations, at.%			Ga/(Al + Ga)		Y/ (Y + Al + + Ga)	k_{ef}(Ce)
		Y	Al	Ga	ICP-AES	XRD		
$Y_3Al_5O_{12}$	Top	13.11	22.59	—	0	0	0.367	0.075
	Bottom	13.52	23.47				0.365	
$Y_3(Al_{0.8}Ga_{0.2})_5O_{12}$	Top	13.13	18.73	4.03	0.177	0.154	0.366	0.074
	Bottom	13.37	19.25	4.06	0.174		0.364	
$Y_3(Al_{0.4}Ga_{0.6})_5O_{12}$	Top	13.92	8.24	15.43	0.652	0.662	0.370	0.133
	Bottom	14.05	8.27	15.48	0.652		0.372	
$Y_3Ga_5O_{12}$	Top	14.74		23.48	1	1	0.386	0.166
	Middle	14.82	—	23.79			0.384	
	Bottom	14.87		23.74			0.385	

Experiments confirmed that there is a continuous series of solid solutions in the $Y_3(Al_{1-x}Ga_x)_5O_{12}$:Ce system. The lattice parameter increases smoothly with Ga concentration (Table 2.2). Deviation from Vegard's law is not observed for YAG and YAGG, in contrast to the results in [106]. According to the X-ray diffraction data, the proportion of Ga in the crystals is 15.4, 36.6, and 66.2 at.% when grown from a melt containing a proportion of Ga of 20, 40, 60 at.%, respectively. Thus, the distribution coefficient of Al and Ga in crystals is approximately 1.

Due to the proximity of the ionic radii of Y^{3+} and Al^{3+}, Y^{3+} can occupy Al^{3+} or Ga^{3+} positions in the crystal lattice («antisite defect»), and vice versa [107]. In

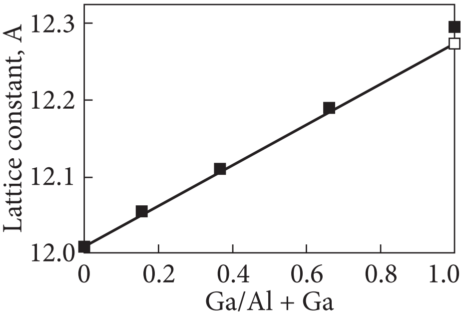

Fig. 2.4. Dependence of the YAGG:Ce unit cell volume on the Ga concentration in the solid solution. Filled symbols correspond to experimental values, empty squares correspond to data [105]

general, the formation of such defects in rare-earth garnets is considered as a negative factor, which leads to a deterioration of the light yield and an increase in the contribution of the slow components of the scintillation response [108, 109]. The probability of such substitution increases when the difference between the ionic radii of Al^{3+} (Ga^{3+}) on the one hand, and Y^{3+} or lanthanide, on the other hand, decreases. It was shown [108] that in the YGG crystal, the excess Y is formed due to the substitution of Ga^{3+} for Y^{3+} in octahedral positions. That is, the real composition of the crystal should be determined by the formula $Y_3(Y_xGa_{2-x})Ga_3O_{12}$ [109]. The lattice constant is 12.274 Å in stoichiometric YGG it increases with x in the case of $Y_3(Y_xGa_{2-x})Ga_3O_{12}$ substitution.

In accordance with this data, the lattice constant value of 12.295 Å in the YGG crystal grown by us corresponds to x about 0.1, i.e., 5 at.% of Ga^{3+} in octahedral positions is replaced by Y^{3+}. However, this is a rough estimate because the data [108] were obtained on powders or crystals grown from solution. In addition, in our case, the crystals also contain large Ce^{3+} cations, which can increase the lattice constant. As a result, there is a deviation of experimental points for YGG from Vegard's law (Fig. 2.4).

AES-ICP data give a detailed picture of the cation distribution in the solid solution. AES-ICP and X-ray diffraction data for the Ga/(Al + Ga) ratio agree within 1% (see Ga/(Al + Ga) column in Table 2.2). A certain increase in the Y/(Al + Ga) ratio is observed with increasing Ga content. The Y/(Y + Al + Ga) ratio clearly increases from YAG to YGG, evidencing the increase in the number of antisite defects. However, the experimental value is only ~1% higher than the theoretical value (3/8 = 0.375) for YGG. Measurements of Al and Ga concentrations in different parts of the crystals indicate extremely small fluctuations of the Al/Ga ratio along the crystals, which indicates their good homogeneity. The Ce segregation coefficient increases with the addition of Ga to the melt from 0.07 in YAG to 0.17 in YGG due to lattice loosening with the addition of larger Ga^{3+} atoms. According to these results, k_{ef}(Ce) in YAGG:Ce with a Ga content of 75—85% is about 0.15.

Unlike the YAG-YGG system, the garnet phase in GAGG is formed in the interval from approximately $x = 2$ [3] and the highest light yield and energy resolution are observed at $x = 2.5$—3 [4, 85]. In our work, crystals of GAGG and GAGG:Ce, $x = 2.5$ (concentration in the melt) with a diameter of up to 45 mm and a length of up to 200 mm without cracks and visible inclusions (Fig. 2.5) were

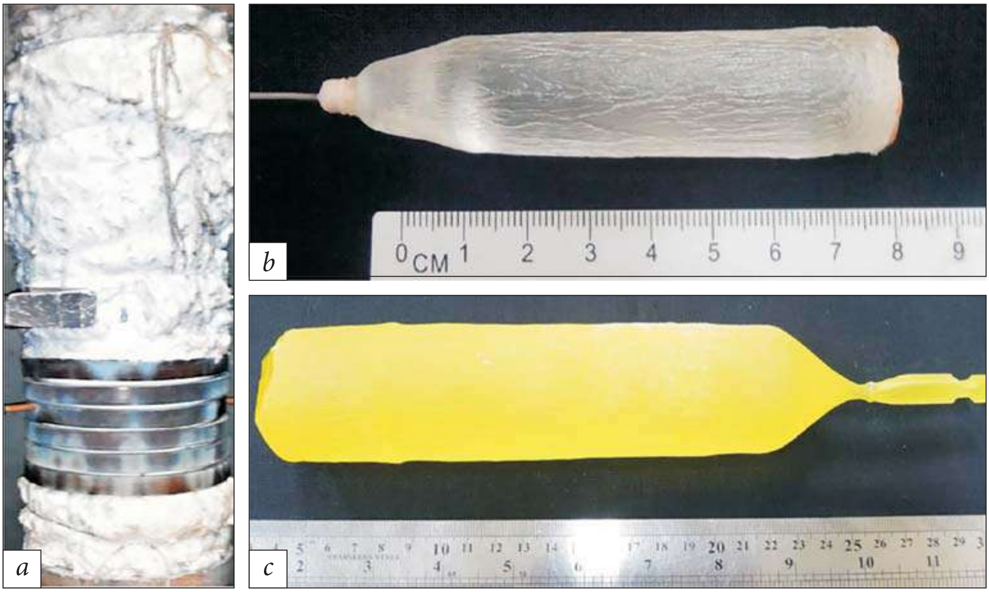

Fig. 2.5. Crystallization unit covered with a layer of kaolin blanket (*a*); manufactured GAGG (*b*) and GAGG:Ce (*c*) crystals

grown on a seed with [100] orientation by the Czochralski method using iridium crucibles with a diameter of 60—90 mm and a height of 60—90 mm. Undoped GAGG crystals, due to the lack of crystal seeds of acceptable quality with a garnet structure that does not contain an activator, were grown on iridium wire with a diameter of 1 mm. Appropriate mixtures of oxide powders of Gd_2O_3, Al_2O_3, Ga_2O_3, and CeO_2 with a purity of 99.99% were used as raw materials. An excess of Ga_2O_3 in the amount of up to 1 wt.% was added to the melt to compensate for its evaporation during growth. The growth atmosphere was Ar + 1% O_2.

Thus, the features of the technology for obtaining single crystals of gadolinium-aluminum-gallium garnet GAGG:Ce are:

«the existence of the garnet phase and congruent melting only in a certain range of gallium concentrations, since the garnet phase does not form at a gallium concentration <20 at.%;

- the melting temperature of the order of 1800 °C (decreases with gallium concentration) allows using the same technological equipment as for the other systems listed above;
- a large isomorphic capacity of the crystal lattice.

Technological complications of the process of obtaining GAGG:Ce single crystals are as follows:

- as in the YAGG system, in GAGG, there is a volatile component, gallium oxide, which begins to evaporate from the melt in the form of $Ga_2O + O_2$, starting at a temperature of 1500 °C, which shifts the stoichiometry of the melt and the crystal;

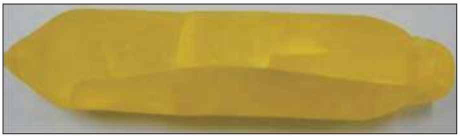

Fig. 2.6. Cracks in the GAGG:Ce crystal that formed just after the crystal was discharged from the growth furnace

- the tendency of crystals to crack due to the large difference in the ionic radii of the trivalent gallium and aluminum ions;
- the high cost of gallium oxide with a purity of 4*N* or higher.

The process of preparing the charge, loading the crucible for GAGG:Ce is described by the solid-phase synthesis equation 2.3:

$$3Gd_2O_3 + (5-x)Al_2O_3 + x\,Ga_2O_3 \rightarrow T \rightarrow 2Gd_3Al_{5-x}Ga_xO_{12}. \quad (2.3)$$

Judging by the amount of gallium oxide that deposited on the walls of a standard thermal unit when growing GAGG:Ce with the addition of oxygen in the chamber atmosphere, the intensity of gallium oxide evaporation was similar to YAGG:Ce crystals. However, in the case of GAGG:Ce, it was not possible to obtain complete, undamaged single crystalline boules. Due to remaining mechanical stress after crystal growth, they sometimes crack just after detachment from the seed holder (Fig. 2.6). To reduce temperature gradients along the grown crystal axis, it was decided to apply another layer of thermal insulation in the form of a kaolin blanket. To avoid the temperature shock that occurs after the crystal is separated from the melt at the end of growth, the crystal was not separated from the melt, but frozen to it. The crystals were cooled down in a thermal assembly after the end of growing for 60 hours. Post-growth annealing of GAGG:Ce crystals was carried out by holding them in a uniform thermal field in an air atmosphere at a temperature of 1100—1500°C for 10 hours with prolonged heating and cooling for 60 hours.

Thus, a necessary requirement for obtaining single crystals based on YAGG:Ce and GAGG:Ce is the need to reduce the axial temperature gradient in the crystal to prevent a temperature shock when the crystal separates from the melt. To prevent cracking of single crystals during cooling and manufacturing of elements, they were annealed in air at temperatures of 1100—1500 °C. This made it possible to obtain high-quality crack-free crystals up to ∅35 × 150 mm for YAGG:Ce and ∅45 × 200 mm for GAGG:Ce.

2.1.2. LGSO:Ce

Crystal lattices of two types of monoclinic symmetry are formed in $Lu_{2x}Gd_{2-2x}SiO_5$:Ce crystals ($0< x< 1$) depending on x [110, 111]. The structural transition is observed around $x = 0.2$ (Fig. 2.7). At $0< x< 0.2$, the monoclinic $P2_1/c$ structure is observed, and at $0.2< x< 1$, the monoclinic $C2/c$ structure is observed. In both intervals, a continuous series of solid solutions is formed with smooth changes in the unit cell volume and lattice parameters. To find out the

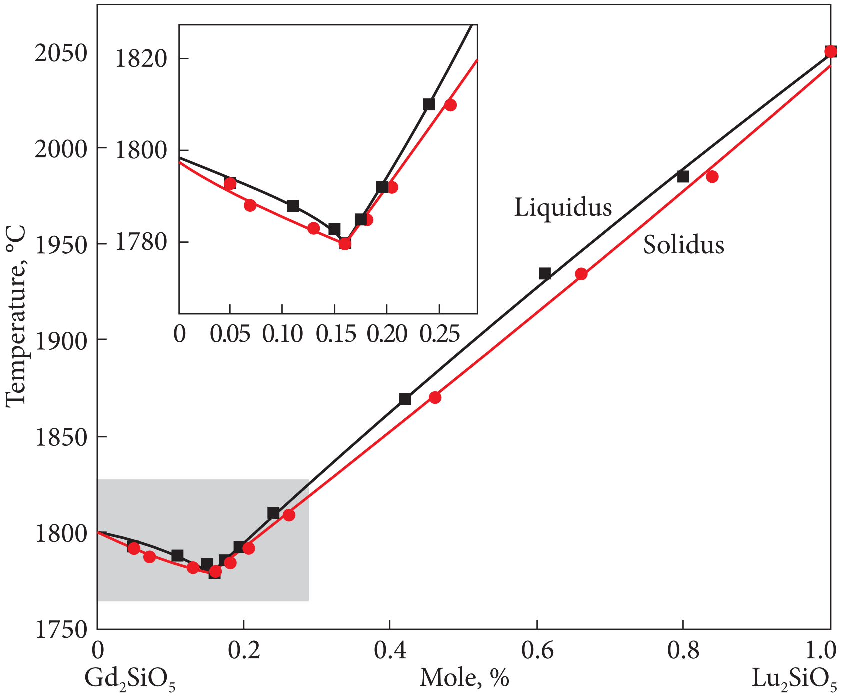

Fig. 2.7. Phase diagram of the Gd_2SiO_5-Lu_2SiO_5 system in accordance with [112]

concentration dependence of the scintillation parameters upon substitution of Lu/Gd in LGSO:Ce, it was necessary to grow single crystals of both phases.

Firstly, small-size LGSO:Ce crystals with a diameter of 30—45 mm and a length of 35—150 mm with different ratios of Lu/Gd were grown by the Czochralski method using the Lu_2O_3, Gd_2O_3, CeO_2, and SiO_2 starting materials with a purity not worse than 99.99% mixed in a stoichiometric ratio. When growing a Ca^{2+}-doped crystal (Ca content 0.05 at.%), Ca^{2+} was introduced into the melt in the form of $CaCO_3$. Crystals were grown in Ir crucibles with pulling rates of 1.5—2 mm/h (Fig. 2.8). A mixture of Ar + 0.3% O_2 was used as the growth atmosphere. Post-growth annealing of ingots was carried out in an oxidizing environment from 1100 to 1200 °C. Additionally, LSO:Ce samples were annealed in an oxidizing atmosphere at 1400 °C, taking into

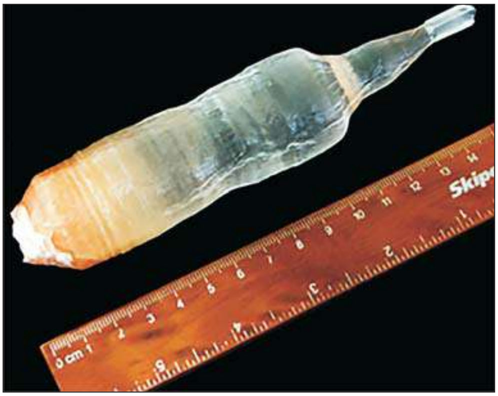

Fig. 2.8. Grown LGSO:Ce,Ca crystal

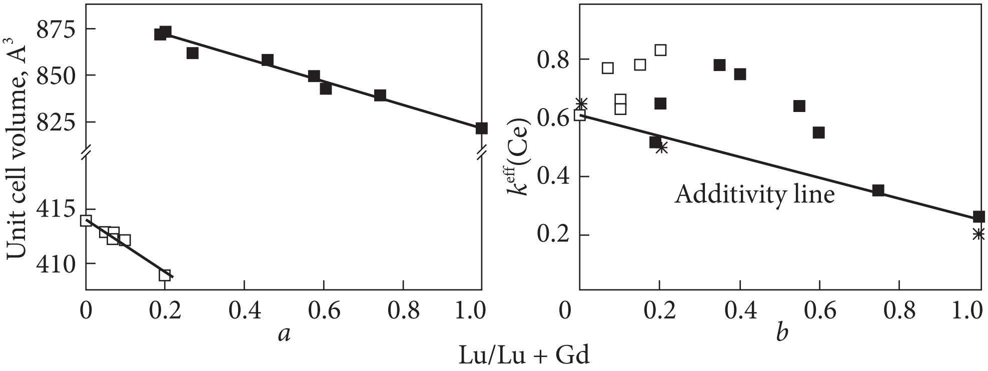

Fig. 2.9. Unit cell volume (*a*), cerium incorporation coefficient (*b*) in LGSO:Ce solid solutions. The asterisks in the figure correspond to literature data [114, 115]

account the slow oxygen diffusion in them [77]. Elements with dimensions of 10 × 10 × 2 and 10 × 10 × 0.5 mm^3 and polished faces of 10 × 10 mm^2 were made from the central parts of the ingots for measuring scintillation and optical characteristics.

The unit cell of LGSO gradually increases by ~5% when going from LSO to $Lu_{0.4}Gd_{1.6}SiO_5$ (Fig. 2.9*a*). Substitution of Lu^{3+} for Gd^{3+} leads to lattice loosening and easier incorporation of Ce^{3+} into the matrix, since the ionic radii of Lu^{3+}, Gd^{3+}, and Ce^{3+} are 86.1, 93.8, and 102 pm, respectively [113]. The dependence of k_{eff} on the host composition (Fig. 2.9*b*) is non-additive with a significant deviation to larger values. While for Lu/Lu + Gd from 1 to ~0.6, k_{eff} increases monotonously from 0.26 to 0.55 and can be explained by the higher content of the large Gd^{3+} cation, the further increase of k_{eff} to 0.8 is caused by some other factor. This phenomenon and significant fluctuations in k_{eff} values near the structural transition are probably associated with inhomogeneities in the crystal, namely, the existence of regions enriched in Lu^{3+} or Gd^{3+}. Conditions at the domain boundaries may favor the incorporation of more activators.

At the next stage, large-size LGSO:Ce crystals were grown to test their suitability for high-energy physics experiments. The main problem in obtaining LGSO single crystals is severe crystal cracking, which increases with increasing gadolinium content. Thus, to preserve the integrity of large-sized crystals, it is desirable to minimize the concentration of gadolinium. At the same time, the addition of gadolinium leads to increased light yield and improved energy resolution [6]. Thus, we chose the $Lu_{1.8}Gd_{0.2}SiO_5$:Ce composition for growing large-size crystals. In addition, to prevent the formation of cracks, we used an extended cooling time of 50—60 hours after crystal growth, as well as a lower growth rate — about 0.5 mm/h. As a result, crystals with a diameter of up to 35 mm and a length of up to 150 mm were obtained without cracks and visible inclusions in the main volume of the crystal.

2.1.3. $GdTaO_4$ and $GdTa_{0.8}Nb_{0.2}O_4$

Czochralski method was also used in the growth of $GdTaO_4$ and $GdTa_{0.8}Nb_{0.2}O_4$ crystals obtained in an Ar atmosphere with an oxygen concentration of up to 1 vol.%. Seed was performed on an iridium wire with a diameter of 1 mm. Due to the extremely high melting temperatures of the crystals, the thermal unit was additionally insulated to prevent damage to the iridium crucible. The crystal pulling speed was 1—2 mm/h, and the rotation speed was 10—20 rpm. Crystals with a diameter of 15 mm and a length of the cylindrical part up to 30 mm were obtained (Fig. 2.10).

Post-growth annealing of the grown crystals was carried out in the air atmosphere at 1500 °C. The crystals demonstrated a tendency to crack along the (010) cleavage plane, similar to that observed in Gd_2SiO_5 crystals having a cleavage plane along (100) [48]. Some parts of the crystals were polycrystalline or contained inclusions. However, the volume of transparent parts was enough to produce samples with dimensions of about $7 \times 7 \times 2$ mm^3 for optical and luminescence measurements.

2.1.4. BGSO

$Bi_4Ge_3O_{12}$ (BGO) crystal with a high density of 7.13 g/cm^3, a high atomic number (74), and a radiation resistance of 10^5—10^6 Rad has proven itself well in the L3 detector of the Large Electron-Positron Collider (LEP) at CERN [116]. However, the 300 ns decay time in BGO does not meet the requirements of Mu2e and similar projects. A sharp increase in the cost of raw materials of germanium oxide in recent years has led to an increase in the cost of BGO production by 2—3 times. This can be avoided by substituting BGO with bismuth silicate $Bi_4Si_3O_{12}$ (BSO), which is an analogue of BGO with the same eulitine crystal structure. Despite the reduced light output in BSO (2000 photons/MeV *vs.* 8000 photons/MeV in BGO) and worse energy resolution (20—25% at 662 keV *vs.* 10—15% in BGO), the decay time of BSO is significantly faster (100 ns *vs.* 300 ns in BGO). The density of BSO (6.8 g/cm^3) is similar to BGO. The main disadvantage of BSO is the difficulty of obtaining large crystals due to the incongruent melting of this composition. The transition to mixed crystals with a eulitine structure by partially replacing Ge with Si in the matrix [117, 118] is one of the possible ways to overcome this complication. There is a continuous series of solid solutions in the $Bi_4(Ge_xSi_{1-x})_3O_{12}$ (BGSO)

Fig. 2.10. Photo of grown GTNO crystal and fabricated samples for optical and scintillation measurements

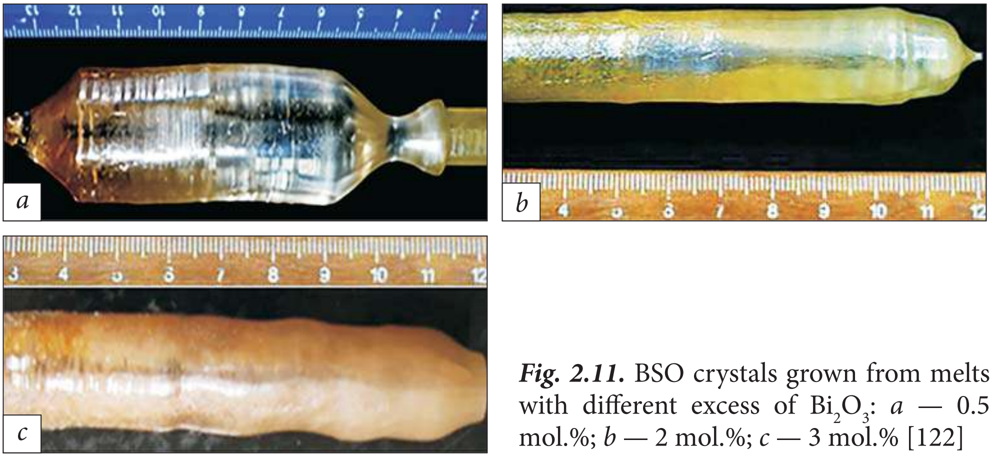

Fig. 2.11. BSO crystals grown from melts with different excess of Bi_2O_3: *a* — 0.5 mol.%; *b* — 2 mol.%; *c* — 3 mol.% [122]

system. The characteristics of BGSO crystals obtained by the methods of Stockbarger and Czochralsky [119, 120] are more similar to BSO than to BGO. The obtained energy resolution in BGSO at 662 keV did not exceed 19% [120]. The authors claim that this is a consequence of the large number of bubbles and inclusions of other phases. Future experiments in high-energy physics require a large number of high-quality crystals with similar characteristics [121], so methods for obtaining BGSO must be optimized.

In this chapter, the process of obtaining BGSO crystals with improved characteristics by the Czochralski method is considered in detail. The influence of the Si/Ge ratio, melt stoichiometry, recrystallization conditions, and post-growth annealing is discussed [122].

Bismuth oxide with a purity of 99.999%, germanium, and silicon oxides with a purity of 99.99% were used as starting materials. The crystals were grown from stoichiometric mixtures with the general formula $Bi_4(Ge_xSi_{1-x})_3O_{12}$, where x = 0, 0.1, 0.4, 0.7, 0.9, and 1. After mixing the oxides, the obtained mixtures were calcined at 850 °C for 10 hours to obtain the eulitine phase by solid-phase reaction. The upper and more transparent parts of BGO and BSO ingots grown earlier from stoichiometric mixtures of oxides were used as raw materials for recrystallization.

Crystals with a diameter of 20 mm were grown by the Czochralski method using Pt crucibles with radiofrequency heating. The pulling speed was 0.5—2 mm/h, the crystal rotation speed was 10—30 rpm. The BGO seeds were oriented in the [100] direction. To reduce the number of growth cycles, the effects of melt stoichiometry and recrystallization were studied only on crystals at $x = 0$ (which corresponds to BSO). Samples of crystals with dimensions of $4 \times 4 \times 6$ mm^3 and $10 \times 10 \times 2$ mm^3 with polished surfaces were prepared for the measurement of scintillation parameters. After growing, the samples were annealed in air at 850 °C for 10 hours.

Controlling the melt stoichiometry is of particular importance when growing crystals with the eulitine structure [122, 123] due to the evaporation of bismuth oxide from the melt, which leads to the melt non-stoichiometry and the formation of foreign phase inclusions in the crystals. To overcome this complication, an excess of Bi_2O_3 in the amount of 3 mol.% was introduced into the melt during the growth of BGSO [118]. At the same time, if the evaporation rate is less than expected, an excess of Bi_2O_3 in the melt can also deteriorate the quality of the crystals, so it was necessary to determine the optimal value of the bismuth oxide excess in the melt.

In [122], the influence of the deviation of the melt composition from stoichiometry on the quality of crystals was studied at $x = 0$ (BSO) with a 0.5 mol.%, 2 mol.%, and 3 mol.% excess of Bi_2O_3 relatively to the stoichiometric composition. Photographs of crystals grown with various excesses of Bi_2O_3 are presented in Fig. 2.11. With an excess of 0.5 mol.%, most of the crystal volume looks transparent, almost colorless. There are no separate absorption bands at in the range of >300 nm (Fig. 2.12). Increasing the excess of Bi_2O_3 to 2 mol.% leads to a greenish color and deterioration of transparency. With an excess of 3 mol.% Bi_2O_3, the crystal surface is opaque, beige in color. The appearance of a new absorption peak near 320 nm in the spectrum of this crystal (Fig. 2.12) and the coloration may be caused by the presence of foreign phases with a different stoichiometry. The color arises because foreign phases, such as silenite, have smaller bandgaps and, as a consequence, longer wavelengths of the fundamental absorption peak than the eulitine phase has. Crystals grown from a melt with a stoichiometric ratio of oxides contain many inclusions, including colored inclusions of other phases. It is highly likely that the optimal excess of bismuth oxide also depends on the Si/Ge ratio and thermal growth conditions.

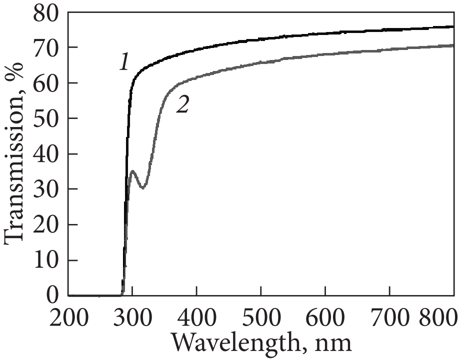

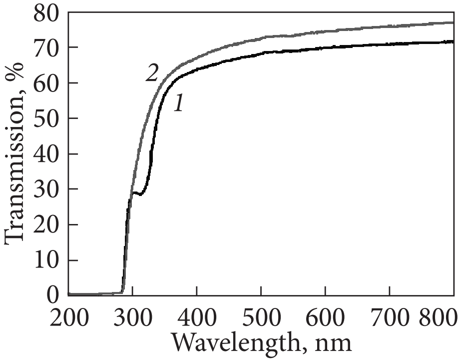

Fig. 2.12. Transmission spectra of BSO crystals grown from a melt of different stoichiometry: *1* — Bi_2O_3 excess is 0.5 mol.%, *2* — 3 mol.% [122]

Fig. 2.13. Optical transmittance of BSO crystals: *1* — grown from a stoichiometric mixture of oxides, *2* — recrystallized [122]

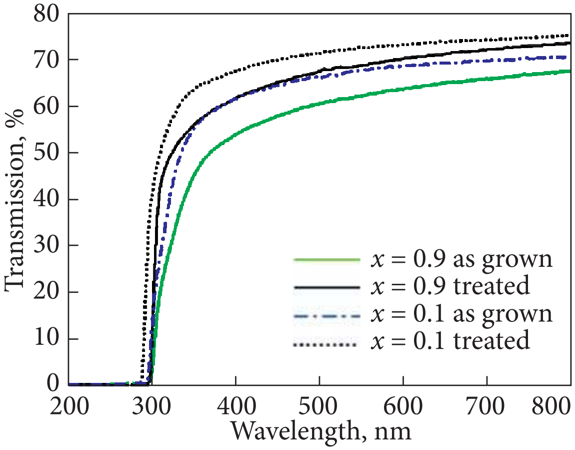

Fig. 2.14. Optical transmission spectra of $Bi_4(Ge_xSi_{1-x})_3O_{12}$ crystals with different x before and after annealing [122].

It is known that the quality of BGO crystals can be improved by recrystallization of the grown crystals, whereby the upper parts of the crystals grown from a mixture of powders were loaded into the crucible and the growth process was repeated [123]. This improves the transparency of the crystal and reduces the amount of gas impurities and inclusions of foreign phases. By analogy, the effect of recrystallization on optical transmission was tested on BSO grown from a melt with a stoichiometric ratio of oxides. As a result, the peak at 320 nm disappears after recrystallization (Fig. 2.13). This absorption peak is similar to that observed in crystals grown from raw materials with an excess of 3 mol.% Bi_2O_3 (see Fig. 2.12). Obviously, in the case of a change in stoichiometry, this peak is associated with the presence of foreign phases in the crystals or color centers.

Methods of improving the energy resolution of BGO crystals by high-temperature annealing in an oxidizing environment [124, 125] can be implemented for both BSO and BGSO with the same structure and similar optical characteristics.

The transmission of two BGSO crystals with different Si/Ge ratio improves in the entire measured wavelength range after annealing for 10 h at 850 °C (Fig. 2.14).In particular, the transmittance increases by 7% at the maximum of the luminescence band at 480 nm. The crystals were grown from a stoichiometric melt.

The presented data show the potential for improving the optical and scintillation characteristics of $Bi_4(Ge_xSi_{1-x})_3O_{12}$ by optimizing the methods of obtaining crystals. In particular, a better energy resolution of 16.2% at 662 keV is achieved in BGSO at $x = 0.7$. Crystal transparency can be improved by optimizing the amount of excess Bi_2O_3 in the melt, recrystallization, and post-growth annealing. Due to the large number of detectors needed for future high-energy physics experiments, future work will focus on identifying the ability to produce large crystals with stable characteristics.

2.2. Obtaining single-crystalline fibers using the micro-pulling-down method

The excellent work of the CMS electromagnetic calorimeter based on $PbWO_4$ (PWO) at CERN helped in the discovery of the Higgs boson [51]. However, increasing dose loads in colliders made it necessary to replace PWO-based detectors with lighter scintillators that suffer less radiation damage due to interaction with high-energy hadrons [126]. The construction of the FAIR calorimeter, the announcement of the renewed Large Hadron Collider (LHC), and its modernization (HL-LHC) [127] and the intensive development of the ILC program [128] will require cheap and radiation-resistant materials suitable for mass production. In addition, concepts of a new generation of high-energy physics experiments include combined electromagnetic and hadronic calorimeters based on simultaneous registration of scintillation and Cherenkov radiation [129]. For some new applications of scintillators, for example, new experiments in particle physics, detectors in the form of single-crystal fibers with a cross-section of 1—6 mm^2 are needed [130]. The production of fibers from large-sized single crystals grown by the Czochralski method is relatively expensive due to the given loss of material during cutting.

One of the effective methods of growing such fibers is the micro-pulling method (m-PD), which provides fibers of the desired size and shape without further mechanical processing [131, 132]. This method (Fig. 2.15) is significant-

Fig. 2.15. General view of the growth setup during micro-PD fiber growth. The crystallization process is monitored using a CCD camera

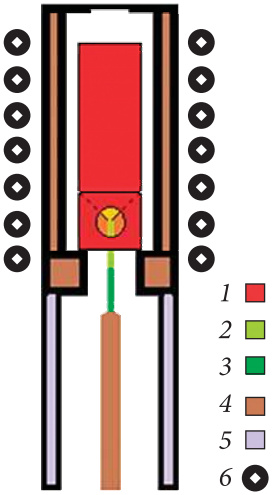

Fig. 2.16. Schematic view of the crystallizer for growing fibers by the micro-pulling method: *1*— crucible and screen; *2* — fiber; *3* — seed crystal; *4* — thermal insulation; *5* — quartz; *6* — HF heating inductor

ly different from the Chochralski method. The process of manufacturing crystals by the micro-pulling method allows the production of single-crystal rods of various shapes with a cross-section of up to ~9 mm^2. The ability to crystallize 100% of the melt is another advantage. The method allows you to reach a growth rate of up to 5 mm/min., which is much faster than that in most growth methods are very convenient for rapid analysis of new crystal compositions.

The production of scintillating materials in the form of fibers has a long history and a wide range of applications in the case of plastic organic scintillators. However, the low effective atomic number (Z_{eff}) of these materials limits the sensitivity of radiation detectors based on them. In recent years, inorganic scintillator fibers have been obtained using the micro-pulling method with a continuous improvement in their quality. The main task is to optimize the technology of growing fibers and achieve a uniform distribution of the activator and other impurities in them [133—138]. In the micro-pulling method, the melt flows through the capillary in the crucible bottom to the crystallization zone (Fig. 2.16). At a sufficient growth rate, the melt flows throughout the capillary so quickly that there is no back diffusion of impurities from the crystallization front through the capillary to the melt, unlike the Czochralski and other melt methods. Thus, the impurities are concentrated at the meniscus periphery and subsequently introduced into the grown fiber. As a result, the distribution of components along the fiber is almost constant. But a significant concentration gradient of the activator and other impurities can arise in the radial direction and negatively affect the optical and scintillation parameters of the fiber.

The μ-PD method has already been used to grow high-temperature oxide scintillators: $Lu_{2x}Y_{2-2x}SiO_5$:Ce (LYSO:Ce) [136], $Bi_4Ge_3O_{12}$ [136], complex borates [138], etc. Fibers with the structure of LuAG:Ce garnets and LYSO:Ce orthosilicates are considered as possible detectors for a new generation of calorimeters with simultaneous reading of scintillation and Cherenkov signals, with the possibility of additional application in PET tomography [139, 140]. LuAG:Ce and LYSO:Ce have good radiation strength and compactness due to their short radiation length.

In particular, a lot of information has been accumulated on the growth of rare-earth garnet fibers. The first reports on growing fibers with a garnet structure using a micro-pulling method are dated back to 2005—2010 [133, 134].

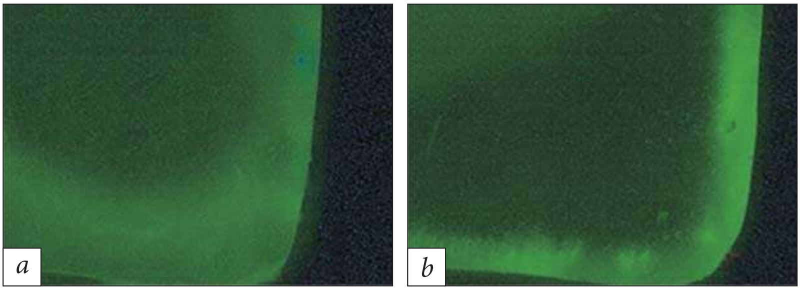

Fig. 2.17. Cross-section of YAG:Ce fibers with a transparency length of 16.5 cm and a cerium concentration of 150 ppm (*a*), and YAG:Ce with a transparency length of 1.7 cm and a cerium concentration of 1000 ppm (*b*) [142]

Both in LYSO:Ce and in garnets, the activator is Ce^{3+}, and there is a problem of its segregation to the periphery of the fiber due to the large difference in the ionic radii of the activator and the matrix cation [134, 135], which negatively affects the transparency of the fiber. The segregation is especially noticeable at a high activator concentration.

The radial gradient of cerium distribution in YAG:Ce fibers grown by micro-pulling with different concentrations of cerium was assessed using the gradient of its luminescence brightness (Fig. 2.17) in the cross-section of LuAG:Ce or YAG:Ce fibers [141—144]. The sample had a higher intensity of luminescence at the periphery than in the middle part, which confirms the high concentration of Ce^{3+} at the periphery of the fiber. However, it turned out that along the fiber axis the concentration of the activator can be maintained constant at a high growth rate, when the rate of melt flow through the capillary exceeds the rate of activator diffusion [142]; in particular, for LuAG:Ce, the rate of 0.5 mm/min was indicated [142]. The stable activator concentration is caused by the peculiarities of convection in the melt and the activator diffusion through the capillary channel of the shaper. At a relatively high pulling speed and the absence of mixing of the melt between the meniscus and the melt in the crucible, the diffusion length $l = D/v$ (v is the movement speed, D is the diffusion speed) is less than the inner length of the crucible capillary (2.5 mm). Thus, no change in Ce concentration along the grown fibers was observed; gas bubbles were often observed, appearing at a certain critical supersaturation of the melt with gas. A tendency to an increase in the number of gas bubbles was observed with an increase in the Ce concentration in the melt [141].

The next step was to optimize the garnet growth procedure to minimize the heterogeneity of the activator distribution in the fiber, including issues of the capillary wetting with the melt, control of the crystal diameter, and the influence of the fiber pulling rate [141, 143—145].

When Ce^{3+} and Pr^{3+} activators are introduced into garnet fibers, no other phases are formed. Separation of the fiber from the melt does not occur even in the event of a drastic change in the pulling speed. A high concentration of Ce (>0.1 at.%) increased the wettability of the melt, the meniscus became convex, and the fiber diameter increased to 2.5 mm [141]. In addition, the segregation of the activator to the periphery of the fiber increased with cerium concentration (Fig. 2.17). Transparent LuAG, YAG fibers have a smooth surface and, when activated with different amounts of cerium and co-activated with magnesium, have different shades of green depending on the cerium concentration (Fig. 2.18). The coloration is caused by increased absorption of Ce^{3+} when its concentration increases. Strong radial segregation of Ce was observed in samples with high concentrations >0.1 at.%. The difference in the atomic radii of Ce^{3+} (103.4 pm) and Lu^{3+} (86.1 pm) [112] is the main reason for the activator segregation in the fibers.

The release of gas that occurs at the liquid-solid interface leads to an increase in the bubble size and their subsequent upward diffusion due to the floating effect. No bubbles were observed in unactivated LuAG crystals grown at pulling speeds of 0.3 mm/min [145]. In activated garnets, the relationship between gas bubbles and the distribution of the activator has not been established. Most of the bubbles were spherical in shape, and some of them were elongated along the growth direction. The bubbles were aligned parallel to the fiber axis (Fig. 2.19).

At growing rates of $0.3< v< 0.5$ (mm/min) and the Ce concentration in the melt <0.1 at.%, the crystallization front is flat and has only one layer of bubbles. The rest of the fiber does not contain bubbles. In the case of a high growth rate, concentration supercooling promotes bubble entrapment. LuAG:Ce fibers grown at low rates have a stable diameter and a smooth surface through a flat

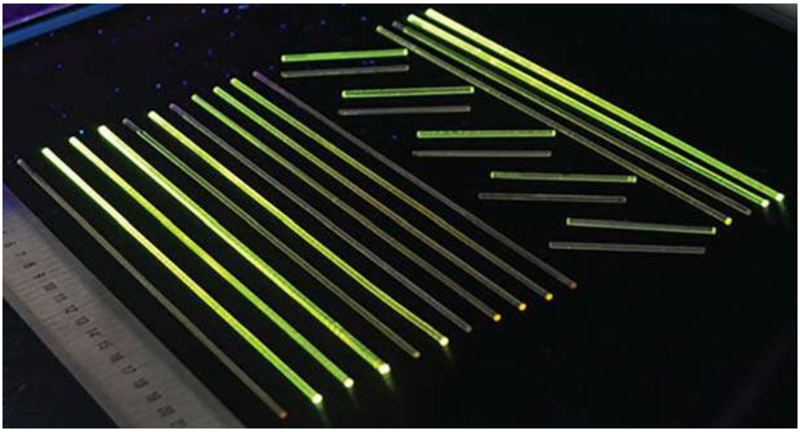

Fig. 2.18. Photo of YAG:Ce and YAG:Ce,Mg fibers with different concentrations of co-activators under UV illumination [144]

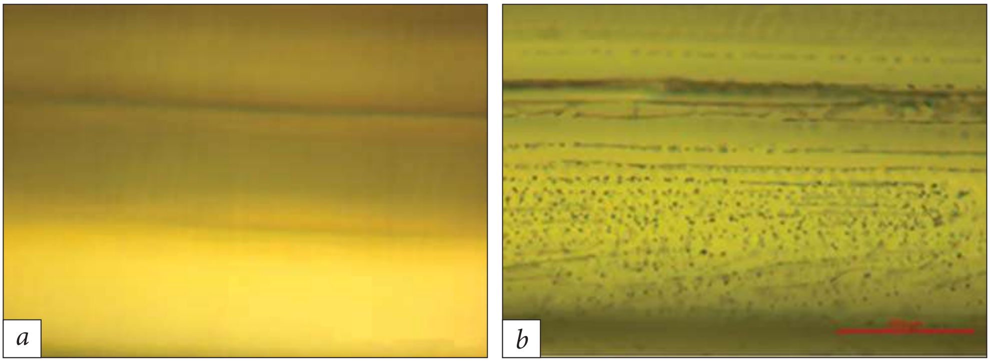

Fig. 2.19. View of the lateral surface of fibers in non-doped (*a*) and 0.12 at.% Ce-doped LuAG (*b*) [141]

crystallization front. To grow fiber without bubbles, it is important to control the growing conditions. A decrease in the growth rate $v \leq 300$ μm/min guarantees obtaining a LuAG:Ce fiber of acceptable quality with a low concentration of bubbles [144].

When growing LuAG:Ce and LuAG:Pr fibers with a length of 22 cm and a pulling speed of 300 μm/min, the heating power from the seeding to the end of growth increased three times faster than in the case of growing unactivated fibers (~0.35% versus 0.12%) [144]. Apparently, this difference was due to an increase in radiant heat transfer through the transparent fiber. The best results were achieved for fibers with a Ce concentration of 0.1 at.%, grown at a rate of 300 μm/min. When growing activated fibers, periodic inclusions were observed along the fibers (this was also observed in some non-activated fibers). These places can be visually observed in transmitted light. There has been no work on growing fibers of mixed crystals, except for experiments with LYSO:Ce [136].

In the case of crystals of solid solutions in our work, the process of growing fibers of mixed crystals by the micro-pulling method was complicated by the difference in the ionic radii of the substituted cations in the matrix, which also causes the larger cation segregation to the periphery. This phenomenon causes cracking of both fibers and bulk crystals. Thus, when growing LGSO:Ce and YAGG:Ce fibers, special attention was paid to the radial distribution of matrix and activator cations.

2.2.1. LGSO:Ce

When growing single-crystalline LGSO:Ce fibers, at the first stage, the chunks of single crystals grown by the Czochralski method with $x = 0.2$ and 0.5 and 0.01 at.% Ce were used. At the next stage, Lu_2O_3, Gd_2O_3, CeO_2, and SiO_2 powders with a purity of no worse than 99.99% were used, mixed in a stoichiometric ratio. The Ce^{3+} activator concentration in the raw material was in the range

Fig. 2.20. Ir crucibles with a round capillary with a diameter of 2 mm (left) and a square capillary 2 × 2 mm^2 (right) [146]

of 0.01—1.5 at.%. The SiO_2 powder was pre-calcined at 300 °C to remove moisture. After mixing the reagents, a second calcination was carried out at a temperature of 1200 °C.

The solid-phase reaction of the synthesis of unactivated and Ce-activated LGSO raw materials, by analogy with the Czochralski method, it was carried out according to equations 2.1 and 2.2. $Lu_{2x}Gd_{2-2x}SiO_5$:Ce fibers with $x = 0.2$ and $x = 0.5$ were chosen for growth due to their optimal combination of scintillation parameters [111] and relatively low melting temperatures [112]. The raw material was loaded into an iridium crucible with a diameter of 16 mm, with a square capillary of 2 × 2 mm^2, with a hole with a diameter of 1 mm in the center (Fig. 2.20). The crucible was mounted on a cylindrical iridium screen with a diameter of 16 mm.

The crucible and screen were thermally insulated using alundum ceramics. The raw material was heated and melted in a crucible using radio frequency heating. To protect the iridium crucible and the screen from oxidation at high temperature, the growth was carried out in an argon flow. The melt flowed out of the capillary through the hole at the bottom of the crucible and crystallized on a seed that contacted the melt meniscus.

The crystallizer was located inside the quartz tube. The screen has a hole on the side surface for visual monitoring of the crystallization process using a CCD camera. During the growing process, the seed was pulled down at a speed of 50—1000 μm/min. LGSO:Ce or LYSO:Ce rods with a cross-section of 2 × 2 mm^2 and oriented along the [210] direction were used as seeds. Crystal growth was carried out in an Ir crucible at a temperature of about 1950 °C in an argon atmosphere (Fig. 2.21).

Fibers with a Lu/Gd = 1/1 ratio and cerium concentrations of 0.01, 0.3, 0.5, 1, 1.5 at.% were obtained. (Fig. 2.22). The crystal cooling process took place in one step, and the temperature was lowered to room temperature within 3—26 hours. First, a series of fibers were grown from chunks of crystals obtained by the Czochralski method with different ratios of lutetium to gadolinium was used to determine the growth conditions. Crystals with $x = 0.2$ (Fig. 3.15) had a greater tendency to crack than fibers with $x = 0.5$ due to the proximity of their composition to the concentration of the polymorphic transition in LGSO:Ce at $x = 0.17$ [112].

Several approaches have been tested to eliminate cracks during growth. Only a decrease in the growth rate and an increase in the cooling time gave

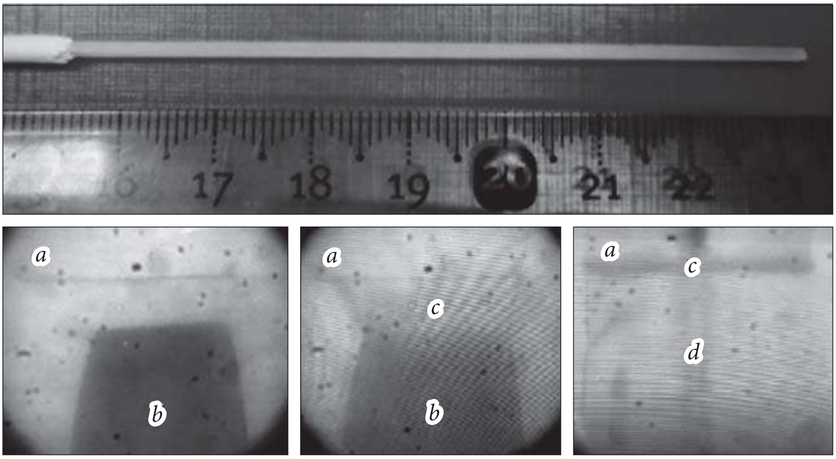

Fig. 2.21. Top: view of a 2 × 2 mm^2 cross-sectional LGSO:Ce seed on a holder. From the bottom: the process of nucleation and growth of a fiber, which is visually monitored using CCD through a hole in the crystallizer: *a* — crucible capillary, *b* — seed, *c*— meniscus (crystallization zone), *d* — fiber [147]

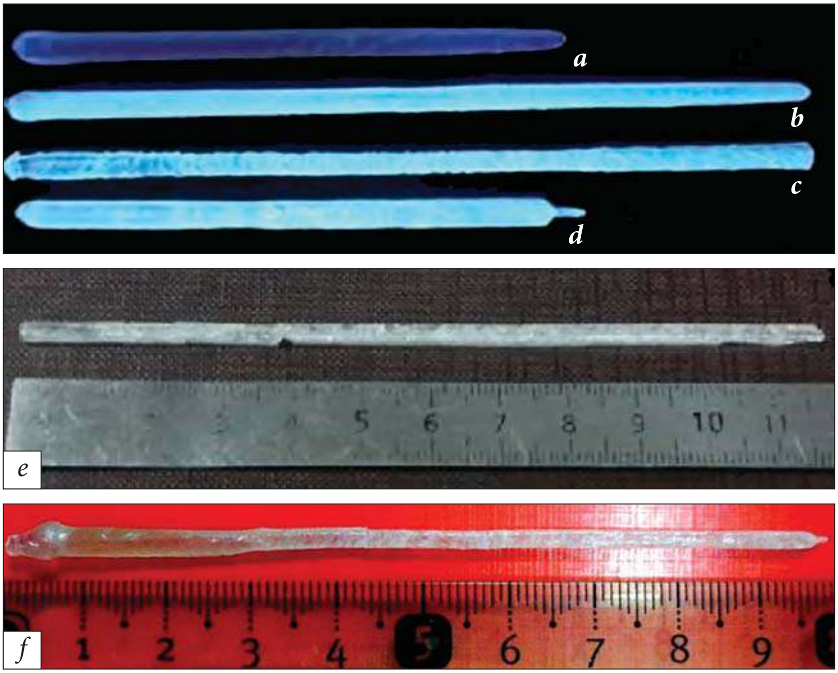

Fig. 2.22. Photo under a UV illumination of $Lu_{2x}Gd_{2-2x}SiO_5$ fibers grown at $x = 0.5$ and cerium concentrations: *a* — 0.01 at.%; *b* — 0.3 at.%; *c* — 0.5 at.%; *d* — 1 at.%. Photo of grown $Lu_{2x}Gd_{2-2x}SiO_5$ fiber with $x = 0.2$ (*e*); Photo of an LGSO:Ce crystal with 1.5 at.% Ce, obtained by overheating the melt (*f*) [144]

a certain result. The temperature regime for growing was selected. Due to the rather massive seed and rapid heat loss in the meniscus, it was difficult to control the diameter of the fibers. As a result, the fiber with 0.01 at.% Ce^{3+} had only a few cracks (Fig. 2.22*a*). The following fibers were obtained from a prepared charge with 0.3, 0.5, and 1 at.% of activator and had a single-crystalline part about 2 cm long (Fig. 2.22*b*–*d*, respectively). A fiber with a transparent single-crystal part of LGSO:Ce with 1.5 at.% Ce was obtained only by overheating the melt and increasing the growth rate up to 1000 μm/min. The first part, with a diameter of 4 mm and a length of 30 mm, was transparent (Fig. 2.22*e*). The rest of the fiber had a large number of inclusions. Other attempts to adjust the diameter stability and obtain a single crystal with 1.5 at.% Ce were unsuccessful.

According to X-ray structural studies of LGSO:Ce (1 mol.% Ce) and LGSO:Ce (1.5 mol.% Ce) fibers they do not contain impurities of foreign phases. Both single crystals belong to the monoclinic system *C*2/c.

2.2.2. YAGG:Ce

The raw materials used were the chunks of YGG and YAG:Ce crystals grown by the Czochralski method. Fibers with a diameter of 2 mm were pulled down onto a seed with crystallographic orientation [111] at a speed of 0.3—0.5 mm/min. The first grown YGG fibers can be conventionally divided into 3 parts by quality (Fig. 2.23*a*):

(*i*) Length 0 → 1.6 cm. Numerous cracks form at the beginning, apparently due to the different lattice parameters of the YAG seed and YGG fiber.

(*ii*) Length 1.6 → 3.2 cm. The fibers become darker. The surface is matte, but there are almost no cracks inside, because the growth process has stabilized, and mechanical stresses due to the mismatch between the lattice parameters of the seed and the fiber are reduced.

(*iii*) Length 3.2 → 4.5 cm. The fiber becomes thicker and slightly deformed. This part of the fiber is transparent, but contains many cracks. Apparently, it was grown from a non-stoichiometric Ga-deficient melt due to its evaporation. The Ga_2O_3 layer was deposited on the inner surface of heat-insulating ceramics (Fig. 2.24).

The YAGG:Ce fiber (75 at.% Ga, 150 ppm Ce) was opaque and fully polycrystalline. Ga was deposited on the crystallizer in a smaller amount compared to the growth of YGG. The YAGG:Ce fiber consists of a brittle opaque layer around a strong middle part, similar to what we observed in the LGSO:Ce fibers. This effect was associated with: (*i*) segregation of larger Ga^{3+} cations in YAGG to the periphery of the crystal, and/or (*ii*) non-stoichiometry of the melt and crystal due to Ga evaporation.

As the first of these factors cannot be eliminated, the second one was minimized by adding excess Ga_2O_3 to the melt to compensate for its losses by evaporation. The addition of gallium excess is a common procedure when growing Ga-

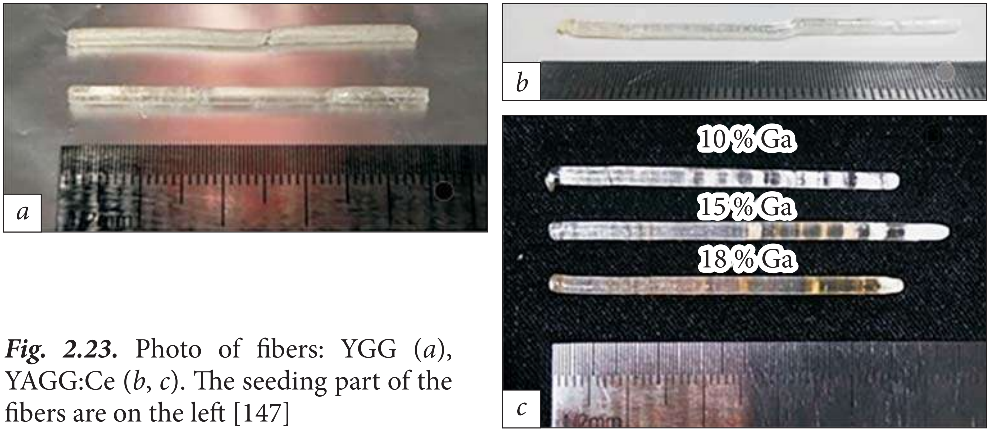

Fig. 2.23. Photo of fibers: YGG (*a*), YAGG:Ce (*b*, *c*). The seeding part of the fibers are on the left [147]

containing oxide single crystals, like when growing YAGG:Ce by the Czochralski method (see Chapter 2.1.1) by adding 1% excess in respect to the stoichiometric composition. In contrast to the Czochralski method, in the micro-pulling method, the evaporation factor is much stronger because the ratio of the melt surface to its volume in the latter is much higher. Taking into account the 2—4 mol.% excess of Ga_2O_3 [148] introduced into the melt during the growth of $Gd_3Ga_5O_{12}$ × × (GGG) crystals by the Czochralski method, and the 1 mol.% excess of Ga_2O_3 that was introduced by us when growing YAGG:Ce by the Czochralski method, the initial fiber was grown from a melt with an excess of 3% Ga (Fig. 2.23*b*). Although the shape of the new 5 cm long fiber was asymmetric, the fiber was transparent and free of cracks except for a ~1 cm long portion at the end of the fiber. This result showed that the compensation of Ga excess is an effective tool for optimizing the growth process in the micro-pulling method as well. By weighing gallium oxide powder deposited on thermal insulation (Fig. 2.24), it was found that when growing a 4—5 cm long YAGG:Ce fiber, about 10% of Ga evaporates from the melt. During the experiments, fibers were grown with an excess of 10, 15, 18% Ga added to the melt. These 3 fibers are presented in Fig. 2.23*c*.

The number of inclusions in the fiber decreases when gallium is added.

Fig. 2.24. Gallium oxide deposite accumulated on thermal insulation after growing YAGG:Ce fiber by the micro-pulling method. The bottom photo illustrates the collected condensate [146]

These periodic inclusions become more frequent as one approaches the end of the fiber, which is obviously associated with concentration supercooling of the melt under conditions of different melting temperatures of the components of a mixed crystal [10]. In this case, the difference between the melting temperatures of YAG and YGG is 140 °C. Adding more Ga excess to the melt negatively affects the YAGG:Ce fiber quality.

Thus, the process of growing YAGG:Ce fibers by the micro-pulling method is greatly complicated by the uncontrolled evaporation of Ga_2O_3 and periodic inclusions caused by the melt concentration supercooling in the YAG:Ce-YGG:Ce mixed system. Since gallium oxide losses due to evaporation are approximately proportional to the duration of the growth process, they will be significantly greater when growing fibers >20 cm in length for high-energy physics experiments. These losses can be minimized by adding more oxygen to the growing atmosphere, or by isolating the melt from the environment. The appearance of periodic inclusions can be prevented by reducing the growth rate, which, in turn, calls into question the possibility of mass production of YAGG:Ce in a short time.

2.3. Solid-phase synthesis of solid solutions

The method of ceramic solid-phase synthesis can be faster and more cost-effective and is usually used to obtain samples of compounds with extremely high melting temperatures, or those that do not melt congruently and cannot be obtained by direct crystallization from the melt. In particular, samples of rare earth tantalates, niobates, and tantaloniobates were synthesized in works [149—152].

To obtain compounds of rare earth tantalates, niobates, as well as mixed systems of tantaloniobates, this work implemented a ceramic method for the synthesis of scintillation materials based on tantalate, in particular, gadolinium tantalate, which includes mixing the initial oxides containing tantalum and niobium oxides, their preliminary drying, calcination, and subsequent cooling to room temperature. The initial oxides were mixed in a stoichiometric ratio that corresponds to the general formula $GdNb_xTa_{1-x}O_4$, where $x = 0.02—0.6$; the resulting mixture was tableted, and the tablets were dried at a temperature of 100—110 °C for 10—12 hours, and after drying, the tablets were calcined at a temperature of 1300— 1400 °C for 25—30 hours.

Tableting the mixture of initial oxides before calcination leads to an increase in the contact surface between the powder particles and an increase in the rate of interaction of the oxides with the formation of the resulting material; this makes it possible to exclude the use of a high-temperature solvent in the synthesis. With this method, the obtaining procedure is significantly simplified due to the absence of the stages of removing the high-temperature solvent and subsequent filtering and drying of the powder. In addition, the synthesized material does not contain residual impurities of the high-temperature solvent or intermediate products of its interaction with the original oxides; the absence of these residual impurities in the material obtained according to the claimed method leads to an improvement in the scintillation characteristics of the material compared to analogues. Another advantage of tableting a mixture of initial oxides is the possibility of obtaining a ready-to-use ceramic scintillation element after calcination. A rather high temperature and prolonged calcination of the tablets leads to the complete conversion of the initial oxides into the synthesized material; this excludes the presence of a residual amount of initial components that can negatively affect the scintillation characteristics of the material.

Drying the tablets at temperatures below 100 °C is ineffective because this mode cannot ensure complete removal of distilled water used to moisten the charge during tableting; the use of temperatures above 110 °C can lead to partial destruction of tablet samples due to the rapid and massive removal of water from tablets. The use of a temperature below 1300 °C for the calcination of tablets to obtain scintillation material by the method of solid-phase synthesis without the use of a high-temperature solvent is ineffective due to the slow course of the reaction of the formation of scintillation material at this temperature. Synthesis temperature above 1400 °C leads to an undesirable phase transition in the material, which in gadolinium tantalate occurs at a temperature of about 1450 °C with a change in structure from M-fergusonite to scheelite, and such a transition can lead to significant changes in the scintillation properties of the material.

As a result of the implementation of our proposed method, a ceramic material was obtained, the dimensions of which are limited only by the mold dimensions. Thus, ready-to-use scintillation elements we are obtained in the form of tablets.

For solid-phase synthesis, oxides La_2O_3, Y_2O_3, Sc_2O_3, Gd_2O_3, Lu_2O_3 and Ta_2O_5 with a purity of not worse than 99.99% were pre-annealed to remove moisture and absorbed CO_2, weighed with a molar ratio of RE_2O_3:Ta_2O_5 components 1:1 ($RETaO_4$); after mixing in an agate mortar, they were used as starting materials. The mixing product was pressed into tablets with a diameter of 10 mm. Then the tablets were calcined at 1400 °C for 10 hours in an inert gas atmosphere. Yttrium and lanthanide orthotantalates with ionic radii in the range from 0.86 Å ($LuTaO_4$) to 0.98 Å ($GdTaO_4$) belong to the structures of M- and M′-fergusonites [61]. Unlike other orthotantalates, $ScTaO_4$ and $LaTaO_4$ have wolframite and orthorhombic structures, respectively [153, 154]. According to the X-ray phase analysis after the solid-phase reaction, the obtained samples contained 92—98% of the orthotantalate phase with the wolframite structure for $ScTaO_4$, the orthorhombic structure for $LaTaO_4$, the structure of M-fergusonite for $GdTaO_4$ and the structure of M′-fergusonite for $YTaO_4$ and $LuTaO_4$ (Table 2.3).

Goldschmidt's rule postulates the formation of a stable solid solution between compounds with a difference in ionic radii between competing atoms of no more than 15%. In this sense, tantaloniobates are unique compounds because the ionic radii of both six-coordinated Ta and Nb in the +5 oxidation state

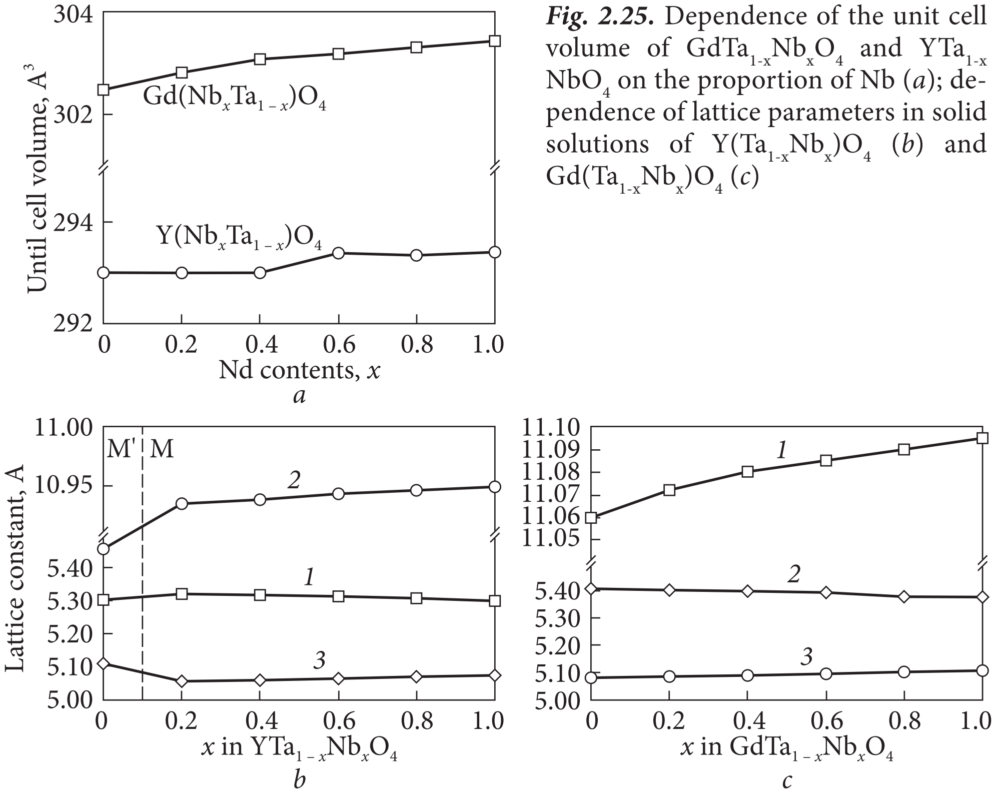

Fig. 2.25. Dependence of the unit cell volume of $GdTa_{1-x}Nb_xO_4$ and YTa_{1-x} NbO_4 on the proportion of Nb (*a*); dependence of lattice parameters in solid solutions of $Y(Ta_{1-x}Nb_x)O_4$ (*b*) and $Gd(Ta_{1-x}Nb_x)O_4$ (*c*)

Table 2.3. **Structural types and lattice parameters of the obtained orthotantalates** [58]

Compound	Crystallographic structure	Lattice parameters			
		a, Å	*b*, Å	*c*, Å	β, deg.
$YTaO_4$	M′-fergusonite	5.299	5.456	5.111	96.412
$LuTaO_4$	M′-fergusonite	5.236	5.432	5.0575	96.029
$LaTaO_4$	Orthorhombic	5.664	14.691	3.946	—
$ScTaO_4$	Wolframite	4.808	5.666	5.113	91.633
$GdTaO_4$	M-fergusonite	5.082	11.078	7.054	94.58

are the same and equal to 0.64 Å [112]. The existence of a stable solid solution for the full range of Nb concentrations in $(Nb_xTa_{1-x})_2O_5$ at $x = 0{,}1$ was shown in [155, 156]. Therefore, one could expect the formation of a mixed crystal in the of the cross-section plane of the ternary system RE_2O_3–Ta_2O_5–Nb_2O_5 at the total molar ratio of components RE_2O_3:[$x Ta_2O_3 + (1-x) Nb_2O_5$] = 1:1, where $x = 0 \div 1$. However, a continuous series of solid solutions in the entire range of concentrations is observed only in $GdTa_{1-x}Nb_xO_4$ (Table 2.3). A structural

Table 2.4. **Lattice parameters of mixed tantaloniobates**

Nb content (*x*)	Spatial group	*a*, Å	*b*, Å	*c*, Å	b, deg	Density, g/cm^3, calculation
$YTa_{1-x}Nb_xO_4$						
0	*P*21/*a*	5.299	5.456	5.111	96.412	7.56
0.2	*I*2/*a*	5.322	10.935	5.057	95.386	7.16
0.4	*I*2/*a*	5.317	10.938	5.059	95.242	6.75
0.6	*I*2/*a*	5.314	10.943	5.065	95.045	6.34
0.8	*I*2/*a*	5.306	10.946	5.069	94.808	5.94
1.0	*I*2/*a*	5.299	10.949	5.073	94.561	5.53
$GdTa_{1-x}Nb_xO_4$						
0	*I*2/*a*	5.405	11.060	5.081	95.620	8.76
0.2	*I*2/*a*	5.401	11.072	5.087	95.460	8.37
0.4	*I*2/*a*	5.395	11.080	5.092	95.276	7.98
0.6	*I*2/*a*	5.387	11.085	5.097	95.042	7.58
0.8	*I*2/*a*	5.379	11.090	5.102	94.812	7.19
1.0	*I*2/*a*	5.372	11.095	5.107	94.563	6.80

transition from monoclinic *P*21/*a* to monoclinic *I*2/*a* symmetry is observed in $YTa_{1-x}Nb_xO_4$ for x in the range from 0 to 0.2. The elementary cell parameters of mixed compounds, as well as their calculated densities, are given in Table 2.4. The density of mixed compounds was calculated based on the data on the rare-earth orthotantalates and orthoniobates in [47] and the assumption that the density of mixed compounds corresponds to the Vegard's law [157]. Lattice parameters *a* and *c* monotonically increase with the Nb content in the matrix (Fig. 2.25*b*, *c*) due to the increase in the distances between A^{5+} and oxygen ions in Nb-based matrices [155, 156]. An increase in lattice parameters with niobium content is possibly due to different Pauling electronegativities of Ta (1.5) and Nb (1.6) and, as a result, different charges on Ta^{5+}, Nb^{5+}, and O^{2-} in covalently bonded compounds. It is known that the ionic radius of an element in a compound with a covalent bond depends linearly on the ion's partial charge and can be calculated using the empirical formula (Sanderson method) [158]: $R = RC - B\delta$, where R is the ionic radius of the ion, RC is the covalent (atomic) radius, B is the constant for a particular ion, and is the partial charge. For various chlorides, it was shown [159] that the ionic radius of chlorine ions varies in the range from 1.24 Å for $CdCl_2$ to 1.95 Å for CsCl, and the partial charge from −0.21 (for $CdCl_2$) to −0.81 (for CsCl). By analogy, in the case of TaO_6^- or NbO_6^- groups, a small increase in cation electronegativity from Ta^{5+} to Nb^{5+} is accompanied by an increase in the ionic radius of O^{2-}. These changes can lead to an increase in the length of $A^{5+}—O^{2-}$ bonds. Along with this, the parameter b in both matrices shows a tendency to decrease with the addition of Nb, which means the rearrangement of the geometry of the TaO_6 or NbO_6 polyhedra when the cation composition changes.

It is also worth noting the positive deviations from the additive values at $x = 0.2—0.6$ for the dependence of the lattice parameter in $Gd(Nb_xTa_{1-x})O_4$. At the same time, the dependence of the unit cell volume in both systems is nonlinear, although the general tendency to increase V with the addition of niobium remains. For GTNO, the maximum deviation from Vegard's law is observed around $x = 0.5$. For YTNO, there are both positive and negative cell volume deviations from linearity.

The deviations of the lattice parameters from Vegard's law were previously noted in mixed crystals of MgO-FeO, MgO-$LiFeO_2$ [160], CdF_2-PbF_2 [161] and were associated with the formation of inhomogeneities (clusters) enriched with one of the substituted atoms. The formation of clusters disrupts short-range ordering in the crystal, which should be reflected in lattice loosening, that is, positive deviations from linearity.

CHAPTER 3

OPTICAL AND SCINTILLATION CHARACTERISTICS OF THE DEVELOPED SCINTILLATORS

3.1. LGSO:Ce

Crystals of lutetium-gadolinium oxyorthosilicate LGSO:Ce have been the subject of active research for the past 25 years. The main pragmatic idea of these studies was to combine the high light yield of LSO:Ce crystals with the cheapness and low afterglow level of GSO:Ce crystals. Before our work, it was shown that the characteristics of LGSO:Ce with Lu concentration <20% are similar to GSO:Ce [162]. In LGSO (20% Lu) the light yield is also low and amounts to about 15 000 photo/MeV, along with a strong afterglow with an amplitude of up to several percent in the microsecond range [163]. The scintillation characteristics of LGSO:Ce with 90% Lu are similar to LSO:Ce [162]. In this work, the optical and scintillation characteristics of this system were determined in detail in the full concentration range of solid solutions.

3.1.1. Optical characteristics

The spectral transparency range of unactivated LGSO is from 200 nm and does not differ significantly from the range for LSO (Fig. 3.1). Instead, many narrow bands in the 250—320 nm range associated with electronic transitions in Gd^{3+} ions are observed in LGSO. In general, the transmission of LGSO in the visible range is slightly lower compared to LSO due to the presence of more scattering centers in the bulk of the crystals. With the Ce addition, 3 absorption bands with maximum at 360, 300, and 260 nm are distinguished in the UV range, corresponding to intracenter transitions $4f \rightarrow 5d_{1\text{-}3}$ in Ce^{3+}.

The photoluminescence spectra of mixed crystals $Lu_{0.8}Gd_{1.2}SiO_5$:Ce and $Lu_{1.}8Gd_{0.2}SiO_5$:Ce in comparison with GSO:Ce are shown in Fig. 3.2*a*. Luminescence bands in the spectral range of 360—600 nm are associated with allowed transitions $5d_1 \rightarrow 4f$ in Ce^{3+} ions, which occupy the 7- and 6-coordinated oxygen positions in the orthosilicate lattice (*Ce*1 and *Ce*2, respectively). The spectral characteristics of these centers will be described in detail in Chapter 5 when considering spatial inhomogeneities in crystals. The photoluminescence band of

LGSO:Ce with a maximum at 435, 410, and 400 nm, respectively, for GSO:Ce, $Lu_{0.8}Gd_{1.2}SiO_5$:Ce, and $Lu_{1.8}Gd_{0.2}SiO_5$:Ce shifts to the short-wavelength side with increasing Lu concentration due to the weakening of the crystal field strength and redistribution of the activator from the *Ce*1 center to the *Ce*2 center [6, 163—167].

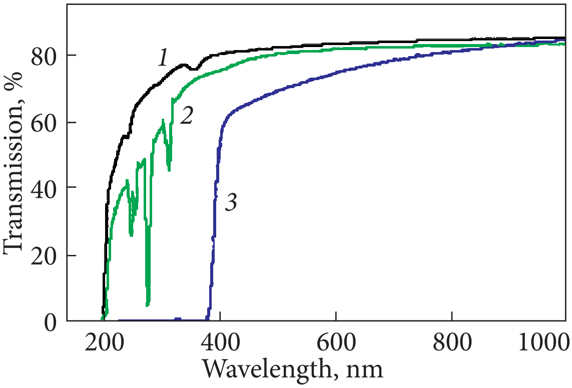

Fig. 3.1. Transmission spectra of oxyorthosilicate crystals: *1* — LSO; *2* — LGSO 50% Gd; *3* — LGSO:Ce 50% Gd

It turned out that Lu^{3+}, Gd^{3+}, and Ce^{3+} cations are unevenly distributed between crystallographic positions in LGSO:Ce. Gd^{3+} and Ce^{3+} cations with larger ionic radii [113] tend to enter positions with a larger radius of the first coordination sphere. These are, respectively, 7-coordinated and 9-coordinated positions (*Ce*1) in lattices of *C*2/*c* and $P2_1/c$ symmetry types. The activator distribution between the crystallographic positions strongly affects the luminescence and scintillation properties of orthosilicates [165—167]. It can be controlled by varying the cation composition of the crystal. It was shown [165, 166] that in LSO:Ce, the number of *Ce*2 centers is very small (5—10%), while in LYSO:Ce the concentrations of *Ce*2 and *Ce*1 centers become comparable due to the lat-

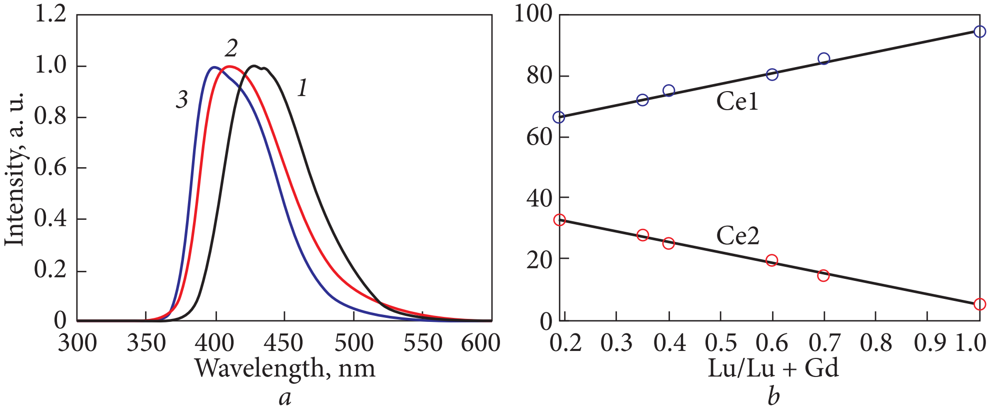

Fig. 3.2. Normalized photoluminescence spectra of GSO:Ce and LGSO:Ce crystals (*a*): *1* — Gd_2SiO_5:Ce, λ_{ex} = 345 nm; *2* — $Lu_{0.8}Gd_{1.2}SiO_5$:Ce, λ_{ex} = 365 nm; *3* — $Lu_{1.8}Gd_{0.2}SiO_5$:Ce, λ_{ex} = 357 nm; relative integral intensities of the *Ce*1 (l_{em} = 420 nm) and *Ce*2 (l_{em} = 510 nm) luminescence bands upon X-ray excitation at *T* = 300 K (*b*) [168, 169]

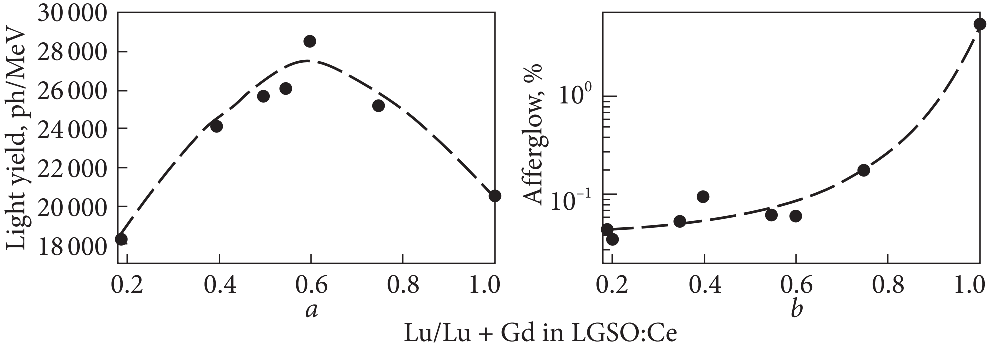

Fig. 3.3. Light yield (*a*) and afterglow level after 5 ms (*b*) in LGSO:Ce crystals with the *C*2/*c* structure depending on the concentration of Lu in the matrix [168]

tice loosening by larger Y^{3+} ions. A similar trend was expected when Gd was added to LSO, because the ionic radius of Gd^{3+} is larger than that of Lu^{3+}.This was confirmed in our work. Regarding the dependence of the intensities of the luminescence bands corresponding to the *Ce*1and *Ce*2 centers in LGSO:Ce with *C*2/*c* symmetry, the contribution of *Ce*2 to the total luminescence yield gradually increases (Fig. 3.2*b*). The ratio of the luminescence intensities of the *Ce*1/*Ce*2 bands in our crystals with a cerium concentration of 1% (in the melt) is significantly higher than in the literature [167], where it is close to unity at a cerium concentration of 2% (in the melt). This confirms that the greater the total concentration of cerium, the greater the proportion of cerium in *Ce*2. However, it should be noted that the exact *Ce*1/*Ce*2 ratio cannot be precisely determined due to the different dependence of their luminescence intensity on temperature (the intensities were measured at room temperature) and the radiative energy transfer from *Ce*1 to *Ce*2 due to the overlap of the absorption and luminescence bands of these centers (these processes are discussed in detail in Chapter 4).

3.1.2. Light yield

In a detailed study of the relationship between the composition and scintillation characteristics in the full range of $Lu_{2x}Gd_{2-2x}SiO_5$:Ce concentrations (0< x< 1), we determined the interval of 30—60% Lu with the optimal combination of scintillation characteristics. A light yield of 29,000 ph/MeV, an energy resolution of 6.7% and an afterglow level of 0.02—0.1% after 5 ms were achieved [169] (by 2—3 orders of magnitude lower compared to LSO:Ce [170, 171]). Considering the lower cost of Gd_2O_3 compared to Lu_2O_3 and the lowering of the crystallization temperature with the addition of Gd, these crystals are good candidates for applications, for example, in X-ray scanners or as a replacement for LSO/LYSO in PET or CT imaging. The dependence of the scintillation parameters on the Lu/Gd ratio is shown in Fig. 3.3.

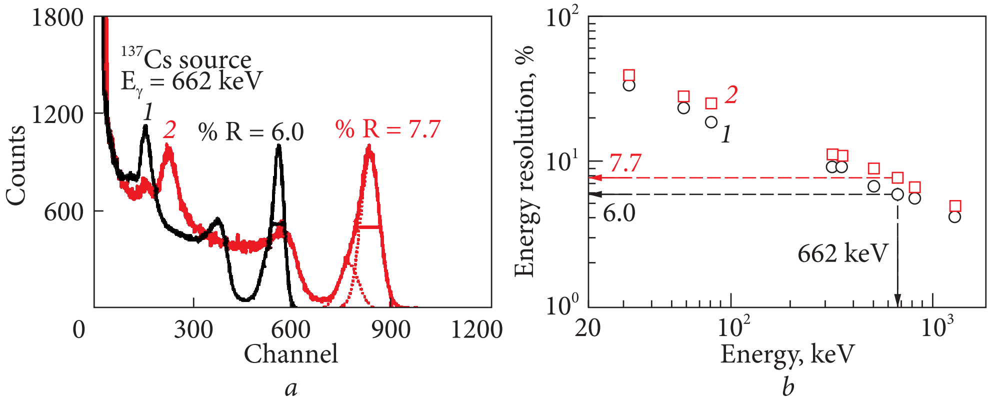

Fig. 3.4. Amplitude spectra of LGSO:Ce crystals of different compositions under g-irradiation of 662 keV (^{137}Cs) (*a*): *1* — $Lu_{0.8}Gd_{1.2}SiO_5$:Ce; *2* — $Lu_{1.8}Gd_{0.2}SiO_5$:Ce; energy resolution depending on the energy of g-quanta for $Lu_{0.8}Gd_{1.2}SiO_5$:Ce and $Lu_{1.8}Gd_{0.2}SiO_5$:Ce crystals [169] (*b*)

As shown in [168], the light yield in the LGSO:Ce system depends on three main factors: the number of defects in the crystals, temperature quenching of Ce^{3+} luminescence and luminescence reabsorption in the crystal. At a Lu/Gd ratio of 1:1, the number of defects is relatively small, and temperature quenching and reabsorption are weak at room temperature [168].

3.1.3. Energy resolution

$Lu_{0.8}Gd_{1.2}SiO_5$:Ce crystals with the optimal combination of scintillation characteristics were compared with the GSO:Ce and $Lu_{1.8}Gd_{0.2}SiO_5$:Ce crystals grown in other laboratories. Light yield and energy resolution were measured upon irradiation with g-quanta with energies from 30 to 1500 keV (Fig. 3.4 *a, b*). The best energy resolution of 6.0% was obtained on the $Lu_{0.8}Gd_{1.2}SiO_5$:Ce crystal. At present, this is a record value, both for LGSO:Ce and for all oxyorthosilicate crystals. The reason for this may be the high distribution coefficient k_{eff} (Ce) = 0.6—0.8 in LGSO:Ce compared to 0.22 in LSO, and, as a result, a more uniform distribution ofthe activator along the crystal.

It was shown [6] that the reasons for the high energy resolution in LGSO:Ce, in addition to the uniform distribution

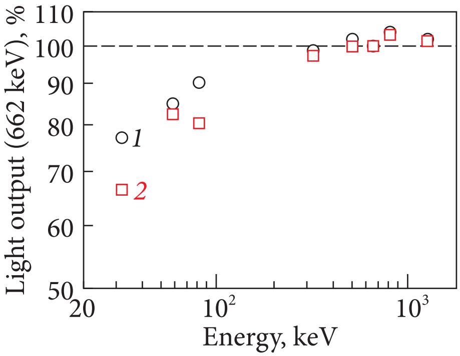

Fig. 3.5. Non-proportionality of the light yield in LGSO:Ce crystals depending on the excitation energy: *1* — $Lu_{0.8}Gd_{1.2}SiO_5$:Ce; *2* — $Lu_{1.8}Gd_{0.2}SiO_5$:Ce [169]

of the activator, is a good proportionality of the scintillation response from the excitation energy, as well as a low level of afterglow, which is more than 100 times lower compared to LSO:Ce. The non-proportionality in LGSO:Ce increases with the concentration of lutetium, so it is much better in LGSO:Ce than in LSO:Ce [6]. The non-proportionality determined with $Lu_{0.8}Gd_{1.2}SiO_5$:Ce crystals produced in ISMA and $Lu_{0.8}Gd_{1.2}SiO_5$:Ce crystals produced in another laboratory confirm the better proportionality in the first one (Fig. 3.5).

3.1.4. Kinetic characteristics of luminescence

The luminescence decay curves of GSO:Ce and LGSO:Ce crystals are shown in Fig. 3.6. The decay time was determined by approximating the curves with a multiexponential function (Equation 3.1):

$$I(t) = \sum A_i \, exp(-t/\tau_i) + B \,, \tag{3.1}$$

where and are the decay time and the corresponding initial intensities of the components, *B* is the background intensity. The relative intensity of its component is expressed as:

$$I_i = A_i \tau_i \Big/ \sum A_i \tau_i \,. \tag{3.2}$$

The results are summarized in Table 3.1. Unlike GSO:Ce, LGSO:Ce crystals possess very short rise times of scintillation pulses (Fig. 3.7). The $Lu_{1.8}Gd_{0.2}$ SiO_5:Ce crystal has a very fast scintillation decay, with almost no contribution from the slow component, which agrees with the highest light yield in this sample. The slower decay in $Lu_{0.8}Gd_{1.2}SiO_5$:Ce may be a consequence of the larger contribution of the *Ce*2 centers (see Fig. 3.2), which has a longer decay time compared to the *Ce*1 center. In a longer period of time, the recombination of *Ce* centers can be slowed down by energy migration along the Gd sublattice, by analogy to GSO:Ce. Also, a possible process occurring at the excited $5d_1$ level of Ce^{3+} is thermal ionization or tunneling between the luminescent center and the nearest electron trap [171—172].

The high light yield and fast decay in $Lu_{1.8}Gd_{0.2}SiO_5$:Ce explain its excellent time resolution (Fig. 3.7, 3.8). To estimate the rise times (time of the signal

Table 3.1. **Scintillation decay time (τ_i), relative intensities (A_i) and rise times (τ_r) for GSO:Ce and LGSO:Ce crystals**

Crystal	τ_1 (A_1), ns,%	τ_1 (A_1), ns,%	τ_1 (A_1), ns,%	τ_r, ns,%
GSO:Ce	32 (88)	220 (12)	—	3.5
$Lu_{0.8}Gd_{1.2}SiO_5$:Ce	18 (20)	58 (42)	252 (38)	0.6
$Lu_{1.8}Gd_{0.2}SiO_5$:Ce	17 (40)	39 (60)	—	0.5

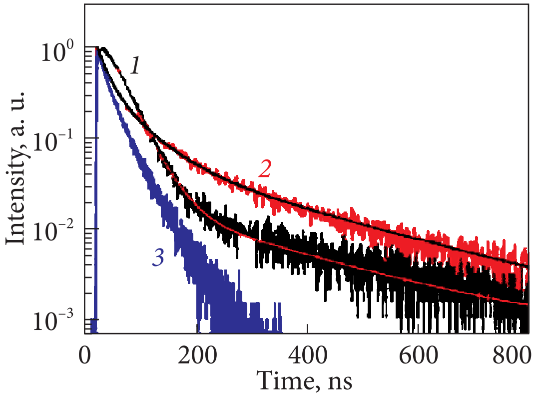

Fig. 3.6. Scintillation decay curves of GSO:Ce and LGSO:Ce crystals. Experimental data are approximated by the $I(t)$ function according to Eq. 3.1 [169]: *1* — Gd_2SiO_5:Ce; *2* — $Lu_{0.8}Gd_{1.2}SiO_5$:Ce; *3* — $Lu_{1.8}Gd_{0.2}SiO_5$:Ce

amplitude increase from 10 to 90% of the maximum level) of the scintillation pulse, scintillation kinetics was also measured in a shorter time interval (Fig. 3.7). Values of 0.5 and 0.6 ns were determined for $Lu_{1.8}Gd_{0.2}SiO_5$:Ce and $Lu_{0.8}Gd_{1.2}SiO_5$:Ce, respectively, compared to 3.5 ns for GSO:Ce.

Fig. 3.8 demonstrates the coincidence time spectrum for GSO:Ce and LGSO:Ce crystals in comparison with the fast BaF_2 detector. The time resolution parameters are summarized in Table 3.2. The measured time resolution was corrected for the contribution of the BaF_2 reference detector (128 ps) and is shown in the second column. The third column displays the decay time (t) of the fast component and its relative intensity. The number of fast component photoelectrons contributing to the 511 keV peak is listed in the fourth column. The last column displays the photoelectron ratio (*N*/t), which is important

Table 3.2. **Time resolution of GSO:Ce and LGSO:Ce samples upon excitation by g-quanta with an energy of 511 keV**

Crystal	δ_t (ps)	τ (contribution) ns,%	*N*(phel) at 511 keV	*N*/t, phel/ns
GSO:Ce	627 ± 13	32 (88%)	1260 ± 60	39 ± 2
$Lu_{0.8}Gd_{1.2}SiO_5$:Ce	442 ± 13	18 (20%)	520 ± 30	29 ± 2
$Lu_{1.8}Gd_{0.2}SiO_5$:Ce	368 ± 13	17 (40%)	1690 ± 80	99 ± 5

Table 3.3. **Total mass absorption coefficient of γ-quanta with the energies of 60 and 662 keV for GSO:Ce and LGSO:Ce [169]**

Crystal	μ_m (cm^2/g) at 60 keV		μ_m (cm^2/g) at 662 keV	
	$(\mu_m)_{ex}$	$(\mu_m)_{th}$	$(\mu_m)_{ex}$	$(\mu_m)_{th}$
GSO:Ce	8.65	8.55	0.0786	0.0800
$Lu_{0.8}Gd_{1.2}SiO_5$:Ce	6.28	5.91	0.0840	0.0826
$Lu_{1.8}Gd_{0.2}SiO_5$:Ce	2.89	2.85	0.0879	0.0856

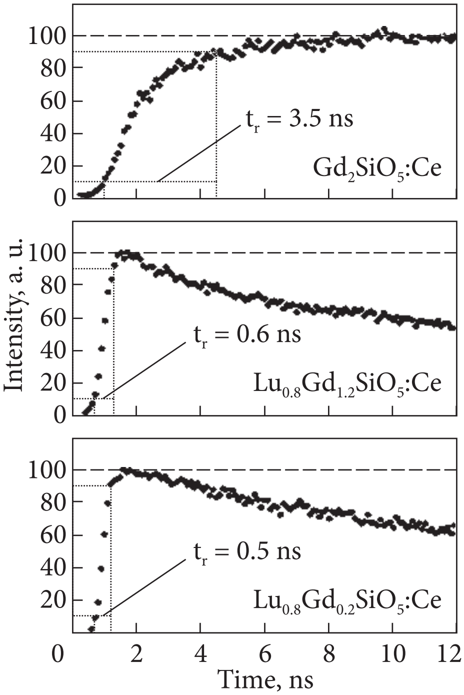

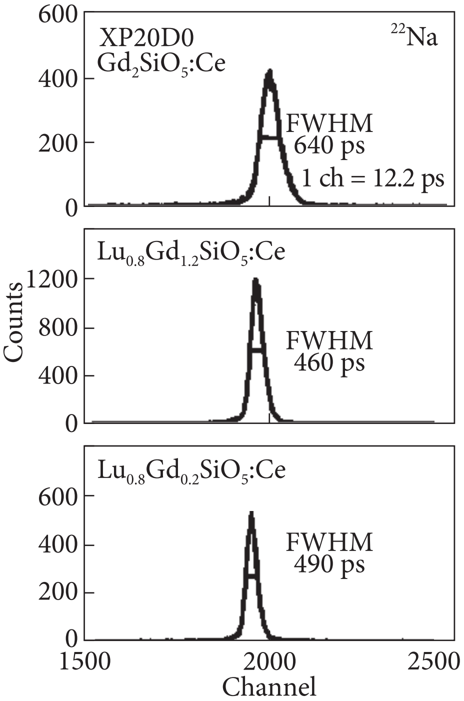

Fig. 3.7. Shape of the scintillation pulse of GSO:Ce and LGSO:Ce crystals during the first 12 ns after the start of irradiation [169]

Fig. 3.8. Spectrum of the time decay of the GSO:Ce and LGSO:Ce detectors relative to the fast BaF_2 detector [169]

for the time resolution of the scintillators. The higher photoelectron ratio in GSO:Ce relative to $Lu_{0.8}Gd_{1.2}SiO_5$:Ce, but the worst time resolution can be explained by the negative contribution of the slow rise time of the scintillation pulse (see Fig. 3.7).

3.1.5. Mass absorption coefficient

The mass absorption coefficient was determined using a parallel beam of monoenergetic γ-quanta with initial energy I_0 absorbed in a crystal with a thickness x in accordance with the equation:

$$I = I_0\, exp(\text{-}\mu_m \rho x)\,, \tag{3.3}$$

where I is the energy of γ-quanta that passes through the absorber, μ_m is the mass absorption coefficient, and r is the density of the absorber. Experimental $(\mu_m)_{ex}$ and theoretical $(\mu_m)_{th}$ mass absorption coefficient values for GSO:Ce and LGSO:Ce crystals for γ-quanta with energies of 60 keV and 662 keV are summarized in Table 3.3.

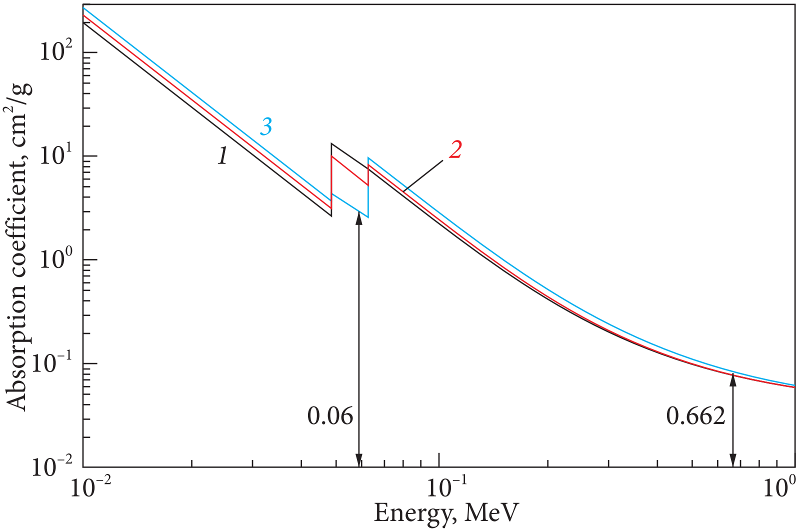

Fig. 3.9. Experimental values of $(\mu_\mathrm{m})_{ex}$ at 60 and 662 keV for GSO:Ce and LGSO:Ce compared with theoretical values of $(\mu_\mathrm{m})_{th}$ in the energy range of 0.1—1 MeV [169]: *1* — Gd_2SiO_5:Ce; *2* — $Lu_{0.8}Gd_{1.2}SiO_5$:Ce; *3* — $Lu_{1.8}Gd_{0.2}SiO_5$:Ce

Fig. 3.9 demonstrates the experimental values $(\mu_\mathrm{m})_{ex}$ in comparison with the values calculated using the WinXCom program [173] in the energy range of 0.1—1 MeV. The value of μ_m at 60 keV increases with the gadolinium content of the crystal due to the increase in the *K*-absorption of Lu and Gd in this energy range.

3.1.6. Luminescent and scintillation characteristics of LGSO:Ce,Ca crystals

In recent years, the potential for further improvement of the scintillation characteristics of various cerium-activated orthosilicates due to co-activation with divalent cations Mg^{2+} or Ca^{2+} has been demonstrated [174—177]. According to one of the hypotheses [176], Ca^{2+} ions in LSO:Ce mainly occupy six-coordinated oxygen positions, «displacing» Ce^{3+} to seven-coordinated positions with higher luminescence efficiency. According to [177], co-activation by a divalent cation leads to the transition of a significant amount of Ce^{3+} to the tetravalent Ce^{4+} state. Energy levels of Ce^{4+} located closer to the bottom of the conduction band compete with the traps for capturing electrons, which leads to an increase in the efficiency of electron transport to the activator.

In this work, upon co-activation of LGSO:Ce,Ca with 83 at.% Lu in the matrix, a light yield of 33700 ph/MeV was achieved (Fig. 3.10*a*). This is 8500 ph/MeV more than without co-activation when compared to the 75 at.%

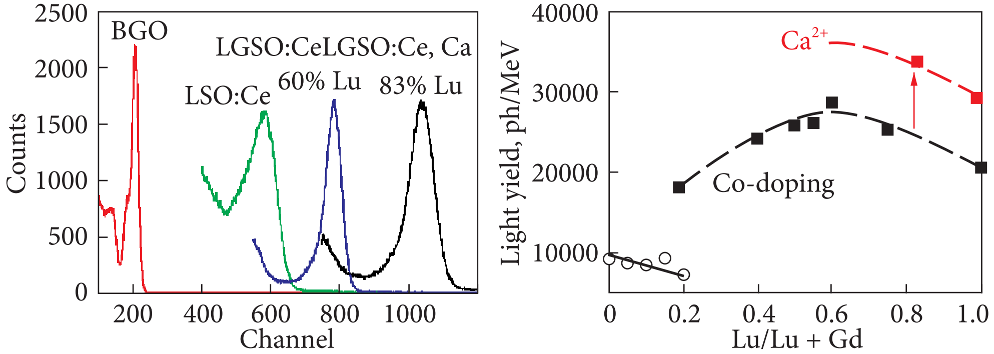

a *b*

Fig. 3.10. Amplitude spectrum of the LGSO:Ce,Ca crystal in comparison with LGSO:Ce, BGO and LSO:Ce (*a*); comparison of light yield in LGSO:Ce and LGSO:Ce,Ca crystals (*b*) [168]. The point for LSO:Ce,Ca is taken from [177]. Dashed lines show the estimated trend of light yield change

Lu sample (the closest by concentration of lutetium). However, the co-activation of Ca^{2+} does not affect the energy resolution of LGSO:Ce (8.1% at 662 keV) and the level of afterglow (0.46% after 5 ms). Taking into account the literature data on the light yield of LSO:Ce and LSO:Ce,Ca [177], a general tendency to increase the light yield in LGSO:Ce with the addition of Ca^{2+} (Fig. 3.10*b*) can be suggested.

Energy relaxation processes during the introduction of Gd^{3+} and Ca^{2+} into LSO:Ce were studied in more detail by measuring in the VUV range the kinetics of luminescence decay spectra depending on the temperature in the energy range of 4—25 eV at the SUPERLUMI facility in HASYLAB, DESY (Germany) [178]. Crystals of Lu_2SiO_5:Ce (LSO), $Lu_{2x}Gd_{2-2x}SiO_5$:0.3at.% Ce (LGSO:Ce) with a gadolinium concentration of 60 at.% relative to lanthanides, $Lu_{2x}Gd_{2-2x}SiO_5$:0.15% Ce, 0.2% Ca (LGSO: Ce,Ca) with a gadolinium concentration of 83 at.% relative to the lanthanides were grown by the Czochralski method (see Chapter 2.1.2).

Fig. 3.11 demonstrates the luminescence spectra of LSO, LGSO, and LGSO:Ca upon excitation in the fundamental absorption band by photons with an energy of 18 eV at room temperature and 8 K; the spectra are normalized to the maximum. The spectra contain broad bands of Ce^{3+} luminescence corresponding to $5d \rightarrow 4f$ transitions; transitions corresponding to individual $4f$ levels can be distinguished at low temperatures.

The asymmetric profile of the luminescence spectra with a long-wavelength shoulder is typical for these compounds and is associated with two types of Ce^{3+} centers in the oxyorthosilicate structure [180]. The spectra of samples containing gadolinium are slightly shifted relative to LSO:Ce towards low energies, although a weaker splitting of the $5d$ levels of Ce^{3+} in the mixed crystal and, con-

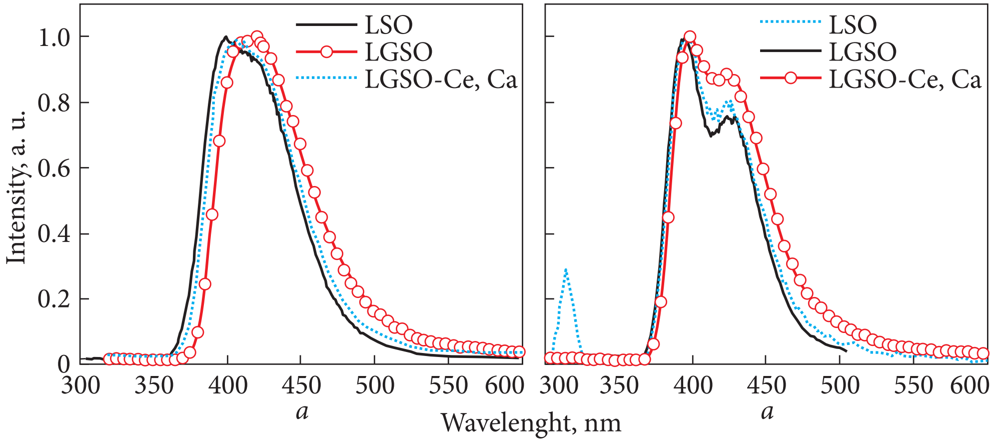

Fig. 3.11. Luminescence spectra of LSO, LGSO, and LGSO:Ca at room temperature (*a*) and 8 K (*b*) upon excitation with an energy of 18 eV [179]

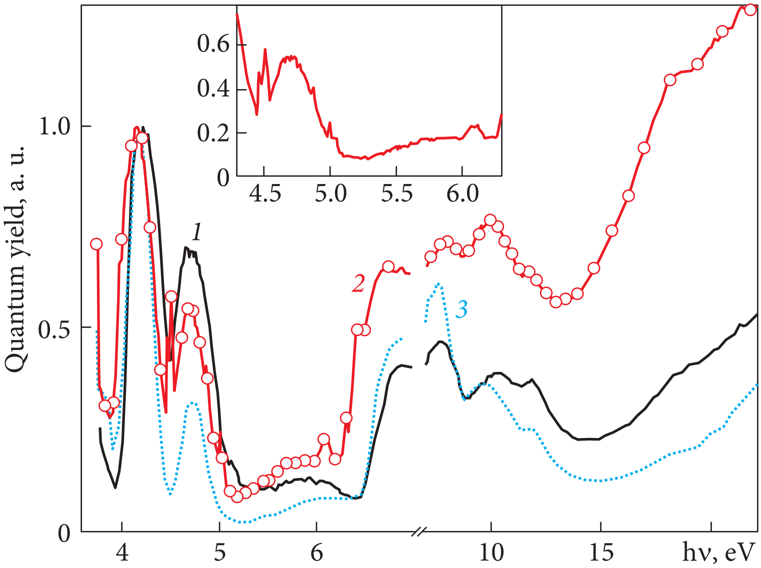

Fig. 3.12. Excitation spectra measured at 8 K normalized by the most intense Ce absorption band [179]: *1* — LSO; *2* — LGSO; *3* —LGSO:Ca

sequently, a larger energy gap between the 4*f* and 5*d* levels could be expected. The ionic radius of Gd^{3+} is larger than the radius of Lu^{3+}, and the introduction of gadolinium causes lattice loosening, creating conditions for the entry of Ce^{3+}. A smaller Stokes shift (and, accordingly, more absorption) in LGSO:Ce samples is responsible for this trend. It is confirmed by the excitation spectra at low energies, where the maximum of the first 4*f*—5*d* absorption band of Ce^{3+} is at

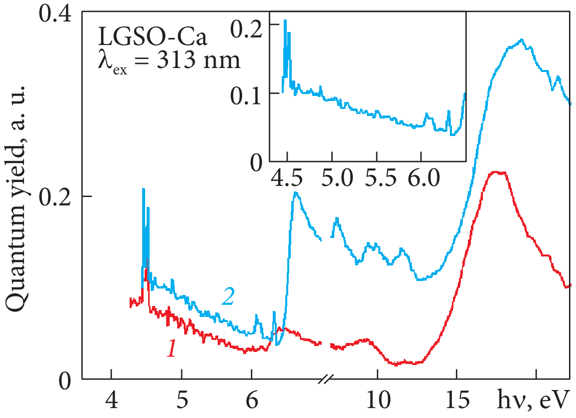

Fig. 3.13. Excitation spectra of Gd luminescence in LGSO:Ce,Ca [179]

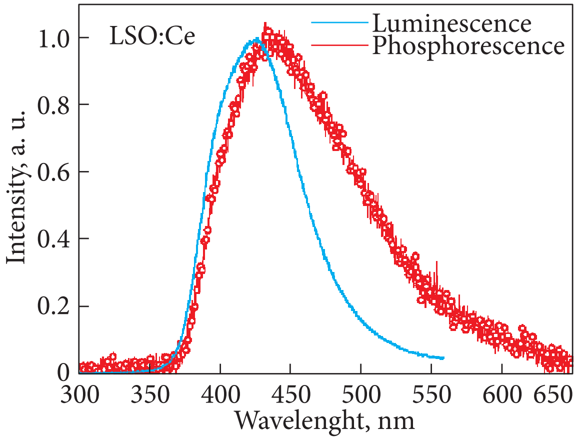

Fig. 3.14. Luminescence and phosphorescence spectra of LSO:Ce at room temperature [179]

~374 nm in LSO and at ~378 nm in LGSO with 60% Lu. The narrow peak at 313 nm in the LGSO:Ce,Ca spectrum in Fig. 3.11 refers to *f*—*f* transitions in Gd^{3+}. A similar peak in LGSO:Se is much weaker.

The spectra of three samples under ~400 nm excitation at 8 K are shown in Fig. 3.12, where they are normalized to maximum of one of the cerium 4*f* —5*d* bands to compare their relative intensity in different parts of the spectrum. The LGSO sample has the highest light output in the range of fundamental absorption >6.6 eV, which ensures a high scintillation output at high-energy excitation. Narrow peaks at 4, 4.5, 5, and 6.3 eV are also observed, related to the 4*f* — 4*f* transitions from the ground level $^8S_{7/2}$ to the excited states ^6P_J, ^6I_J, ^6D_J, and ^6G_J of the Gd^{3+} ion (the inset in Fig. 3.13).

Energy transfer from Gd^{3+} to Ce^{3+} was studied in detail [181—183] for GSO:Ce crystals. Our results indicate that such transfer also occurs in the concentration series of LGSO:Ce crystals. The intensity of the normalized spectrum of the sample co-doped with calcium at energies >10 eV is lower than in LSO:Ce. Fig. 3.13 indicates a possible alternative channel: in contrast to LGSO:Ce, in LGSO:Ce,Ca, the transfer of energy from gadolinium to cerium is not efficient, and part of the energy is released in the form of slow luminescence at 314 nm. The higher the intensity of this luminescence, the lower the intensity of cerium luminescence: the luminescence intensity in LGSO:Ce,Ca is higher than in LSO at 7.0 eV, the ratio is the opposite at 12 eV.

A characteristic feature of LSO:Ce is afterglow, which is a drawback for many practical applications. The luminescence and phosphorescence spectra of LSO:Ce (Fig. 3.14) are somewhat different: the phosphorescence spectrum

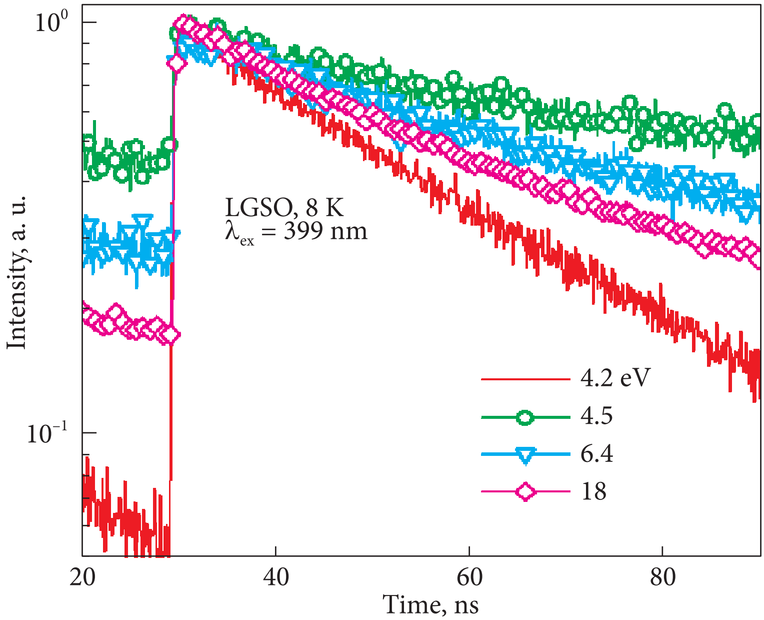

Fig. 3.15. Decay curves of Ce luminescence in LGSO:Ce at 8 K for the indicated excitation energies [179]

is shifted to the long-wavelength side, and it is significantly wider. This may mean that the centers responsible for fast luminescence are also involved in phosphorescence, i.e., may be formed by cerium ions with a nearby trap. If there is a way to prevent the formation of these traps, the phosphorescence would be reduced (or completely eliminated). The addition of gadolinium reduces phosphorescence in all samples, which is illustrated in Fig. 3.15. However, this is not the only consequence of the Gd introduction on the LGSO:Ce decay kinetics. The LGSO:Ce decay curves measured at 8 K are demonstrated in Fig. 3.15. Excitation of cerium luminescence in the *f* — *f* absorption bands of Ce^{3+} (4.5 and 6.3 eV) leads to a significantly longer decay time, as well as to a noticeable luminescence broadening at the initial stage. Figs. 3.15 and 3.16 with the two pairs of curves provides a comparison of the decay curves of LGSO:Ce and LGSO:Ce,Ca samples.

The excitation energy of 4.5 eV corresponds to the $^8S_{7/2} \rightarrow {}^6I_J$ transitions in Gd^{3+}; photons with the energy of 18 eV were chosen as an example of excitation at energies above the fundamental absorption band. Luminescence at 399 nm is characterized by a decay time of ~29 ns; however, in the curve for the LGSO:Ce sample with efficient energy transfer from gadolinium, there is a slow component. Its decay constant was not determined in our measurements since the time interval between excitation pulses of 100 ns is too short. The contribution of the slow component is the strongest during excitation in the *f* — *f* absorption bands of gadolinium.

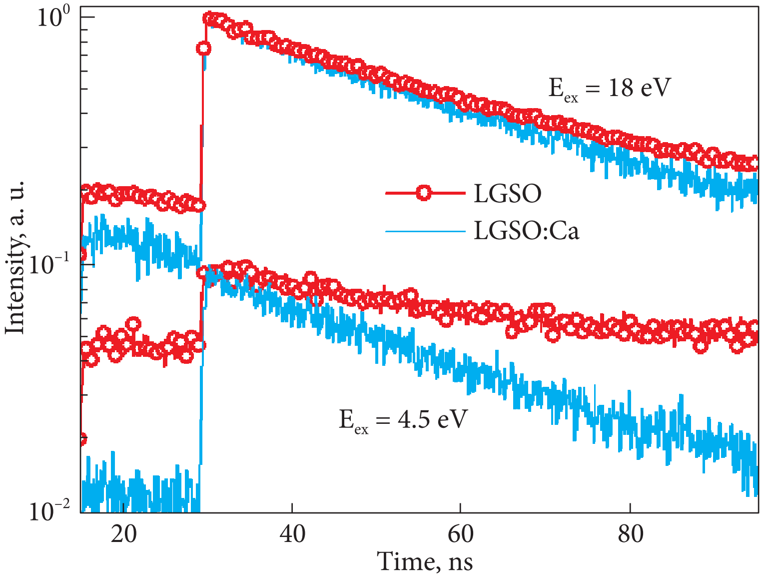

Fig. 3.16. Kinetics of cerium luminescence at the wavelength of 399 nm at 8 K in LGSO:Ce and LGSO:Ce,Ca [179]

The resulting luminescence properties demonstrate two roles played by gadolinium in LGSO:Ce:, it can play a role in efficient energy transfer to cerium, or compete with cerium. In the second case, the increase in light yield is accompanied by luminescence decay. In both cases, the gadolinium ion provides an additional relaxation channel through its 4*f* electronic states and prevents charge carriers from trapping, that reduces the level of afterglow.

3.2. GTNO and YTNO

Evaluation of the luminescence spectra of ceramic samples of undoped orthotantalates under X-ray excitation [58,184] allows us to estimate the integral intensity of luminescence in them. By comparing the areas under the peaks, yttrium orthotantalate was determined to be the brightest among the unactivated orthotantalates with a light yield of about 110% relative to BGO. In addition, the fast decay time of 550 ns and a weak afterglow in $YTaO_4$ should be noted. $GdTaO_4$ possessed a lower light yield, but its decay time was much longer [58]. Gadolinium orthotantalate emits in the red spectral region and matches better with Si photodiodes. In parallel, the scintillation properties of $GdTaO_4$ single crystals grown by the Czochralski method were studied [184]. A strong luminescence was recorded with a main decay time of 72.6 ns [18]. The $GdTaO_4$ light yield was about 3 times higher than that of $PbWO_4$. However, $GdTaO_4$ is significantly «slower» than $PbWO_4$, where about 95% of scintillations correspond to the fast component with a decay time of less than 20 ns.

Thus, a systematic study of the luminescent and scintillation properties of rare earth tantalates made it possible to consider $YTaO_4$ and $GdTaO_4$ as promising scintillation matrices for X-ray diffraction and high-energy physics. The next stage was the engineering of mixed systems of yttrium and gadolinium tantaloniobates and a thorough study of their luminescent and scintillation parameters.

3.2.1. Optical and luminescent properties

Rare-earth orthotantalates are transparent from 250—300 nm in the UV and visible range (Fig. 3.17) according to their bandgap, which is about 5 eV [73]. For example, the shift of the fundamental absorption band from GTO to GTNO (see Fig. 3.17) corresponds to literature data on the bandgap reduction from 5.41 eV in GTO to 4.58 eV in GNO [80]. In the transparency band, only peaks at 310—315 nm and 273 nm are observed, corresponding to the *f* — *f* transitions $^8S_{7/2} - {}^6P_{3/2}, {}^6P_{5/2}, {}^6P_{7/2}$ (300—312 nm) and $^8S_{7/2} - {}^6I_{7/2} + {}^6D_{9/2}$, respectively, in Gd^{3+} ions. The peak at 273 nm is distinguished only in the GTO spectrum, and with the addition of niobium, it merges with the fundamental absorption band. Judging by the differential spectrum, where there are no signs of new absorption bands, the higher *k* in the mixed crystal is associated with the presence of scattering centers.

The luminescence of orthotantalates and orthoniobates is caused by the AO_6 groups (A = Ta, Nb) [63, 64, 69]. Rare-earth niobates exhibit bright luminescence, while high densities can be achieved in orthotantalates, in which luminescence is very weak. Based on these data, we searched for tantaloniobate compositions that combine reasonable light yield and high density. It was also necessary to investigate the luminescence decay in mixed systems.

The properties of tantaloniobate solid solutions are promising hosts for optoelectronics and X-ray intensifying screens were studied in [185—187]. In particular, the luminescent properties of yttrium tantaloniobates with a low content of Nb in the matrices were studied in [187, 189]. Luminescence mechanisms in gadolinium tantaloniobate have not been investigated before. The excitation and luminescence spectra of the synthesized samples are presented in Fig. 3.18*a*. They agree well with

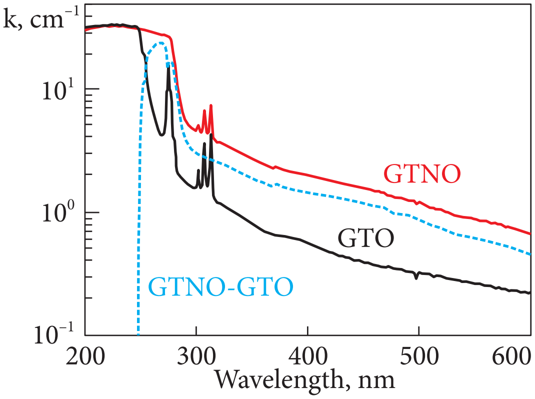

Fig. 3.17. Absorption spectra of GTO, GTNO crystals and differential spectrum (dashed line), *T* = 300 K [184]

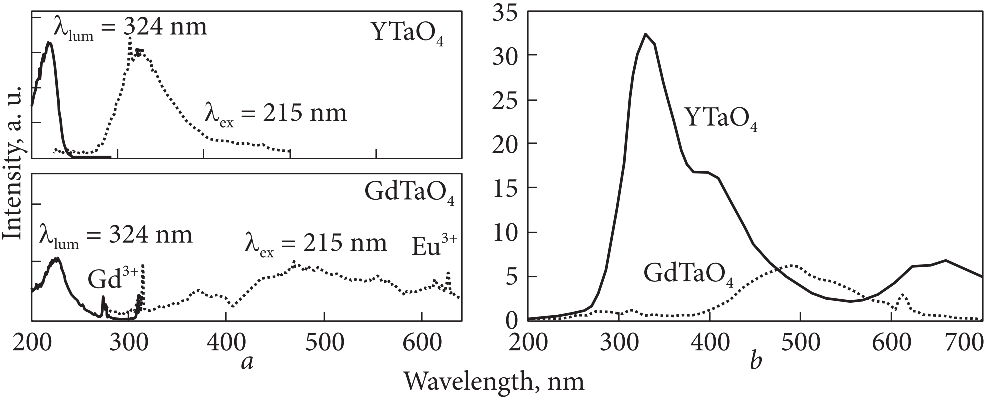

Fig. 3.18. Spectra of selective excitation and luminescence (*a*), X-ray luminescence spectra (*b*) of orthotantalates [58]

literature data [190] regarding the intrinsic luminescence of lutetium orthotantalate with a maximum at 320—350 nm. The luminescence excitation band of the TaO$_6$ group for all the hosts is around 220 nm. An additional peak at 273 nm in the GdTaO$_4$ excitation spectrum is associated with the ^8S – ^6I transition in the gadolinium ion and indicates energy transfer from Gd^{3+} to the TaO$_6$ group. All luminescence spectra show a narrow peak around 315 nm associated with intracenter transitions in Gd^{3+}.This may indicate energy transfer from the TaO$_6$ group to Gd^{3+} or to higher energy levels of Gd^{3+} that can be excited at 215 nm with subsequent emission associated with the $^6P_{7/2}$ – $^8S_{7/2}$ transition in Gd^{3+}. This peak is also observed in YNb$_x$Ta$_{1-x}$O$_4$, where the concentration of uncontrolled impurity Gd is several ppm. The main luminescence band of YTaO$_4$ is at 320—330 nm (Fig. 3.18*a*). In GdTaO$_4$ at room temperature, the registered luminescence is red-shifted by 100 nm compared to other orthotantalates, despite the data [63] that GdTaO$_4$ does not exhibit bright luminescence at room temperature. Such a shift can be explained by another lattice structure type (see section 2.4) and a higher strength of the crystal field in the *M*-fergusonite structure in GdTaO$_4$. The spectrum of GdTaO$_4$ also contains peaks associated with Gd^{3+} (315 nm) and the uncontrolled impurity of Eu^{3+} (610—615 nm).

The X-ray luminescence spectrum (Fig. 3.18*b*) of YTaO$_4$ contains a double peak with the first maximum in the range of 320—350 nm, associated with the luminescence of the TaO$_6$ group, and the second maximum at 410 nm, which can be associated with the TaO$_5$V$_O$ group, where V$_O$ is an oxygen vacancy [65, 149]. At the same time, the last peak was observed during UV and cathodic excitation at temperatures of 4.2 K and 77 K, respectively [64]. Temperature quenching of the TaO$_5$V$_O$ group luminescence occurs around 100 K. At room temperature, the TaO$_5$V$_O$ group acts as a luminescence quenching center of the TaO$_6$ group. Therefore, the nature of the second luminescence maximum at 410 nm in the YTaO$_4$ spectrum at room temperature is not elucidated.

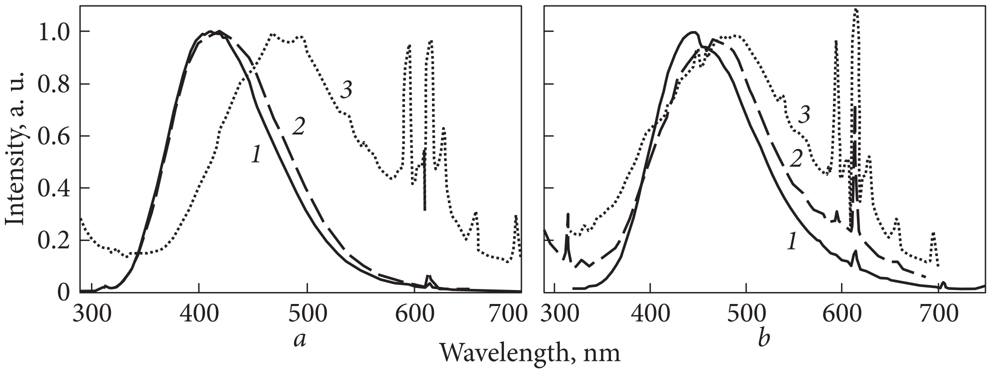

Fig. 3.19. Normalized photoluminescence spectra of yttrium (*a*): *1* — $YNbO_4$; *2* — $YNb_xTa_{1-x}O_4$ (Nb 40at%); *3* — $YTaO_4$ and gadolinium (*b*): *1* — $GdNbO_4$; *2* — $GdNb_xTa_{1-x}O_4$ (Nb 40at%); *3* — $GdTaO_4$ tantaloniobates upon excitation at 255 nm (*a*) and 260 nm (*b*), respectively [191]

The spectrum of X-ray luminescence (as well as photoluminescence) of $GdTaO_4$ is shifted relative to $YTaO_4$ to the red region of the spectrum. It is believed that the TaO_6 group captures most of the electron-hole pairs formed during X-ray excitation, and an $O_2 \rightarrow Ta^{5+}$ charge transfer transition occurs [56, 74]. The most efficient transfer is observed in orthotantalates with the *M′*-fergusonite structure (yttrium and lutetium orthotantalates). In gadolinium orthotantalate, luminescence is weakened by the energy transfer of $TaO_6 \rightarrow Gd^{3+}$ with subsequent concentration quenching of Gd^{3+} luminescence.

In mixed crystals, broad, powerful bands at 415 nm and 455 nm in the photoluminescence spectra of $Y(Ta_{1-x}Nb_x)O_4$ and $Gd(Ta_{1-x}Nb_x)O_4$ (Fig. 3.19*a*, *b*) are usually associated with the NbO_6 group [64]. Broad emission bands in tantalates are red-shifted and associated with the TaO_6 group, but the narrow peaks of Eu^{3+} uncontrolled impurity in the 590—615 nm range are much more intense. Narrow peaks associated with ${}^6P_{7/2} \rightarrow {}^8S_{7/2}$ transitions in Gd^{3+} (315 nm) are also observed in this series of solid solutions. This means that the Gd^{3+} admixture is also present in the $Y(Ta_{1-x}Nb_x)O_4$ samples and proves the efficient transfer of energy from Gd^{3+} to the NbO_6 and TaO_6 groups. It is noteworthy that, while in YTNO, the spectrum of the mixed crystal is almost similar to that of YNO, even when 60% of Nb is replaced by Ta, the spectrum of GTNO is more identical to the spectrum of GTO.

Luminescence spectra upon X-ray excitation [191] or synchrotron radiation [192] contain bands corresponding to the luminescence of NbO_6– and TaO_6– groups at 425—450 nm in $Y(Ta_{1-x}Nb_x)O_4$ and at 450—475 nm in $Gd(Ta_{1-x}Nb_x) \times \times O_4$. Weak emission bands of the Eu^{3+} impurity in the range of 600—615 nm are also observed [191]. The luminescence spectra of $Gd(Ta_{1-x}Nb_x)O_4$ obtained at 5 and 300 K under synchrotron excitation with an energy of 22 eV, corresponding to interband electronic transitions, are similar.

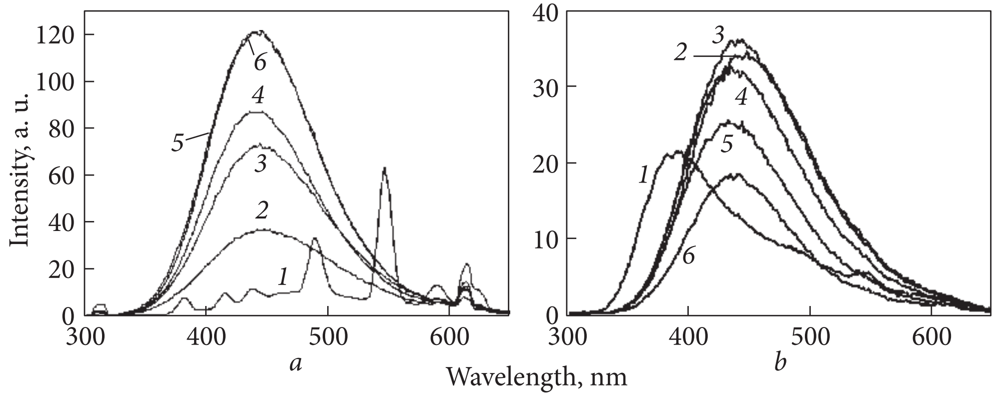

Fig. 3.20. Normalized luminescence spectra of $Gd(Ta_{1-x}Nb_x)O_4$ ($x = 0$ (*1*); $x = 0.2$ (*2*); $x = 0.4$ (*3*); $x = 0.6$ (*4*); $x = 0.8$ (*5*) and $x = 1$ (*6*)) excited by synchrotron radiation, $E_{ex} = 22$ eV and $T = 300$ K (*a*), $T = 5$ K (*b*) [193]

The luminescence spectra of $Gd(Ta_{1-x}Nb_x)O_4$ at $T = 300$ K are demonstrated in Fig. 3.20*a*. At $x \neq 0$, all samples exhibit a broad luminescence band with a maximum of around 450 nm. The luminescence spectra of rare-earth tantalo-niobates have a complex structure and consist of a short-wave band peaked at 415 nm associated with the excitonic luminescence of regular oxyanion complexes NbO_6, and a long-wave band peaked at 460 nm associated with point defects, in particular, oxygen vacancies (group NbO_5V_O) [193]. As a consequence, the luminescence of $Gd(Ta_{1-x}Nb_x)O_4$ recorded at room temperature can be attributed to defects. Intrinsic matrix luminescence is not manifested, probably due to temperature quenching or due to energy transfer from the host to defects. A broad but weak luminescence band in the $GdTaO_4$ spectrum (Fig. 3.20*a*, curve *1*) is red-shifted and associated with the TaO_5V_O group [65]. Several sharp peaks at 380, 420, 440, 490, 550, 590, and 610 nm in the $GdTaO_4$ spectrum refer to the luminescence of Eu^{3+} and Tb^{3+} impurities.

The luminescence spectra of $Gd(Ta_{1-x}Nb_x)O_4$ ($x \neq 0$) at $T = 5$ K (Fig. 3.20*b*) are similar to the spectra at $T = 300$ K with a maximum around 450 nm. Thus, excitonic luminescence of regular NbO_6 oxyanion complexes is also not observed at low temperatures. A broad band with a maximum of around 395 nm was registered for $GdTaO_4$ (Fig. 3.20*b*, curve *1*). In [65], the intrinsic luminescence of $GdTaO_4$ at T = 77 K was associated with defects, by analogy with the luminescence in $YTaO_4$ with a maximum at 400—420 nm. Thus, the band at 395 nm observed in this work can be associated with the intrinsic luminescence of $GdTaO_4$. It should be noted that this band is completely absent both in the spectrum of $Gd(Ta_{1-x}Nb_x)O_4$ ($x \neq 0$) at $T = 5$ K, confirming the effective transfer from regular TaO_6 groups to defect states, and in the luminescence spectrum of $GdTaO_4$ at $T = 300$ K, confirming the temperature quenching of intrinsic luminescence.

3.2.2. Defects in $Gd(Ta_{1-x}Nb_x)O_4$ solid solutions

Since the main type of luminescence in the investigated mixed tantaloniobates is associated with NbO_5V_O and TaO_5V_O defect groups, the defect structure of these compounds was analyzed. Thermally stimulated luminescence (Fig. 3.21*a*) curves contain a lot of useful information about defects in a solid solution. Up to five peaks can be noted on the curves of thermal stimulated luminescence (TSL) in $Gd(Ta_{1-x}Nb_x)O_4$. We can note two TSL peaks present in all samples: a weak one at ~150 K and an intense one at ~ 250 K. The peak below 200 K is the most intense in $GdTaO_4$ and may be associated with the TaO_6 group. The weaker intensity of these peaks in the rest of $Gd(Ta_{1-x}Nb_x)O_4$ samples, $x \neq 0$), confirms the energy transfer from the TaO_6 to defect groups. Phosphorescence peaks at 200—350 K are associated with deeper traps, which probably belong to oxygen vacancies near TaO_6 or NbO groups. An interesting feature is the presence of an additional high-temperature peak at 280—320 K only in $GdTaO_4$ or $GdNbO_4$.

The gradual shift of these peaks to lower temperatures with increasing x corresponds to a decrease in the energy of the corresponding traps. This trend is associated with a decrease in the averaged bandgap (the average value of the bandgap in the crystal volume averaged over inhomogeneities) from $GdTaO_4$ to $GdNbO_4$.

The gradual shift of these peaks to lower temperatures with increasing x corresponds to a decrease in the energy of the respective corresponding traps. This trend is associated with a decrease in the average bandgap (the average value of the bandgap in the crystal volume, averaged over inhomogeneities) from $GdTaO_4$ to $GdNbO_4$. It is worth noting that the width of the TSL peaks also depends on the value of x. The half-width of the strongest peak at ~250 K depends nonlinearly on x with a maximum at $x = 0.4$ (Fig. 3.21*b*).

3.2.3. Scintillation properties

The integrated luminescence intensity in the spectral range of 250—700 nm (light yield) was measured upon excitation by synchrotron radiation at temperatures of 16 K (Fig. 3.22). At 300 K, the dependence of light yield on x is close to a linear one according to Vegard's law, while at 16 K it deviates significantly from the linear dependence for intermediate concentrations. Effective transfer from regular groups of TaO_6 to defect states can cause a significant increase in light yield for intermediate values of x in $Gd(Nb_xTa_{1-x})O_4$ $(x \neq 0)$ at $T = 16$ K, while the luminescence of regular groups of TaO_6 is thermally quenched at $T = 300$ K.

Dependencies of light yield at room temperature on the Ta/Nb ratio are shown in Fig. 3.23. The light yield of yttrium orthotantalate was taken as unity. In mixed samples, the light yield increases up to 7 times relative to $YTaO_4$. In GTNO, it increases monotonically with the Nb concentration, and in the yttrium system, it is difficult to follow the trend of the light yield change. The

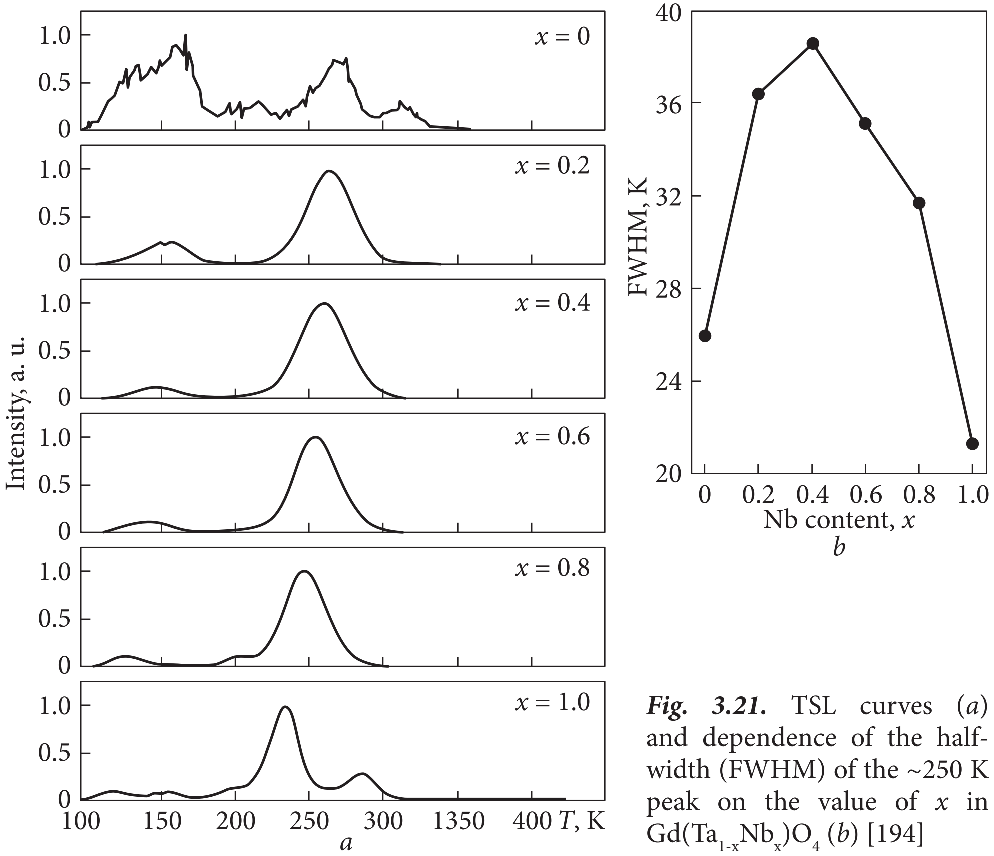

Fig. 3.21. TSL curves (*a*) and dependence of the half-width (FWHM) of the ~250 K peak on the value of *x* in Gd(Ta$_{1-x}$Nb$_x$)O$_4$ (*b*) [194]

light yield of YTaO$_4$ is much lower compared to other samples, probably due to the difference in the crystal structure, see Table 3.3. The tendency of decreasing light yield with an increase in the tantalum content may be related to the average distance between Nb^{5+} and O^{2-}, which is larger compared to the distance between Ta^{5+} and O^{2-} [184]. This can lead to temperature quenching of luminescence in the tantalate matrix [64, 195]. It is noteworthy that the intensity of luminescence at low temperatures in mixed compositions is up to 2 times higher than that of their components (Fig. 3.23*b*).

The absolute light yield determined on GTO and GTNO single crystals under ^{137}Cs (662 keV) excitation as 1250 and 1400 phot/MeV, respectively, qualitatively agrees with [184] and the data on the relative light yield of ceramic samples given above. Kinetic characteristics of X-ray luminescence are presented in Table 3.4. The luminescence decay curves of Y(Ta$_{1-x}$Nb$_x$)O$_4$ involve fast and slow components. Decay constants and contributions of fast and slow decay components were estimated by approximating the experimental points according to the function $I = I_0 + A_1 \cdot \exp(-t/\tau_1) + A_2 \cdot \exp(-t/\tau_2)$, where t is time, τ_1, τ_2 are decay constants, A_1, A_2, and I_0 are constants. In Gd(Ta$_{1-x}$Nb$_x$)O$_4$, the τ_1 constants

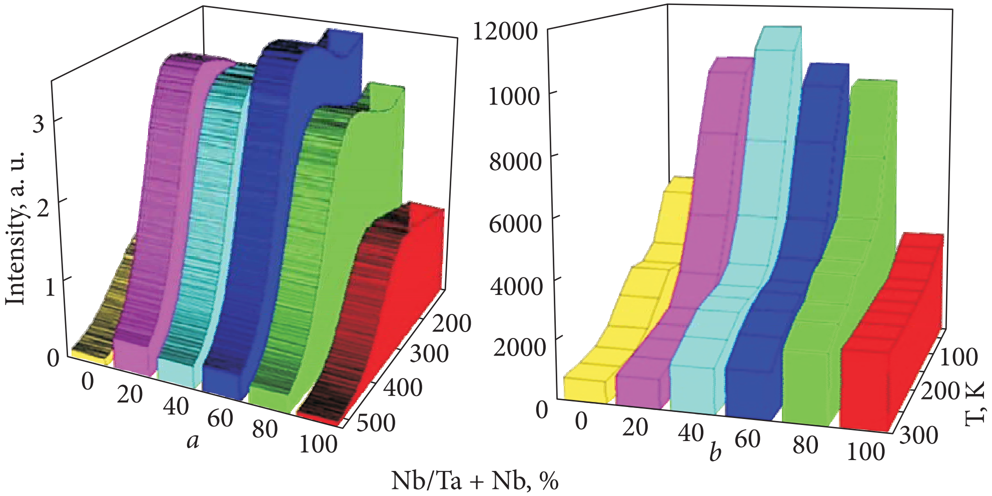

Fig. 3.22. Dependence of light output on temperature and Nb concentration in $Y(Nb_xTa_{1-x})O_4$ (*a*) and $Gd(Nb_xTa_{1-x})O_4$ (*b*) [194]

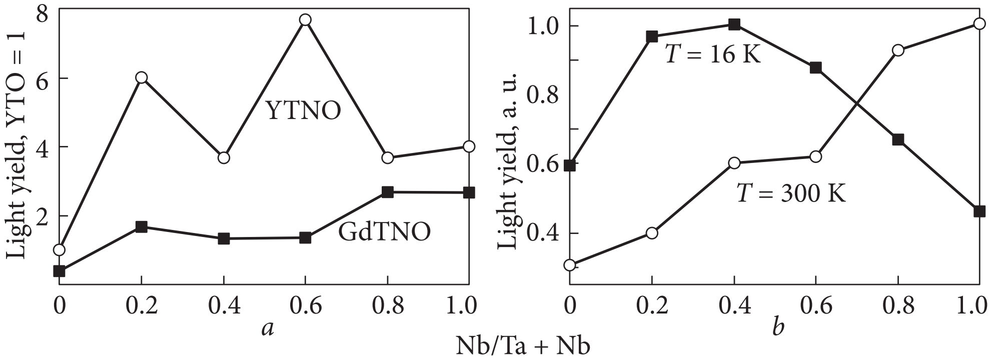

Fig. 3.23. Light yield in tantaloniobates depending on the Ta/Nb ratio. *T* = 300 K (*a*); dependence of the $Gd(Nb_xTa_{1-x})O_4$ light yield of during X-ray excitation at temperatures of 16 K and 300 K (*b*) [194]

were determined by approximating the experimental points according to the function $I = I_0 + A_1 \cdot \exp(-t/\tau_1)$ during the first 50—100 ns. The decay constants of the slow components in $Gd(Ta_{1-x}Nb_x)O_4$ were not determined because of the strong build-up and too small available measurement time gates.

The decay times τ_1 and τ_2 in $Y(Ta_{1-x}Nb_x)O_4$ vary in the range of 130—390 ns and 1.95—2.67 μs, respectively, and depend on the Ta/Nb ratio. The fast decay component prevails only in $YNbO_4$. A completely different situation is observed in gadolinium tantaloniobates. The fast component τ_1 = 5—93 ns is accompanied by a build-up that appears after ~50 ns. A similar luminescence build-up was detected earlier in the system of gadolinium borates and phosphates

[196—198]. The presence of build-up in Gd-containing complex oxides may indicate the role of the Gd^{3+} sublattice in energy transfer [199].

The decay constant of 93 ns in $GdTaO_4$ agrees well with the time of 72.6 ns obtained in [186]. The difference in decay constants can be attributed to different methods of sample preparation: single crystal growth by the Czochralski method in [186] and solid-phase synthesis of ceramic samples in this work. At the same time, a rather unexpected result was obtained in mixing tantaloniobates. The slow component is completely absent in the sample with x = 0.2, while in the remaining samples, its contribution during the first microsecond is at least 81%. The data on the decay kinetics of single-crystalline samples qualitatively agree with the data on ceramic samples. The decay time of the fast component is 23 ns in GTO and 17 ns in GTNO. In the latter case, the contribution of the fast component is very high (Table 3.4).

Time-resolved luminescence [200] indicates that the fast component is associated with luminescence bands peaking at 375 nm for GTO and 415 nm for GTNO. The intensity of the «fast» and «slow» luminescence bands is comparable in GTNO, however, the low spectral sensitivity of the EMI 9954 PMT at >500 nm [201], with the cutting out of the slow component, causes such a large contribution of fast luminescence to the total signal (Table 4.5).

Thus, the spectral and scintillation properties of solid solutions of rare-earth tantalates and niobates were systematically investigated. The GTNO light yield at 300 K increases linearly with an increase in the proportion of niobium in the matrix. At the same time, at 5 K, the dependence of the light yield has a non-linear character with a maximum of 20—40% niobium in the matrix. This dependence in the literature [64, 195] was associated with the improvement

Table 3.4. **Kinetic characteristics of scintillations under X-ray excitation. Coefficients A_1, A_2 when approximating the attenuation curves of $Y(Ta_{1-x}Nb_x)O_4$ are given in parentheses. In $Gd(Ta_{1-x}Nb_x)O_4$, the contribution of the fast component to the integral luminescence within 1 μs after the termination of X-ray excitation is given in parentheses [194]**

Nb content, (x)	τ_1, μs (A_1)	τ_2, μs (A_2)	τ_1, ns (A_1)	
	$Y(Ta_{1-x}Nb_x)O_4$ ceramics		$Gd(Ta_{1-x}Nb_x)O_4$	
			Ceramics	Single crystal
0	0.13 (62%)	2.21 (38%)	93 (11%)	23 (3%)
0.2	0.32 (38%)	2.43 (62%)	12 (100%)	17 (94%)
0.4	0.38 (33%)	2.63 (67%)	19 (4%)	—
0.6	0.39 (29%)	2.67 (71%)	32 (19%)	—
0.8	0.27 (17%)	2.24 (83%)	33 (17%)	—
1.0	0.38 (15%)	1.95 (85%)	5 (4%)	—

of energy transfer from TaO_6 groups to defects; however, its mechanism was unclear and may be related to the heterogeneity of the solid solution, which is discussed in detail in Chapter 4. In particular, evidence of inhomogeneity of the GTNO solid solution is an increase in the TSL peaks FWHM in the mixtures (see Fig. 4.21). In contrast, the dependence of the light yield in YTNO solid solutions were difficult to estimate due to the wide spread of values in ceramic samples; herein, the light yield in mixed compositions also increases significantly at low temperatures.

3.3. YAGG:Ce and GAGG:Ce

Cerium-activated rare-earth garnet-based scintillators are candidates for many applications due to their good mechanical properties, high light yield, and fast luminescence. In recent years, the engineering of crystals with the garnet structure has become one of the main directions of search for new scintillation materials. $Y_3Al_5O_{12}$:Ce (YAG) and $Lu_3Al_5O_{12}$ (LuAG) activated by Ce or Pr, since their discovery in the 60s [202] and application as cathodoluminescent screens in the 70s, they were considered less promising compared to denser and faster perovskites $YAlO_3$ (YAP) [203] and $LuAlO_3$ (LuAP) activated by Ce or Pr [204], as well as brighter orthosilicates Lu_2SiO_5 (LSO) [50] and $Lu_{2-x}Y_xSiO_5$ (LYSO) activated by cerium [205]. Luminescence in the green spectral range was another drawback of garnets activated by cerium, as it did not match with the sensitivity range of the «blue» PMTs that were popular at the time. The renaissance of cerium-activated garnets began in the 2010s due to advances in YAG:Ce and LuAG:Ce crystal manufacturing technology and the discovery of mixed Gd-Lu-Y/Al-Ga substituted scintillators with unexpectedly high light yield and energy resolution — $Lu_3Al_{5-x}Ga_xO_{12}$ (LuAGG), $Gd_3Al_{5-x}Ga_xO_{12}$, $Gd_{3-x}Y_xAl_{5-x}Ga_xO_{12}$ (GYAGG) [3, 4, 206], etc. In turn, the $Y_3Al_{5-x}Ga_xO_{12}$:Ce (YAGG:Ce) scintillator can become an alternative to analogues based on lutetium and gadolinium. The $Y_3Al_{5-x}Ga_xO_{12}$ system, unlike its gadolinium counterpart, forms a continuous series of solid solutions in the entire range of x values. Thus, it is a convenient object for a detailed study of the relationship between the composition and optical, luminescence, and scintillation properties of mixed garnets. In addition, YAGG:Ce crystals contain light and medium-weight ions, and their radiation tolerance to high-energy hadrons should be better compared to PWO and other heavy scintillators [207, 208].

Garnets activated by Ce^{3+} possess rather slow luminescence decay due to a high concentration of defects, primarily antisite RE-Al/Ga defects and oxygen vacancies and their complexes, which act as carrier traps and slow down the carrier transport to Ce^{3+} [209—211]. In addition, aluminum-based garnets exhibit very long-wavelength Ce^{3+} luminescence due to the fundamental $\tau \sim \lambda^3$ limitation [87] (τ is the luminescence decay time, λ is the luminescence wavelength) and strong Ce^{3+} level splitting compared to orthosilicates and perovskites. These factors together increase the decay time of the slow component of Ce^{3+} luminescence to 60—120 ns. There are also slow components with a decay time of hundreds of ns, caused by the influence of defects in the crystal on the luminescence excitation process. The slow decay component is a serious drawback, for example, for applications in high-energy physics, where the time interval between particle collisions at the High-Luminosity Large Hadron Collider is 25 ns [139, 140, 212].

Thus, cerium-activated garnet crystals have an attractive combination of high light yield and moderate density. Bandgap engineering due to substitution by a rare earth cation and/or Al^{3+}/Ga^{3+} and co-doping with divalent ions provides the possibility of precise regulation of garnet scintillation properties. Another advantage of garnets is chemical stability and a relatively simple process of obtaining crystals of various shapes. This section describes the optical, luminescence, and scintillation properties of mixed garnet crystals using the examples of Ce-doped $Y_3Al_{5-x}Ga_xO_{12}$ and $Gd_3Al_{5-x}Ga_xO_{12}$ in the entire range of x from 0 to 5.

3.3.1. Optical properties

Absorption spectra of $Y_3Al_{5-x}Ga_xO_{12}$:Ce crystals with different Ga contents are shown in Fig. 3.25*a* in comparison with the $Y_3Al_5O_{12}$ absorption spectra of. A change in the cation composition affects the positions of the absorption bands associated with $4f(^2F_{5/2}) \rightarrow 5d_{1.2}(^2E)$ and $4f \rightarrow 5d_{3\text{-}5}(T_{2g})$ transitions in Ce^{3+} ions (marked as E_1, E_2, and E_3 bands, respectively), as well as the energy gap $E = E_1 - E_2$ between them. Such changes in the value of ΔE reflect a change in the crystal field strength in the dodecahedral positions in the garnet lattice occupied by Ce^{3+} ions, particularly, the weaker crystal field strength in YGG:Ce than in YAG:Ce. A strong shift of the absorption edge in $Y_3Al_{5-x}Ga_xO_{12}$:Ce in the UV range (Fig. 3.24*a*) indicates a decrease in the bandgap in these garnets with increasing Ga content. Namely, the value of the bandgap E_g decreases by ~1.0 eV in YGG compared to YAG (inset in Fig. 3.24*a*).

The absorption spectrum of $Gd_3Al_{2.5}Ga_{2.5}O_{12}$:Ce crystals (Fig. 3.24*b*) consists of strong bands at 445 and 340 nm corresponding to energy transitions $4f \rightarrow 5d_{1.2}$ in Ce^{3+} ions. The edge of the fundamental absorption band is located at 210 nm. Narrow bands around 275 nm and 310 nm corresponding to energy transitions in Gd^{3+} ions are also observed on the spectrum.

3.3.2. Luminescence upon selective excitation

Fig. 3.25 summarizes the luminescence spectra of $Y_3Al_{5-x}Ga_xO_{12}$:Ce in the UV (*a*) and visible (*b*) range when excited by synchrotron radiation with energy in the range of excitonic (*a*) and interband transitions (*b*). Like in the X-ray and cathodo-luminescence spectra, the replacement of Al^{3+} cations with Ga^{3+} caus-

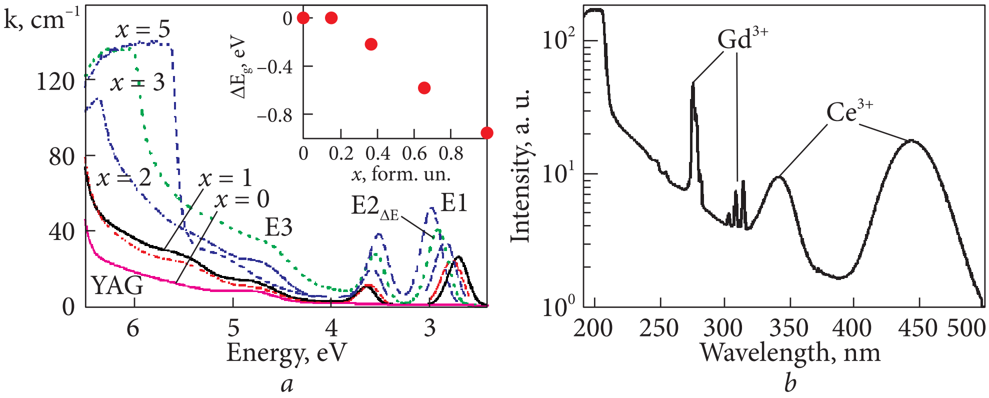

Fig. 3.24. Absorption spectra of $Y_3Al_{5-x}Ga_xO_{12}$:Ce crystals with different concentrations of gallium (*a*). In the inset: the shift of the absorption edge with increasing *x* indicates a decrease in the bandgap by 1.0 eV in YGG compared to YAG; absorption spectrum of GAGG:Ce crystal (*b*) [213]

es a high-energy shift of the radiation spectra in the visible range, caused by $5d_1 \rightarrow 4f\ (^2F_{5/2,7/2})$ transitions in Ce^{3+} ions (Fig. 3.25*b*). In particular, the maximum of the $Y_3Al_2Ga_3O_{12}$:Ce emission spectrum is shifted to 515 nm compared to 567 nm for YAG:Ce. At the same time, the $Y_3Ga_5O_{12}$:Ce emission spectrum almost coincides with the $Y_3Al_2Ga_3O_{12}$:Ce spectrum (Fig. 3.25*b*, curves *4* and *3*, respectively). It is interesting to note that the Ga substitution also changes the shape of the emission spectrum caused by a change in the probability of radiative transitions in YAG:Ce (to the $^2F_{7/2}$ level) and in $Y_3Al_2Ga_3O_{12}$:Ce (to the $^2F_{5/2}$ level) (Fig. 3.25*b*, curves 1 and 3 , respectively).

Fig. 3.25*a* demonstrates the spectra of $Y_3Al_{5-x}Ga_xO_{12}$:Ce intrinsic luminescence in the UV range at *x* = 0, 1, and 2. The complex structure of the YAG:Ce emission spectrum is related to the luminescence of excitons «localized around» and «associated with» antisite defects, with the maxima at 4.12 and 3.43 eV, respectively (denoted as *ex*(*AD*) and Y_{Al}), as well as the luminescence of $F^+{-}Y_{Al}$ centers peaked at 3.095 eV (F^+ is an oxygen vacancy with one captured electron [215, 216]). It is important to note that the addition of Ga^{3+} greatly reduces the intensity of luminescence associated with antisite defects, and for $Y_3Al_3Ga_2O_{12}$:Ce and $Y_3Al_2Ga_3O_{12}$:Ce, the emission of these centers completely disappears (Fig. 3.25*a*, curves *2* and *3*). The narrow peak at 317 nm is associated with the luminescence of the Gd^{3+} impurity.

Excitation spectra of Ce^{3+} luminescence in $Y_3Al_{5-x}Ga_xO_{12}$:Ce in different spectral ranges are summarized in Fig. 3.26. These spectra consist of two bands at >3.7 eV and 5.37—5.49 eV, associated with $4f \rightarrow 5d\ (^2E$ and $T_{2G})$ transitions in Ce^{3+} ions. Intense bands in the exciton excitation range of 6.0—6.9 eV correspond to the formation energy of excitons associated with Ce^{3+} ions.

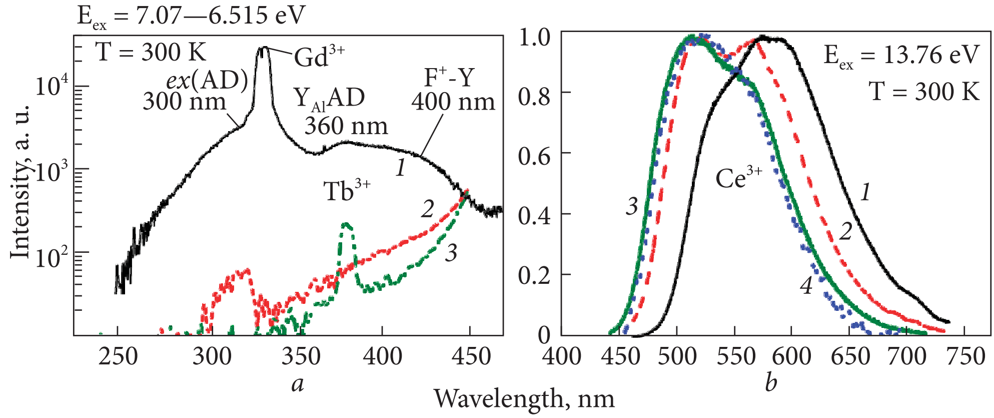

Fig. 3.25. Luminescence spectra of $Y_3Al_{5-x}Ga_xO_{12}$:Ce in the UV range (*a*, logarithmic scale) and visible range (*b*, normalized) under synchrotron excitation in the exciton band (*a*) and in the range of interband transitions (*b*); *a* — *1* — $Y_3Al_5O_{12}$:Ce; *2* —$Y_3(Al_{0.6}Gd_{0.4})_5O_{12}$:Ce; 3 — $Y_3(Al_{0.4}Gd_{0.6})_5O_{12}$:Ce; *b* — *1* — $Y_3Al_5O_{12}$:Ce; *2* — $Y_3A_3Ga_2O_{12}$:Ce; *3* — $Y_3Al_2Ga_3O_{12}$:Ce; *4* — $Y_3Ga_5O_{12}$:Ce; *T* = 300 K [213]

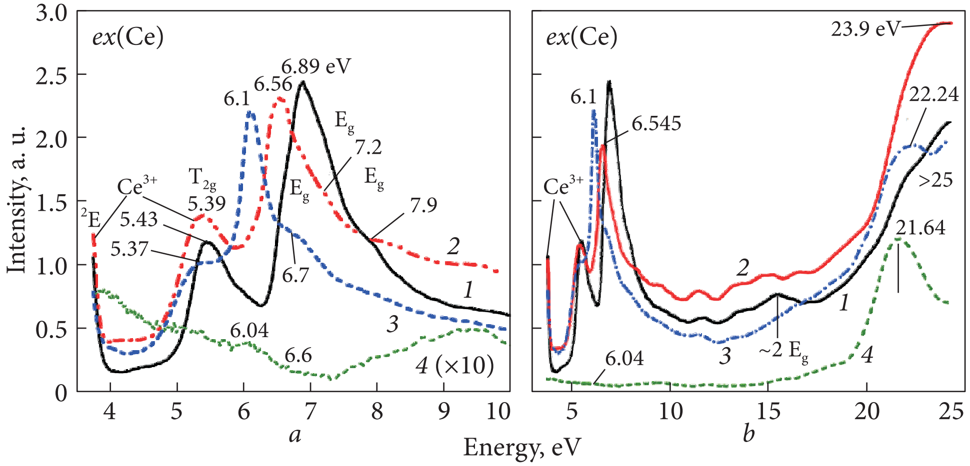

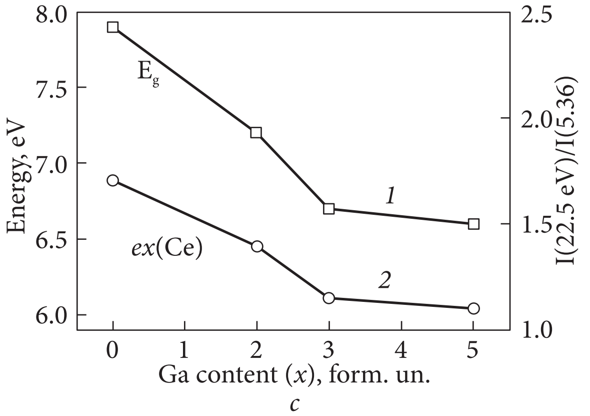

Fig. 3.26. Excitation spectra of Ce^{3+} luminescence in $Y_3Al_{5-x}Ga_xO_{12}$:Ce with different *x* at 300 K in the spectral ranges of 3.5—10 eV (*a*) and 3.5—25 eV (*b*); (*c*) dependence of the bandgap width (*1*, left scale), the formation energy of Ce^{3+}-bound excitons *ex*(Ce) (*2*, left scale) on the Ga content [213]: *1* — YAG:Ce; *2* — $YAl_{0.6}Ga_{0.4}G$:Ce; *3* — $YAl_{0.4}Ga_{0.6}G$:Ce; *4* — YGG:Ce

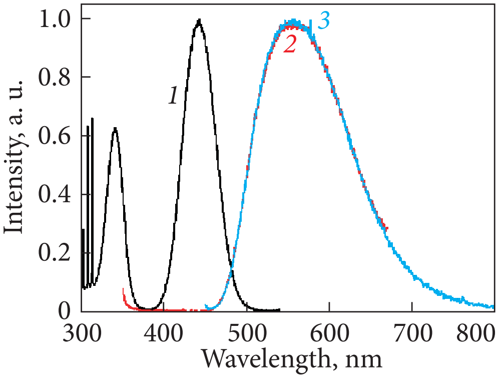

Fig. 3.27. GAGG:Ce luminescence excitation spectrum at 555 nm (*1*), GAGG:Ce luminescence spectra upon excitation at 340 nm (*2*) and 440 nm (*3*)

The peaks in the range of 6.6—7.9 eV correspond to the beginning of interband transitions in YAG. These spectra confirm that with increasing Ga content, the bandgap E_g of $Y_3Al_{5-x}Ga_xO_{12}$ garnets decreases from 7.9 eV for YAG to 6.7 eV for $Y_3Al_2Ga_3O_{12}$ (Fig. 3.26*c*, curve *1*). The bandgap of the YGG host can be estimated at 6.6 eV (Fig. 3.26*a*, curve *4*. The energy of exciton formation associated with Ce^{3+} ions (*ex*(Ce)) also decreases from 6.89 eV for YAG:Ce to 6.1 eV for $Y_3Al_2Ga_3O_{12}$:Ce (about 0.3 eV per one formula unit of Ga), and then to 6.04 eV for YGG:Se (Fig. 3.26*c*, curve *2*). Due to the different slopes of the dependences, for example, $E_g(x)$ and *ex*(Ce)(*x*) presented in Fig. 3.26*c*, the energy distance between E_g and *ex*(Ce) decreases strongly with increasing Ga content in the range of $x = 0 \div 3.0$ and practically does not change at $x > 3.0$. A strong increase in the luminescence intensity of Ce^{3+} in $Y_3Al_{5-x}Ga_x$O12:Ce is observed when excited by synchrotron radiation with an energy higher than 14—15 eV, and peak values in the range of 21.6—25 eV, which correspond to the $2E_g$ and $3E_g$ energies of the electron-hole pairs multiplication (Fig. 3.26*b*), respectively.

The spectra of selective excitation of Ce^{3+} luminescence in $Gd_3Al_{2.5}Ga_{2.5}O_{12}$:Ce (GAGG:Ce), Fig. 3.27, is similar to that of YAGG:Ce. The luminescence spectra under intracenter excitation of cerium at 340 and 440 nm are absolutely identical to the maximum at 555 nm, which roughly corresponds to the luminescence spectrum of YAG:Ce. Meanwhile, the GAGG:Ce luminescence spectrum is red-shifted compared to YAGG:Ce, indicating a stronger crystal field in the Gd-containing system. The luminescence excitation spectrum of GAGG:Ce at 555 nm consists of strong bands at 445 and 340 nm corresponding to the $4f \rightarrow 5d_{1,2}$ energy transitions in Ce^{3+} ions. Narrow bands around 310 nm corresponding to energy transitions in Gd^{3+} ions are also observed on the spectrum. The kinetics of Ce^{3+} luminescence decay in $Y_3Al_{5-x}Ga_xO_{12}$:Ce upon excitation in the range of interband transitions and in the absorption band of Ce^{3+} are demonstrated in Fig. 3.28*a*, *b*, respectively. One can see that the addition of Ga to YAG:Ce leads to a strong decrease in the Ce^{3+} luminescence decay time under both types of excitation. At the same time, the kinetics of decay upon excitation in the range of interband transitions in $Y_3Al_2Ga_3O_{12}$:Ce and YGG:Ce crystals are noticeably non-exponential. This indicates the energy transfer from the ex-

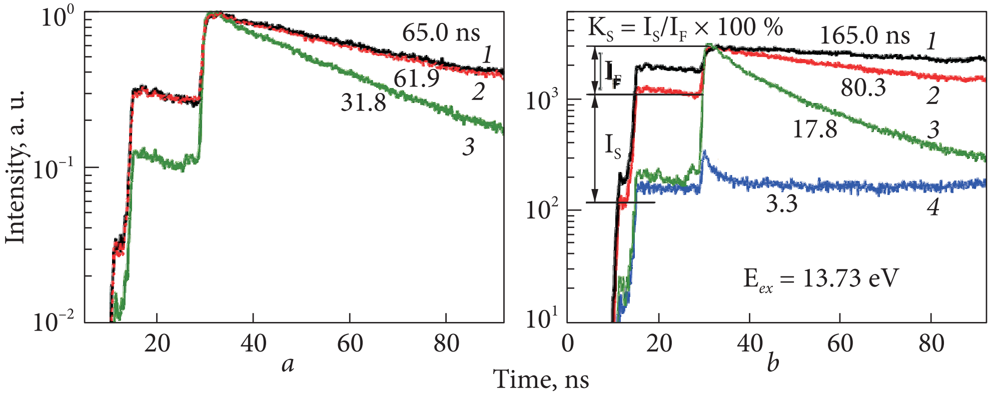

Fig. 3.28. Luminescence decay curve of Ce^{3+} in $Y_3Al_{5-x}Ga_xO_{12}$:Ce: *a*) upon synchrotron excitation in the range of interband transitions at 13.76 eV: *1* — $Y_3Al_5O_{12}$:Ce; $t(1/e)$ = 165 ns, K_S = 123.6%; *2* —$Y_3Al_3Ga_2O_{12}$:Ce; $t(1/e)$ = 80.3 ns; K_S = 55.5%; *3* — $YAl_2Ga_3O_{12}$:Ce; $t(1/e)$ = 17.8 ns; K_S = 5.4%; *4* — $Y_3Ga_5O_{12}$:Ce; $t(1/e)$ = 3.3 ns; t_2 ~ ms range; *b*) in the Ce^{3+} absorption band at 3.7 eV: *1* — YAG:Ce; $t(1/e)$ = 65 ns; *2* — $YAl_{0.6}Ga_{0.4}O_{12}$:Ce; $t(1/e)$ = 61.9 ns; *3* — $YAl_{0.4}Ga_{0.6}O_{12}$:Ce; $t(1/e)$ = 31.8 ns [213]

cited state of Ce^{3+} ions and may be the reason for the decrease in scintillation efficiency of these garnets at x above 3.0.

The content of slow components $K_S = I_S/I_F \cdot 100\%$ in the Ce^{3+} luminescence decay in $Y_3Al_{5-x}Ga_xO_{12}$:Ce was also calculated (see Fig. 3.28). The value of K_S strongly decreases with increasing Ga content in $Y_3Al_{5-x}Ga_xO_{12}$:Ce up to $x = 3.0$. Namely, the content of the slow component in Ce^{3+} luminescence is only 5.4% in $Y_3Al_2Ga_3O_{12}$:Ce compared to 55.5% and 123.6% in $Y_3Al_2Ga_3O_{12}$:Ce and $Y_3Al_5O_{12}$:Ce, respectively. These data also reflect a significant improvement in the scintillation properties of $Y_3Al_{2-3}Ga_{3-2}O_{12}$:Ce crystals compared to YAG:Ce due to the reduction of the role of antisite defects in energy transfer from the host to Ce^{3+} under high-energy excitation.

3.3.3. Cathode- and X-ray luminescence spectra

X-ray luminescence spectra of some Ce-doped garnet crystals are shown in Fig. 3.29. The curves were obtained under the same conditions, and the relative intensities of the peaks can be compared. The luminescence band is shifted by ~50 nm when adding 66 at.% Ga to YAG:Ce. At the same time, only weak intrinsic host luminescence is observed in YGG:Ce. The luminescence spectrum of GAGG:Ce under X-ray excitation, along with a strong band with a maximum at 555 nm, contains a weak band at 360—390 nm, which, by analogy with the YAGG:Ce system corresponds to the luminescence of antisite defects when Gd^{3+} occupies the Al^{3+} position.

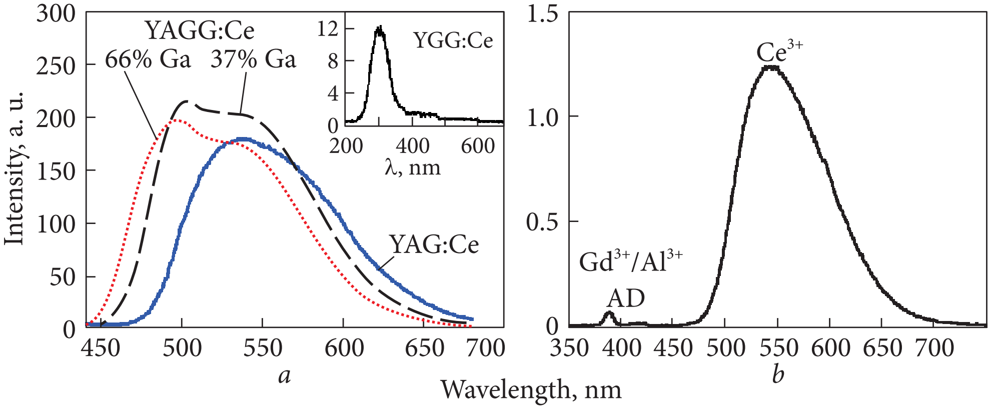

Fig. 3.29. Luminescence spectra upon X-ray excitation of Ce-activated crystals YAG, YGG and YAGG (*a*) [217], and GAGG (*b*)

Cathodoluminescence spectra of $Y_3Al_{5-x}Ga_xO_{12}$:Ce crystals with different Ga contents are shown in Fig. 3.30*a* compared to the spectrum of undoped YAG. The dominant emission band in the visible range is associated with $5d_1 \rightarrow 4f\,(2F_{5/2.7/2})$ transitions of Ce^{3+} ions in the above-mentioned garnet hosts. Compared to the CL spectrum of YAG:Ce with a maximum at 2.21 eV (560 nm) at 300 K (Fig. 3.30*a*, curve *2*), the Ce^{3+} emission band maxima of mixed crystals with Ga $x = 2.0$ and 3.0 are shifted to high energies by 2.32 eV (534 nm) and 2.41 eV (513 nm) due to the decrease in the crystal field strength (Fig. 3.30*a*, curves *3* and *4*, respectively). Unlike the cathodoluminescence spectra of the last two crystals, the YAG:Ce spectra (Fig. 3.30*a*, curve *5*) are shifted to a lower energy of 2.28 eV (543 nm).

Note also the broadening of the Ce^{3+} luminescence band in $Y_3Al_{5-x}Ga_xO_{12}$:Ce with increasing Ga content (Fig. 3.30*b*, curve *2*). Taking into account the positions of the E_1 bands presented in Fig. 3.24*a*, the Stokes shift of Ce^{3+} luminescence in $Y_3Al_{5-x}Ga_xO_{12}$:Ce is practically constant in the range of $x = 0 \div 3.0$ and amounts to 0.49—0.5 eV; but at higher values of $x > 3$, it strongly increases to 0.705 eV in YGG:Ce (Fig. 3.30*b*, curve *3*). In the UV range (200—420 nm), the spectra of YAG cathodoluminescence consists of a complex emission band (Fig. 3.30*a*, curve *1*), caused by the presence of antisite defects in them, which play the role of luminescence centers in garnet crystals (for more detailed information, see also [215—220]). In YAG:Ce, the luminescence intensity in the UV range decreases (Fig. 3.30*a*, curve *2*) due to competition between Ce^{3+} and antisite luminescence centers. It is important to note that the emission bands associated with antisites completely disappeared in the spectra of $Y_3Al_{5-x}Ga_xO_{12}$:Ce at $x = 2.0$ and 3.0. Another band of self-emission in the ultraviolet range at 300 nm appears in the spectra of $Y_3Ga_5O_{12}$ crystals. Most likely, it is associated with the luminescence of Y-Ga related antisites [216]). The

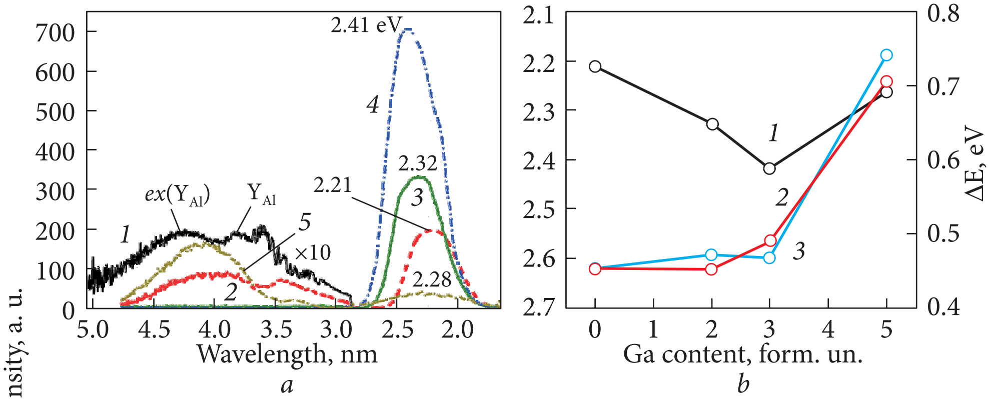

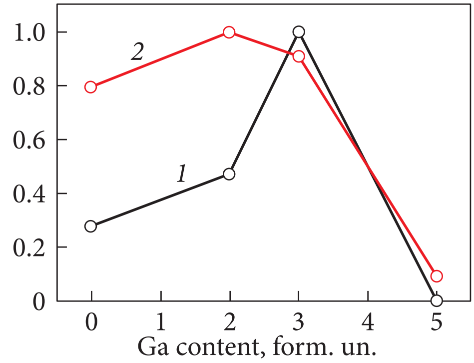

Fig. 3.30. *a* — CL spectra of $Y_3Al_{5-x}Ga_xO_{12}$:Ce crystals with different Ga contents at 300 K. The UV parts of spectra *1*—*4* and the entire spectrum *5* are multiplied by a factor of 10: *1* — YAG; *2* — YAG:Ce; *3* — $Y_3Al_3Ga_2O_{12}$:Ce; *4* — $Y_3Al_2Ga_3O_{12}$:Ce; *5* — YGG:Ce; *b* — positions of maxima (*1*, left scale), half-width (FWHM) of Ce^{3+} emission band (*2*, right scale) and Stokes shift of Ce^{3+} luminescence (*3*, right scale) depending on Ga concentration (*x*); *c* — dependence of CL (*1*) and XRL (*2*) intensity on Ga content [213]: *1* — CL intensity; *2* — RL intensity

dependence of the light yield of CL in $Y_3Al_{5-x}Ga_xO_{12}$:Ce on the Ga content is demonstrated in Fig. 3.30*c*, curve *1*. The replacement of Al^{3+} cations with Ga^{3+} in the concentration range $x = 0 \div 3$ leads to a strong increase in the light yield of X-ray luminescence in YAGG:Ce. In particular, the light yield of luminescence in $Y_3Al_3Ga_2O_{12}$:Ce and $Y_3Al_2Ga_3O_{12}$:Ce is 1.5 and 2.5 times higher, respectively, than in YAG:Ce (Fig. 4.31*c*, curve *1*). At the same time, an increase in the Ga^{3+} content above $x = 3.0$ leads to a strong decrease in the light yield of Ce^{3+} luminescence in $Y_3Al_{5-x}Ga_xO_{12}$:Ce crystals (Fig. 3.30*c*, curve *1*). The substitution of Al^{3+} with Ga^{3+} also leads to a noticeable increase in the light yield in YAGG:Ce (Fig. 3.30*c*, curve *2*) upon excitation by a-particles with an increase in the Ga content to $x = 2 \div 3$. At larger x, the YAGG:Ce light yield is greatly reduced. Finally, the light yield of XRL in $Y_3Ga_5O_{12}$:Ce at 300 K is practically zero, similar to the data in [218—220].

3.3.4. Light yield and energy resolution under γ-irradiation

The light yield in YAGG:Ce reaches a maximum at a Ga concentration of about 75% and drops to 0 when Al is completely replaced by Ga (Table 3.5). At high concentrations of gallium, the light yield decreases due to strong temperature quenching — a very low light yield is observed in the sample with a concentration of 85% Ga. Co-activation with Ca^{2+} reduces the light yield in the 75% Ga sample to the BGO level. The magnitudes and trend of the light yield are similar to the pulse shaping times of 2 μs and 8 μs, which indicates an insignificant contribution from slow luminescence components. The energy resolution in YAGG:Ce is 17—19% at 662 keV, significantly worse than the best values of ~5—7% for measurements published for other multicomponent garnets [85, 221].

During parallel studies of a sample with 75% Ga under γ-radiation of ^{22}Na at 511 keV (Fig. 3.31), the light yield was about 20% relative to the GAGG:Ce standard with a light yield of about 50.000 photons/MeV.

Amplitude spectra of GAGG:Ce samples cut from different parts of the same crystal in comparison with the BGO standard (Fig. 3.31*b*) gives a light yield in the range of 45 000—50 000 photons/MeV and an energy resolution of samples with dimensions of 10 × 10 × 1 mm^3 in the range of 7.6—8.8% at 662 keV, which agrees with literature data on these crystals. The similarity of the scintillation parameters in different samples indicates good macrohomogeneity in the crystal volume. The dependence of light yield in YAGG:Ce and GAGG:Ce crystals are similar (Fig. 3.32) with a maximum at an Al/Ga ratio close to unity. The light yield of mixed YAGG crystals reaches 130% relative to YAG:Ce (Fig. 3.32*a*). No light yield was detected in YGG:Ce. The same result was re-

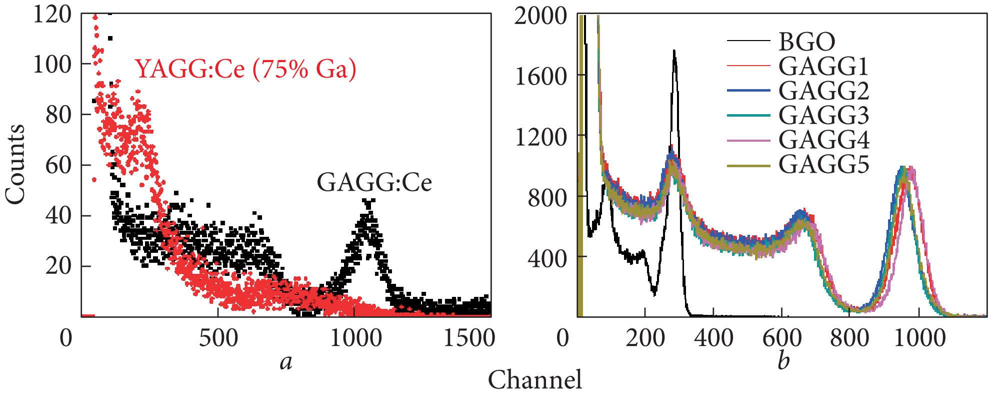

Fig. 3.31. Amplitude spectra of YAGG:Ce (75% Ga) crystals when under g-radiation from a ^{22}Na source compared to GAGG:Ce. YAGG:Ce light yield was determined by the number of photopeaks at 511 keV (shown by arrows) (*a*); amplitude spectra of GAGG:Ce and BGO crystals under ^{137}Cs, 662 keV excitation (*b*). The pulse shaping time is 8 μs [217]

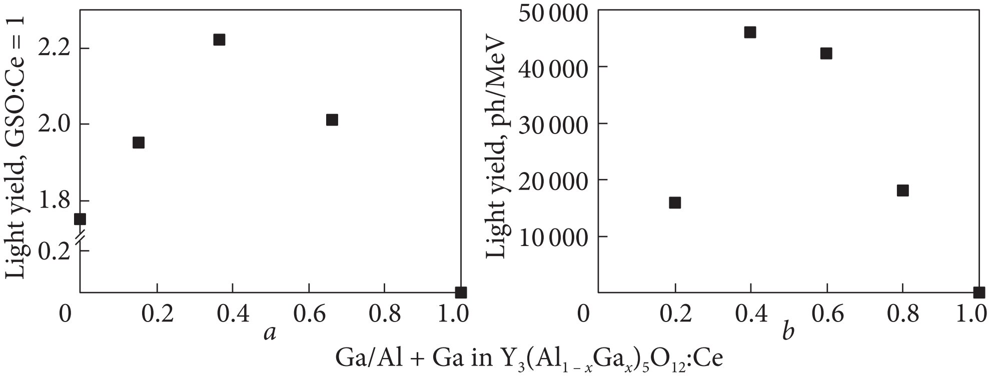

Fig. 3.32. Light yield of YAGG (*a*), [217]) and GAGG (*b*) [83] depending on Ga concentration

Table 3.5. **Scintillation parameters of YAGG:Ce crystals under irradiation with g-rays from a ^{137}Cs 662 keV source [217]**

Composition,% Ga	Light yield (BGO = 100%) for pulse forming time		Energy resolution,% at 662 keV for a pulse formation time of 2 μs	Decay time, ns	Afterglow,% (after 0.6 μs)
	2 μs	5 μs			
0	51	56	14.9	135	7.9
20	ND	70	ND	105	7.7
40	85	108	17.6	92	8.5
60	150	148	19.2	28	1.6
75	234	232	18.1	37	1.4
75(+Ca)	99	99	22.9	21	0.2
85	15	15	18.0	ND	~60
100	0	0	—	—	—

ND — not determined.

ported for Ce activated lutetium-gadolinium garnet (Fig. 3.32*b*) [76]. The dependence of the light yield on the Ga fraction is also perfectly consistent with the results for $Lu_3(Al_{1-x}Ga_x)_5O_{12}$:Ce — in both cases, the maximum values are observed at x ~0.4. The mechanisms of improving light yield in mixed garnets are discussed in [12]. The light yield increases with the addition of Ga^{3+} due to the change in the bandgap, which shifts the energy levels of shallow electron traps with an energy up to 0.3 eV into the conduction band. This «bandgap engineering» approach provides a good interpretation of the scintillation process that occurs in activated rare earth garnets. It also explains the lack of light yield in $Y_3Ga_5O_{12}$:Ce — 5*d* cerium levels in this compound, just like the electron trap levels, are positioned within the conduction band.

3.3.5. Decay time and afterglow

Based on their scintillation properties, the studied crystals can be divided into three groups (Fig. 3.33*a*). The first group has a main decay component of about 100 ns (one-exponential approximation) consisting of YAG:Ce as well as YAGG:Ce with 20 and 40% Ga. The second group consists of YAGG:Ce crystals with a Ga content of 60 and 75%. The shortest decay time of 21 ns is achieved in a crystal 75% Ga co-activated with Ca. The luminescence of the YAGG:Ce crystal with 85% Ga is too slow to correctly determine the decay time, and no luminescence was recorded in the YGG:Ce crystal.

It is difficult to explain the reason for such a sharp drop in the decay time between samples with 40 and 60% Ga, although there is a clear trend toward a decrease in the decay time with Ga concentration. As will be shown below, Ga^{3+} ions preferentially occupy tetrahedral positions in the YAGG crystal lattice (although one could expect that larger Ga^{3+} atoms would occupy octahedral positions of greater volume). The interval between 40 and 60% Ga corresponds to the situation when the number of Ga ions exceeds the number of Al ions, and mass Al^{3+}/Ga^{3+} substitution begins in octahedral positions. It is possible that

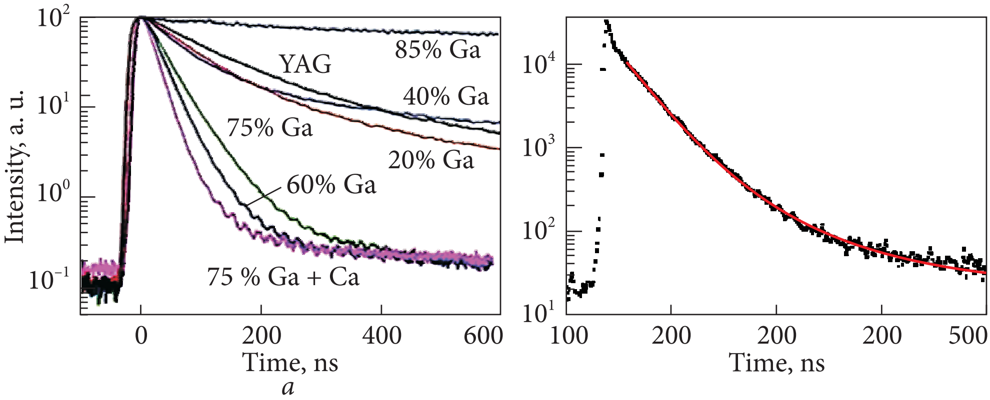

Model	ExpDecay2		
Equation	y = y0+A1*exp(−(x−x0)|/t1 + A2*exp(−(x−x0)/t2		
Reduced Ch-Sqr	1977.40374		
Adj. R-Square	0.99951		
		Value	Standard Error
B	A1	12684.3513	100.9608
B	t1	28.37621	0.26102
B	A2	585.56287	117.55785
B	t2	89.39617	8.87568

b

Fig. 3.33. Luminescence decay curves in YAGG:Ce under excitation by g-radiation with an energy of 662 keV from a ^{137}Cs source (*a*); scintillation decay curves in a YAGG:Ce crystal (75% Ga) upon g-excitation from a ^{22}Na source (511 keV) (*b*) [217]

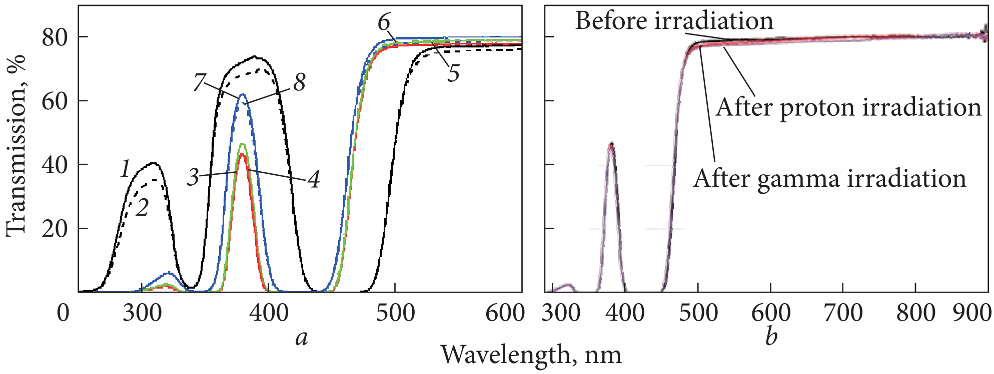

Fig. 3.34. Effect of g-irradiation with a dose of 100 Gy on the transmission of YAGG:Ce crystals with different Ga content (*a*): *1* — YAG:Ce (before irradiation), *2* — YAG:Ce (after irradiation), *3* — YAGG:Ce, 20% Ga (before irradiation), *4* — YAGG:Ce, 20% Ga (after irradiation), *5* — YAGG:Ce, 60% Ga (before irradiation), *6* — YAGG:Ce, 60% Ga (after irradiation), *7* — YAGG:Ce, 75% Ga (before irradiation), *8* — YAGG:Ce, 75% Ga (after irradiation; *b*): Optical transmission spectra of a 10 mm thick YAGG:Ce (65% Ga) sample measured at room temperature before and after g-irradiation with a dose of 100 Gy and 5 months after irradiation with protons with an energy of 150 MeV with a fluence of $5 \cdot 10^{13}$ particles/cm^2 [217]

the introduction of Ga into octahedral positions greatly affects the geometry of luminescent Ce^{3+} centers and their characteristics.

Scintillation decay was also measured under excitation of ^{22}Na (511 KeV) (Fig. 3.33*b*). Approximation by two exponentials gives a reduction of the decay time of both the fast component to 28 ns with a 96% contribution, and the slow component reduction to 89 ns with a 4% contribution. Thus, the data obtained in different laboratories agree well in general, and minor differences in decay times can be explained by differences in measurement procedures.

3.3.6. Radiation resistance

Samples with different Ga contents were irradiated with g-quanta, a dose of 100 Gy. As an indicator of radiation damage, optical transmittance was measured before and after irradiation (Fig. 3.34*a*). A stronger influence of irradiation is observed in YAG:Ce and YAGG:Ce (40% Ga) samples. At the same time, no visible changes in optical transmittance were observed in samples with a higher concentration of gallium. The largest changes in transmittance are observed in the UV range, where irradiation has little effect on transmittance in the Ce^{3+} luminescence range at 500—550 nm. This indicates a good tolerance to irradiation with g-quanta. Since YAGG:Ce does not contain heavy atoms, good radiation resistance to high-energy hadrons could be expected.

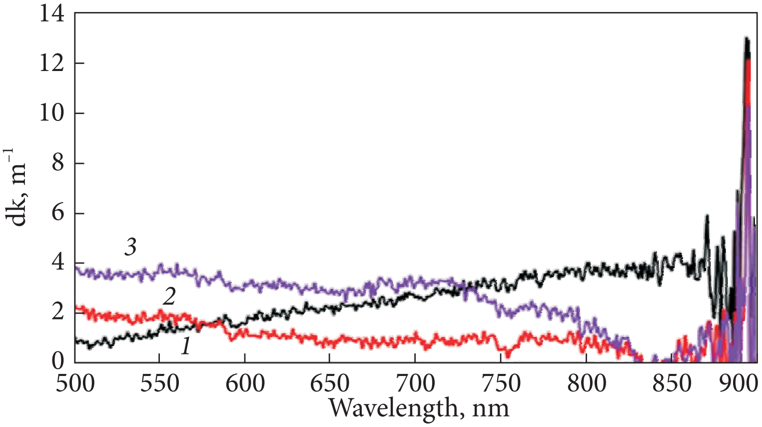

Fig. 3.35. Induced absorption spectra after g-irradiation with a dose of 100 Gy and subsequent annealing at 850 °C for 24 hours, as well as 5 months after irradiation with protons with an energy of 190 MeV and a fluence of $5 \cdot 10^{13}$ particles /cm^2 [217]: *1* — gamma irradiation; *2* — proton irradiation 190 MeV; *3* — annealing at 850 °C

Fig. 3.34*b* demonstrates the optical transmission spectra of YAGG:Ce samples with a gallium content of 65% before and after irradiation with protons with an energy of 150 MeV. Spectra of induced absorption of crystals after irradiation with γ-quanta and protons (Fig. 3.34) are very similar — a small decrease in transmittance is observed only in the UV range, and there is no visible effect of irradiation on optical transmittance in the luminescence range of YAGG:Ce. Thus, the material is radiation resistant to high-energy hadrons.

3.3.7. Reduction of luminescence decay time in garnets by co-doping with divalent cations

Reducing the decay time of scintillations in garnets is highly demanded for practical applications, in particular, high-energy physics. The introduction of divalent cationic dopants is an effective method of suppressing slow decay components in various cerium-activated scintillators (see, for example, [176, 222—225]). It was suggested that charge compensation in the crystal when the host trivalent cation (Lu^{3+}, Gd^{3+}, Y^{3+}, Al^{3+}) is replaced by a divalent cation (Ca^{2+}, Mg^{2+}) promotes the transition of Ce^{3+} to the tetravalent Ce^{4+} state. Tetravalent cerium, previously considered as a negative factor, competes with other traps for electron capture from the conduction band, thus increasing the contribution of fast luminescence. However, a decrease in the decay time in most cases leads to a parallel decrease in the light yield due to the ionization of electrons to the conduction band from the excited levels of the cerium ion.

Doping with Ca^{2+} ions provided a decrease in the afterglow level in YAGG:Ce to 0.2% after 0.6 μs. Similar to the co-activation of Mg^{2+}, the addition

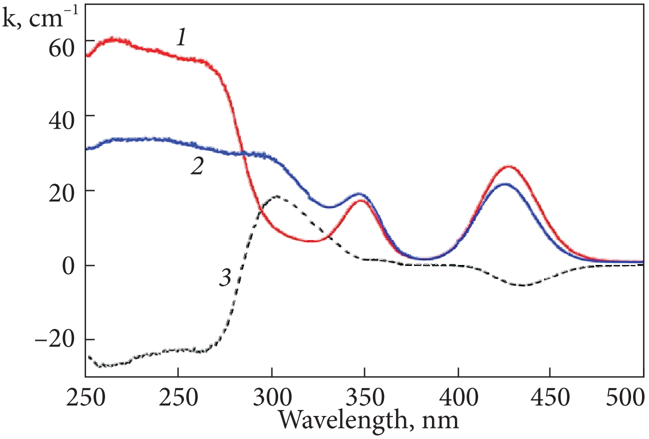

Fig. 3.36. Absorption spectra of YAGG:Ce (75% Ga) and YAGG:Ce,Ca (75% Ga) crystals and the spectrum of induced absorption upon introduction of Ca^{2+} [217]: *1* — YAGG:Ce 75% Ga; *2* — YAGG:Ce,Ca 75% Ga; *3* — induced absorption

of Ca^{2+} should cause competition for carrier capture between shallow electron traps and deep traps associated with Ce^{4+}, leading to suppression of afterglow. A parallel decrease in light yield with co-activation of Ca^{2+} evidences luminescence quenching. Thus, the gallium content of 60—75% in the YAGG matrix in combination with Ca^{2+} co-doping is the optimal composition of YAGG:Ce crystals to achieve fast quenching while maintaining a high light yield. The presence of cerium in the tetravalent state in a crystal co-activated with Ca^{2+} is evidenced by an absorption band around 300 nm associated with charge transfer complexes Ce^{4+}— O^{2-} (Fig. 3.36) in accordance with numerous articles on the co-activation of, garnets [222—224] and perovskites [225]. Ca^{2+} promotes the cerium transition to the tetravalent state and accelerates the luminescence decay. It should be noted that the addition of Ga^{3+} to multicomponent garnets can itself promote the transition of cerium to the Ce^{4+} state [226].

Thus, in this subsection, the optical properties of single crystals of $Y_3Al_{5-x}Ga_xO_{12}$:Ce^{3+} garnets with x in the 0÷5.0 range were investigated in our work using absorption cathodoluminescence and X-ray luminescence spectra upon excitation by an electron beam and alpha particles, as well as of luminescence spectroscopy under excitation by synchrotron radiation in the range of 3.7—25 eV. Based on the changes in the location of absorption and emission bands associated with 4*f*—5*d* transitions in Ce^{3+} ions, it was concluded that the optical properties of $Y_3Al_{5-x}Ga_xO_{12}$:Ce garnets change monotonically with increasing Ga concentration in the range of $x = 0 \div 3$. With a higher content of Ga ($x > 3$), the dependence had a different character. Possible reasons for such a dependence of the optical properties of $Y_3Al_{5-x}Ga_xO_{12}$:Ce on the Ga content can be assumed, taking into account the results of NMR studies on the site occupancy upon Al^{3+}/Ga^{3+} substitution (see Chapter 4). It was shown that Ga ions in the $x = 0 \neq 3$ concentration range are mainly localized in tetrahedral positions in the garnet structure. In the mentioned concentration range, the optical properties of $Y_3Al_{5-x}Ga_xO_{12}$:Ce change according to Vegard's law. At a higher concentration of Ga (x> 3), Ga ions are also incorporated into octahedral positions instead of Al. Such a change in the occupancy of positions in the garnet structure is reflected in a different behavior of the $Y_3Al_{5-x}Ga_xO_{12}$:Ce optical properties on the Ga content.

From the excitation spectra of Ce^{3+} luminescence, the formation energy of excitons associated with Ce^{3+} (ex(Ce)) in the entire range of x from 0 to 5 for $Y_3Al_{5-x}Ga_xO_{12}$:Ce, and the width of the bandgap at in the range of $x = 0 \neq 3$ were determined. The values of ex(Ce) and E_g decrease with increasing Ga content by 0.4 eV and 0.3 eV per one formula unit of Ga, respectively. It was also found that when the bandgap of $Y_3Al_{5-x}Ga_xO_{12}$:Ce garnets decreases with increasing Ga content in them from 7.9 eV in YAG to approximately 6.6 eV in YGG, the energy gap between the level of excitons associated with Ce^{3+} and the bottom of the conduction band is greatly reduced. This also leads to a strong quenching of Ce^{3+} luminescence in $Y_3Al_{5-x}Ga_xO_{12}$:Ce at $x > 3$ upon excitation by photons or high-energy particles. At the same time, an increase in the excitation efficiency of Ce is observed during the sequential capture of electrons and holes by cerium from separated electron-hole pairs at high-energy excitation ~$3E_g$. This may indicate that the separation of electrons and holes in the pair becomes smaller compared to YAG:Ce in crystals with $x = 2$ and 3. This assumption is confirmed by the increase in light yield and energy transfer efficiency in intermediate compositions previously observed in other mixed Ce-activated crystals: $Lu_{1-x}Y_xAlO_3$ [11] and $Lu_{2-2x}Gd_{2x}SiO_5$ [6]. The same trend in the excitation efficiency of Ce in different ionic crystals can be related to the limitation of the diffusion length of carriers due to the inhomogeneity of the atom distribution in mixed crystals, which is discussed in more detail in Chapter 4.

3.4. $Bi_4(Ge_{1-x}Si_x)_3O_{12}$ (BGSO)

All grown BGSO crystals are transparent in the range of 300—800 nm (Fig. 3.37). The shift of the fundamental absorption edge in the optical transmission spectra from 300 to 285 nm with increasing Si concentration corresponds to a larger bandgap in BSO, which was theoretically predicted in [227].

The highest transmission at the wavelength of the luminescence maximum (480 nm) is registered in the sample with $x = 0.4$, as well as in BSO and BGO. X-ray luminescence spectra of BGSO with different Ge content (Fig. 3.38) are represented by one broad band in the range of 350—700 nm with a maximum at about 480 nm. This coincides with previous data [229]. There is a tendency for a weak (< 10 nm) blue shift of the peaks with increasing Si content.

Amplitude spectra of BGSO when irradiated with 662 keV γ-quanta from a ^{137}Cs source are presented in Fig. 3.39. This trend is not linear, with a negative deviation from the rule of additivity (Fig. 3.40, Table 3.6) and is similar to the dependences obtained in [229, 230] for crystals grown by the Stockbarger and

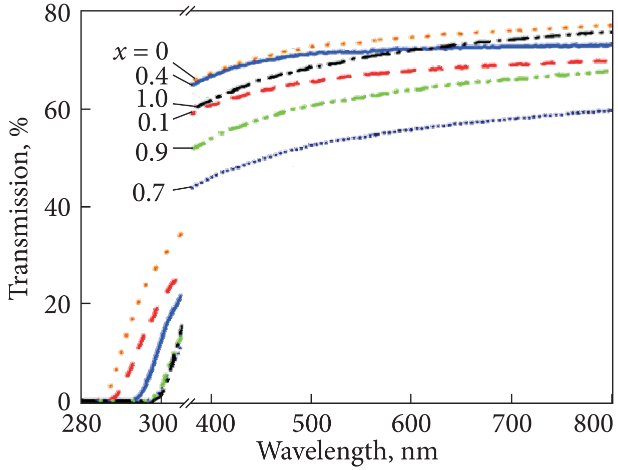

Fig. 3.37. Optical transmission spectra of $Bi_4(Ge_xSi_{1-x})_3O_{12}$ crystals [228]: *1* — x = 0; *2* — x = 0.1; *3* — x = 0.4; *4* — x = 0.7; *5* — x = 0.9; *6* — x = 1

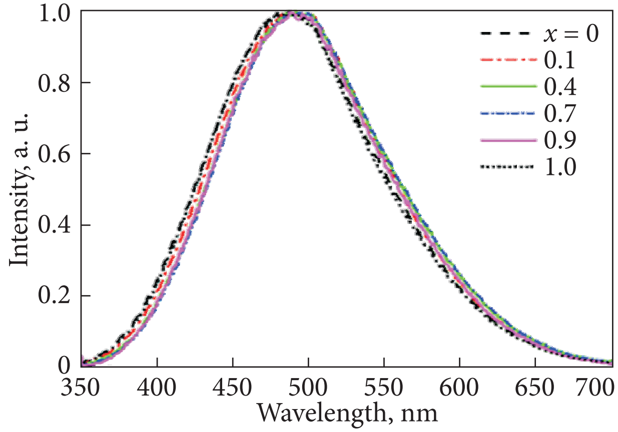

Fig. 3.38. The X-ray luminescence spectra of $Bi_4(Ge_xSi_{1-x})_3\times$ $\times O_{12}$ crystals are normalized to the maximum [228]

the Czochralski methods. Thus, the light yield behavior does not depend on the method of growing the crystal. The negative deviation from the additivity rule in BGSO, in contrast to many other scintillators based on mixed crystals, can be attributed to a decrease in the BGSO transparency compared to its constituents — BGO and BSO (Fig. 3.38) and/or due to spatial inhomogeneities in the distribution of substitutional Si^{4+} and Ge^{4+} ions [100—104]. The difference in the ionic radii of these cations is 32.5%, which is far beyond the 15% limit of the solubility range according to the Goldschmidt rule.

However, the achieved energy resolution in BGSO (Fig. 3.40, Table 3.6) is better compared to any previous data presented in the literature. There is a tendency to improve the energy resolution from BSO to BGO corresponding to an increase in light yield. For all crystals in the range of $0.4 < x < 0.9$, the energy is better than 20%. The best result of 16.2% was achieved for the sample with $x = 0.7$.

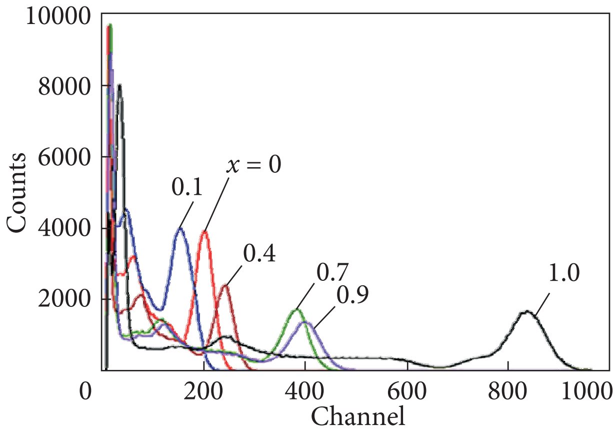

Fig. 3.39. Amplitude spectrum of $Bi_4(Ge_xSi_{1-x})_3O_{12}$ crystals with waried x excited by γ-quanta with energy of 662 keV from a ^{137}Cs source [228]

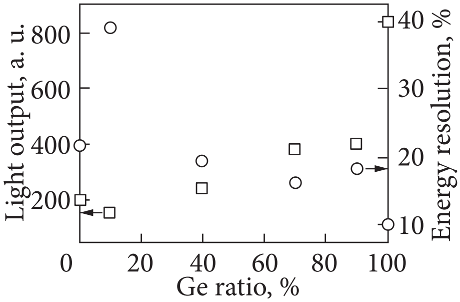

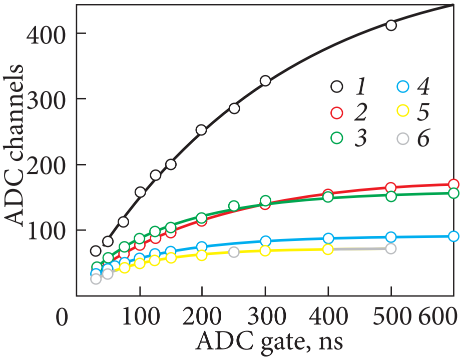

Fig. 3.40. Dependences of light output and energy resolution on x in $Bi_4(Ge_xSi_{1-x})_3O_{12}$ [228]: □ — light output; ○ — energy resolution

Fig. 3.41. The maximum of the 662 keV ^{137}Cs photopeak depends on the time gate duration [228]: *1* — BGO, τ = (292.4 ± 0.6) ns; *2* — BGSO, 90% Ge, τ = (220.3 ± 0.9) ns; *3* — BGSO, 70% Ge, τ = (152.3 ± 0.6) ns; *4* — BGSO, 40% Ge, τ = (132.9 ± 1.2) ns; *5* — BGSO, 10% Ge, τ = (109.5 ± 1.5) ns; *6* — BSO, τ = (100.6 ± 1.1) ns

Table 3.6. **Scintillation properties of $Bi_4(Ge_xSi_{1-x})_3O_{12}$ crystals under γ-irradiation with an energy of 662 keV**

x	0	0.1	0.4	0.7	0.9	1
Relative light yield,%	24	18	29	46	48	100
Energy resolution (FWHM),%	21.7	39.1	19.5	16.2	18.2	10.0
Decay time t, ns	100.6	109.5	132.9	152.3	220.3	292.4
P_0	72.25	16.57	18.86	18.72	16.3	5.83
P_1	−13.47	56.4	72.38	138.4	164.8	496.6

The decay time of the BGSO was determined by measuring the total absorption peak from the duration of the ADC gate, i.e., the luminous flux versus the integration time (Fig. 3.41) The scintillation decay in BGSO can be approximated by 1, 2, or even 3 exponents [230]. Without delving into the approximation procedures, we estimated the attenuation by one exponent, $P = P_0 + P_1 \cdot (1-\exp(-t/\text{t})$, where t is the decay time, P_0, P_1 are constants, t is time (Table 2.1).

The decay time of the main component $Bi_4(Ge_xSi_{1-x})_3O_{12}$ increases with the Ge content. However, this increase is not linear, and at $x < 0.7$, the decay constant is less than 150 ns (Table 3.6). Thus, in most of the x range, the BGSO decay time is 2—3 times faster than in BGO.

Thus, this chapter presents the optical, luminescence, and scintillation properties of solid solution crystals of $Lu_{2-2x}Gd_{2x}SiO_5$:Ce, $Y_3Al_{5-x}Ga_xO_{12}$:Ce, $GdTa_{1-x}Nb_xO_4$, $Bi_4(Ge_xSi_{1-x})_3O_{12}$, and $YTa_{1-x}Nb_xO_4$ in the full concentration intervals of cation substitution. The light yield in the $Lu_{2-2x}Gd_{2x}SiO_5$:Ce, $Y_3Al_{5-x}Ga_xO_{12}$:Ce systems, depending on the ratio of substituted cations, show positive deviations from linearity in accordance with Vegard's law, with maximum deviations of 1.8 and 2.9 times, respectively. The light yield of $Bi_4(Ge_xSi_{1-x})_3O_{12}$ solid solutions is lower than that of its components. The dependence of light yield in the $GdTa_{1-x}Nb_xO_4$ system is close to the additivity rule. The scatter of the experimental points in $YTa_{1-x}Nb_xO_4$ and the presence of a polymorphic transition in this system do not make it possible to clearly determine the concentration dependence of the light yield.

CHAPTER 4

PHENOMENOLOGICAL APPROACH TO THE OPTIMIZATION OF THE SCINTILLATION PARAMETERS OF SUBSTITUTIONAL SOLID SOLUTIONS

Based on the literature review and the data presented in the previous chapter, solid solution systems of inorganic scintillators can be divided into 3 groups according to the concentration dependence of the light yield in them [88, 231] (Fig. 4.1).

1. Systems where the light yield of a mixed crystal depends linearly on the ratio of components in accordance with Vegard's law $L_{\mathrm{Veg}} = C_a L_a + C_b L_b$, where C and L are the molar concentrations and light yield of the solid solution components. Examples of such systems are $GdTa_{1-x}Nb_xO_4$ or $Lu_{2-x}Y_xSiO_5$:Ce (LYSO:Ce).

2. Systems with positive deviations of the light yield from the linear dependence in the mixed crystal, for example, $Lu_{2x}Gd_{2-2x}SiO_5$:Ce (LGSO:Ce) or $Y_3Al_xGa_{5-x}O_{12}$:Ce (YAGG:Ce).

3. Systems with negative deviations of the light yield from the linear dependence in the mixed crystal are observed, for example, $Bi_4Ge_{3-x}Si_xO_{12}$ (BGSO).

In Chapter 1, three possible factors were distinguished that could explain the concentration dependence of the light yield in a mixed crystal:

1. The number of defects in crystals, such as carrier traps. Capture of secondary electrons or holes formed as a result of crystal irradiation by high-energy particles, causes delayed luminescence or non-radiative losses.

2. Modification of the crystal energy structure affects the number of formed electron-hole pairs and the positions of the energy levels of the luminescent center and carrier traps in the forbidden band.

3. The third group of factors causing a decrease in the path length of thermalized charge carriers and the probability of their genetic recombination is electron-phonon interaction, as well as spatial inhomogeneities in crystals caused by the uneven distribution of substituted atoms in the solid solution. These cause spatial modulations of the conduction band bottom and the top of the valence band.

This chapter addresses each of these factors in detail. By comparing experimental data on solid solution systems, conclusions are drawn regarding the influence of the listed factors on the light yield in them.

4.1. Changing the number of defects in crystals

A possible change in the number of defects in a mixed crystal compared to its components is, at first glance, the most obvious reason that can affect the transport of carriers to the activator and the magnitude of light yield in scintillation crystals. However, according to the literature data, this issue has not been systematically investigated in any system of mixed crystals before. We chose the LGSO:Ce system for consideration, where the number of oxygen vacancies — the main type of defects in these crystals was carefully analyzed depending on their cationic composition. The question of the number of defects in scintillators, of course, has not only scientific but also practical significance. Modern applications of scintillation materials often require fast scintillation decay in the range of nanoseconds. The slow emission of light, also called phosphorescence or afterglow, is a significant problem in the development of fast scintillators.

The mechanism of afterglow in mixed oxyorthosilicates activated by cerium was studied by time-resolved thermally stimulated luminescence (TSL) and X-ray luminescence methods [16]. Crystals of $Lu_{2x}Gd_{2-2x}SiO_5$:Ce of different composition ($0 \leq x \leq 1$) and $Lu_{1.8}Y_{0.2}SiO_5$ grown by the Czochralski method (the growth procedure is described in detail in Chapter 2) were taken into consideration. A detailed analysis of the TSL curves showed that thermal tunneling of trapped electrons occurs in all compositions, followed by recombination at the Ce luminescent centers. The afterglow reduction when gadolinium or yttrium is added to the matrix is accompanied by a decrease in the concentration of traps manifested in the TSL intensity. It turned out that a decrease in the concentration of oxygen vacancies correlates with a decrease in the melting temperature of the crystal when gadolinium or yttrium is introduced. Temperature, in turn, determines the oxygen partial pressure. The influence of this mechanism on the scintillation properties and capture of charge carriers in other scintillators was also discussed.

Oxyorthosilicate crystals doped with Ce—Lu_2SiO_5 (LSO), $Lu_{2x}Y_{2-2x}SiO_5 \times$ $\times$ (LYSO), Gd_2SiO_5 (GSO), $Gd_2Y_{2-2x}SiO_5$ (GYSO) are scintillators for applications in medical diagnostics, high-energy physics, and geological exploration [232]. Most of these applications require fast scintillators with short luminescence decay times in the nanosecond range and a low afterglow.

High light yield and fast luminescence decay in cerium-activated oxyorthosilicates is caused by a relatively low concentration of lattice defects, which play the role of small charge carrier traps. In other complex oxide matrices, such as Ce-doped aluminum garnets or perovskites, such traps slow down the recombination at the Ce^{3+} luminescent centers and are responsible for the slow components of luminescence [233, 234]. Practical usage of orthosilicates was limited in fields where a high signal-to-noise ratio in the scintillation signal is important, such as most of tomographic applications. This is caused by intense afterglow — luminescence lasting up to seconds and even hours, with an am-

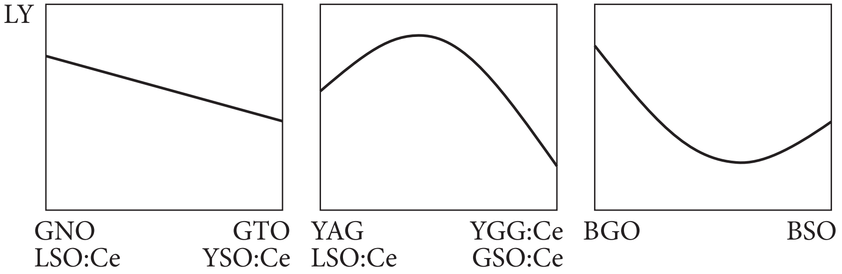

Fig. 4.1. Examples of concentration dependences of light yield (LY) in scintillators based on solid solutions [88, 231]

plitude reaching several percent relative to the amplitude of the initial signal [235]. Such afterglow is associated with the capture of electrons by deep traps associated with oxygen vacancies [236]. These traps are manifested in intense peaks of thermostimulated luminescence above room temperature. In LSO and LYSO:Ce, the depth of these traps, calculated based on TSL data, is approximately 1 eV [237].

The key role of oxygen vacancies as deep traps capturing electrons upon irradiation was confirmed in recent studies of oxyorthosilicates, as well as other oxide scintillation materials [236—240]. The ability to control the number of defects in such materials depends on understanding the role of defects in optical properties and reducing their concentration by optimizing the technology of growing single crystals. Research in this direction contributes to obtaining materials with improved scintillation decay parameters. In the case of LYSO:Ce, co-activation with divalent cations reduces the number of defects and reduces the decay time of the scintillation response (see Chapter 3). In parallel, several remarkable properties were discovered in crystals based on solid solutions. It was shown that the afterglow in $Lu_{2x}Gd_{2-2x}SiO_5$:Ce (LGSO:Ce) crystals decreases with gadolinium concentration (see Chapter 3.1). As for the physical mechanisms of this phenomenon, analysis of existing data enables us to formulate two main hypotheses. The weakening of the afterglow in gadolinium-enriched crystals can be caused by: i) a lower concentration of oxygen vacancies compared to LSO:Ce, or ii) a larger distance between the traps and the luminescence centers, which reduces the probability of radiative recombination by tunneling electrons to the luminescence center occurring in LSO:Ce [237].

In this subsection, the mechanisms of afterglow suppression in gadolinium-enriched oxyorthosilicates are studied by TSL curve analysis and afterglow measurements in a series of LGSO:Ce crystals with different Lu/Gd ratios, as well as in GSO:Ce, LSO:Ce, and LYSO:Ce. In parallel, the relative change in the concentration of oxygen vacancies in the crystals was compared with the dependence of the oxygen partial pressure in the growth atmosphere on the melting temperature for all considered compositions.

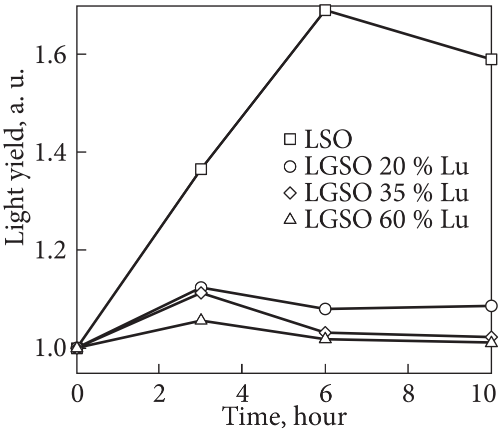

Fig. 4.2. Dependence of the light yield of crystal samples with the dimensions 10 × 10 × 2 mm^3 upon gamma excitation by ^{137}Cs with an energy of 662 keV on the annealing time in an air atmosphere at 1150 °C [238]

$Lu_{2x}Gd_{2-2x}SiO_5$:Ce (LGSO:Ce) samples of different stoichiometry ($x = 1$, 0.75, 0.6, 0.55, 0.50, 0.4, 0.35, 0.20, 0.15, 0.1, 0.05, 0) were selected for the study. Furthermore, in the text, they are designated as LSO, LGSO75, and so on. Measurements were also performed on $Lu_{1.8}Y_{0.2}SiO_5$:Ce (LYSO) crystals grown under the same conditions. For the correctness of the experiment, it was necessary to have samples with the same cerium concentration, so LGSO:Ce and GSO:Ce crystals with a cerium concentration of 0.37 ± 0.08 at.% were selected. The concentration of cerium in LSO:Ce and LYSO:Ce was 0.2 and 0.1 at.%, respectively.

The total concentration of oxygen vacancies in crystals may depend on their melting temperature. The intensity of evaporation of the melt components is determined by the pressure of their vapors above the melt, which, in turn, depends on the temperature. For mixed oxyorthosilicates, the differences in melting temperatures are significant; they vary from 2050 K in $Lu_{0.34}Gd_{1.66}SiO_5$ to 2320 K in LSO [214]. The severe oxygen deficiency in crystals of this type is confirmed by the results of post-growth annealing of LSO:Ce, LYSO:Ce, and YSO:Ce crystals [77]. The light output in LSO:Ce, YSO:Ce, and LYSO:Ce increases after annealing in the air atmosphere [77].

Similar experiments were performed with LGSO:Ce crystals. Annealing was carried out in a resistive furnace in an open-air atmosphere at 1150 °C with different exposure times. The light yield in LGSO:Ce crystals did not change within +/– 5% (however, the energy resolution improved significantly). In turn, the light yield in the LSO:Ce crystal increased by 70% (Fig. 4.2), which indicates a much larger initial number of oxygen vacancies in the latter.

4.1.1. Estimation of defect concentration in mixed crystals

The relative change in the concentration of oxygen vacancies in the crystal can be estimated using a simple relationship between the oxygen partial pressure (P) and the absolute temperature (T), determined by the Clausius — Clapeyron

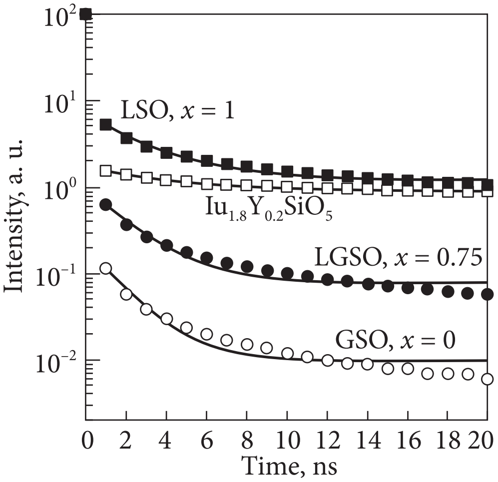

Fig. 4.3. Intensity of afterglow in the millisecond interval (symbols) and its approximation by an exponential function (curves) for some studied oxyorthosilicate crystals [237]

equation [241]:

$$gP = A - (B/(T + C)), \qquad (4.1)$$

where A, B, and C are constants (their values for each material are presented, for example, in [241]). The melting points for all LGSO compositions were taken from [112], and the LYSO melting point was taken from [242]. Thus, if electron traps appear on oxygen vacancies, the relative change in TSL or afterglow intensity should correspond to the relative change in oxygen vapor pressure above the melt. Since the vapor pressure of lanthanide oxides is 2—3 orders of magnitude lower than that of SiO_2 [249], the evaporation of Lu_2O_3, Gd_2O_3, and Ce_2O_3 can be neglected, and it can be assumed that the lack of oxygen in the melt is due solely to the evaporation of SiO_2 or its dissociation products. Thus, the temperature dependence of oxygen vapor pressure in LGSO:Ce can be estimated by introducing constants for $logP_{O_2}$ into equation (4.1). These coefficients (equation 4.2) were determined separately for Si and O_2 in [240] for the temperature range from 1996 to 3000 °C when approximating mass spectrometry data on the dissociation of SiO_2 evaporation products:

$$logP_{O_2} = -26462/T + 7.84 \qquad (4.2)$$

Fig. 4.3 demonstrates the results of measurements of the afterglow level in oxyorthosilicates (LSO:Ce and GSO:Ce) and their mixtures (LYSO:Ce and LGSO:Ce). These data very clearly display a decrease in signal intensity (by more than 2 orders of magnitude) when moving from LSO:Ce to GSO:Ce.

Table 4.1. **Parameters for approximating decay curves**

x in $Lu_{2x}Gd_{2-2x}SiO_5$:Ce	1	0.75	0.6	0.55	0.4	0.35	0.2	0.15	0.1	0.05	0	LYSO:Ce
y_0	1.22	0.08	0.02	0.027	0.040	0.022	0.015	0.02	0.031	0.02	0.01	0.89
A	5.46	0.88	0.45	0.39	0.58	0.36	0.19	0.69	0.47	0.3	0.18	0.79
t, ms	2.89	2.06	1.72	1.86	1.88	1.79	1.97	1.46	1.84	1.88	1.70	4.64

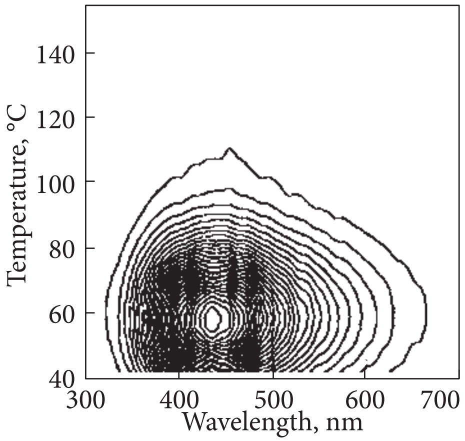

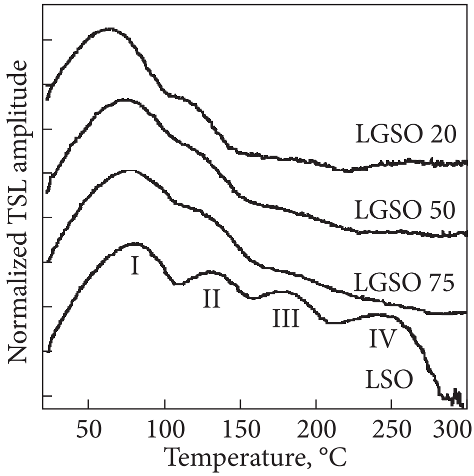

Fig. 4.4. Wavelength resolved heatmap on the example of the LGSO50 sample after X-ray irradiation at room temperature. The intensity of TSL is displayed on a linear scale. For this reason, a weak signal above 120 °C is not displayed [237]

Fig. 4.5. TSL curves on a logarithmic scale after X-ray irradiation at room temperature, normalized by maximum intensities. The curves are shifted relative to each other on a vertical scale for ease of display [16]

The light detected at excitation by pulsed X-ray radiation is caused by various factors. In addition to fast luminescence with a decay time of the order of tens of nanoseconds, and a slow luminescence with a millisecond decay time due to the recombination of trapped charge carriers, the background signal of the electronic circuit is recorded, as well as the background, with intensity proportional to the concentration of its own radioactive isotopes in the crystal, primarily ^{176}Lu. To determine the afterglow due to carrier trapping, we have to distinguish it from the contributions of scintillation and background signals. For this reason, the experimental dependences of the afterglow were approximated in the time gate of 1—20 ms (excluding the first millisecond, where the scintillation signal makes a large contribution) by the exponential function $y = A\exp(-t/\mathrm{t}) + y_0$. Next, the equation $y = A\exp(-t/\mathrm{t})$ was integrated in the time interval 0—10^5 ms to exclude the background contribution included in the parameter y_0. The parameters obtained from the approximation are shown in Table 4.1.

Time-resolved TSL measurements of the LGSO:Ce sample with 50 at.% Lu (Fig. 4.4) demonstrates that the luminescence is associated with $5d_1 - 4f$ transitions in Ce^{3+} ions. No signs of Gd^{3+} luminescence near 315 nm or other luminescence components were detected.

TSL curves of LGSO:Ce samples at temperatures above room temperature are displayed on a logarithmic scale (Fig. 4.5). In this case, the TSL intensity was recorded using an EMI 9635QB photodetector. Peaks on the afterglow curves

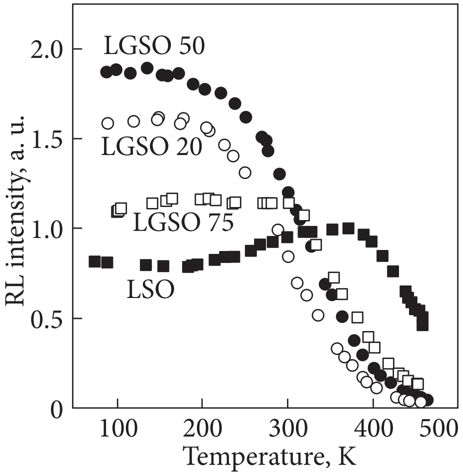

Fig. 4.6. Temperature dependence of X-ray luminescence intensity in LGSO: Ce samples [238]

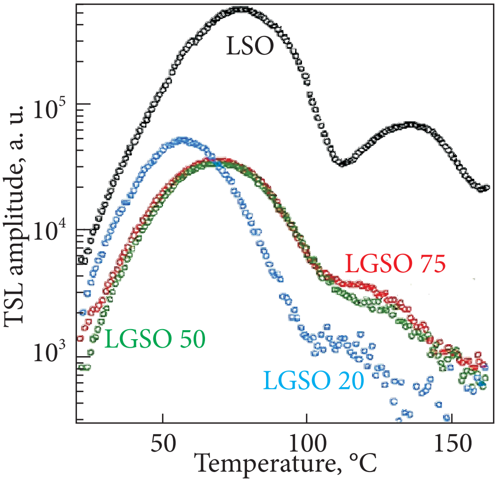

Fig. 4.7. TSL curves of all samples, taking into account the temperature dependence of X-ray luminescence [238]

were recorded around 80 °C, 130 °C, 180 °C, and 240 °C. These peaks associated with the thermal tunneling of electrons from oxygen vacancies to Ce centers [238] are present in samples with different Lu concentrations, although they are less distinct with increasing gadolinium concentration. However, the peak at 300 °C attributed to electron transport to the activator via ionization to the conduction band in LYSO:Ce [239] was not observed in any of the samples. The effect of the Lu and Gd concentration on the trap concentration was investigated by comparing the TSL curves obtained at the same irradiation dose (0.02 Gy). The TSL intensity depends both on the trap concentration (if the concentration of luminescence centers in the samples is approximately constant), and on the efficiency of the Ce^{3+} luminescence center, which was assessed by measuring the intensity of X-ray luminescence as a function of temperature (Fig. 4.6).

Thus, each TSL curve was corrected taking into account the temperature dependence of X-ray luminescence. Since the temperature dependence of X-ray luminescence was measured only up to 180 °C, the correction can be made only for the two main TSL peaks at 80 °C and 130 °C. The corrected TSL curves are shown in Fig. 4.7.

The thermoluminescence curves in LGSO:Ce are more than an order of magnitude weaker compared to LSO:Ce. A strong drop in the TSL intensity is observed after the introduction of more than 25% Gd, while with the subsequent addition of gadolinium, the TSL intensity remains almost constant. Thus, the intensity of TSL correlates with the intensity of the afterglow.

4.1.2. Phenomenological analysis of the influence of melting temperatures on light yield and afterglow

In accordance with previous studies, the presence of strong afterglow in orthosilicates is associated with a high concentration of oxygen vacancies, which are deep electron traps [235, 236]. Under conditions of oxygen deficiency in the melt, the formation of oxygen vacancies should be more energetically favorable at oxygen positions that do not belong to SiO_4 tetrahedra. In the monoclinic $C2/c$ structure in LSO, LYSO, and $Lu_{2-x}Gd_xSiO_5$ ($x < 1.6$), there are 20% of such oxygen atoms in the lattice. The bonds of these oxygen atoms with Gd and Lu in LGSO are weak because their length is more than 2.6 Å compared to 1.6 Å for Si-O bonds. It is important to note that, while the afterglow is very strong in crystals with the LSO:Ce $C2/c$ structure [236], the afterglow is weak in GSO:Ce and GYSO:Ce [244], which has a different type of monoclinic structure ($P2_1/c$), although both structural types has the same number of non-bonded silicon atoms [243] with approximately the same distances between them and the lanthanide atoms.

An alternative hypothesis to the decrease in the concentration of oxygen vacancies in GSO:Ce compared to LSO:Ce or LYSO:Ce is a change in the spatial distribution of traps and luminescent centers. The mechanism of thermal electron tunneling from the traps to the luminescent centers was proposed for cerium-activated LSO:Ce and LYSO:Ce [236], as well as Lu-Y aluminum perovskites [238]. This mechanism strongly depends on the distance between the traps and luminescent centers. The introduction of a larger cation, such as cerium, into the LSO:Ce (LYSO:Ce) lattice should lead to the formation of oxygen vacancies near Ce^{3+} to compensate for the deformation of the crystal lattice due to the introduction of a large cation. Defects in the vicinity of luminescent centers should enhance tunneling recombination and afterglow. The decrease in afterglow and increase in light yield due to the introduction of Gd^{3+} into LGSO:Ce mixed crystals may be of the same nature. A large amount of Gd^{3+} or cations with similar ionic radii can effectively compete with Ce^{3+} for the redistribution of oxygen vacancies from Ce^{3+} to other large cations. Thus, even if the total concentration of defects does not decrease, most of them will be allocated around Gd^{3+}, whose concentration is about 100 times higher than that of Ce^{3+}. As a result, electron traps may be too far from Ce^{3+} to ensure efficient tunnelling recombination.

The trap parameters were estimated by analyzing the TSL curves. In particular, the trap depth was evaluated by the Initial Rise Method, which is described in detail in [245]. In this case, the temperature dependence of the radioluminescence intensity was taken into account when approximating all thermoluminescence peaks (in fact, the beginning of even the highest temperature peak is well below 180 °C). The same trap depth value of about 1.0 eV with an error of less than 10% (Fig. 4.8) was obtained for all TSL peaks for all samples.

The frequency factors s of TSL peaks were calculated according to the formula:

$$\frac{\beta E}{kT_m^2} = s \cdot exp\left(-\frac{E}{kT_m}\right). \tag{4.3}$$

In the process of temperature tunneling, the frequency factor s can be expressed as [246]:

$$S = x\upsilon_T\, exp\left(\frac{\Delta S}{k}\right), \tag{4.4}$$

where x is the permeability coefficient of the energy barrier, υ_T is the temperature frequency coefficient, and $\frac{\Delta S}{k}$ is the entropy coefficient. The permeability coefficient of the energy barrier is determined by the formula [247]:

$$x = exp(-\phi r), \tag{4.5}$$

where ϕ is a constant and r is the distance between the trap and the luminescent center.

The frequency factors dependences on the distance (r) of oxygen — lanthanide (O—Ln) in the LnO_7 polyhedra of the $C2/c$ monoclinic structure are shown in Fig. 4.9. Experimental data agree well with the exponential dependence of the frequency factor on the O—Ln distance. Thus, analysis of TSL measurements demonstrates that the same thermal tunneling mechanism works in all the studied crystals, which indicates a similar spatial distribution between traps and Ce^{3+} in all samples, regardless of the Gd concentration in them.

In Fig. 4.10, the thick line shows the dependence of oxygen vapor pressure P on temperature T, built based on equation 4.2. Also, the graph shows the areas under the TSL curves (from Fig. 4.7) and the areas under the afterglow curves for crystals of different composition. Both values reflecting the change in the number of oxygen vacancies correlate well with each other. The qualitative agreement between the theoretical dependence for P and the experimental TSL and afterglow data indicates that melt evaporation significantly affects the concentration of traps and afterglow in oxyorthosilicates and, in particular, in LGSO:Ce.

It should be noted that there is an excellent agreement between the experimental points and the analytical curves for LSO:Ce and GSO:Ce, while the points corresponding to mixed crystals deviate slightly from the theoretical dependence. This may be related to the influence of other factors on the afterglow, for example, a decrease in the thermalization length of charge carriers due to inhomogeneities in the crystal or electron-phonon interaction in mixed crystals [13]. Also, a different trend is observed for crystals with monoclinic structures $C2/c$ and $P2_1/c$ (the latter corresponds to points for GSO and $x = 0.05—0.1$).

Thus, the analysis indicates that the decrease in TSL intensity and afterglow occurs due to a decrease in the concentration of oxygen vacancies with an increase in the gadolinium concentration in the matrix. The decrease in the

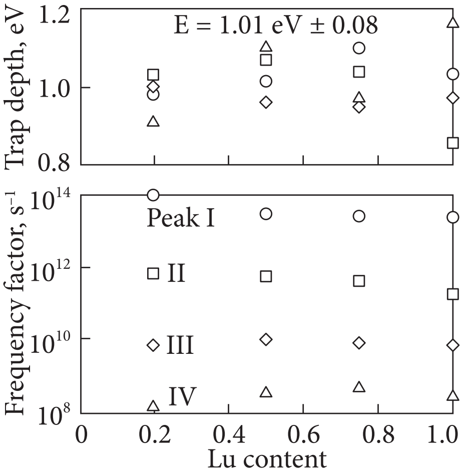

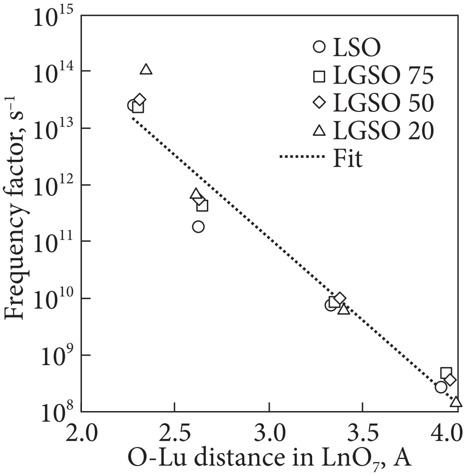

Fig. 4.8. Trap depths estimated by the Initial Rise Method for peaks I—IV for all the samples. The dependence of the corresponding frequency factors of the traps is in the inset. The standard error in determining frequency factors is ~50% [238]

Fig. 4.9. Frequency factors dependence on the Ln—O distance in LGSO:Ce, determined from X-ray diffraction data. The dashed line represents the approximation by the exponential function (explanation is in the text) [238]

concentration of oxygen vacancies occurs due to a decrease in the melting temperature, which causes weakening of the melt evaporation. At the same time, by analogy with the previous results for LSO:Ce and LYSO:Ce, the presence of four TSL peaks corresponding to traps of the same depth in LGSO:Ce are interpreted as the presence of one type of traps (oxygen vacancies) at different distances from the Ce^{3+} luminescence center. Radiative recombination between electrons and holes occur by the thermal tunneling mechanism. Thus, the TSL results combined with data on vapor pressure above the melt do not support the hypothesis that the intensity of the afterglow is related to the different distribution of vacancies and luminescent centers relative to each other when the gadolinium concentration changes.

Due to the development of mixed scintillators based on Lu and Gd oxyorthosilicates, the performance of these scintillators has been significantly improved, as evidenced by the comparative table of scintillation parameters important for practical applications. The properties of the $Lu_{0.4}Gd_{1.6}SiO_5$:Ce crystal are compared with other scintillators for X-ray computed tomography (Table 4.2).

In particular, the level of afterglow (and, accordingly, its reciprocal «signal-to-noise ratio») is significantly decreased in $Lu_{0.4}Gd_{1.6}SiO_5$:Ce compared to LYSO:Ce and LSO:Ce, without simultaneous deterioration of other parameters, except for a decrease in the density of the material. In addition, according to Table 4.2, LGSO:Ce has the lowest level of afterglow compared to other scintillators. This indicates the prospect of using these crystals in modern computer

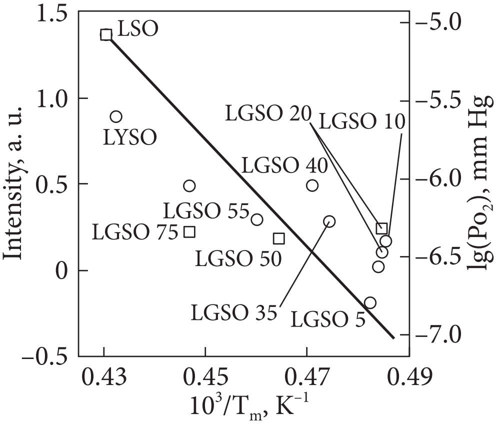

Fig. 4.10. Areas under TSL curves in Fig. 4.7 (asterisks, left scale); areas under afterglow curves in the range of 0 to 10^5 ms (circles, left scale); O_2 vapor pressure above the melt (curve, right scale) depending on the reciprocal absolute temperature. The error in determining the areas under the TSL and afterglow curves is about 20% [238]

tomography and positron emission tomography, where the signal-to-noise ratio is the decisive parameter.

The resulting correlation between carrier trapping and melting temperatures raises questions about the role of this effect in other solids solution-based scintillator systems. The exact answer to this question is difficult to formulate due to the small amount of available TSL and/or afterglow data obtained under the same conditions and by the same procedure in solid solutions. Considering that the light yield and afterglow are inversely proportional, an alternative way is to compare the light yield and melting temperatures of crystals that have the same type of structure and differ only in the substitution of one of the atoms.

Table 4.2. **Parameters of Ce-activated LGSO, LYSO, and LSO crystals in comparison with literature data on traditional scintillators for X-ray computed tomography** [248, 249]

Scintillator	Density, g/cm^3	Relative light yield, %	Luminescence maximum, nm	Main decay time, ms	Afterglow level, % per 3 ms	Signal-to-noise ratio
$CdWO_4$	7.9	100	530	2.15	0.1	1000
CsI:Tl	4.51	330	550	1	>0.3	330
$(Y,Gd)_2O_3$:Eu	5.9	152	610	1000	5	20
Gd_2O_2S:Pr,Ce	7.34	180	520	2.4	0.1	1000
Gd_2O_2S:Tb(Ce)	7.34	180	550	600	0.7	140
$Gd_3Ga_5O_{12}$:Cr,Ce	7.09	138	730	150	0.1	1000
$Lu_{0.4}Gd_{1.6}SiO_5$:Ce	6.55	52	420	0.05	0.05	2000
LYSO:Ce	7.1	50	420	0.04	1.3	77
LSO:Ce	7.4	35	420	0.04	2.9	34

Such a comparison is shown in Table 4.3, where data on the light yield in several pairs of materials of the same chemical nature and crystal structure are presented in combination with the melting temperatures of these compounds. This table does not represent mixed crystals (e.g., LGSO:Ce), where the light yield may vary due to other factors discussed in this chapter. Values of light yield and melting temperature are taken from [6, 13, 82, 247—251].

In most compounds activated by Ce^{3+}, Pr^{3+}, or Eu^{2+}, the light yield increases by 1.1—1.9 times in the material with a lower melting temperature, which confirms the assumption of a decrease in the concentration of traps with a decrease in the melting temperature. The only exception is the pair $LaBr_3$:Ce/$LaCl_3$:Ce, while in $Lu_3Al_5O_{12}$:Pr/$Y_3Al_5O_{12}$:Pr, the melting temperatures and light yield are the same. It is interesting that in both of the given pairs of scintillators with intrinsic luminescence — $ZnWO_4$/$MgWO_4$ and $Bi_4Ge_3O_{12}$/$Bi_4Si_3O_{12}$ — the opposite trend is observed. Since tungsten and bismuth oxyanions are the emission centers in these compounds with intrinsic luminescence, their concentration is 2—3 orders of magnitude higher compared to the number of luminescent centers in materials with activated luminescence. Therefore, the diffusion length of charge carriers to the luminescent center should be shorter in scintillators with intrinsic luminescence, and the scintillation process in the latter is less sensitive to the presence of defects in the crystal lattice. It should be noted that when comparing the light yield and melting temperature of scintillators, it is necessary to take into account other factors, for example, the placement of ener-

Table 4.3. **Melting temperatures (higher (*HT*) and lower (*LT*) temperatures) and light yield of some L_{LT} and L_{HT} scintillation crystals with lower and higher melting temperatures, respectively**

Compounds	$YAlO_3$:Ce $LuAlO_3$:Ce	$Y_3Al_5O_{12}$:Ce $Lu_3Al_5O_{12}$:Ce	$Y_3Al_5O_{12}$:Pr $Lu_3Al_5O_{12}$:Pr	Y_2SiO_5:Ce Lu_2SiO_5:Ce	$MgWO_4$ $ZnWO_4$
Melting points (K)	2 143 2 203	2 223 2 253	2 223 2 253	2 243 2 323	1 493 1 631
L_{LT}, L_{HT} (ph/MeV)	18 000 11 400	16 700 12 500	16 000 17 000	27 500 20 500	5 500 8 000
L_{LT}/L_{HT}	1.6	1.3	~1	1.4	0.7

Compounds	$LaCl_3$:Ce $LaBr_3$:Ce	$BaBr_2$:Eu BaI_2:Eu	SrI_2:Eu BaI_2:Eu	$CsBa_2Br_5$:Eu $CsBa_2I_5$:Eu	$Bi_4Si_3O_{12}$ $Bi_4Ge_3O_{12}$
Melting points (K)	1 001 1 121	984 1 130	807 984	883 915	1 303 1 323
L_{LT}, L_{HT}, (ph/MeV)	50 000 75 000	8 000 40 000	112 000 58 000	102 000 92 000	2 000 8 000
L_{LT}/L_{HT}	0.7	1.45	1.9	1.1	0.25

gy levels of activators and traps in the bandgap. These aspects will be discussed in the following subsections.

Thus, we demonstrated that the concentration of oxygen vacancies decreases when gadolinium is added to the mixed oxyorthosilicate $Lu_{2x}Gd_{2-2x}SiO_5$:Ce. A similar effect was also observed in the $Lu_{2x}Y_{2-2x}SiO_5$:Ce system when yttrium was introduced. Thus, the introduction of Gd or Y cations makes it possible to reduce the concentration of oxygen vacancies, that is, to reduce the concentration of charge carrier traps and the accumulation of free charge carriers during irradiation with ionizing particles. The effect is also due to changes in the melting temperature of the crystals, which weakens the melt evaporation.

The strategy for reducing the concentration of charge carrier traps associated with oxygen vacancies, demonstrated by the example of the substitution of Lu and Gd cations in LGSO:Ce, can be applied to other scintillators, in which the melting temperature is significantly reduced with the isovalent substitution of atoms. Due to the mechanism of reducing the defect concentration, the scintillation properties of mixed oxyorthosilicates have been significantly improved, which makes them attractive for use in imaging devices.

Finally, a comparison of the light yield and melting temperatures of some scintillators proved that the formation of defects in the crystal during growth from a non-stoichiometric melt is an important factor affecting the scintillation properties of crystals activated by rare earth ions.

4.2. Engineering of the electronic structure of solid solutions

Chapter 1.3.1 illustrated how bandgap engineering, i.e., controlling the position of the activator energy levels and charge carrier traps in scintillation crystals, allows for effective control of their scintillation parameters. The most remarkable positive results were obtained in solid solutions of Al^{3+}/Ga^{3+}-substituted scintillators based on lutetium and gadolinium garnet, where the light yield of the solid solution exceeded the light yield of each of its components by 3—4 times. At the same time, in many systems where deviations of light yield from additive values of 50—100% are observed, the energy structure practically does not change. To analyze the influence of the energy structure modification factor on the scintillation properties of mixed systems, the $Y_3Al_{5-x}Ga_xO_{12}$:Ce and $Lu_{2x}Gd_{2-2x}SiO_5$:Ce systems were analyzed.

4.2.1. Energy structure of YAGG:Ce

It is noteworthy that in aluminum-gallium garnet systems, a very significant change in the bandgap is observed, reaching 1.6 eV [12]. The Ce^{3+} luminescence in these systems is strongly shifted to the red region, which indicates a strong crystal field and a strong splitting of the energy levels in the activator. As noted in Chapter 3, the $Y_3Al_{5-x}Ga_xO_{12}$:Ce yttrium-aluminum-gallium garnet system

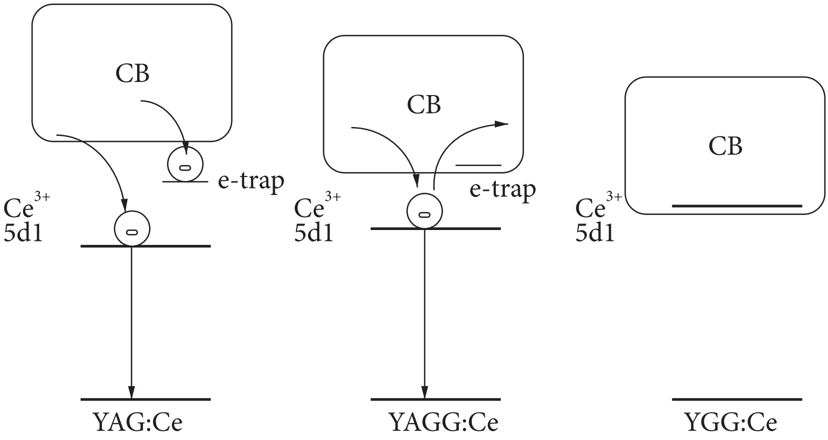

Fig. 4.11. The effect of cation substitution on the energy structure of the YAG:Ce—YGG:Ce system [105]

forms a continuous series of solid solutions from YAG:Ce to YGG:Ce and is a very convenient object for studying the modification of its energy structure. In this subsection, based on the data of absorption spectra and TSL curves, the width of the bandgap, the strength of the crystal field, and the position of Ce^{3+} levels and electronic traps in the bandgap are estimated.

The energy structure of YAGG:Ce was determined based on absorption spectra, selective excitation and luminescence spectra (Chapter 3.3.2), as well as TSL curves. A strong shift of the $Y_3Al_{5-x}Ga_xO_{12}$:Ce absorption edge in the UV range (see Fig. 3.26) indicates a decrease in the bandgap by 1.0 eV in YGG compared to YAG.

On the example of $Lu_3Al_{5-x}Ga_xO_{12}$:Ce, it was shown [12] that the shift of the valence band edge is an order of magnitude weaker than for the conduction band (0.1 eV versus 1.6 eV). Such a strong shift of the edge of the conduction band is because [12] it is formed by the 4*s* levels of Ga instead of the 5*d* levels of Lu^{3+}. At the same time (see Fig. 3.27*b*), the X-ray luminescence spectrum shifts to the blue region by ~70 nm from YAG to YAGG, and the splitting of the 5*d* levels of Ce^{3+} decreases due to the decrease in the strength of the crystal field.

Based on the spectral-kinetic properties of luminescence in YAGG:Ce, the evolution of the band structure with the addition of Ga looks as follows (Fig. 4.11): the light yield improves due to the deactivation of shallow electron traps, the levels of which in YAG:Ce are located below the conduction band. The addition of >75% Ga shifts the $5d_1$ levels of Ce^{3+} closer to the edge of the conduction band and completely suppresses the 5*d*-4*f* radiative transitions in Ce^{3+} in YGG:Ce. At a high Ga content, electrons are ionized from the 5*d* levels of Ce^{3+} to the conduction band, causing strong phosphorescence (afterglow), as can be seen in the sample with 85% Ga. Thus, optimization of the cation composition in a solid solution makes it possible to achieve optimal values for scintillation applications of the bandgap and the energy gap between the bandgap edges and the ground 4*f* and excited 5*d* levels of Ce^{3+}, at which the energy required for the formation of an electron-hole pair decreases, and the number of electron traps that prevent the transfer of carriers to the activator decreases (see Fig. 4.11). Along with that, the closeness of the 5*d* level of cerium to the conduction band causes a strong afterglow, which can be a problem in the practical application of this class of scintillators.

The mechanism of thermally stimulated luminescence in garnet crystals is based on the release of electrons from deep traps from structural defects (mainly oxygen vacancies and antisite defects) and their recombination with holes localized around Ce^{3+} ions. Thus, the study of TSL in $Y_3Al_{5-x}Ga_xO_{12}$:Ce with a variable Ga(x) content can reflect the change in the location of the energy levels of defects in relation to the bottom of the conduction band in the presence of Ga in tetrahedral and octahedral positions. Since the bandgap of $Y_3Al_{5-x}Ga_xO_{12}$:Ce varies greatly, the deep trap levels should shift inside the conduction band, and the corresponding TSL peaks will disappear completely.

The study of thermally stimulated luminescence makes it possible to determine the parameters of charge carrier traps and their position in the bandgap of the crystal. The results of TSL measurements of $Y_3Al_{5-x}Ga_xO_{12}$:Ce crystals under b- and a-irradiation above room temperature are shown in Fig. 4.12. The TSL peak temperatures of $Y_3Al_{5-x}Ga_xO_{12}$:Ce crystals with different Ga contents and the depths of the corresponding traps are shown in Table 4.5. The mechanism of TSL in this solid solution is associated with electrons released from deep traps, which are most likely oxygen vacancies [252—255], and their subsequent recombination with holes localized around Ce^{3+} ions. The main high-energy TSL peak in $Y_3Al_5O_{12}$:Ce corresponds to temperatures of 586—590 K (Fig. 4.12*a*,

Table 4.4. **Parameters and excitation energies of TSL peaks in $Y_3Al_{5-x}Ga_xO_{12}$:Ce and energies of releasing electrons from the corresponding traps [213]**

Crystal	Temperature of the high-energy peak, T (K); trap depth (eV) upon excitation by β-particles	Temperature of the low-energy peak, T (K); trap depth (eV) upon excitation by β-particles	Temperature of the high-energy peak, T (K); trap depth (eV) upon excitation by α-particles	Temperature of the low-energy peak, T (K); trap depth (eV) upon excitation by α-particles
$Y_3Al_5O_{12}$:Ce	437; 590 (1.43 eV)	361; 426 (1.09 eV)	443; 586 (1.34 eV)	372; 423 (1.04 eV)
$Y_3Al_3Ga_2O_{12}$:Ce	417; 528 (0.62 eV)	390 (0.76 eV)	427; 530 (0.76 eV)	389 (0.6 eV)
$Y_3Al_2Ga_3O_{12}$:Ce	429 (0.54 eV)	360 (0.48 eV)	381; 421 (0.59 eV)	359 (0.64 eV)
$Y_3Ga_5O_{12}$:Ce	357 (0.50 eV)	—	(0.50 eV)	—

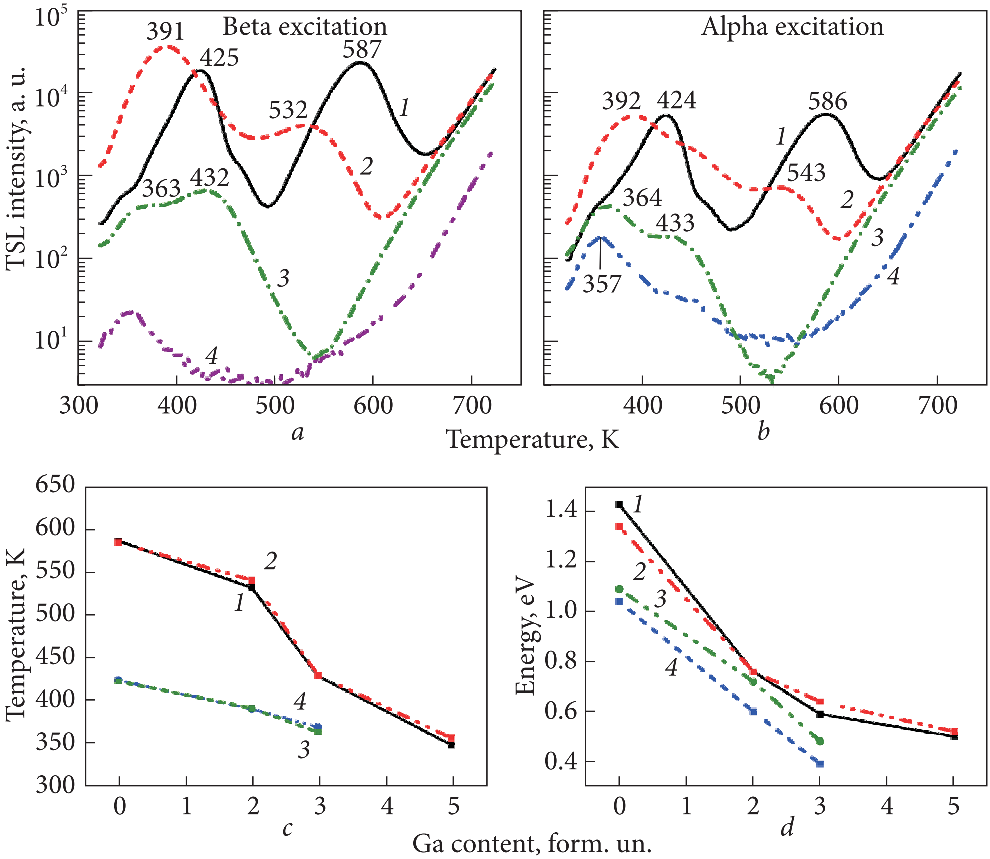

Fig. 4.12. TSL parameters of $Y_3Al_{5-x}Ga_xO_{12}$:Ce crystals depending on gallium content (x): when irradiated with β-particles (*a*) and α-particles (*b*); corresponding dependences of the positions (*c*) and excitation energy (*d*) of the high- and low-energy peaks on the TSL curves [212]; *a*, *b*: *1* — $Y_3Al_5O_{12}$:Ce; *2* — $Y_3Al_3Ga_2O_{12}$:Ce; *3* — $Y_3Al_2Ga_3O_{12}$:Ce; *4* — $Y_3Ga_5O_{12}$:Ce; *c*, *d*: *1*, *2* — high tempereture peaks; *3*, *4* — low tempereture peaks; *1*, *3* — beta excitation; *2*, *4* — alpha excitation [213]

curve *1*, Table 4.4). When the Ga content in the crystals increases to $x = 2$, the position of the high-energy TSL peaks is shifted to temperatures of 528—530 K (Fig. 4.12*a, b*, curves *2*). When the Ga content increases to $x > 2.0$, this TSL peak is significantly shifted to temperatures of 421—429 K (Fig. 4.12*a, b*, curves *3*, Table 4.4) and to 357—355 K for $Y_3Ga_5O_{12}$:Ce (Fig. 4.12*a, b*, curve *4*, Table 4.4). Thus, the dependence of the main TSL peak intensity on the Ga content in the intervals x = 0—2 and 2—5 can be displayed in the form of two straight lines with different slopes. At the same time, this type of dependence on the Ga content is typical for other optical properties of $Y_3Al_{5-x}Ga_xO_{12}$:Ce crystals, namely the positions of the absorption and luminescence peaks (see Fig. 3.27*b*), as well as the exciton formation energies associated with Ce^{3+} ions (see Fig. 3.28*b*). The nonlinear dependence of the optical properties of the $Y_3Al_{5-x}Ga_xO_{12}$:Ce solid solution correlates with the predominant inclusion of gallium and aluminum in tetrahedral and octahedral positions, respectively (the issue of structural inhomogeneities is discussed in detail in Chapter 4.3).

The Ga admixture in $Y_3Al_{5-x}Ga_xO_{12}$:Ce leads to a strong weakening of the intensity of the main TSL peaks in the range of 425—650 K. This result correlates well with a significant increase in light yield (see chapter 3.3.4), apparently due to the exclusion of charge carrier capture centers from the scintillation process in samples of the appropriate composition. At the same time, in crystals with a higher content of gallium ($x > 3$) and $Y_3Ga_5O_{12}$:Ce, TSL is practically absent above room temperature. In addition to the high-energy peak, there is a low-energy peak at 423—426 K for $Y_3Al_{5-x}Ga_xO_{12}$:Ce crystals. This peak is shifted to lower temperatures in the range of 380—390 K for $Y_3Al_3Ga_2O_{12}$:Ce (Fig. 5.12*a,b*, curves *2* and Table 5.5) and within 350—360 K for $Y_3Al_2Ga_3O_{12}$:Ce (Fig. 5.12*a,b*, curve *3* and Table 5.4); and for the $Y_3Ga_5O_{12}$:Ce crystal, it is definitely below 323 K, beyond the operating range of the TSL measurement setup.

4.2.2. Energy structure of LGSO:Ce

For rare-earth silicates, such as Lu_2SiO_5 (LSO), Gd_2SiO_5 (GSO), there are no noticeable changes in the bandgap depending on the type of rare-earth cation, however, the spread of values for the same compound in different sources reaches 0.8 eV. For example, various references give E_g values from 6.1 to 6.6 eV for GSO [256, 257] and from 6 to 6.8 eV for LSO [258—260]. Since the conduction band edge in the entire range $0< x< 1$ of $Lu_{2x}Gd_{2-2x}SiO_5$:Ce is formed by the 5*d* wave functions of Lu^{3+} and Gd^{3+}, and the valence band is formed by the 2*pO* wave functions, only small bandgap changes with *x* can be predicted.

The positions of Ce^{3+} levels, as well as the bandgap width in LGSO:Ce crystals with a monoclinic *C*2/*s* structure can be estimated using the excitation spectra of cerium luminescence (Fig. 4.13*a*, *b*). The spectra were measured under identical conditions and normalized by the intensity of the first Ce^{3+} excitation band (the difference in cerium concentration between samples was taken into account). In general, the excitation spectra of the *Ce*1 centers of LGSO:Ce (*C*2/*s*) crystals differ from LSO by the position of some bands; but for some LGSO:Ce solid solutions with the *C*2/*s* structure are similar in the entire range of concentrations. Only the band positions change.

As was shown in Fig. 2.9*a*, the volume of the LGSO unit cell gradually increases by ~5% when going from LSO to $Lu_{0.4}Gd_{1.6}SiO_5$. This leads to weak changes in the strength of the crystal field and a shift in the 5*d* levels of Ce^{3+} in the bandgap (Table 4.5). For example, the high sensitivity of the position of Ce^{3+} levels to Y^{3+} impurity was shown in LYSO:Ce [99]. In LGSO:Ce, the energies of $4f$—$5d_1$, $5d_4$, and $5d_5$ transitions of Ce^{3+} slightly decrease by 0.05—0.1 eV, while

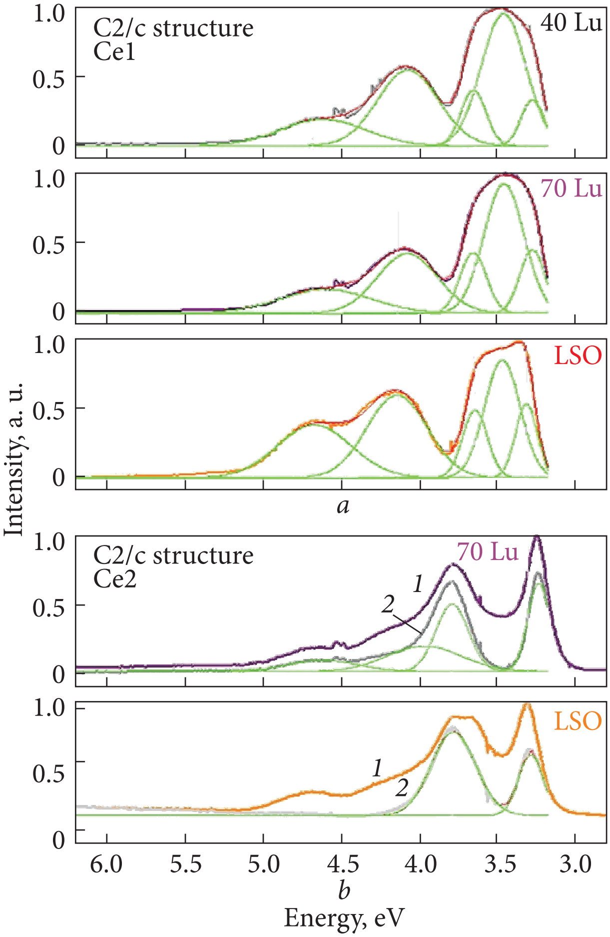

Fig. 4.13. Excitation spectra of *Ce*1 centers (l_{lum} = 395 nm) and *Ce*2 centers (l_{lum} = 515 nm) in LGSO crystals with the *C*2/*s* structure. In the excitation spectra of *Ce*2 centers, there is a significant contribution from *Ce*1 centers. Therefore, curve *1* corresponds to the excitation spectrum of *Ce*2 centers, curve *2* — to the excitation spectrum of *Ce*2 centers minus the contribution from *Ce*1 centers. Measurements of the selective excitation spectra of LGSO:Ce at DESY (Germany) were carried out by Dr. A. Belski. The results were processed and discussed together with Dr. S. Neicheva

the energies of 4*f*—5d_2 and 4*f*—5d_3 remain unchanged (Table 4.6). The position of Ce^{3+} relative to the conduction band changes by no more than 0.1 eV, while, in accordance with our estimates (Table 4.5), the bandgap from LSO to $Lu_{0.4}Gd_{1.6}SiO_5$ (within the range of *C*2/*c* symmetry) decreases by 0.15 eV. Since, judging by the location of the energy levels, the center of gravity of the electron shell also shifts, the probability of electron capture from the conduction band to the activator and ionization of Ce levels can be predicted to be constant over the entire range of solid solutions $0.2 < x < 1$. For six-coordinated cerium, the transition energies can only be reliably determined for the first two levels. As can be seen from Table 4.5, the energy changes of the latter are also insignificant within 0.05 eV.

Based on the obtained data, a scheme of excited 5*d* levels of Ce^{3+} ions in some LGSO:Ce solid solution crystals of both structural types was constructed (Fig. 4.14). The addition of gadolinium to LSO:Ce in the *C*2/*c* structure leads to a change in the splitting parameters of the 5*d* levels of Ce^{3+} ions.

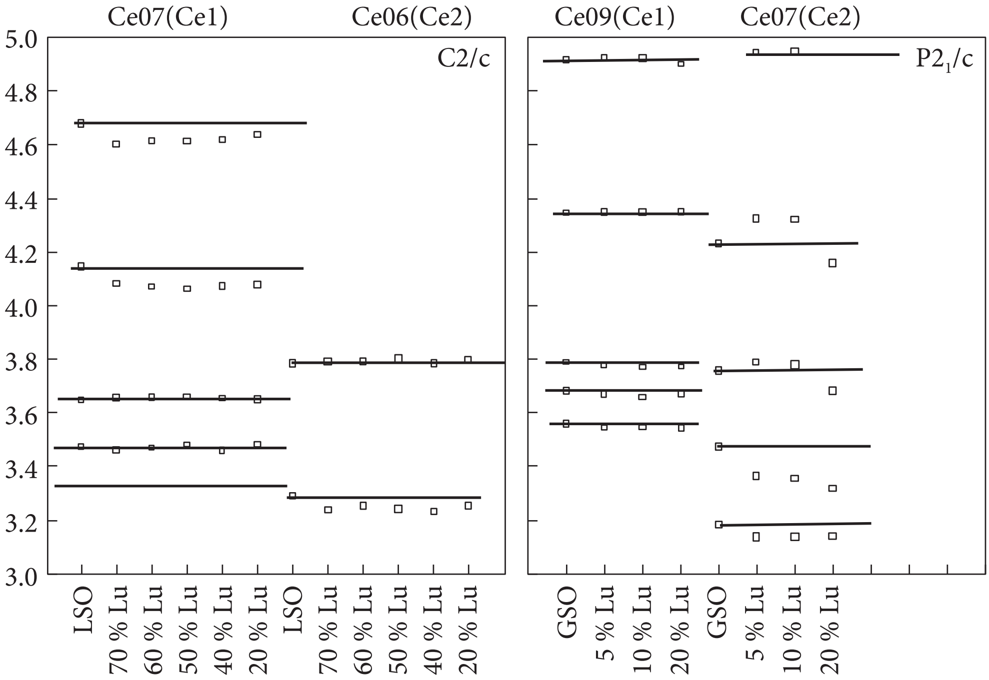

Fig. 4.14. Scheme of 5*d* levels of Ce^{3+} ions in different environments, built on the basis of the approximation of the excitation spectra in Fig. 5.13 by Gaussian functions

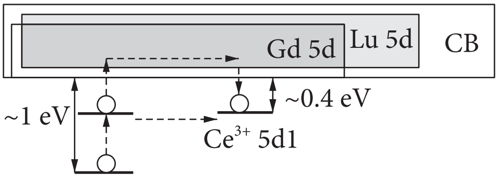

Fig. 4.15. The effect of cation substitution on the energy structure of LGSO:Ce crystals. Arrows depict possible schemes of electron transport from traps to a Ce^{3+} activator ion

However, there is no clear dependence on the concentration of gadolinium in the range of 30—80% Gd. For *Ce*1 (CeO_7) centers in LGSO:Ce, a shift of the $5d_1$, $5d_4$, and $5d_5$ levels are observed in comparison with LSO:Ce. For *Ce*2 (CeO_6) centers, while the 5*d* level is split into only 2 levels. In this case, only the low-energy level shifts toward lower energies relative to the splitting in LSO:Ce. Thus, both centers react to the introduction of gadolinium, but the magnitude of the level shift does not depend on the Gd concentration in the region of 30—80%. In LGSO:Ce, the *Ce*1 luminescence bands are shifted to the long-wavelength side, however, this shift is practically independent of the concentration of gadolinium in the solid solution, and is due to a change in the splitting of the excited 5*d* levels of *Ce*1 and the shift of $5d_1$ closer to the 4*f* ground state. It should be noted that, in contrast to *Ce*1 centers, *Ce*2 centers exhibit a shift in the luminescence maximum to longer wavelengths with increasing Gd concentra-

Table 4.5. **Energies (eV) of the 4*f*-5*d* transitions obtained from the excitation spectra of $Lu_{2x}Gd_{2-2x}SiO_5$:Ce crystals at the maximum of the luminescence band of 7-coordinated Ce (*Ce*1, λ_{lum} = 395 nm) and 6-coordinated Ce (*Ce*2, λ_{lum} = 515 nm); and energies of the first absorption maximum near the fundamental absorption peak in the VUV excitation spectra, λ_{lum} = 400 nm (its shift is proportional to the shift in the bandgap (E_g))**

Crystal composition	0.20	0.40	0.50	0.60	0.75	1
E_g	6.55	—	—	—	—	6.7
CeO_7 $5d_1$	3.30	3.28	3.29	3.29	3.28	3.31
CeO_7 $5d_2$	3.49	3.47	3.49	3.47	3.46	3.48
CeO_7 $5d_3$	3.66	3.66	3.67	3.66	3.66	3.65
CeO_7 $5d_4$	4.07	4.07	4.06	4.07	4.08	4.14
CeO_7 $5d_5$	4.62	4.62	4.62	4.62	4.60	4.68
CeO_6 $5d_1$	3.25	3.23	3.24	3.25	3.24	3.29
CeO_6 $5d_2$	3.80	3.79	3.80	3.79	3.79	3.79

tion, although the position of the lower excited level does not change in a series of solid solutions with a gadolinium concentration of 30—80 at.%.

Based on this data, as well as the depths of electron traps (see Chapter 4.1), a model of the band structure of LGSO:Ce crystals can be built (Fig. 4.15). The bandgap changes only by 0.15 eV, or by ~2—3% relative to E_g; this cannot cause a significant increase in the number of electron-hole pairs formed per unit of ionizing radiation energy (see equation 1.1). While in LSO, the lowest $5d_1$ level of cerium is 0.5—0.6 eV below the lower edge of the conduction band [99], the Lu^{3+}/Gd^{3+} substitution reduces this distance to 0.4 eV, which causes the ionization of electrons from this level to the conduction band; this is confirmed by the temperature dependence of the light yield (see Fig. 4.6*a*): with the addition of gadolinium, the thermal stability of the light yield deteriorates above room temperature, which is one of the reasons for the decrease in the light yield in LGSO:Ce with a gadolinium concentration above 50%.

4.2.3. Phenomenological analysis of the ΔE_g effect on the light yield of solid solutions

Thus, in the example of the LGSO:Ce and YAGG:Ce solid solution systems, it is demonstrated that the modification of the crystal energy structure can significantly affect the light yield, even if these changes amount to a few tens of eV as a result of the substitution of atoms in the solid solution. To find out the contribution of the bandgap change factor, we evaluated its correlation with the concen-

Fig. 4.16. Procedure for estimating the deviation of the light yield from linearity in scintillators based on solid solutions [88]

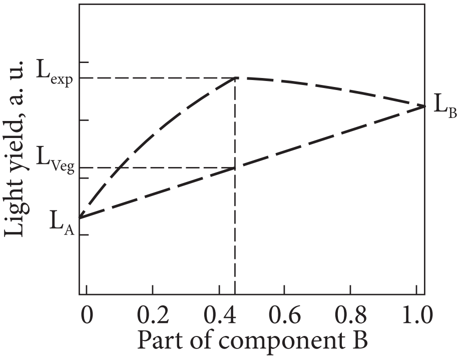

tration dependence of the light yield for known scintillators based on solid solutions. Namely, the analysis of the deviation of the light yield (L_{exp}) from the additive values (L_{Veg}) in the $A_xB_{1-x}C$ solid solution systems (where A and B are substituted atoms in the solid solution) was carried out. For analysis, systems were selected in which a continuous series of solid solutions is formed over the entire concentration range from $x = 0$ to $x = 1$, the concentration of the activator (if present) does not change significantly, the type of structure is maintained throughout the entire range of atomic substitution, and there are no impurities of foreign phases. The only exception is the $Lu_xY_{1-x}BO_3$ system [258], where up to 5% of the calcite phase is present in the vaterite phase at a Lu concentration >50 at.%. If, in some cases, the main phase is present only in part of the concentration range *x*, this particular range is taken into consideration. That is, in $Lu_{2x}Gd_{2-2x}SiO_5$:Ce the interval $0.2 < x < 1$ is considered, where the monoclinic structure *C*2/*c* exists; for $Gd_3(Al_{1-x}Ga_x)_5O_{12}$:Ce, the $0.2 < x < 1$ interval with a garnet structure is considered; and for $Lu_{1-x}Sc_xBO_3$:Ce, the studied interval is $0.1 < x < 0.9$ with the calcite phase. As a result, 21 systems of solid solutions were analyzed [88].

The deviation of the light yield values from additivity in accordance with Vegard's law was considered [156]. This empirical law postulates a linear dependence of lattice parameters, density, and bandgap on the concentration of components in a mixed crystal:

$$\mu_S = C_A\mu_A + C_B\mu_B, \tag{4.6}$$

where C_A, C_B are molar concentrations of components, m is one of the above parameters. In our case, it is assumed that in a solid solution, the light yield in the general case also obeys Vegard's law.

The method of estimating the deviation of the light yield from the additive (linear) dependence is shown in Fig. 4.16. In most cases, the experimental light yield exceeds the additive values, that is, the corresponding points are above the straight line $L_{Veg} = C_AL_A + C_BL_B$. The deviation from the linear dependence can be expressed by the parameter $(L_{exp}/L_{Veg})_{max}$, where L_{exp} corresponds to experimental points, and L_{Veg} is the light yield in accordance with Vegard's law. According to this procedure, the maximum deviation of the light yield from the linearity $(L_{exp}/L_{Veg})_{max}$ depending on the amplitude of the bandgap change in the

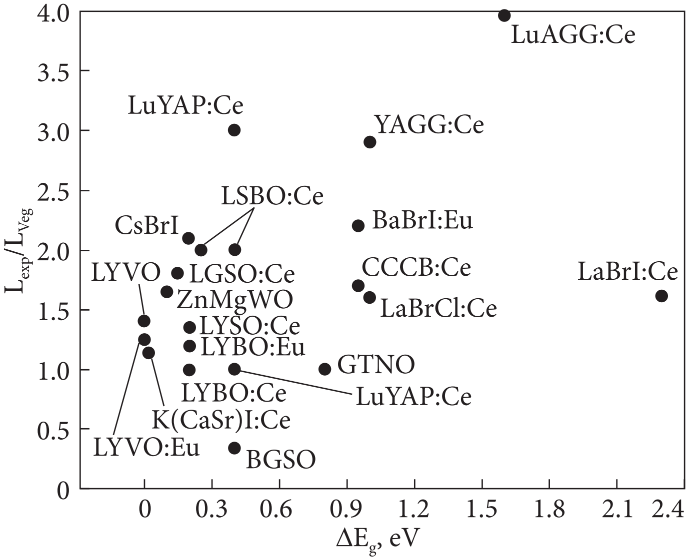

Fig. 4.17. Deviation of the light yield at room temperature from linearity depending on the difference in bandgap widths DE_g of the components of mixed crystals: $GdTa_{1-x}Nb_xO_4$ (GTNO), $Lu_{1-x}Y_xBO_3$:Ce (LYBO:Ce), $Lu_{1-x}Y_xBO_3$:Eu^{3+} (LYBO:Eu), $Lu_{1-x}Y_xVO_4$:Eu^{3+} (LYVO:Eu), $Lu_{1-x}Y_xVO_4$ (LYVO), $Lu_{1-x}Y_xSiO_5$:Ce (LYSO:Ce), $Zn_{1-x}Mg_xWO_4$ × × (ZnMgWO), $CeBr_{3-x}Cl_x$ (CeBrCl), $LaBr_{3-x}Cl_x$:Ce (LaBrCl:Ce), $LaBr_{3-x}I_x$:Ce (LaBrI:Ce), $Lu_{2-2x}Gd_{2x}SiO_5$:Ce (LGSO:Ce), $CsBr_{1-x}I_x$ (CsBrI), $BaBr_{2-x}I_x$:Eu^{2+} (BaBrI:Eu), $Lu_{1-x}Y_xAlO_3$:Ce (LuYAP:Ce), $Y_3(Al_{1-x}Ga_x)_5O_{12}$:Ce (YAGG:Ce), $Lu_3(Al_{1-x}Ga_x)_5O_{12}$:Ce (LuAGG:Ce), $Lu_{1-x}Sc_xBO_3$:Ce, $Ca_{1-x}Sr_xS$:Ce (CaSrS:Ce), $Bi_4(Ge_{1-x}Si_x)_3O_{12}$ (BGSO), $K(Ca_{1-x}Sr_x)I_3$:Eu^{2+}, $CsCaCl_{3-x}Br_x$:Eu (CCCB:Eu) [88]

mixed crystal is plotted in Fig. 4.17. In addition to the systems studied in our works, bandgap values from the literature are given [88].

Despite the significant improvement in light yield in garnets and some halides with $\Delta E_g > 0.9$, large positive deviations were also observed in systems with small changes in E_g; for example, $\Delta E_g = 0.15$ eV in $Lu_{2x}Gd_{2-2x}SiO_5$:Ce. The large spread of experimental points indicates that the DE_g parameter is not determining factor for predicting the concentration dependence of the light yield in a solid solution. Another reason for the large spread of points in Fig. 4.17 is that there may be different methods of determining the bandgap width in the literature sources used — in some cases, it is determined experimentally by luminescence absorption or excitation spectra, in other sources, E_g was determined theoretically.

The light yield should be more sensitive not to the overall change in the bandgap width, but to the position of the activator energy levels relative to the edges of the conduction band and/or valence band. Such an effect was demonstrated in [92] for $LaBr_{3-x}I_x$:Ce and by us for LGSO:Ce [6]. In contrast, in the brightest multicomponent garnets $(Lu,Gd,Y)_3(Al,Ga)_5O_{12}$:Ce (see [76] and many subsequent publications), the lowest excited level $5d_1$ in Ce^{3+} is far enough from the conduction band edge, and the shallow trap levels merge with the conduction band. A similar situation was observed in $Lu_{1-x}Sc_xBO_3$:Ce [98]. In principle, based on available literature data (see [259—264] and references therein) for solid solutions containing an activator, a phenomenological dependence between the light yield and the energy gap between the activator levels and the edges of the bandgap can be plotted. However, it is quite obvious that the obtained trend, for example, for scintillators activated by Ce^{3+}, will follow the predictions [264]: (*i*) the larger the energy gap between the ground state and the valence band edge of the activator, the less likely is hole capture on Ce^{3+} because phonons and photons with higher energy are required for the energy transition; (*ii*) the lowest 5*d* level should not be located close to the conduction band to prevent thermal ionization of electrons from it.

On the other hand, in systems where atomic substitution strongly affects the energy structure, there are more opportunities to find the optimal position of the energy levels of the activator and/or traps relative to the bandgap edges, as was shown for garnets [12, 76]. Thus, systems with a large ΔE_g are more promising in the search for scintillators based on solid solutions with improved light yield.

4.3. Clusterization in solid solutions and its causes

4.3.1. Inhomogeneities in metal alloys

In the structure of crystals of solid solutions, there are volumetric spatial inhomogeneities (or clusters, domains) enriched in one of the substituted atoms. For the first time, this was clearly shown in metal alloys, where the formation of potential barriers at inhomogeneities in the crystal causes a limitation of the diffusion of charge carriers and an increase in their electrical resistance, as was indicated in Chapter 1.3.2. The clustering effect in metal alloys is called «short-range order» [265—268] in contrast to the long-range translational order of the arrangement of atoms in a single crystal. Signs of the formation of domains in alloys are the broadening of the X-ray diffuse scattering peaks, as well as the deviation of the dependencies of physical properties (lattice parameters, electrical resistance) from Vegard's law. To describe short-range ordering in metals, the parameter of short-range ordering (SRO) energy was introduced [265—267], according to formula 4.8, obtained under the condition that each atom, due to its interatomic interactions polarizes the surrounding atoms of different types, which, in turn, are in the field of surrounding atoms polarizing the medium:

$$U_{SRO} = \frac{1}{2} C_A \left(1 - C_A\right) \sum \upsilon\left(\vec{r}_j - \vec{r}_i\right) \alpha_j \alpha_i \,, \tag{4.8}$$

where C_A is the concentration of *A* atoms; $\upsilon\left(\vec{r}_j - \vec{r}_i\right)$ is the partial ordering energy; α_i, α_j are the SRO parameters for the $_i$-th and *j*-th atomic layers around a certain atom. The $C_A(1 - C_A)$ factor is universal for any system and has a maximum of around 0.5. In turn, the SRO parameters, which are also called the Warren-Cowley parameters (formula 4.9) depend on the probability ρ_l^{AB} of atom B being at a distance r_j from atom A at concentration C_B of atom B in the solid solution:

$$\alpha_l = 1 + \rho_l^{AB} / C_B \,. \tag{4.9}$$

For most of the more than 50 investigated alloys, the value of α_l turned out to be negative. These include, in particular, alloys of noble and transition metals with each other and with base metals. Typical examples are Cu-Au, Ag-Au, Ni-Pt, Fe-Al, Au-Pd, Ni-Al, Ag-Mg, Cu-Zn, V-Nb, Mo-Ti, Pd-W. Nevertheless, among such groups of metals, there are also alloys with $\alpha_l > 0$, for example, Ni-Au, Cu-Ni, Al-Ag (at $C_{Al} >> C_{Ag}$), Nb-Ti, Mo-W. Various criteria have been proposed to predict the dependence of the α_l parameter (ionic radii of the components, the average valence of the alloy, or a comparison of the valences of the solvent and the dissolving element). But it turned out that such criteria can be extended to a sufficiently small number of alloys. It turned out that to calculate short-range ordering, it is necessary to calculate the ordering energy within the framework of the modern electronic theory of short-range ordering, which takes into account not only direct interionic interactions, but also interionic interactions through a gas consisting of conduction electrons [266, 267].

4.3.2. Manifestations of nanoscale inhomogeneities in mixed dielectric crystals

In dielectric crystals, spatial stratification can cause limited diffusion of charge carriers with low energies of the order of kT. Limiting the diffusion of electrons and holes should increase the probability of genetic recombination (recombination of an electron and a hole formed in one act of carrier reproduction). It is noteworthy that the concentration dependences of the light yield in most of the solid solutions of the scintillators we considered have a maximum at a component ratio of 1:1 (Fig. 4.1). For the first time, the connection of light yield with the limitation of charge carrier diffusion on inhomogeneities in scintillation crystals was assumed in [11] for LuYAP:Ce. As confirmation of the better diffusion of carriers to the luminescent center, it was proposed to evaluate it in relation to the intensity of the VUV luminescence excitation spectra. One pair with energy close to E_g is formed upon excitation near the edge of the fundamental absorption. Two–four e-h pairs can be formed upon excitation by photons with energies of 3—5E_g, if the average energy of electrons and holes is approximately 0.5E_g in relation to the bottom of the conduction band and the upper edge of the valence band. During thermalization, some of them can diffuse to a distance greater than the radius of capture by the cerium ion and not participate in the scintillation process, but lead to afterglow and other slow processes. Thus, the

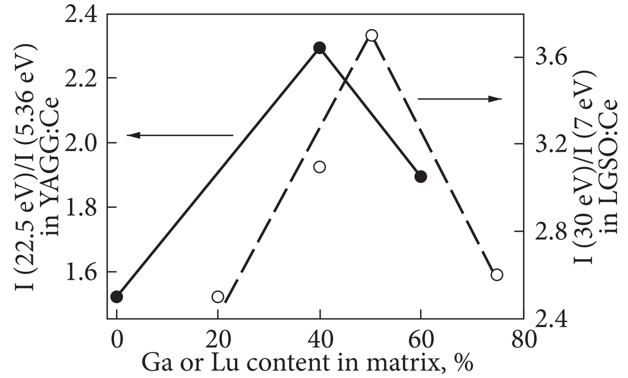

Fig. 4.18. Excitation transfer efficiency of the Ce^{3+} luminescent center: *a* — in LGSO:Ce (ratio of 400 nm luminescence excitation spectrum intensities, *I*(30 eV)/*I*(7 eV)); b — in YAGG:Ce (ratio of 520—540 nm luminescence excitation spectra intensities, *I*(22.3 eV)/*I*(5.36 eV) [88]

ratio of luminescence intensities upon excitation at 20—30 eV (~$4E_g$) and 6—7 eV (~E_g) is a characteristic of the participation of electron-hole pairs in the scintillation process.

The ratio of $I(\sim 4E_g)$ to $I(\sim E_g)$ in the LuYAP:Ce solid solution was the largest in the range of intermediate concentrations around $x = 0.5$ (Fig. 1.11). In this work, similar dependencies were calculated for the LGSO:Ce and YAGG:Ce systems (Fig. 4.18). Both dependencies have a maximum at a component ratio of about 1:1. In LGSO:Ce, this ratio was measured separately upon excitation of the *Ce*1 and *Ce*2 centers. The excitation efficiency of *Ce*1 turned out to be approximately twice as high as that of *Ce*2. Similarly, based on excitation spectra over a wide energy range (Fig. 3.26), the efficiency of the excitation process of Ce in YAGG:Ce at energies $>>\Delta E_g$ was estimated, which involves the sequential capture of a hole and an electron by cerium of separated electron-hole pairs (Fig. 4.18). The efficiency of energy transfer to the activator increases by 1.5 times in the intermediate composition relative to YAG:Ce.

The dependence of the efficiency of charge transfer to the luminescent center is significant, but indirect evidence of the contribution of inhomogeneities to the scintillation process. Since the size of such inhomogeneities did not exceed several tens of nm, their direct observation is complicated. According to the authors' experience, Transmission Electron Microscopy (TEM) is not effective because the sample thickness must be comparable to these inhomogeneities (domains). Crystal samples a few nanometers thick with atomically pure surfaces are very difficult to prepare. Apparently, the limit of this method is Y-fluctuations of ~50—100 nm size in LYSO:Ce, which were observed by the TEM method in combination with Energy Dispersive Spectroscopy [269].

Among other indirect evidence of the existence of inhomogeneities in dielectrics, by analogy with metals, we should once again recall the nonlinear dependence of lattice parameters on the ratio of components in MgO-FeO, MgO-LiFeO [159] and PbF_2-CdF_2 [160]. Based on the studies presented in this monograph, other signs of the influence of heterogeneity on the scintillation process can be noted. In $Gd(Nb_xTa_{1-x})O_4$, although the ionic radii of Nb^{5+} and

Ta^{5+} are identical [112] and the light yield at room temperature varies linearly with the composition of the solid solution [190], we have obtained facts indicating the existence of spatial inhomogeneities (see Section 3.2.2), namely:

- the broadening of thermally stimulated luminescence peaks for intermediate concentrations (Fig. 3.21) means a wider distribution of the activation energy of the traps corresponding to these peaks, i.e. the traps are in a different cationic environment, and their depth depends on the spatial fluctuations of the bandgap;
- nonlinearity of light yield at 16 K and its linearity at 300 K (Fig. 3.23*b*). Since charge carriers in crystals are in a periodic electrostatic field formed by matrix ions, in a mixed crystal, the amplitude of fluctuations of the crystal field increases in the case of the formation of clusters enriched with one of the substituted atoms. The difference in the bandgap (ΔE_g) also matters, so the cluster boundaries become potential barriers that reduce electron and hole scattering at $\Delta E_g >> kT$. In the system under consideration, ΔE_g between $GdTaO_4$ and $GdNbO_4$ is 0.8 eV [63]). Since kT is 19 times greater at 300 K than at 16 K, the limitation of carrier diffusion at 16 K causes an increase in the light yield in intermediate compositions, while at 300 K it changes additively. It is also necessary to take into account the increase in the radius of the Onsager sphere at low temperatures.

4.3.3. Selective incorporation of substituted atoms into the crystal lattice in a solid solution

When considering the reasons that cause inhomogeneities in the crystal lattice, first of all, it is necessary to identify systems where the replaced atoms can occupy different non-equivalent positions. The characteristic sizes of these inhomogeneities range from several angstroms (equal to the distance between equivalent crystallographic positions in the crystal lattice). We studied in detail the distribution of substituted atoms in non-equivalent positions in two solid solution systems activated by cerium —LSO-GSO and YAG—YGG.

In the structure of oxyorthosilicates, the rare-earth cation occupies two crystallographic positions in the REO_7 (RE1) and REO_6 (RE2) polyhedra. X-ray structural analysis and optical methods showed that in both structural types of the LGSO:Ce monoclinic lattice, Gd^{3+} and Ce^{3+} atoms with larger ionic radii occupy seven-coordinated oxygen positions with a larger average distance from the rare earth atom to the oxygen environment (Fig. 4.19). The dynamics of Lu^{3+} incorporation into matrices with different types of spatial symmetry is shown in Fig. 4.20.

The distribution coefficient of Gd into LSO estimated from these data is 1.2 in LnO_7 polyhedra and 0.8 in LnO_6 polyhedra. An even more remarkable difference in the incorporation coefficient $k(Lu) = 0.65$ is observed for the symmetry $P2_1/c$ in LnO_7, while for LnO_9 polyhedra, the amount of Lu does not exceed

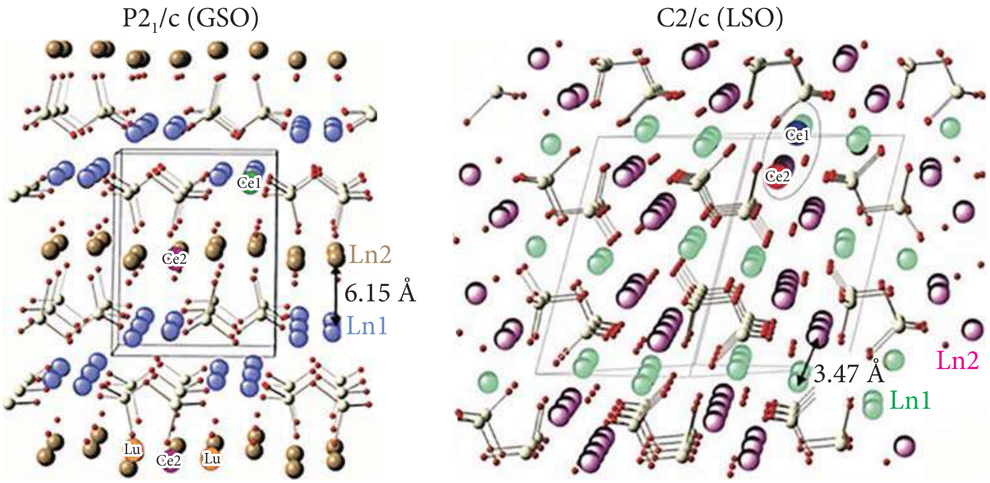

a *b*

Fig. 4.19. Crystal lattices of GSO (monoclinic structure $P2_1/c$) and LSO (monoclinic structure $C2/c$) assembled using the program «Balls&Sticks» [269]). Colored balls indicate lanthanide atoms with different oxygen coordination. SiO_4 polyhedra are marked with small balls [88]

the error of the X-ray diffraction method. Thus, Gd atoms mainly occupy seven-coordinated positions in LGSO with $C2/c$ symmetry and nine-coordinated positions in LGSO with $P2_1/c$ symmetry. This result is natural, since Gd^{3+} ions with an ionic radius of 0.94 Å tend to substitute Lu^{3+} ($r = 0.86$ Å) in a position with a larger volume, where the average bond length between Lu^{3+} and the surrounding oxygen atoms are 2.32 Å (2.23 Å in a six-coordinated position) [164].

The phase analysis of LGSO:Ce fibers grown by the micro-pulling method [144] confirms the substitution of Lu/Gd in six- and seven-coordinated polyhedra in the crystals; this indicates that the distribution of atoms over crystallographic positions are independent of the growth method.

As for the spatial heterogeneity (Fig. 4.19), it should be noted that the LnO_7 and LnO_6 polyhedra form columns or layers oriented along certain crystallographic directions. The relative placement of Ln1 and Ln2 is different in the $P2_1/c$ and $C2/c$ structures. The example of the $P2_1/c$ structure clearly shows the spatial inhomogeneity of the arrangement of Ln1 and Ln2 in the corresponding layers alternating along the [100] direction with a minimum distance of 6.15 Å between them. Thus, there is a clear spatial separation of Lu and Gd enriched layers. In contrast to $P2_1/c$, there is no obvious segregation of Lu and Gd in the $C2/c$ structure, and we can only talk about columns enriched in the corresponding atoms. Moreover, the smallest distance between the Ln1 and Ln2 positions is only 3.47 Å.

The distribution of Ce^{3+} possesses the largest ionic radius among the lanthanides (1.02 Å) is even more heterogeneous; this in turn affects the scintil-

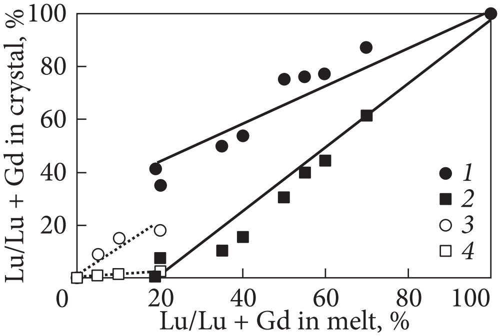

Fig. 4.20. Lu concentration in different oxygen coordination positions in LGSO depends on Lu concentration in the melt according to X-ray diffraction data [110, 144]. Dashed lines indicate a possible trend [88]: *1* — 6-coord C2/c; *2* — 7-coord C2/c; *3* — 7-coord $P2_1/c$; *4* — 9-coord $P2_1/c$

lation parameters of the crystals. According to EPR and Raman spectroscopy data for LSO:Ce, the fraction of Ce located in the six-coordinated position is 5—10% [164, 165]. Thus, Ce^{3+} is also mainly concentrated in Ln1 polyhedra.

The change in the splitting parameters of the 5*d* levels in Ce^{3+} (Table 4.5) and the change in the probability of electronic transitions (Fig. 4.14) indicates that the Ce centers in LSO, GSO, and for medium LGSO concentrations have different environments. The arrangement of cerium in the corresponding positions can be estimated using the kinetics of the luminescence decay of these centers. The decay times of the *Ce*1 and *Ce*2 centers in LSO and GSO coincides with literature data [271—272]. The luminescence kinetics of *Ce*1 and *Ce*2 centers in LGSO solid solutions differs significantly from the kinetics in solid solution components (Fig. 4.21 and Table 4.6).

In GSO:Ce and LGSO:Ce crystals with the $P2_1/c$ structure, the decay kinetics of *Ce*1 centers, as well as their excitation and luminescence spectra (Fig. 4.13), practically do not depend on the introduction of lutetium and are described by a single exponent with a characteristic decay time of ~22 ns, while the kinetics of *Ce*2 centers significantly depends on the crystal composition (Fig. 4.21 and

Table 4.6. **Luminescence decay times of *Ce*1 and *Ce*2 centers in LGSO:Ce**

Structure type	Crystal composition	Decay time at 300 K, ns	
		*Ce*1	*Ce*2
$P2_1/c$	GSO: 0.6% Ce	23	4 (100%)
	LGSO:Ce 5% Lu	22	5 (46%) + 23 (54%)
	LGSO:Ce 10% Lu	22	5 (30%) + 25 (70%)
	LGSO:Ce 20% Lu	21	6 (25%) + 30 (75%)
C2/c	LGSO:Ce 20% Lu	7 (31%) + 23 (69%)	42
	LGSO:Ce 40% Lu	8 (21%) + 26 (79%)	47
	LGSO:Ce 50% Lu	9 (20%) + 27 (80%)	47
	LGSO:Ce 75% Lu	12 (18%) + 31 (82%)	46 + background
	LSO	30	42 + background

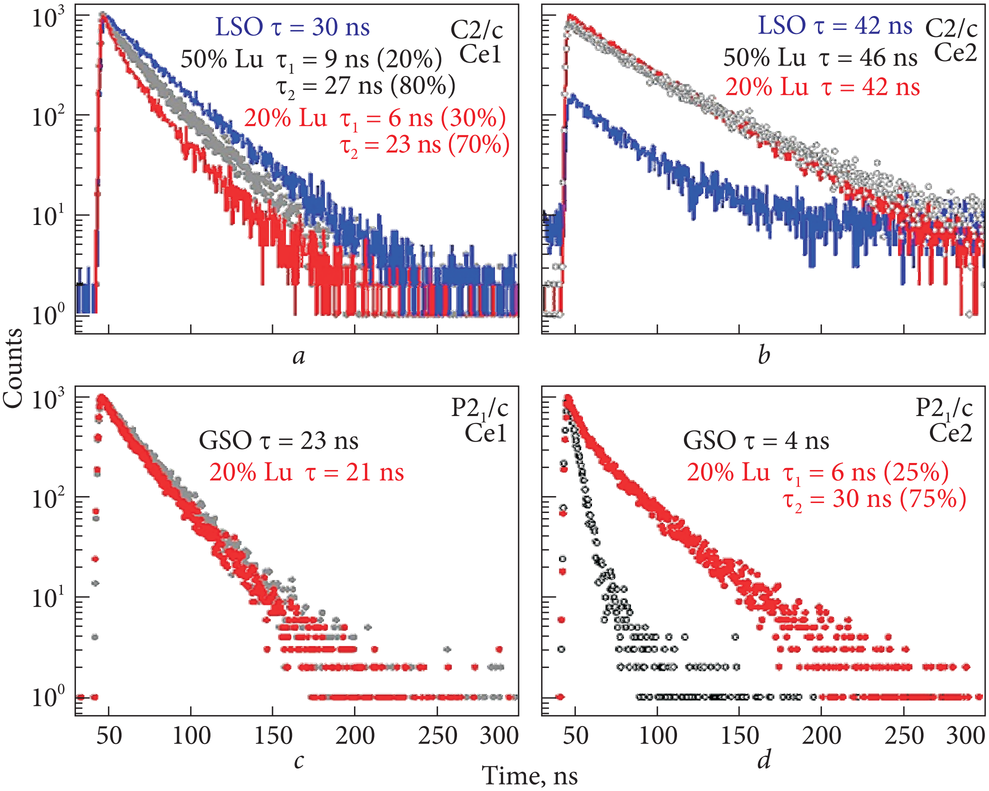

Fig. 4.21. Luminescence decay curves of *Ce*1 (λ_{exc} = 300 nm, λ_{lum} = 395 nm) and *Ce*2 (λ_{exc} = 325 nm, λ_{lum} = 525 nm) centers in GSO:Ce, LSO:Ce and LGSO:Ce crystals with different gadolinium content. Measurements of LGSO:Ce decay kinetics were carried out by Dr. S. Neicheva (ISMA)

Table 4.6). At the same time, a change in the splitting of the 5*d* levels is observed for *Ce*2 (Figs 4.13, 4.14, and Table 4.5). In this case, the decay kinetics also changes: along with the short component (4 ns) due to temperature quenching of Ce2 centers [180], an additional long component (~25 ns) appears, and the contribution of this component increases with increasing lutetium concentration. Taking into account the presence of lutetium in the Ln2 positions, it can be predicted that part of the *Ce*2 centers is located in the «normal» environment of gadolinium ions, and the other part of *Ce*2 has lutetium ions in the immediate environment. As a result: 1) the symmetry of the crystal field changes, which affects the splitting of energy levels, and 2) lattice parameters change, which leads to a change in the energy expenditure for the relaxation of *Ce*2 centers, and, accordingly, to a change in the temperature dependence of the luminescence kinetics. Considering the layered structure of GSO and sufficiently large distances between the layers (Fig. 4.19*a*), it can be stated that the *Ce*2 centers are surrounded by lutetium, and *Ce*1 is mainly surrounded by gadolinium.

In the *C*2/*c* structure, the luminescence of the *Ce*1 and *Ce*2 centers is characterized by monoexponential decay with constants of 30 ns and 42 ns, respectively, which corresponds to literature data [271—272]. In LGSO:Ce with the *C*2/*c* structure, the luminescence decay of *Ce*2 centers is delayed ($\tau = 47$ ns) compared to LSO:Ce, but does not depend on the crystal composition in the range of 30—60% Gd. A fast component appears in the decay kinetics of *Ce*1 centers and its contribution increases with the concentration of gadolinium ions. With the addition of gadolinium, the decay time of the second, slower component decreases from 30 ns (similar to the decay time of *Ce*1 in LSO) to 23 ns (similar to the decay time of *Ce*1 in GSO). The change in the decay kinetics of *Ce*1 centers indicates that the introduced gadolinium is located around *Ce*1, while the environment of *Ce*2 remains unchanged. In addition, the appearance of a fast decay component in mixed compositions indicates the energy transfer from the *Ce*1 center to *Ce*2. This is due to the close location (about 3.47 Å) of the centers in the Ln1 and Ln2 crystallographic positions in the *C*2/*c* structure.

Thus, the *Ce*1 and *Ce*2 luminescent centers are in different environments in LGSO:Ce crystals, which confirms the spatial inhomogeneity in the Lu and Gd distribution in these solid solutions, caused by the selective occupation of non-equivalent positions by atoms in the crystal lattice. The selective occupation of crystallographic positions with Al^{3+} and Ga^{3+} ions was investigated in the $Y_3Al_{5-x}Ga_xO_{12}$ system, which, as noted above, forms a continuous series of solid solutions with the garnet phase in the entire x range from 0 to 5. In YAGG:Ce, Al^{3+} and Ga^{3+} can occupy a tetrahedral position coordinated by four oxygen atoms and an octahedral position coordinated by 6 oxygen atoms [273]. In the stoichiometric structure of garnet, the ratio of the number of tetrahedral positions to octahedral positions is 3 to 2 (Fig. 4.22).

In Chapters 2 and 4, it was shown that the optical properties of $Y_3Al_{5-x}Ga_xO_{12}$:Ce garnets vary nonmonotonically with respect to x. In this case, it is possible to distinguish concentration intervals $x \leq 3$ and $x > 3$ with different types of optical and luminescence properties, which may be caused by Ga^{3+} ions occupying different crystallographic positions in these intervals. At the same time, the features of Al/Ga substitution in octahedral and tetrahedral positions in $Y_3Al_{5-x}Ga_xO_{12}$:Ce crystals were not fully elucidated. However, this issue is very important in the development strategy of multicomponent garnets for both scintillators and phosphors [275] and luminescent converters for LEDs [276]. Due to the relative proximity of their ionic radii [138], aluminum and gallium can occupy both tetrahedral and octahedral positions in the garnet structure. In experiments [107, 277], and as a result of theoretical calculations [278—279], a predominant occupation of tetrahedral positions with Ga^{3+} ions in the garnet structure was observed. However, in other works, it was claimed that octahedral positions are predominantly occupied by gallium [283].

Since the occupation of crystallographic positions affects the energy structure and optical properties of the crystal, this phenomenon required a more

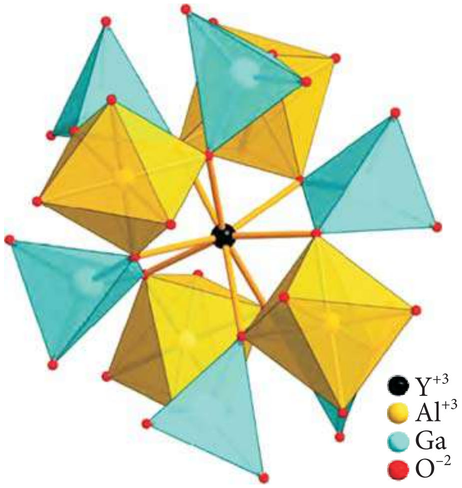

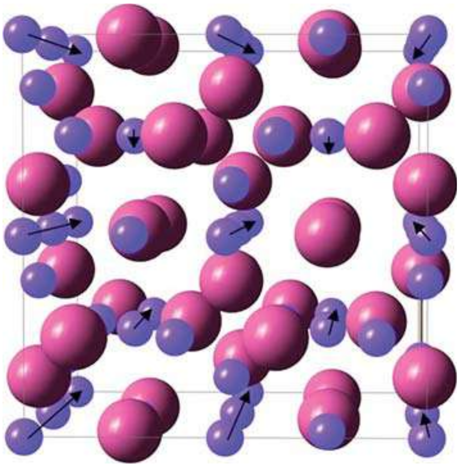

Fig. 4.22. Structure of YAGG:Ce crystals [273]

Fig.4.23. Spatial structure of garnet $RE_3(Al,Ga)_5O_{12}$, constructed using the Balls&Sticks program [270]. Large balls indicate rare earth atoms in dodecahedral positions, small balls indicate Al and Ga atoms in tetrahedral or octahedral positions (oxygen atoms are not shown for simplicity). Arrows indicate columns of atoms in tetrahedral coordination along the [100] crystallographic direction, which in a mixed crystal preferably contain Ga^{3+} [88]

detailed study. In recent years, aluminum occupancy of crystallographic positions in $Y_3Al_5O_{12}$, $Y_3Ga_5O_{12}$ powder samples and mixed $Y_3Al_{5-x}Ga_xO_{12}$ ($x = 0, 1, 2, 3, 4.5$) was investigated by NMR and EXAFS methods [277—284]. Nuclear magnetic resonance (NMR) provides a unique opportunity to quantitatively determine the occupation of crystallographic positions, and is the optimal tool for such studies.

It was determined that (*i*) gallium ions preferentially occupy smaller tetrahedral positions, while (*ii*) Al ions preferentially occupy octahedral positions, despite the smaller ionic radius compared to Ga. Based on the obtained results, the non-monotonic dependence of the optical properties of $Y_3Al_{5-x}Ga_xO_{12}$:Ce on the Ga/Al ratio can be associated with the predominant occupancy of tetrahedral and octahedral positions in the garnet structure by Ga and Al ions, respectively. However, unlike LGSO:Ce crystals with a monoclinic structure, where lanthanide atoms form layers enriched with one of the atoms along a certain crystallographic direction, in the structure of garnet, tetrahedral, and octahedral positions enriched with Al^{3+} or Ga^{3+} are arranged in the form of columns oriented along certain crystallographic directions (Fig. 4.23). In particular, in the gadolinium gallium garnet $Gd_3Ga_5O_{12}$ structure, gallium-enriched columns of atoms are oriented along the [100], [010], [001] directions with interatomic distances of 6.191 Å and along the [111] direction with interatomic distances of 5.362 Å. The aluminum-enriched columns are oriented along the [110], [101], [011] directions with interatomic distances of 3.461 Å.

To date, there is no explanation why Ga^{3+} predominantly occupies tetrahedral sites in $Y_3(Lu_3)Al_{5-x}Ga_xO_{12}$ mixed garnets. Moreover, the exact determination of the Ga/Al distribution in yttrium garnets and, especially, in lutetium ones is an important problem, because the occupation of cation positions strongly affects the energy structure and location of the 5*d* levels of Ce^{3+}, as well as the energy levels of other impurities and lattice defects in the bandgap. The explanation of this phenomenon is also a task for theoretical research [279—284].

4.3.4. Study of microinhomogeneities in dielectric crystals

Inhomogeneity in the form of domains or clusters enriched with one of the substituted atoms can also be related to certain features of the solid solution or the method of crystal obtaining. The size of such clusters can range from several angstroms (the distance between equivalent crystallographic positions in the crystal lattice) to several micrometers. Using confocal luminescence microscopy, we experimentally demonstrated the existence of such microinhomogeneities — domains, 1—3 μm in size, enriched with Lu or Gd, in LGSO:Ce.

In bulk crystals grown by the Czochralski method or similar methods, the concentration of impurities usually increases smoothly from the point of nucleation to the point of separation of the crystal from the melt. The concentration gradient of impurity and matrix atoms in the mixed crystal is convenient to observe on the fibers obtained by the micro-pulling method. The phenomenon of radial segregation of matrix cations in a solid solution is conveniently studied using the example of LGSO:Ce fibers (the procedure for their preparation is described in Section 2.3.1). The *Ce*1 and *Ce*2 excitation spectra (Fig. 4.24) are significantly overlapped, thus their contributions to the total spectrum are difficult to separate. At the same time, excitation at 405 nm used in confocal microscopy made it possible to selectively excite *Ce*2 centers.

Since the cerium luminescence band wavelength and luminescence intensities of the *Ce*1 (CeO_7) and *Ce*2 (CeO_6) centers depend on the Lu/Gd ratio in the host (Fig. 3.2), the use of high spatial resolution microscopy, when both *Ce* centers are excited with a halogen lamp, and the spatial distribution of the concentration of Lu/Gd matrix cations in the crystals can be estimated by selective laser excitation of CeO_6 centers.

The general view of the samples irradiated with electrons is shown in Fig. 4.25. Inclusions in the form of rods or twisted planes oriented along the fiber axis are clearly visible. The thickness of these rods and planes is 1—3 μm, and the length is up to several mm. Bright lines on the periphery of the longitudinal section look like cracks. Nevertheless, there are no visible brightness gradients from the center to the periphery, or along the fiber, unlike, for example, LuAG [143] studied under similar conditions. This indicates a fairly homoge-

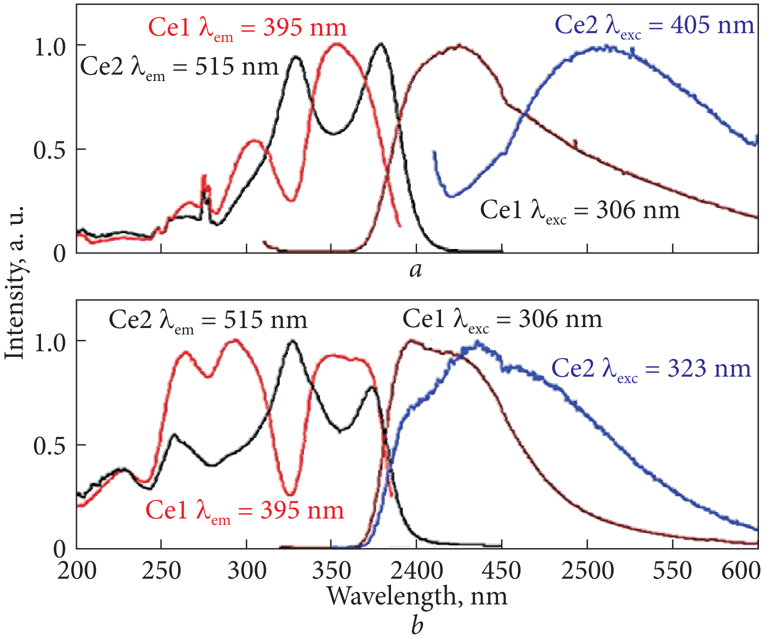

Fig. 4.24. Excitation and luminescence spectra of *Ce*1 and *Ce*2 centers in LSO:Ce (*b*) and $Lu_{0.5}Gd_{1.5}SiO_5$:Ce (*a*) [285]

neous Ce^{3+}distribution in LGSO. Photographs of the samples under excitation with a halogen lamp are shown in Fig. 4.26. Areas *1* and *2* (red rectangles in Fig. 4.25) are the «center» and «periphery» of sample *2*, areas *3* and *4* are the «middle» and «periphery» of sample *3*.

As can be seen, the samples are not similar; however, there is no noticeable change in the luminescence intensity from the center to the periphery in the cross-section (area *2*) and also along the fiber in the longitudinal section (area *3*). The bright lines on the longitudinal section are obviously cracks. Many bands of inclusions along the fiber axis are clearly visible as well in Fig. 4.26. As can be seen (section 1), the central part of the fiber has a diameter of about 1 mm without visible inclusions; along the periphery (area *2*), there are a few cracks with a large number of inclusions, which appear brighter. The brightest color of the inclusions can be explained by both a local increase in the Ce concentration in them and by light scattering. Photos of areas *2—4* clearly demonstrate that these inclusions have the shape of twisted plates oriented along the fiber axis.

The evolution of the luminescence spectra of the samples upon simultaneous excitation of both Ce^{3+} centers is illustrated in Fig. 4.27. The spatial integrated intensity of photoluminescence was greater in the peripheral regions in both samples. The photoluminescence spectra consist of two overlapping bands with maxima around 500 and 570 nm. The peak at 500 nm is associated with CeO_6 emission, and the band at 570 nm is associated with defects around Gd. This

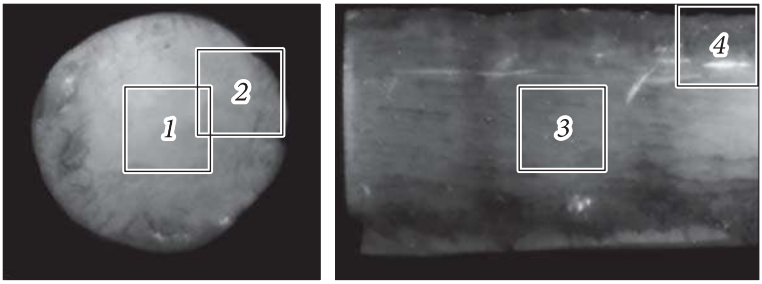

Fig. 4.25. Photo of transverse (left) and longitudinal (right) sections of samples under cathodoluminescence excitation. The studied areas are numbered from 1 to 4 [285]

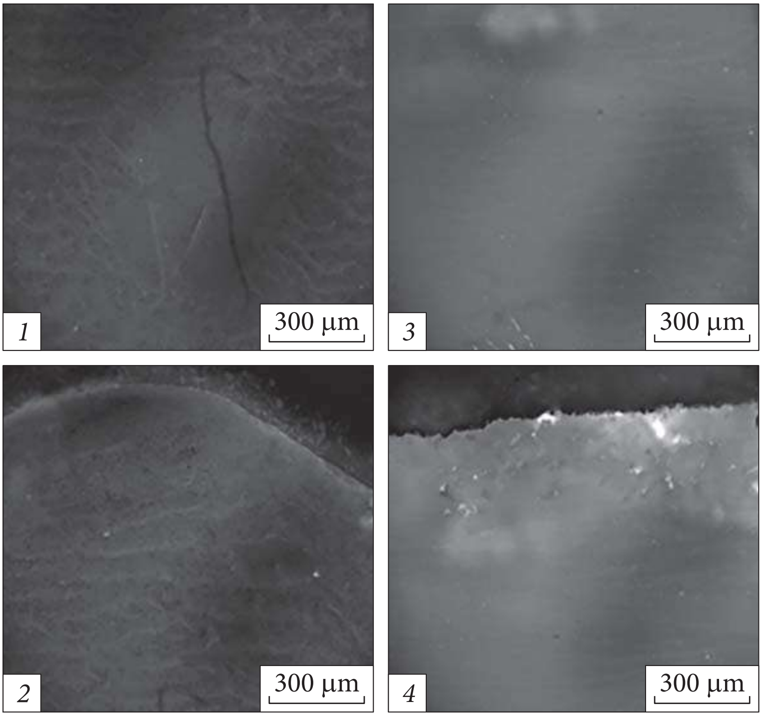

Fig. 4.26. Microscope photo of areas selected in Fig. 4.25 of samples excited by a halogen lamp [285]

confirms that both the total cerium concentration and the Gd concentration increase from the center to the periphery of the fiber. The emission of CeO_7 with a peak at 420 nm is not clearly distinguished due to the cutoff of the luminescence at <420 nm by the filter used in the experiment.

To find out whether the Gd content increases monotonically from the center to the periphery or if its distribution is inhomogeneous, the spatial distribution of photoluminescence in the same samples was studied using high-resolution

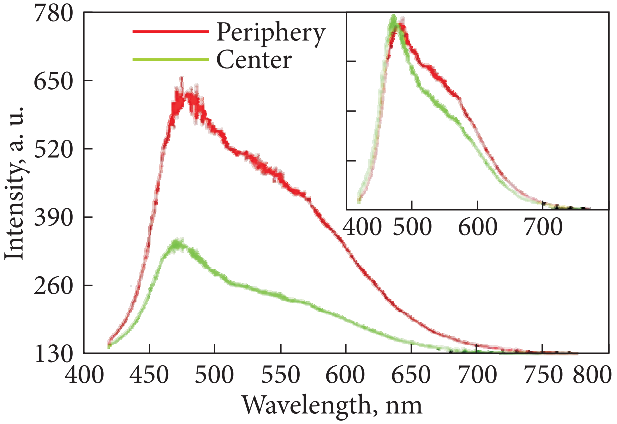

Fig. 4.27. Photoluminescence spectra of different areas of sample *2* (*a*), and spectra normalized to the maximum (*b*) [284]

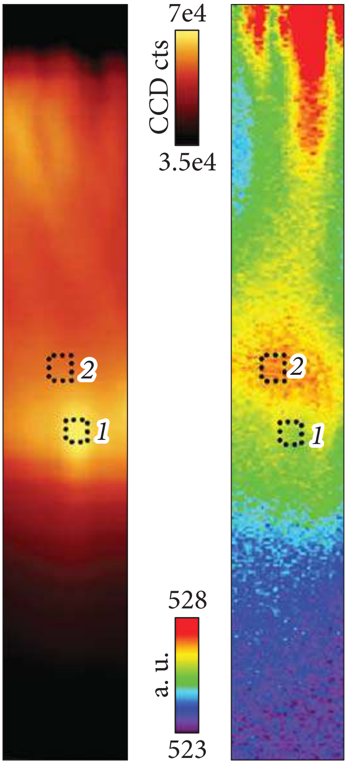

▶

Fig. 4.28. Spatial distribution of intensities of LGSO:Ce photoluminescence peaks and their LGSO:Ce mass centers (left) upon excitation at 405 nm [285]

confocal microscopy (Fig. 4.28). Here you can trace areas with different luminescence parameters. In particular, you can compare the spectra of luminescence, bright and dark areas.

Since inclusions are accumulated on the periphery, Fig. 4.28 presents a small section of area *4*. It can be seen that the changes in the luminescence intensity between areas *1* and *2* in the figure on the left correspond to the change in the center of mass of the spectrum in the figure on the right. The spectra measured in different regions and the differential spectrum (Fig. 4.29) certainly contains a spectral component of 550—600 nm, present only in Gd-containing samples and can be tentatively attributed to Gd-related defects. If visually brighter areas correspond to inclusions (area *1* in Fig. 4.28), it can be concluded that Gd mainly accumulates in inclusions.

The obtained results have shown that the LGSO:Ce fiber consists of a solid central part with a diameter of about 1 mm and a periphery with a large number of inclusions and cracks. The diameter of the central part coincides with the inner diameter of the crucible capillary (1 mm). There is no noticeable increase in total luminescence intensity from the center to the periphery of the fiber. It should be noted that the brighter luminescence observed in the inclusion regions can also be caused by light scattering. The inclusions in the peripheral part have the shape of intersecting lines or layers forming single-crystalline col-

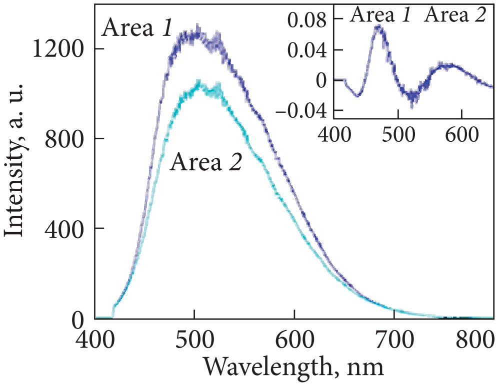

Fig. 4.29. Photoluminescence spectra of areas *1* and *2* highlighted in Fig. 4.28, and the differential spectrum of areas *1* and *2* during selective excitation [285]

umns oriented along the fiber axis. The brightest luminescence, excited by a halogen lamp (Figs 4.25, 4.26) and the appearance of the luminescence band in the range of 550—600 nm upon selective excitation of *Ce*2 (Fig. 4.29) in the regions of inclusions indicate the accumulation of both Gd and Ce in them. Thus, the radial distribution of Gd and Ce outside the central part of the fiber is inhomogeneous, with a higher concentration in the inclusion regions.

Thus, the results obtained confirm the existence of bulk clusters 1—3 μm in size, enriched in Gd ions in LGSO:Ce crystals. The existence of such large clusters makes obvious also the existence of nano-sized clusters, although existing methods are not capable of direct experimental confirmation. The inclusions form scattering centers and lead to a decrease in optical transparency and, as a consequence, a drop in the light yield in the fibers is observed [145]. Since Gd and Ce have significantly larger ionic radii, their concentration leads to loosening of the lattice and the appearance of cracks on the periphery of the fiber. Thus, the large difference in the ionic radii of the competing Lu^{3+}, Gd^{3+}, and Ce^{3+} cations does not allow producing fibers completely free of cracks using the micro-pulling method. Mainly, the cracking is apparently related to Gd, whose concentration is 2 orders of magnitude higher than Ce.

At the same time, single-crystalline columns separated by cracks and inclusions and oriented along the fiber axis can, in fact, be used in scintillation detectors to visualize X-ray or g-measurements with high spatial resolution. There are well-known examples of phase-separated fibers based on CsI [285] and in the Gd_2O_3—Al_2O_3 system [287], as well as in the LiF/CaF_2/$LiBaF_3$ ternary system [288] formed the due to a targeted shift in the composition of the melt from the stoichiometry to the eutectic composition. As a result, the columnar structure of the scintillator with a higher refractive index (for example, $GdAlO_3$ (GAP:Ce)) is located in a matrix with a lower refractive index (Al_2O_3). Light propagates in such scintillator columns due to the complete light reflection. In the case of LGSO:Ce fibers grown by the micro-pulling method, compartments are formed due to the segregation of Gd^{3+} to the periphery of the fiber. Reflection or scattering of light can occur due to the opacity of inclusions and cracks between single-crystalline columns. The size of the columns should depend on the Gd and possibly the Ce content, so it is a matter of optimizing the fiber growth technology.

4.3.5. Phenomenological analysis of the correlation between the ratio of the volumes of substituted ions $(R_A/R_B)^3$ and the light yield in solid solutions

Analysis of the cluster formation mechanisms and their manifestation in the physical properties of mixed crystals (sections 4.3.1.—4.3.4) has shown that, from a practical point of view, the most important issue is the ability to predict clustering phenomena in a solid solution based on the parameters of its components. In other words, how can the affinity of substituted *AA*, *BB,* or *AB* atoms can be controlled in the $A_{1-x}B_xC$ solid solution system?

Factors causing clustering can be divided into chemical and physical ones. As for chemical factors, in each specific case, the presence of chemical compounds between substituted atoms should be taken into account. Among systems of mixed scintillators, clustering is more likely in halide scintillators with substitution for the anions I^-/Br^-, I^-/Cl^-, Br^-/Cl^-, which are form diatomic molecules I_2, Br_2, Cl_2 in a free state. Although such molecules exist only in the gaseous state, it is possible to foresee a certain affinity between them in the composition of solid dielectrics and, therefore, the tendency to form *AA* or *BB* clusters. If there are chemical compounds between *A* and *B*, such as $2Nb_2O_5 \cdot Ta_2O_5$ in the binary system, Nb_2O_5—Ta_2O_5, the affinity of the *AB* type can be expected.

In general, to assess the affinity of the *AB* type, it is necessary to take into account for the covalent chemical bond energy between these two elements (relative to the hypothetical covalent bond between them), which is proportional to the difference in their electronegativities according to Pauling's empirical formula (c_A and c_B — electronegativities of elements *A* and *B*):

$$0.208 \cdot \Delta(A\text{-}B)1/2 = |\chi_A - \chi_B|. \qquad (4.10)$$

The Nb-Ta affinity estimated in $Gd(Nb_xTa_{1-x})O_4$ is low due to similar electronegativities of 1.5 in Ta and 1.6 in Nb according to the Pauling scale [289]. The D(Ta—Nb) value is about 30 kJ/mol. At an average covalent chemical bond energy of several hundred kJ/mol, the value of D(Ta—Nb) can be neglected. Among the solid solutions we are considering, Zn and Mg ($Zn_{1-x}MgWO_4$ system) have the largest electronegativity difference of 0.3 units. Consequently, in most solid solution systems, there are no clear chemical factors causing *AB* affinity.

The size factor is also considered as an important reason for clustering. The selective substitution of atoms in the lattice is caused predominantly by the ionic radii of these atoms; however, in the case of large clusters of the same type atoms, when the sizes of the substituted atoms are close, R_A » R_B, the deformation of the crystal lattice is insignificant. In systems with too large differences in ionic radii (according to the Goldschmidt criterion, at $R_A/R_B > 1.15$), there is a danger of the formation of a block structure and the destruction of the single crystal, or at least the formation of inclusions of another phase, or cracks due

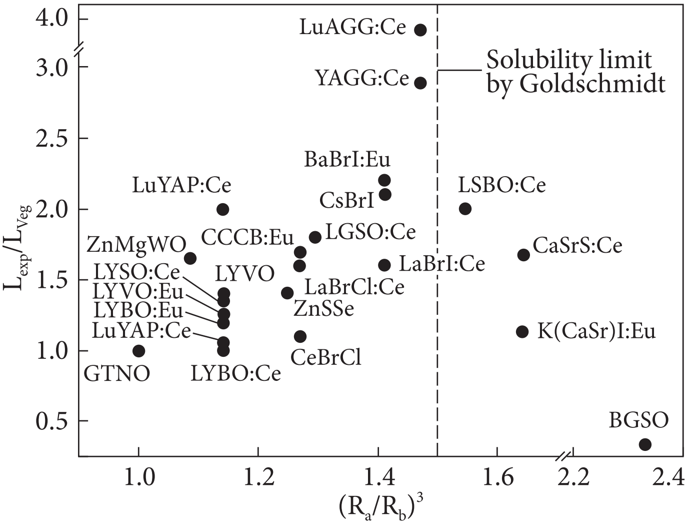

Fig. 4.30. Correlation between the maximum deviation of light yield from Vegard's law at room temperature and the ratio of the volumes occupied by substituted atoms for the following compounds: $GdTa_{1-x}Nb_xO_4$ (GTNO), $Lu_{1-x}Y_xBO_3$:Ce (LYBO:Ce), $Lu_{1-x}Y_xBO_3$:Eu^{3+} (LYBO:Eu), $Lu_{1-x}Y_xVO_4$ (LYVO), $Lu_{1-x}Y_xVO_4$:Eu^{3+} (LYVO:Eu), $Lu_{1-x}Y_xSiO_5$:Ce × (LYSO:Ce), $Zn_{1-x}Mg_xWO_4$ (ZnMgWO), $CeBr_{3-x}Cl_x$ (CeBrCl), $LaBr_{3-x}Cl_x$:Ce (LaBrCl:Ce), $LaBr_{3-x}I_x$:Ce (LaBrI:Ce), $Lu_{2-2x}Gd_{2x}SiO_5$:Ce (LGSO:Ce), $CsBr_{1-x}I_x$ (CsBrI), $BaBr_{2-x}I_x$:Eu^{2+} (BaBrI:Eu), $Lu_{1-x}Y_xAlO_3$:Ce (LuYAP:Ce), $Y_3(Al_{1-x}Ga_x)_5O_{12}$:Ce (YAGG:Ce), $Lu_3(Al_{1-x}Ga_x)_5O_{12}$:Ce (LuAGG:Ce), $Lu_{1-x}Sc_xBO_3$:Ce (LSBO:Ce), $Ca_{1-x}Sr_xS$:Ce (CaSrS:Ce), $Bi_4(Ge_{1-x}Si_x)_3O_{12}$ (BGSO), $K(Ca_{1-x}Sr_x)I_3$:Eu^{2+} (KCaSrI:Eu), $CsCaCl_{3-x}Br_x$:Eu^{2+} (CCCB:Eu) [88]

to mechanical stresses, which negatively affects the optical transparency and scintillation parameters. This estimate is very approximate and in each specific case, the isomorphic capacity of each specific type of crystal lattice should be taken into account. To maintain the lattice integrity and minimize mechanical stresses in it at $R_A >> R_B$, the size of these clusters should be limited, and layers or clusters enriched with the other atoms should form around them. Therefore, the physical factor causing the affinity of *AA* and *BB* atoms (see section 1.3) should be the ratio of their sizes R_A/R_B.

To check the correlation between the ratio of the ionic radii of substituted atoms and the concentration dependence of the light yield in crystals of solid solutions, a phenomenological dependence of the light yield deviation from the additive values $(L_{exp}/L_{Veg})_{max}$ on the ratio of the volumes occupied by the substituted ions $(R_A/R_B)^3$ was built (Fig. 4.30) by analogy with the procedure used in subsection 4.2, Figs. 4.16, 4.17. There is an obvious tendency to increase in the light yield in solid solution with an increasing ratio in the ionic radii at $(R_A/R_B)^3$ from 1 to 1.5 (corresponds to the ratio of ionic radii from 1 to 1.15). When $(R_A/R_B)^3$ increases above 1.5, the parameter $(L_{exp}/L_{Veg})_{max}$ tends to de-

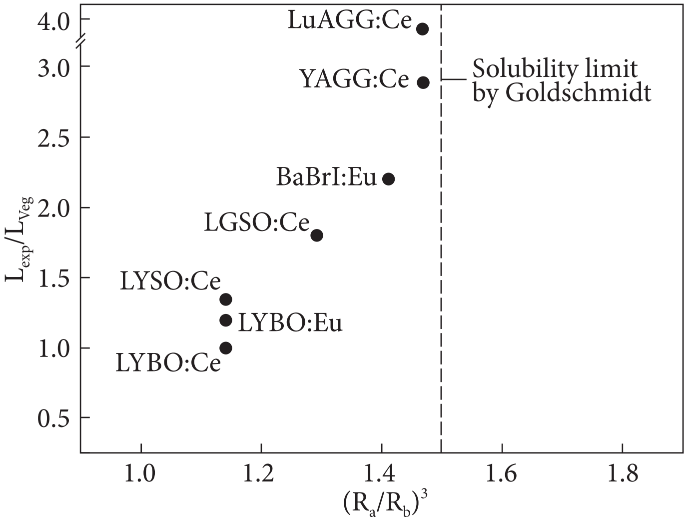

Fig. 4.31. Correlation between the maximum deviation of the light yield at room temperature from Vegard's law depending on the volume ratio occupied by substituted atoms for the following compounds with selective substitution of atoms in the crystal lattice: $Lu_{1-x}Y_xBO_3$:Ce (LYBO:Ce), $Lu_{1-x}Y_xBO_3:Eu^{3+}$ (LYBO:Eu), $Lu_{1-x}Y_xSiO_5$:Ce (LYSO:Ce), $Lu_{2-2x}Gd_{2x}SiO_5$:Ce (LGSO:Ce), $BaBr_{2-x}I_x:Eu^{2+}$ (BaBrI:Eu), $Y_3(Al_{1-x}Ga_x)_5O_{12}$:Ce (YAGG:Ce), $Lu_3(Al_{1-x}Ga_x)_5O_{12}$:Ce (LuAGG:Ce), $Lu_{1-x}Sc_xBO_3$:Ce [88]

crease. The maximum on this dependence corresponds to the solubility limit at $R_A/R_B = 1.15$ in accordance with Goldschmidt's rule, which indicates the possibility of isomorphic substitution of atoms with a difference in ionic radii of up to 15% in the crystal lattice. This empirical relationship was established using a perovskite-type lattice as an example, but can be a guide for other types of crystal structure. In the case of a large difference between the ionic radii, according to our observations, the systems are very inhomogeneous due to the presence of a block structure and inclusions, which negatively affects the transparency and scintillation parameters of the crystals. However, in powdered samples, this may not have a negative effect on the recorded light yield. It should be noted that the demonstrated correlation between $(L_{exp}/L_{Veg})_{max}$ and $(R_A/R_B)^3$ is valid regardless of the type of substitution (cationic or anionic), the chemical nature of the solid solution (oxides, halides), the type of luminescence mechanism (activator or intrinsic) and the growing method (Czochralski, Bridgman, or other).

Noteworthy there are 2 obvious deviations from this trend — crystals of $ZnMgWO_4$ and LuYAP:Ce and systems with a garnet structure — YAGG:Ce and LuAGG:Ce. In the first case, the difference in the electronegativity between Zn and Mg (0.3), which is the largest among the considered atomic substitutions, may play a role. A large difference in electronegativity (>0.6 according to the Goldschmidt criteria) also leads to poor solubility in these systems, despite a small difference in ionic radii. For the LuYAP:Ce system, there are different data on the concentration dependence of the light yield which does not agree with each other, so the diagram involves both parts. As for garnet systems, the very high positive deviations of the light yield from additivity are probably also associated with a combination of spatial inhomogeneity of the distribution, with a strong spatial modulation of ΔE_g and a shift of the energy levels of the activator and traps in the bandgap (see subsection 4.2).

Thus, the difference in the ionic radii of substituted atoms in solid solutions is a key factor that causes the formation of one-dimensional or two-dimensional inhomogeneities in the case of selective substitution of atoms in non-equivalent crystallographic positions, and/or the formation of bulk clusters enriched in one of the components in crystals. One can try to separate the contribution from one- and two-dimensional inhomogeneities, as well as from bulk ones, by considering separately the systems where substituted ions occupy two crystallographic positions. For 8 mixed crystals, the correlation between the improvement of light yield and $(R_A/R_B)^3$ is even more pronounced (Fig. 4.31).

4.4. Summarizing the data on light yield in crystals of solid solutions

A phenomenological analysis of the main factors influencing the concentration dependence of the light yield in solid solution crystals was used to analyze the systems of mixed scintillators. In this chapter, for the first time, the influence of these factors is systematized, and criteria are developed by which the highest light yield can be achieved. Four parameters of mixed systems are considered:

1. The number of charge carrier traps in it, in other words, the non-stoichiometry of the crystal. In oxide systems, as a rule, oxygen vacancies are the main type of defects. They are formed when a crystal is grown and annealed in a certain atmosphere. A convenient example is oxyorthosilicates, where the presence of deep traps formed on oxygen vacancies reduces light yield in favor of slow luminescence components (afterglow). The concentration of deep traps on oxygen vacancies can be estimated from the high-temperature TSL peaks. We have shown that in the LGSO:Ce system, the number of oxygen vacancies depends on the oxygen vapor pressure above the melt, which, in turn, is a function of the crystallization temperature. Therefore, in the general case, **the greater the difference in the crystallization temperatures of the components**, the number of defects in the mixed crystal changes more sharply. However, no obvious correlation was found between melting temperatures and light yield. Probably, in each specific case, it is necessary to take into account the vapor pressure of its components above the melt.

2. Modification of the energy structure in a mixed crystal is more significant when the bandgap difference ΔE_g is larger. This effect was clearly demon-

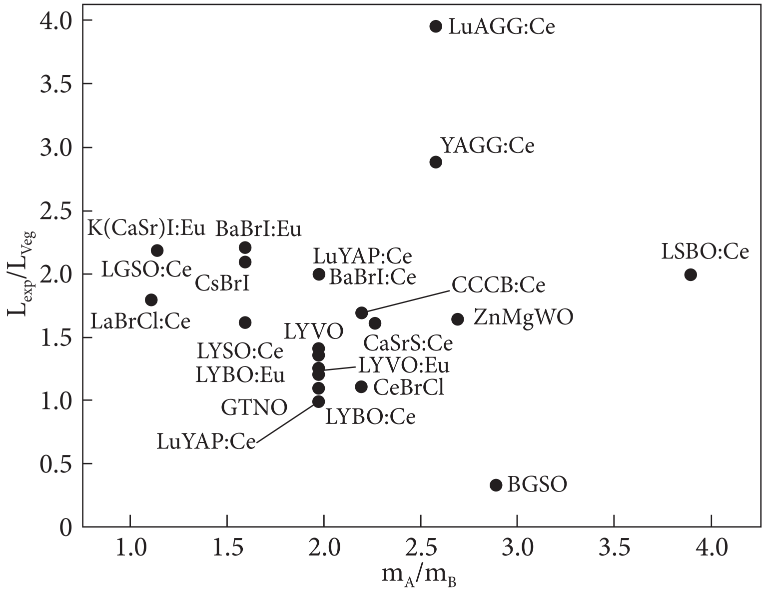

Fig. 4.32. Correlation between the maximum deviation of light yield from Vegard's law at room temperature and the difference in atomic weights of substituted atoms for the following compounds: $GdTa_{1-x}Nb_xO_4$ (GTNO), $Lu_{1-x}Y_xBO_3$:Ce (LYBO:Ce), $Lu_{1-x}Y_xBO_3$:Eu^{3+} (LYBO:Eu), $Lu_{1-x}Y_xVO_3$:Eu (LYVO:Eu), $Lu_{1-x}Y_xVO_4$ (LYVO), $Lu_{1-x}Y_xSiO_5$:Ce × (LYSO:Ce), $Zn_{1-x}Mg_xWO_4$ (ZnMgWO), $CeBr_{3-x}Cl_x$ (CeBrCl), $LaBr_{3-x}Cl_x$:Ce (LaBrCl:Ce), $LaBr_{3-x}I_x$:Ce (LaBrI:Ce), $Lu_{2-2x}Gd_{2x}SiO_5$:Ce (LGSO:Ce), $CsBr_{1-x}I_x$ (CsBrI), $BaBr_{2-x}I_x$:Eu^{2+} (BaBrI:Eu), $Lu_{1-x}Y_xAlO_3$:Ce (LuYAP:Ce), $Y_3(Al_{1-x}Ga_x)_5O_{12}$:Ce (YAGG:Ce), $Lu_3(Al_{1-x}Ga_x)_5O_{12}$:Ce (LuAGG:Ce), $Lu_{1-x}Sc_xBO_3$:Ce, $Ca_{1-x}Sr_xS$:Ce (CaSrS:Ce), $Bi_4(Ge_{1-x}Si_x)_3 \times O_{12}$ (BGSO), $K(Ca_{1-x}Sr_x)I_3$:Eu^{2+}, $CsCaCl_{3-x}Br_x$:Eu (CCCB:Eu) [88]

strated in rare-earth garnets, where the bandgaps vary by 1—1.6 eV in several solid solutions. Accordingly, the energy levels of the activator and charge carrier traps in the bandgap are significantly shifted, which affects the conditions of carrier transport to the luminescent center. When clusters are formed in mixed crystals enriched in one of the components, a large ΔE_g causes strong modulations of the conduction and valence band edges, which limit the thermalized diffusion of charge carriers. Therefore, an important parameter determining the concentration dependence of the light yield in mixed crystals is **the difference in the bandgaps, ΔE_g of the solid solution components.**

3. The electron-phonon interaction intensifies when new bands with energies different from the existing ones appear in the phonon spectrum. As was shown in Chapter 1, the effect of reducing the thermalization length should be manifested with a strong difference in the energies of optical phonons in the components of the mixed crystal. These energies should depend both on the distance between atoms, i.e. the ratio of the ionic radii of substituted atoms

R_A/R_B, and on the ratio of their atomic weights, m_A/m_B. That is, **the ratio of atomic weights and ionic radii of substituted atoms in a solid solution are important**.

4. The inhomogeneity in the crystal will also depend on **the ratio of the ionic radii of substituted atoms**, and, to be more precise, on their volume. In solid solutions, one- and two-dimensional inhomogeneities are formed due to the selective occupation of crystallographic positions by atoms of different sizes, as well as volumetric clusters (domains) enriched with one of the substituted atoms. These inhomogeneities cause spatial modulations of the energy structure of the crystals, which affect the efficiency of carrier transport to the luminescent center.

After analyzing the concentration dependence of the light yield depending on the melting temperatures of the components (Table 4.3), ΔE_g (Fig. 4.17), as well as $(R_A/R_B)^3$ (Figs. 4.30, 4.31) in 21 mixed crystals, the correlation between $(L_{exp}/L_{Veg})_{max}$ and m_A/m_B were also studied. However, despite the large difference in atomic masses, reaching 4 times in some systems, the diagram Fig. 4.32 shows no obvious correlation between these two parameters. Perhaps the contribution of the electron-phonon interaction is easier to estimate by the correlation between the light yield and the energy difference of the optical phonons associated with substituted atoms.

Thus, based on the phenomenological analysis of the correlation between the concentration dependence of light yield in mixed systems and the physical parameters of these systems, it is possible to formulate three main characteristics of the systems where a significant improvement in light yield can be expected:

1. The difference in the ionic radii of substituted atoms should be 7—15% (a particularly promising interval is 10—15%). This difference in ionic radii ensures the formation of spatial inhomogeneities in the distribution of substituted atoms; the sizes of these inhomogeneities reach the radius of the Onsager sphere (in the systems under consideration, it is 5—10 nm), which increases the contribution of geminate recombination of charge carriers and scintillation efficiency.

2. A large difference in the bandgaps ΔE_g of the solid solution components. In general, by reducing E_g, it is possible to increase the number of electron-hole pairs formed in the scintillator per unit of absorbed energy (see Eq. 1.1). However, in all considered mixed systems, $\Delta E_g/E_g$ does not exceed 20%, so it cannot cause changes in light yield up to 4 times as observed in the systems studied. The mechanism of ΔE_g influence on the concentration dependence of the light yield in a solid solution is obviously different. Firstly, under conditions of large ΔE_g, it is possible to control over a wide range the positions of the energy levels of the activator and traps in the crystal bandgap by substituting matrix atoms. Secondly, according to the hypothesis about the variation of ΔE_g on spatial inhomogeneities in the crystal, the amplitude of the crystal potential jumps on the boundaries of these inhomogeneities will be higher. This reduces the distance between geminate electrons and holes and reduces the probability of stochastic

recombination in the scintillator. The energy structure of a solid solution can be effectively influenced by the presence of a strong crystal field; its strength can be estimated by the splitting of the activator levels. For example, according to [261, 262] the splitting energy of the 5*d* Ce^{3+} levels is 27000 cm^{-1} in $Y_3Al_5O_{12}$:Ce, 20700 cm^{-1} in Lu_2SiO_5:Ce, > 18500 cm^{-1} in $LuBO_3$:Ce (vaterite structure), 12700 cm^{-1} in $YAlO_3$:Ce.

3. Perhaps a large difference in electronegativity is a positive sign; however, the available data do not allow us to unambiguously assess the influence of this factor. An example of such a system is $Zn_{1-x}Mg_xWO_4$, in which the electronegativity difference between Zn and Mg is 0.3, and the system has poor solubility in accordance with the Goldschmidt rules despite a small difference in ionic radii of 2.8%.

Based on these findings, the most promising ion pairs can be selected for possible isovalent substitutions (some of them are already used in scintillators) (Table 4.7). According to the R_A/R_B ratio, pairs of cations or anions can be divided into 3 groups. The first column contains pairs of atoms with a difference of ionic radii up to 5%. According to the diagram in Fig. 4.30, the light yield in them slightly deviates from Vegard's law.

The middle column presents pairs where R_A/R_B is in the optimal range of 5—15%. In these systems, the $(L_{exp}/L_{Veg})_{max}$ parameter reaches 4. Substitution of some of these atomic pairs is already used in the engineering of efficient scintillation crystals (Br^-/Cl^-, Br^-/I^-, Ba^{2+}/Sr^{2+}, Al^{3+}/Ga^{3+}). At the same time, the sys-

Table 4.7. **The difference of ionic radii in some atomic pairs according to [112]**

0—5%		5—15%		>15%	
Ion pair	R_A/R_B,%	Ion pair	R_A/R_B,%	Ion pair	R_A/R_B,%
Ta^{5+}/Nb^{5+}	0	Cd^{2+}/Hg^{2+}	7.4	Lu^{3+}/Sc^{3+}	15.6
Hf^{4+}/Zr^{4+}	1.4	S^{2-}/Se^{2-}	7.6	Ca^{2+}/Sr^{2+}	18.0
Mo^{6+}/W^{6+}	1.6	Br^-/Cl^-	8.3	V^{5+}/Nb^{5+}	18.5
Zn^{2+}/Mg^{2+}	2.8	Lu^{3+}/Gd^{3+}	9.0	Ti^{4+}/Zr^{4+}	19.0
Gd^{3+}/Y^{3+}	4.2	Rb^+/Cs^+	9.9	La^{3+}/Lu^{3+}	19.8
Y^{3+}/Lu^{3+}	4.5	La^{3+}/Gd^{3+}	10.0	Zn^{2+}/Cd^{2+}	28.3
		K^+/Rb^+	11.0	Ga^{3+}/In^{3+}	29.0
		La^{3+}/Y^{3+}	11.5	Sn^{4+}/Ge^{4+}	30.1
		Se^{2-}/Te^{2-}	11.6	Si^{4+}/Ge^{4+}	32.5
		Br^-/I^-	12.2	F^-/Cl^-	36.1
		Al^{3+}/Ga^{3+}	13.7		
		Ba^{2+}/Sr^{2+}	14.4		

tems with S^{2-}/Se^{2-}, Lu^{3+}/Gd^{3+}, La^{3+}/Y^{3+}, Rb^{+}/Cs^{+}, K^{+}/Rb^{+} substitutions are insufficiently studied. For such differences in ionic radii, it is desirable to have crystal structures with a large isomorphic capacity, such as rare-earth garnets. For example, crystals of garnets with Al-Ga substitution (the difference in the radii of the substituted cations is 13.7%) up to 2—3 inches in diameter are successfully grown nowadays [289]. But with such a difference in the radii of substituted atoms, the crystals are prone to cracking (here we should mention LGSO:Ce [167] and mixed crystals of alkaline earth halides [82]).

Finally, the right column contains atom pairs with poor solubility with a difference in ionic radii of substituted atoms greater than 15%, according to Goldschmidt's rules. In most cases, these mixed crystals are impossible or very difficult to produce with high quality, although a known exception is the BGSO system, for which large-sized crystals have been successfully obtained. However, such systems may be suitable for the synthesis of polycrystalline ceramics or powdered samples.

CHAPTER 5

APPLICATION OF DEVELOPED SCINTILLATORS

5.1. LGSO:Ce and LYSO:Ce crystals for high energy physics experiments

Optimizing the properties of LGSO:Ce and LYSO:Ce crystals is associated with increasing requirements for light yield and speed of scintillators necessary for the implementation of projects in the search for muon-to-electron conversion processes ($\mu 2e$ experiments at *Fermilab* (USA) [53] and COMET in KEK (Japan) [54]. To test the suitability of scintillators in future high-energy physics experiments (ILC, LHCb, etc.), LGSO:Ce and LYSO:Ce crystals were selected, which are one of the most promising scintillators with high density and effective atomic number, chemically stable and non-hygroscopic, having rapid luminescence decay, high temperature stability, and radiation resistance. These materials have the potential to meet the requirements of the $\mu 2e$ project, namely an energy resolution of 2% at 105 MeV, a decay time of <100 ns, a spatial resolution of $s_{r,z} = 1$ cm, and a time resolution of 1 ns [53].

To achieve this goal, large-sized crystals and scintillation elements were manufactured at the ISMA NAS of Ukraine. It was necessary to optimize the cationic composition of the crystals to obtain optimal scintillation parameters and minimal cracking of the crystals, and to test the resulting crystals. Crystals of the following composition were selected: LYSO:Ce (10% Y relative to Lu), LGSO:Ce (10% Gd relative to Lu). The activator concentration was 0.2 at.% relative to lanthanides. Large-sized crystals of LGSO:Ce and LYSO:Ce with a diameter of up to 48 mm and a cylindrical part length of up to 150 mm were grown using the Czochralski method. Samples of $10 \times 10 \times 1$ mm^3 for optical and $10 \times 10 \times 2$ mm^3 for scintillation measurements were made from the crystals. Large-sized samples for testing were also manufactured (Fig. 5.1).

Fig. 5.2 demonstrates the transmission spectra of the grown crystals in comparison with commercially available crystals LSO:Ce (Siemens, USA) and LYSO:Ce (CPI, USA). In the range of 200—350 nm, bands corresponding to $4f$-$5d$ transitions in Ce^{3+} ions were observed in all studied crystals. The edge of the transparency band for all crystals is about 375 nm; for LSO:Ce and LGSO:Ce, the edge is shifted to the

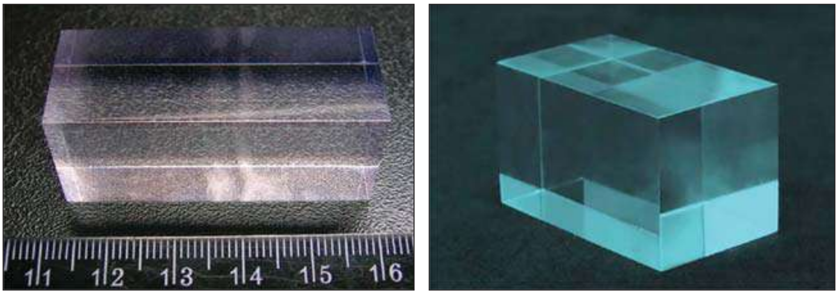

Fig. 5.1. Scintillation elements LGSO:Ce 20 × 20 × 50 mm (left) and LYSO:Ce 30 × 30 × × 50 mm (right) manufactured by ISMA NAS of Ukraine to test the suitability of the crystals for muon-electron conversion experiments in high-energy physics [291]

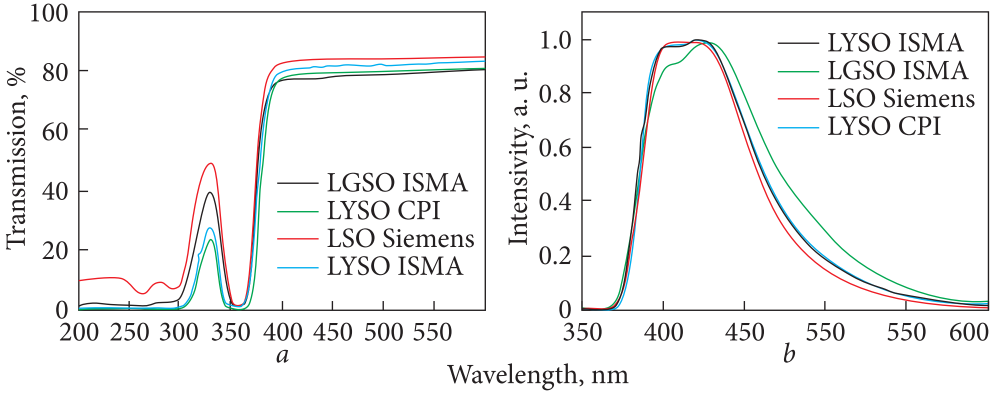

Fig. 5.2. Transmission spectra of samples with a thickness of 1 mm (*a*) and luminescence spectra under X-ray excitation (*b*) [291]

short-wavelength region by ~5 nm relative to LYSO:Ce. For LYSO:Ce crystals grown in ISMA and CPI, the wavelength of the transparency edge is the same. In the optical range, the LGSO:Ce transmittance is 76—82%, which is slightly less than in other crystals. The reason for this is the presence of light scattering centers in LGSO:Ce. Transmittance of LYSO:Ce crystal grown in ISMA is by 1.5—2.5% better than in its counterpart made in CPI.

The luminescence spectra of crystals under X-ray excitation (Fig. 5.2) consists of two maxima at 405 and 422 nm, which correspond to the $5d$—$4f_{1,2}$ radiative transitions in Ce^{3+} ions. The LSO:Ce and LYSO:Ce spectra are very similar; the only difference is a more intense long-wavelength shoulder in the LYSO:Ce spectra due to a more intense reabsorption of the short-wavelength edge of the LYSO:Ce spectrum and/or redistribution of activator ions between positions in the crystal lattice. For LGSO:Ce, the peak intensity is even more redistributed in favor of the 422 nm band.

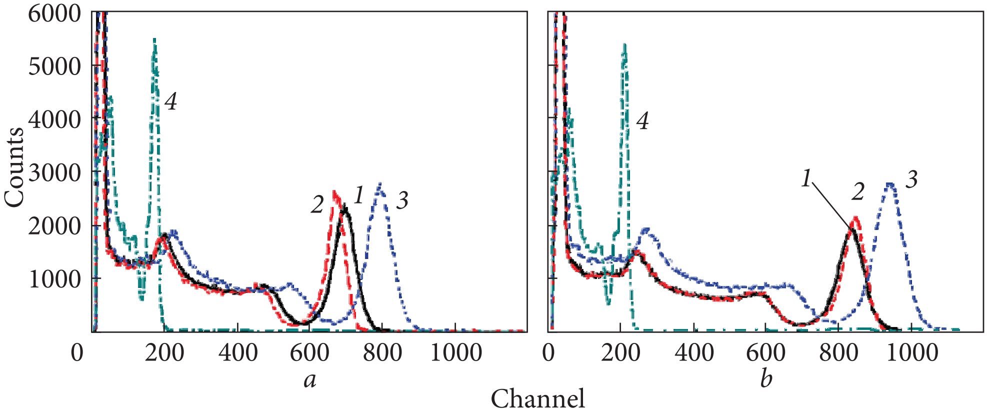

Fig. 5.3. Amplitude spectra of 10 × 10 × 2 mm samples under 662 keV excitation without optical contact (*a*) and with optical contact (*b*) [290]: *1* — LYSO; *2* — LGSO; *3* — LSO; *4* — BGO [291]

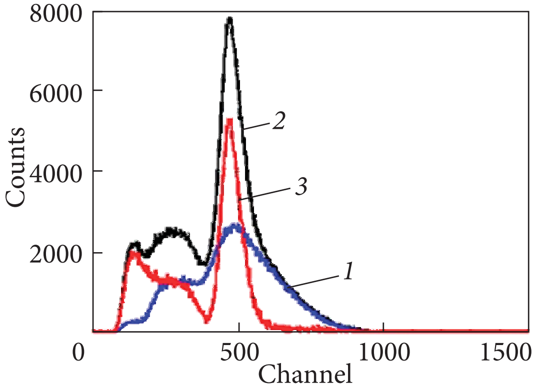

Fig. 5.4. Amplitude spectra of LGSO:Ce (explanation in the text) [291]

Fig. 5.5. Dependences of scintillation yield and energy separation *s/E* on g-excitation energy [291]

▼

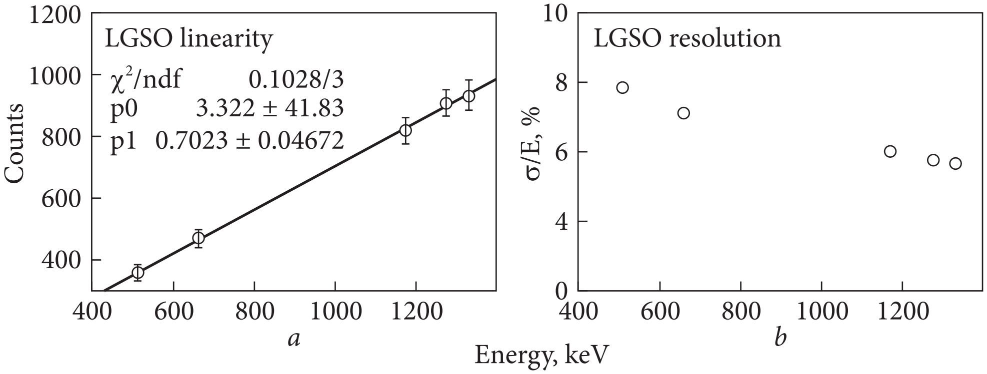

The scintillation yield and energy resolution were determined by excitation of a ^{137}Cs source by γ-radiation with an energy of 662 KeV on an installation based on an R1307 photovoltaic cell, with an integration time of 2 μs. To deter-

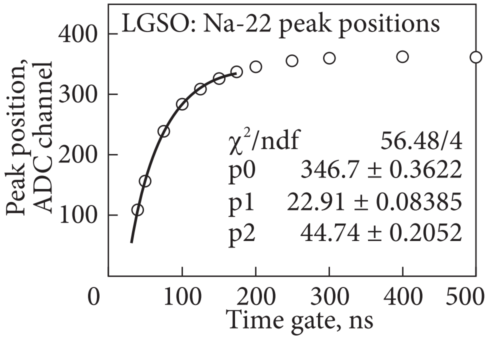

Fig. 5.6. The position of the Na-22 peak depends on the value of the time gate [291]

mine the light yield using the Monte Carlo method, we simulated the light collection coefficients t for the cases without and with an optical contact, as well as the coefficients for matching the luminescence spectrum of the crystal and the sensitivity range of the photoelectric converters (PEC) (Table 5.1). The amplitude spectra are shown in Fig. 5.3. The results for the measurements without and with an optical contact are qualitatively the same. The LSO:Ce amplitude peak is located ~100 channels to the right of the LYSO:Ce and LGSO:Ce peaks. In absolute terms, the LSO:Ce light yield is 2000—3000 photons/MeV higher (Table 5.1). The LYSO:Ce and LGSO:Ce peaks are almost identical, but the LGSO:Ce light yield in measurements with optical contact is 1300 photons/MeV higher due to the worse agreement of the luminescence band with the sensitivity range of photoelectric multiplier (PEM): $C_{PEM} = 0.903$ versus 0.872 (see Table 5.1). Thus, when using other photodetectors, for example, silicon PEMs, the technical light yield of LGSO:Ce samples should be higher than that of LYSO:Ce and, possibly, LSO:Ce. The best energy resolution at 662 keV is obtained in LGSO:Ce and is 8.4% with optical contact and 7.9% without optical contact. In LYSO:Ce and LSO:Ce, the resolution is noticeably worse and ranges from 9.6 to 10.3%.

Large-sized LGSO:Ce crystals with dimensions of 20 × 20 × 50 mm^3 were tested in a wide excitation energy range (see Fig. 5.1). The contribution of the crystal's intrinsic radioactivity to the amplitude spectrum was very significant due to the ^{176}Lu isotope (Fig. 5.4). This contribution (curve *1*) was 5650 counts/s or 53.9% of the resulting peak of 10480 counts/s (curve *2*).

The energy resolution *s/E* determined from curve 3 (Fig. 5.4) was 6.38%, as the difference between the resulting spectrum and the spectrum of intrinsic radioactivity. In terms of FWHM, denoted by *R* according to Equation 5.1, we obtain an energy resolution of 15.07%. LGSO:Ce showed good linearity of

Table 5.1. **Parameters for evaluating the absolute light yield (OC is optical contact)**

Scintillator	Number	l_{max}, nm	Without OC	With OC	C_{PEM}
BGO	7	490	0.476	0.700	0.592
LSO	«Siemens»	420	0.476	0.700	0.920
LYSO	4—12	420	0.476	0.700	0.903
LGSO	7—12	430	0.476	0.700	0.872

scintillation response versus excitation energy in the range of 400—1400 keV Fig. 5.5). The energy resolution *s/E* improves with increasing energy and reaches 4.6% at ~1300 keV

$$R = \Delta E/E = 2.36 \cdot \sigma/E. \quad (5.1)$$

The decay curves of LGSO:Ce were measured upon excitation by ^{22}Na in time gates from 40 to 500 ns (Fig. 5.6). The decay time of the fast component was 44.7 ns, which is consistent with the decay time of Ce^{3+}-activated oxyorthosilicates.

Thus, we produced large-sized single crystals of LGSO:Ce with a diameter of up to 45, and a length of up to 150 mm without cracks. Their perspective for use in high-energy physics experiments to search for the conversion of muons into electrons is shown.

5.2. GAGG:Ce crystals for geological exploration

Recently, the efficiency of mineral exploration has decreased since the search for new deposits requires deeper drilling throughout hard rock. Increasing the efficiency of searching for such deep deposits requires advanced drilling technologies, in particular, a «predictive drilling» technology platform that systematically maps mineral deposits in the surrounding crust while drilling. The technology platform for predictive drilling must include low-cost hard rock drilling methods. This can be provided by continuous drilling technology. The key advantages of continuous drilling are a high rate of penetration through hard rock, high reliability, and continuous lifting of spent rock to the surface [292].

Scintillators for detecting γ-radiation used in mineral exploration probes must meet the following requirements:

a) the high energy resolution of the photopeak as well as the high effective atomic number and density of the material are very important in distinguishing it from the Compton scattering spectrum; a high signal-to-noise ratio (low afterglow) is also required;

b) low intrinsic radioactivity to distinguish background radioactivity of the rock: the g-background should not exceed a maximum of 1000 counts/s, and optimally should not exceed 10—100 counts/s. Fast scintillation decay is less important compared to background characteristics;

c) the spectral range of luminescence is an important, but not a determining factor;

d) good temperature stability of scintillation characteristics. Typical temperatures in a narrow well (diameter <75 mm) are 25—45 °C due to the rapid circulation of the drilling fluid and rarely exceeds 70 °C (in addition, the depth of such wells does not exceed 2 km);

e) the simplicity of connecting the scintillator to the photodetector is important. The use of a shifter or concentrator of light is allowed. The green-red

Table 5.2. **Promising scintillators for predictive drilling (crystals selected for experiments are in bold)**

Crystal	Density, g/cm^3	Light yield, photons/MeV	Energy resolution at 662 keV,%	Decay time with γ-excitation	Notes
Gd_2SiO_5 (GSO) $Gd_{2-x}Y_xSiO_5$ (GSO)	6.7 6.5	(8,11) · 1000	9—11	5	Tendency to cracking
Lu_2SiO_5 (LSO) Ce^{3+}	7.4	30 000	7.3—9.7	50	Own background
Y_2SiO_5 (YSO) Ce^{3+}	4.4	30 000	15	40	Poor temperature stability
$Lu_2Si_2O_7:Ce^{3+}$(LPS)	6.2	26 000	9.5	60	Own background
$Gd_2Si_2O_7:Ce^{3+}$(GPS)	5.5	(35,39) · 1000	5—10	38	Tendency to cracking
$Y_3Al_5O_{12}:Ce^{3+}$ (YAG:Ce)	4.55	24 000	7.3	85 + + slowly	
$Y_3Al_5O_{12}:Pr^{3+}$ (YAG:Pr)	4.55	16 000		14	Maximum luminescence at 320 nm
$Gd_3(AlGa)_5O_{12}:Ce^{3+}$ (GAGG:Ce)	6.6	(45,60) · 1000	7	220	
$Lu_3Al_5O_{12}:Ce^{3+}$ (LuAG)	6.7	12 500	No data	44	Own background
$YAlO_3:Ce^{3+}$ (YAP:Ce)	5.35	21 000	6.7	27	
$YAlO_3:Pr^{3+}$ (YAP:Pr)	5.35	13 000		13	Maximum luminescence at 270 nm
$LuAlO_3:Ce^{3+}$ (LuAP:Ce)	8.34	11 000	14	16 + + slowly	Background, complexity of results
$CdWO_4$	7.9	14 000—27 000	8.9	13 000	
$ZnWO_4$	7.85	~50% of CWO	8—11	21—28 000	Tendency to cracking
$SrI_2:Eu^{2+}$	4.6	100 000	3—5	1200	Hygroscopicity
$LaBr_3:Ce^{3+}$	5.1	70 000	3	30	Hygroscopicity

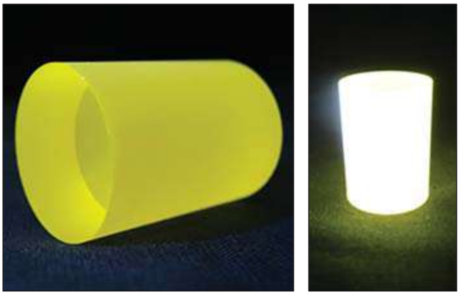

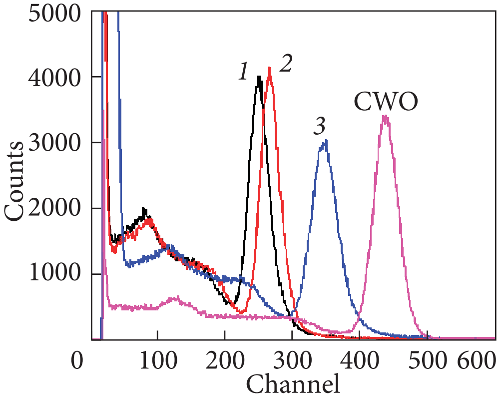

Fig. 5.7. On the left: the appearance of the GAGG:Ce element ∅35 × 50 mm made from the grown crystal; on the right: the same element when exposed to a UV lamp

Fig. 5.8. Amplitude spectra of GAGG:Ce samples with a diameter of 36 mm and a height of 50 mm

Table 5.3. **Parameters of manufactured detectors ∅25 × 35 mm**

Scintillator	Light yield (%) relative to 25 × 25 mm NaI:Tl	Energy resolution,%	Scintillator	Light yield (%) relative to 25 × 25 mm NaI:Tl	Energy resolution,%
$YAlO_3$:Ce	27	Not distinguished	GAGG:Ce	95	11.4
CdWO*	120	18.1	SrI2:Eu	150	6.5

Table 5.4. **Scintillation parameters of large GAGG:Ce detectors**

Detector	Size, mm	Sample	Relative light yield		Energy resolution (*R*),% at 662 keV
			Channel number	LY relative to CWO,%	
CWO standard	∅40 × 25	3	435	100.0	9.5
GAGG(Ce)	∅36 × 50	1	250.5	56.4	12.8
GAGG(Ce)	∅36 × 50	2	266.5	60.0	13.1
GAGG(Ce)	∅36 × 50	3	371	83.6	13.1

spectral range of luminescence is preferred, but the 350—450 nm range is also acceptable. High light yield is important when using luminescence shifters;

f) hygroscopicity and mechanical resistance are desirable, but not mandatory conditions;

g) the space for the crystal detector is limited to 40 mm, but, due to the need for a protective housing, the diameter of the crystal should not exceed 35 mm.

The crystal length should be less than 100 mm; but it is limited to 50 mm for greater uniformity and better energy resolution of the g-photopeak.

When choosing a scintillator for this application, we considered the following crystals (Table 5.2).

Based on the analysis of this table, the following scintillators were chosen for further tests: GAGG:Ce, YAP:Ce, SrI_2:Eu, $CdWO_4$*. Moreover, the last of them is a standard scintillator for geological exploration; regarding other scintillators, there was no information about their use in this area. Detectors with a diameter of 25 mm and a height of 35 mm with one polished end were made from these crystals and sealed in an aluminum container with protective glass. The test results are presented in Table 5.3. Light yield and energy resolution were measured under the following conditions: PEM Hamamatsu R1307; ^{137}Cs as a source of γ-irradiation; 662 KeV; the source was located at a height of 5 cm above the center of the detector; integration time 8 μs.

Despite the highest light yield and the best energy resolution of the SrI_2:Eu crystal, the denser and non-hygroscopic GAGG:Ce crystal was chosen by the customer for further tests. Elements with sizes ∅35×50 mm (Fig. 5.7) and ∅25×35 mm were made from the grown crystals. The results of testing the detectors according to a similar procedure are presented in Table 5.4 and in Fig. 5.8. Energy resolution of about 13% at 662 keV met the customer's requirements.

Thus, large-sized GAGG:Ce single crystals and scintillation elements were manufactured for geological exploration of mineral deposits. Their compliance with consumer requirements was shown — light yield up to 47000 photons/MeV; energy resolution of 11—13% (for elements with ∅35 × 50 mm); high density (6.6 g/cm^3).

5.3. GAGG:Ce, LYSO:Ce substrates for thin-film detectors with high spatial resolution

In recent years, there has been a fairly rapid development of microtomography techniques using both traditional X-ray sources and synchrotron radiation. The areas of application of such microtomography with resolution in the micron range are non-destructive testing of objects under study in industry and various bran ches of science, in particular in materials science, medicine, biology, paleontology, etc. A constituent part of the detector for microtomography is a scintillation screen in the form of a thin crystal or a single-crystal film with a thickness in the micron range. Currently, scintillation screens based on thin single crystals of YAG:Ce and LuAG:Ce garnets, and screens based on single crystal films of LuAG:Eu and GGG:Tb garnets obtained by liquid phase epitaxy (LPE) have already been created; screens based on Lu_2SiO_5:Tb (LSO:Tb) and Lu_2SiO_5:Tb,Ce (LSO:Tb,Ce) films emitting in the visible region of the spectrum have also been manufactured.

---

* The $CdWO_4$ detector was manufactured at ISMA by the group of Dr. I. Tupitsyna.

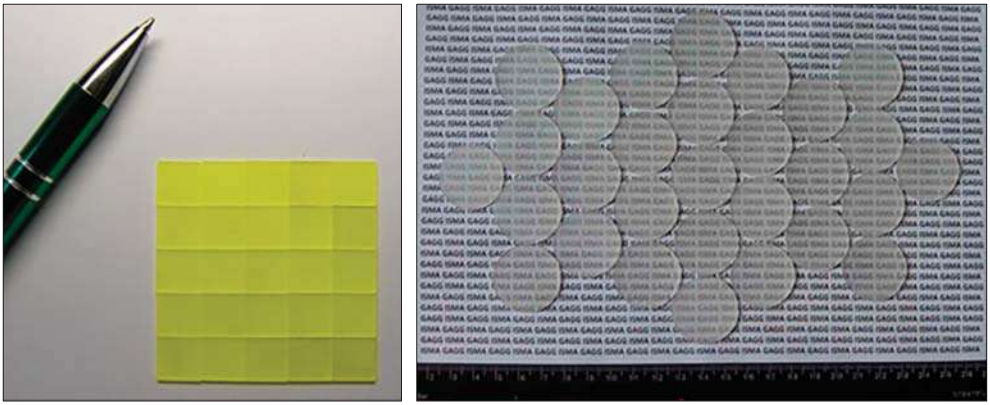

Fig. 5.9. GAGG:Ce substrates with dimensions of 10 × 10 × 1 mm (left) and GAGG:Ce ∅30 × 1 mm (right)

At the same time, the further development of this microtomography technique, in particular, the creation of detectors with resolution in the submicron range, requires new types of scintillation screens with a significantly greater X-ray absorption capacity proportional to $\rho \cdot Z^4_{\mathrm{eff}}$, where ρ and Z_{eff} are the density and the effective atomic number of the scintillator material. Matrices of mixed garnets and orthosilicates GAGG, LYSO, and LGSO have a significantly higher density (6.7—7.4 g/cm^3) and effective atomic number (61—65) compared to YAG and GGG garnets, currently used for scintillation screens produced by the LPE method. This is why mixed garnets and silicates are very promising materials for the development of new types of scintillation screens based on these compounds to create tomographic detectors with spatial separation in the submicron range [293].

A new detector concept for microtomography was recently proposed [292]. It comprises a complex scintillator containing several layers; the optical signal is recorded from each scintillation layer separately, followed by superimposition of images from different parts of the complex scintillator. With a multilayer film scintillator, the contrast and spatial separation of images can be significantly improved, even in the submicron range. This new concept also provides for the creation of various types of efficient thin-film scintillators deposited on luminescent and non-luminescent substrates.

The liquid phase epitaxy (LPE) method makes it possible to create fundamentally new types of hybrid scintillators (HC) based on multilayer single-crystal epitaxial structures containing one or two single-crystal film scintillators grown on single-crystal scintillator substrates from selected types of oxide compounds [54]. Compared to known single-layer analogues, screens based on HS provides significantly better spatial separation and contrast of images due to mixing optical signals from each HS component, emitting in different regions of the spectrum. Such hybrid screens will have a significantly higher X-ray ab-

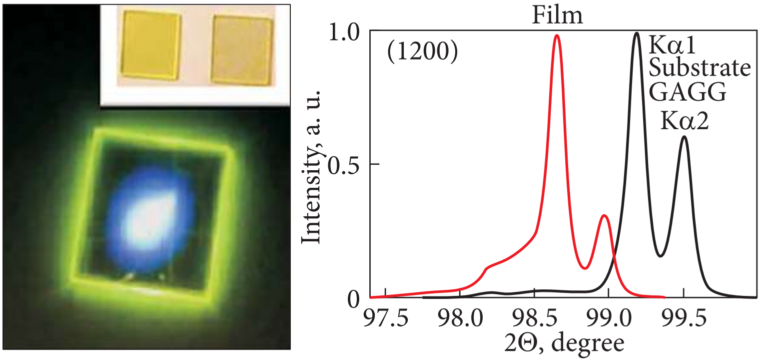

Fig. 5.10. Left: luminescence of a $Gd_{1.5}Lu_{1.5}Al_{2.75}Ga_{2.25}O_{12}$:Ce (BaO) film under laser excitation at a wavelength of 350 nm. On the insert: $Gd_3Al_{2.5}Ga_{2.5}O_{12}$ (GAGG) substrates with deposited $Gd_{1.5}Lu_{1.5}Al_{2.75}Ga_{2.25}O_{12}$:Ce and $Gd_3Al_{2.35}Ga_{2.65}O_{12}$:Ce films. Right: XRD patterns of (1200) planes of $Gd_{1.5}Lu_{1.5}Al_{2.75}Ga_{2.25}O_{12}$:Ce and $Gd_3Al_{2.75}$ $Ga_{2.25}O_{12}$:Ce films grown on a substrate; the misfit in lattice parameters is 0.73% and –0.3%, respectively [295]

sorption capacity due to an increase in the overall thickness of the scintillator and specific adjustment of the *K*-edge of absorption in solid solutions of garnets and orthosilicates containing Lu, Gd, and Y ions.

For crystallization of high-quality films by liquid-phase epitaxy, the misfit between the substrate and film lattice parameters should not exceed a certain value; in particular, for garnet with a sufficiently high isomorphic lattice capacitance, this misfit can reach approximately 1%. For this reason, standard YAG or LuAG substrates are not suitable for producing high-quality films of multicomponent Al/Ga-substituted garnets due to too small lattice parameters. For this purpose, we prepared $Gd_3Al_{5-x}Ga_xO_{12}$ (GAGG) and $Gd_3Al_{5-x}Ga_xO_{12}$: Ce (GAGG:Ce) substrates at $x = 2.5—3$ (Fig. 5.9).

Due to the larger lattice constant in $Gd_3Al_{2.5}Ga_{2.5}O_{12}$ (GAGG), 12.228 Å compared to $a = 10.008$ Å in YAG, the $Gd_{3-x}Lu_xAl_{5-y}Ga_yO_{12}$:Ce films** were grown on GAGG substrates. Good optical quality $Gd_{3-x}Lu_xAl_{5-}yGayO_{12}$:Ce films with $x = 1.5$, 1.0, and 0 in the range of $y = 1.5 \div 3.0$ were successfully crystallized onto GAGG substrates with (100) orientation.

To determine the structural quality of films of different compositions, X-ray diffraction measurements were used (DRON 4 spectrometer, CuK_a X-ray source) (Fig. 5.10). Based on XRD analysis data for $Gd_{3-x}Lu_xAl_{5-y}Ga_yO_{12}$:Ce films at $x = 1.5 \div 0$ and $y = 1.5 \div 3.0$, the lattice parameters of crystals with different compositions and the misfit between the lattice parameters of films and GAGG substrates $m = (a_{SCF} - a_{sub})/\ a_{sub} \times 100\%$ were determined (Table 5.5).

** Films were grown at LNU named after I. Franko (Lviv) and Kazimierz Veliky University in Bydgoszcz (Poland) under the supervision of Prof. Yu. Zorenko and Dr. V. Gorbenko.

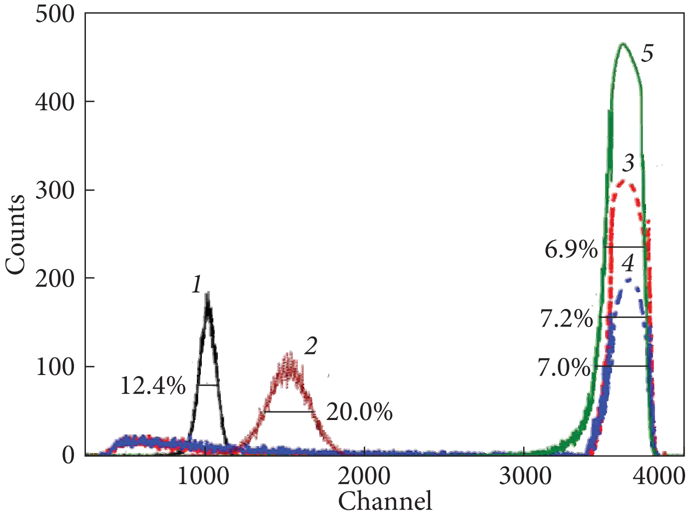

Fig. 5.11. Amplitude spectra of the films: (*2*) $Gd_{1.5}Lu_{1.5}Al_{2.75}Ga_{2.25}O_{12}$:Ce (PbO) (LY = 145%; *R* = 20%), (*3*) $Gd_{1.5}Lu_{1.5}Al_{2.75}Ga_{y}O_{12}$:Ce (BaO) (LY = 346%; *R* = 7.2%) and (*4*) $Gd_3Al_{2.35}Ga_{2.65}O_{12}$:Ce (BaO) (LY = 347%; *R* = 7.0%) relative to film (*1*) (LY = 100%, *R* = 12.4%) and single crystal (*5*) $Gd_3Al_{2.5}Ga_{2.5}O_{12}$:Ce (LY = 364%; *R* = 7.0%;) under excitation by a-particles of Pu^{239} (5.15 MeV) and recorded at an integration time of 12 µs. The type of flux for growing films by the LPE method is indicated in brackets [295]

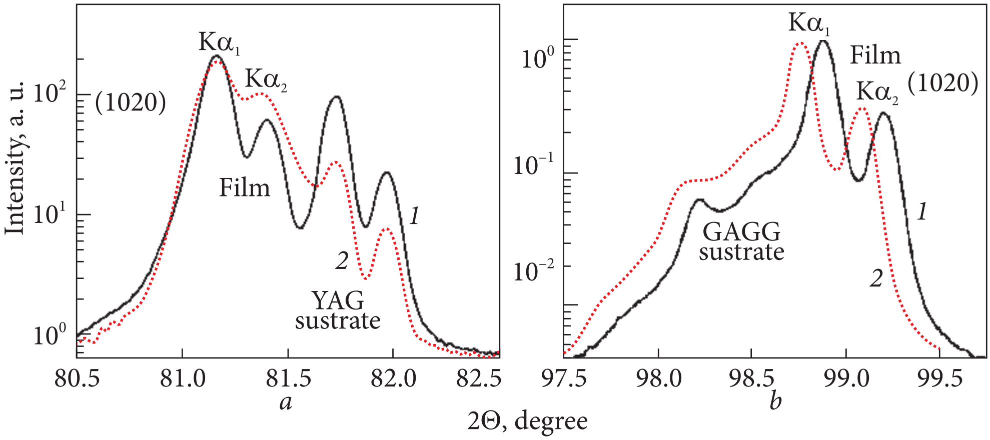

Fig. 5.12. X-ray diffraction pattern of the (1020) plane of $LuTb_2Al_{3.3}Ga_{1.5}O_{12}$:Ce (*1a*) and TbAG:Ce (*2a*) films grown on YAG substrates (*a*), and the (1200) plane of single crystal films of $Tb_3Al_3Ga_2O_{12}$:Ce (*1b*) and $Tb_3Al_{2.5}Ga_{2.5}O_{12}$:Ce (*2b*) grown on GAGG substrates [296]; *a*: *1* — $LuTb_2Al_{3.5}Ga_{1.5}O_{12}$:Ce, m = 0.57%, a = 12.076 A; *2* — $Tb_3Al_5O_{12}$:Ce, m = 0.53%, a = 12.074 A; *b*: *1* — $Tb_3Al_3Ga_2O_{12}$:Ce, m = 0.49%, a = 12.168 A; *2* — $Tb_3Al_{2.5}Ga_{2.5}O_{12}$:Ce, m = 0.44%, a = 12.174A [295]

The lattice constants varied from 12.139 Å in $Gd_{1.5}Lu_{1.5}Al_{2.75}Ga_{2.25}O_{12}$:Ce to 12.235 Å in $Gd_3Al_2Ga_3O_{12}$:Ce, and the misfit decreased from m = –0.73% in $Gd_{1.5}Lu_{1.5}Al_{2.75}Ga_{2.25}O_{12}$:Ce to 0.15% in $Gd_3Al_2Ga_3O_{12}$:Ce.

The scintillation parameters of $Gd_{3-x}Lu_xAl_{5-y}Ga_yO_{12}$:Ce films of different compositions grown on GAGG substrates under excitation by ^{239}Pu a-particles (5.15 MeV) and measured with an integration time of 12 μs are shown in Table 5.6 and Fig. 5.11. Optimizing the cationic composition of the film made it possible to increase the light yield by 3.5 times compared to the YAG:Ce standard. This is the highest light yield obtained in garnet-based film scintillators [295—296].

Optimizing the cationic composition of the film and crystal makes it possible to control the placement of energy levels of activators and traps in the bandgap of the crystal.

At the same time, the energy resolution (R) of $Gd_{1.5}Lu_{1.5}Al_{2.75}Ga_{2.25}O_{12}$:Ce and $Gd_3Al_{2.75\text{-}2.35}Ga_{2.25\text{-}2.65}O_{12}$:Ce films are similar to high-quality crystals of $Gd_3Al_{2.5\text{-}2}Ga_{2.5\text{-}3}O_{12}$:Ce (Fig. 5.11). Also, according to a similar procedure, $Lu_{3-x}Tb_xAl_{5-x}Ga_xO_{12}$ garnet films were crystallized on YAG substrates with a lattice constant of 12.007 Å and GAGG substrates with a lattice constant of 12.228 Å. Scintillation films $Lu_{3-x}Tb_xAl_{5-x}Ga_xO_{12}$:Ce, x = 0.2÷3, grown from a PbO-based flux on a GAGG substrate, have a very high structural quality, illustrated in Fig. 5.12. They have a high light yield and a relatively fast scintillation response. The optimized composition of the films provided a light yield

Table 5.5. **Properties of $Gd_{3-x}Lu_xAl_{5-x}Ga_xO_{12}$:Ce films deposited on GAGG substrates in comparison with standards — a YAG:Ce film deposited on a YAG:Ce substrate and GAGG:Ce single crystals (*m* is the misfit between the substrate and film lattice parameters); λ_{max} is the wavelength luminescence maximum); $t_{1/e}$ is the scintillation decay time; light yield upon excitation by α-particles relative to the YAG:Ce reference film with a light yield of 360 photoel/MeV according to [296]**

Film composition	Substrate composition	m,%	λ_{max}	$t_{1/e}$	Light yield, %
YAG:Ce	YAG		535	67.3	100
$Gd_{1.5}Lu_{1.5}Al_{3.5}Ga_{1.5}O_{12}$:Ce	GAGG	–0.92	518	73.1	268
$Gd_{1.5}Lu_{1.5}Al_{2.75}Ga_{2.25}O_{12}$:Ce	GAGG	–0.75	522	285	346
$Gd_3Al_{2.75}Ga_{2.25}O_{12}$:Ce	GAGG	–0.30	549	328	344
$Gd_3Al_{2.35}Ga_{2.65}O_{12}$:Ce	GAGG	0.05	547	318	347
$Gd_3Al_2Ga_3O_{12}$:Ce	GAGG	0.15	546	332	344
—	$Gd_3Al_{2.5}Ga_{2.5}O_{12}$:Ce (GAGG:Ce)	—	547	440.8	380
—	$Gd_3Al_2Ga_3O_{12}$:Ce (GAGG:Ce)	—	549	239.4	365

2.35 and 1.15 times higher, respectively, than the light yield of YAG:Ce and LuAG:Ce films crystallized on a YAG:Ce substrate under similar conditions. By optimizing the Al^{3+}/Ga^{3+} and Lu^{3+}/Tb^{3+} ratios, films with a very low level of thermally stimulated luminescence at temperatures above room temperature, and relatively fast scintillation decay were also obtained (Table 5.6).

Thus, new scintillators based on single-crystalline films can be proposed for various applications, above all, for scintillation screens for microtomography. These films grown on GAGG substrates can also be used to create new types of combined film-substrate detectors for simultaneous detection of various components of ionizing particle fluxes.

LYSO:Ce, GAGG, GAGG:Ce single-crystalline plates were manufactured as substrates for $Gd_3Al_{5-x}Ga_xO_{12}$:Ce, $Lu_{3-x}Gd_xAl_{5-x}Ga_xO_{12}$:Ce and $Tb_{3-x}Lu_xAl_{5-x}Ga_xO_{12}$:Ce thin-film detectors with a garnet structure for microtomographic techniques with submicron spatial separation. In particular, the light yield of $Gd_3Al_{5-x}Ga_xO_{12}$:Ce and $Lu_{3-x}Gd_xAl_{5-x}Ga_xO_{12}$:Ce thin films is ~350% relative to the YAG:Ce standard, which is the highest value among films with the garnet structure known today.

Table 5.6. **Properties of $Tb_{3-x}Lu_xAl_{5-x}Ga_xO_{12}$:Ce films deposited on GAGG substrates in comparison with standards — YAG:Ce and LuAG:Ce films deposited on a YAG:Ce substrate and GAGG:Ce single crystals (*m* is the misfit between the lattice parameters of the substrate and the film; λ_{max} is the wavelength of the luminescence maximum; $t_{1/e}$ is the scintillation decay time); the light yield upon excitation by α-particles relative to the YAG:Ce reference film with a light yield of 360 ph/MeV according to [295]**

Film composition	Substrate composition	*m*,%	λ_{max}, nm	$t_{1/e}$, ns	Light yield,%	Refs
YAG:Ce (PbO)	YAG	—	535	67	100	
LuAG:Ce (PbO)	YAG	−0.82	509	205		[299]
$Gd_{1.5}Lu_{1.5}Al_{3.15}Ga_{1.85}O_{12}$:Ce	YAG	−0.86	522	51	130	
$Gd_{1.5}Lu_{1.5}Al_{2.75}Ga_{2.25}O_{12}$:Ce	GAGG	−0.73	519	155	145	[298]
$Tb_2LuAl_{3.5}Ga_{1.5}O_{12}$:Ce	YAG	+0.57	543	130	120	[297]
$Tb_2LuAl_{2.75}Ga_{2.25}O_{12}$:Ce	YAG	+0.77	543	292	96	
$Tb_3Al_5O_{12}$:Ce	YAG	+0.53	555	435	123	
$Tb_3Al_3Ga_3O_{12}$:Ce	GAGG	−0.49	543	456	200	
$Tb_3Al_{2.5}Ga_{2.5}O_{12}$:Ce	GAGG	−0.37	543		235	
	$Gd_3Al_{2.5}Ga_{2.5}O_{12}$:Ce (GAGG:Ce)		547	440.8	380	[297]
	$Gd_3Al_2Ga_3O_{12}$:Ce (GAGG:Ce)		549	239.4	365	[297]

REFERENCES

1. Derenzo S.E. et al. The quest for the ideal inorganic scintillator. *Nuclear Instruments and Methods in Physics Res. Section A: Accelerators, Spectrometers, Detectors and Associated Equipment*. 2003. Vol. 505, No. 1—2. P. 111—117.
2. Lecoq P., Gektin A., Korzhik M. Inorganic Scintillators for Detector Systems. *Physical Principles and Crystal Engineering.* Switzerland, 2017. 420 p.
3. Kurosawa S. et al. Czochralski growth of $Gd_3(Al_{5-x}Ga_x)O_{12}$ (GAGG) single crystals and their scintillation properties. *J. of Crystal Growth*. 2014. Vol. 393. P. 134—137.
4. Philip O. et al. Scintillation properties of single-crystal and ceramic GGAG(Ce) and ceramic GYGAG(Ce) at temperatures up to 200 °C. *IEEE Nuclear Science Sympos. and Medical Imaging Conf.* (31 Oct. — 7 Nov., 2015, San Diego, USA). 2016. P. 1—7.
5. Chen J., Zhang L., Zhu R.-Y. Large size LYSO crystals for future high energy physics experiments. *IEEE Transactions on Nuclear Science*. 2005. Vol. 52, No. 6. P. 3133—3140.
6. Sidletskiy O. et al. Structure-Property correlations in a Ce-doped $(Lu,Gd)_2SiO_5$:Ce scintillator. *Crystal Growth* & *Design*. 2012. Vol. 12, No. 9. P. 4411—4416.
7. Bourret-Courchesne E.D. et al. Eu^{2+}-doped Ba_2CsI_5, a new high-performance scintillator. *Nuclear Instruments and Methods in Physics Res. A*. 2009. Vol. 612. P. 138—142.
8. Lecoq P. Development of new scintillators for medical applications. *Nuclear Instruments and Methods in Physics Res. A.* 2016. Vol. 809. P. 130—139.
9. Pfann W G. Zone Melting. *Science.* 1962. Vol. 135. P. 1101—1109.
10. Brandle C. D., Valentino A.J. Czochralski growth of rare earth gallium garnets. *J. of Crystal Growth*. 1972. Vol. 12. P. 3—8.
11. Belsky A. N et al. Progress in the Development of $LuAlO_3$-Based Scintillators. *IEEE Transactions on Nuclear Science*. 2001. Vol. 48. P. 1095—1100.
12. Fasoli M. et al. Band-gap engineering for removing shallow traps in rare-earth $Lu_3 Al_5O_{12}$ garnet scintillators using Ga^{3+} doping. *Physical Review. B*. 2011. Vol. 84, No. 8.
13. Gektin A., Belsky A., Vasil'ev A. Scintillation efficiency improvement by mixed crystal use. *IEEE Transactions on Nuclear Science*. 2014. Vol. 61, No. 1. P. 262—270.
14. Wilson C. et al. Strontium iodide scintillators for high energy resolution gamma ray spectroscopy. *Proc. SPIE*. 2008. Vol. 7079.
15. Van Loef Edgar V. et al. Crystal Growth and Scintillation Properties of Strontium Iodide Scintillators. *IEEE Transactions on Nuclear Science.* 2009. Vol. 56. P. 869—872.
16. Alekhin M. et al. Improvement of gamma-ray energy resolution of $LaBr_3:Ce^{3+}$ scintillation detectors by Sr^{2+} and Ca^{2+} co-doping. *AppliedPhysics Letters.* 2013. Vol. 102, No. 16.
17. Alekhin M. et al. Optical and scintillation properties of $CsBa_2I_5:Eu^{2+}$. *J. of Luminescence.* 2014. Vol. 145. P. 723—728.

18. Stand L. et al. Scintillation properties of Eu^{2+}-doped KBa_2I_5 and K_2BaI_4. *J. of Luminescence.* 2016. Vol. 169. P. 301—307.
19. Van Loef E.V. et al. Scintillation properties of $Cs_2LiLaBr_6$ (CLLB) crystals with varying Ce^{3+} concentration. *Nuclear Instruments and Methods in Physics Res. A.* 2011. Vol. 652. P. 268—270.
20. Lindsey Adam C. et al. Crystal growth and characterization of europium doped $KCaI_3$, a high light yield scintillator. *Optical Materials*. 2015. Vol. 48. P. 1—6.
21. Van Loef E.V. et al. Scintillation properties of $LaCl_3$:Ce^{3+} crystals: Fast, efficient, and high-energy resolution scintillators. *IEEE Transactions on Nuclear Science*. 2001. Vol. 48. P. 341—345.
22. Guss P. et al. Results for aliovalent doping of $CeBr_3$ with Ca^{2+}. *J. of Applied Physics*. 2015. Vol. 115, No. 3.
23. Burger A. et al. Cesium hafnium chloride: a high light yield, non-hygroscopic cubic crystal scintillator for gamma spectroscopy. *Applied Physics Letters*. 2015. Vol. 107.
24. Samulon E.C. et al. Luminescence and scintillation properties of Ce^{3+}-activzated $Cs_2NaGdCl_6$, Cs_3GdCl_6, $Cs_2NaGdBr_6$ and Cs_3GdBr_6. *J. of Luminescence.* 2014. Vol. 153. P. 64—72.
25. Stand L., Zhuravleva M., Melcher C.L., Wei H. Crystal growth and scintillation properties of potassium strontium bromide. *Optical Materials*. 2015. Vol. 46. P. 59—63.
26. Stand L. et al. Eu^{2+}-activated $BaCl_2$, $BaBr_2$ and BaI_2 scintillators revisited. *Nuclear Instruments and Methods in Physics Res. A.* 2014. Vol. 735. P. 83—87.
27. Dorenbos P. et al. Scintillation properties of $RbGd_2Br_7$:Ce^{3+} crystals; fast, efficient, and high density scintillators. *Nuclear Instruments and Methods in Physics Res. B.* 1997. Vol. 132. P. 728—731.
28. Shirwadkar U. et al. Promising Alkaline Earth Halide Scintillators for Gamma-Ray Spectroscopy. *IEEE Transactions on Nuclear Science*. 2013. Vol. 60. P. 1011—1015.
29. Gundiah G. et al. Structure and scintillation properties of Ce^{3+}-activated $Cs_2NaLaCl_6$, Cs_3LaCl_6, $Cs_2NaLaBr_6$, Cs_3LaBr_6, Cs_2NaLaI_6 and Cs_3LaI_6. *J. of Luminescence.* 2014. Vol. 149. P. 374—384.
30. Boatner L.A. et al. Bridgman growth of large SrI_2:Eu^{2+} single crystals: A high-performance scintillator for radiation detection applications. *J. of Crystal Growth.* 2013. Vol. 379. P. 63—68.
31. Parameters of SrI_2:Eu. URL: https://c-and-a.jp/assets/img/products/104180228_SrI2.pdf (Last accessed: 02.09.2024)
32. Globus M.E., Grynyov B.V. Inorganic scintillators. New and traditional materials. Kharkiv, 2000. 408 p. [in Russian].
33. Atroshchenko L.V. Scintillator crystals and detectors of ionizing radiation on their base. Kyiv, 1998. 310 p. [in Russian].
34. Lecoq P. et al. Inorganic Scintillators for Detector Systems. Physical Principles and Crystal Engineering. Verlag Berlin Heidelber: Springer, 2005. 252 p.
35. Nikl M. Scintillator detectors for X-rays. *Measurement Science and Technology.* 2006. Vol. 17, No. 4. P. R37—R54.
36. LuAG:Ce Technical parameters. URL: http://www.crytur.cz/materials/luagce/ (Last accessed: 02.09.2024).
37. Pidol L. et al. High efficiency of lutetium silicate scintillators, Ce-doped LPS, and LYSO crystals. *IEEE Transactions on Nuclear Science*. 2004. Vol. 51. P. 1084—1087.

38. Nikl M., Yoshikawa A. Recent R&D Trends in Inorganic Single-Crystal Scintillator Materials for Radiation Detection. *Advanced Optical Materials*. 2015. Vol. 3. P. 463—481.
39. Haruna J. et al. Response function measurement of $Gd_2Si_2O_7$ scintillator for neutrons. *IEEE Nuclear Science Symposium Conf. Record,* (28 Oct. — 3 Nov., 2007, Honolulu, USA). 2007. Vol. 2. P. 1421—1425.
40. Galunov Nikolai Z. et al. Development of New Composite Scintillation Materials Based on Organic Crystalline Grains. *IEEE Transactions on Nuclear Science*. 2009. Vol. 56, No. 3. P. 904—910.
41. Gerasymov I. et al. Growth of bulk gadolinium pyrosilicate single crystals for scintillators. *J. of Crystal Growth*. 2011. Vol. 318. P. 805—808.
42. Yoshikawa A. et al. Czochralski J. Growth of 2 Inch Ce-Doped $(La,Gd)_2Si_2O_7$ for Scintillator Application. *J. of Crystal Growth.* 2016. Vol. 452. P. 57—64.
43. Zhu R.Y. et al. A study on the properties of lead tungstate crystals. *Nuclear Instruments and Methods in Physics Res. A*. 1996. Vol. 376, No. 3. P. 319—334.
44. Burachas S. et al. Peculiarities of growing $PbWO_4$ scintillator crystals for application in high-energy physics. *J. of Crystal Growth*. 1998. Vol. 186. P. 175—180.
45. Weber M. J., Monchamp R. R. Luminescence of $Bi_4Ge_3O_{12}$: Spectral and decay properties. *J. of Applied Physics*. 1973. Vol. 44. P. 5495.
46. Takagi K., Fukuzawa T. Improvement in the scintillation conversion efficiency of $Bi_4Ge_3O_{12}$ single crystals. *J. of Crystal Growth*. 1981. Vol. 52, No. 2. P. 584—587.
47. Borovlev Yu. A. et al. Progress in growth of large sized BGO crystals by the low-thermal-gradient Czochralski technique. *J. of Crystal Growth*. 2001. Vol. 229, No. 1. P. 305—311.
48. Burachas S. et al. Advanced scintillation single crystals based on complex oxides with large atomic number. *Semiconductor Physics Quantum Electronics* & *Optoelectronics*. 2000. Vol. 3, No. 2. P. 237—239.
49. Takagi K., Fukuzawa T. Cerium-activated Gd_2SiO_5 single crystal scintillator. *Applied Physics Letter*s. 1983. Vol. 42, No. 1. P. 43—45.
50. Melcher C.L. A promising new scintillator: cerium-doped lutetium oxyorthosilicate. *Nuclear Instruments and Methods in Physics Res. A*. 1992. Vol. 314. P. 212—214.
51. Chatrchyan S. et al. Observation on a new boson at a mass of 125 GeV with the CMS experiment at the LHC. *Physics Letters B*. 2012. Vol. 716, No.1. P. 30—61.
52. Dormenev V. et al. Restart of the Production of High-Quality $PbWO_4$ Crystals for Calorimetry Applications. 2017. P. 104113.
53. Mu2e Conceptual Design Report [number FERMILAB-TM-2545]/Mu2e Collaboration. 2012. P. 562.
54. Experimental Search for Lepton Flavor Violating $\mu^- - e^-$ Conversion at Sensitivity of 10–16 with a Slow-Extracted Bunched Proton Beam (COMET). 2009. URL: https://inspirehep.net/files/c8b0ea571cf05de599451a299352eb91 (last accessed: 02.09.2024)
55. Melcher C.L. Scintillation crystals for PET. *J. of Nuclear Medicine.* 2000. Vol. 41. P. 1051—1055.
56. Voloshyna O.V. et al. Growth and scintillation properties of gadolinium and yttrium orthovanadate crystals. *Nuclear Instruments and Methods in Physics Res. A.* 2012. Vol. 664. P. 299—303.
57. Fujimoto Y. et al. Comparative study of optical and scintillation properties of YVO_4, $(Lu_{0.5}Y_{0.5})VO_4$, and $LuVO_4$ single crystals. *Nuclear Instruments and Methods in Physics Res. A*. 2011. Vol. 635. P. 53—56.

58. Voloshyna O. et al. Luminescent and scintillation properties of orthotantalates with common formulae $RETaO_4$ (RE = Y, Sc, La, Lu and Gd). *Materials Science and Engineer. B*. 2013. Vol. 178. P. 1491—1496.
59. Popovici E.-J. et al. Studies concerning the properties of some europium activated phosphors based on yttrium tantalate. *Physics Procedia*. 2009. Vol. 2, No. 2. P. 185—190.
60. Karsu E.C. et al. Luminescence study of some yttrium tantalate-based phosphors. *J. of Luminescence*. 2011. Vol. 131. P. 1052—1057.
61. Brixner L.H., Chen H.-Y. On the structural and luminescent properties of the M'-$LnTaO_4$ rare earth tantalates. *J. of the Electrochemical Society*. 1983. Vol. 130, No. 12. P. 2435—2443.
62. Liu G., Jacquier B. Spectroscopic properties of rare earths in optical materials. Berlin, 2005. 550 p.
63. Krumpel A.H. et al. Lanthanide 4f-level location in $AVO_4:Ln^{3+}$ (A = La, Gd, Lu) crystals. *J. of Physics: Condensed Matter*. 2009. Vol. 21, No. 11. P. 115503—115510.
64. Blasse G., Brill A. Luminescence phenomena in compounds with fergusonite structure. *J. of Luminescence*. 1970. Vol. 3, No. 2. P. 109—131.
65. Kazakova L.I., Dubovsky A. B., Ivanova O. A. Luminescence of $YTaO_4$ single crystals. *Radiation Measurements*. 1995. Vol. 24, No. 4. P. 359—360.
66. Bourret E.D. et al. Scintillation of Tantalate compounds. *J. of Luminescence*. 2018. Vol. 202. P. 332—338.
67. Patent 5367172 USA, G03C5/17. Radiological system employing phosphors of different densities. J. Beutel, S. Issler, D. Mickewich. Applicant and patent owner Agfa-Gevaert NV. Appl. No. US5367172; filed 01.06.2003; date of patent 22.11.2004.
68. Patent WO 2008/094184, G01T1/2018. APparatus for asymmetric dual-screen digital radiography. John Yorkston, Kwok-Leung Yip, Timothy Wojcik. Applicant and patent owner Carestream Health Inc, John Yorkston, Kwok-Leung Yip, Timothy Wojcik. Appl. No. PCT/US2007/015972; filed 12.07.2007; date of patent 20.11.2008.
69. SchiPer W.J., Hoogendorp M.F., Blasse G. The luminescence and X-ray storage properties of Pr^{3+} and Ce^{3+} in $YNbO_4$ and M'-$YTaO_4$. *Journal of Alloys and Compounds*. 1993. Vol. 202, No. 1—2. P. 283—287.
70. Ungurecan M.-L., Coloçi T. Method of numerical simulation for the air pollution dispersion. *IEEE Int. Conf. on Automation, Quality and Testing, Robotics (AQTR)*. (2010, Cluj-Napoca, Romania). Vol. 3. P. 1—4.
71. Bleier Grant C., Nyman May, Rohwer Lauren E.S., Rodriguez Mark A. Seeking the optimal $LaTaO_4$:Eu phosphor. *J. of Solid State Chemistry*. 2011. Vol. 184, No. 12. P. 3221—3227.
72. Dorenbos P. et al. Lanthanide level location in transition metal complex compounds. *Optical Materials*. 2010. Vol. 32, No. 12. P. 1681—1685.
73. Krumpel A.H., Boutinaud P., van der Kolk E., Dorenbos P. Charge transfer transitions in the transition metal oxides $ABO_4:Ln^{3+}$ and $APO_4:Ln^{3+}$ (A=La, Gd, Y, Lu, Sc; B=V, Nb, Ta; Ln=lanthanide). *J. of Luminescence*. 2010. Vol. 130, No. 8. P. 1357—1365.
74. Li B., Gu Z., Lin J., Su M.-Z. X-ray luminescence properties of rare-earth doped orthotantalate. *Materials Res. Bull.* 2000. Vol. 35, No. 12. P. 1921—1931.
75. Petrosyan A.G. et al. Growth and light yield performance of dense Ce^{3+}-doped (Lu, Y)AlO_3 solid solution crystals. *J. of Crystal Growth*. 2000. Vol. 211. P. 252—256.
76. Kamada K. et al. Composition Engineering in Cerium-Doped $(Lu,Gd)_3(Ga,Al)_5O_{12}$ Single-Crystal Scintillators. *Crystal Growth & Design*. 2011. Vol. 11. P. 4484—4490.

77. Patent 7166845 USA, GOIT L/20. Method of Enhancing performance of cerium doped lutetium yttrium orthosilicate crystals and crystals produced thereby. Chai B. Applicant and patent owner Crystal Photonics Incorporated. Appl. No. 2005/0253072 A1; filed 17.11.2005; date of patent 19.12.2006.
78. Gundiah G. et al. Structure and scintillation of Eu^{2+}-activated solid solutions in the $BaBr_2$-BaI_2 system. *Nuclear Instruments and Methods in Physics Res. A*. 2011. Vol. 652. P. 234—237.
79. Belsky A.N. et al. X-ray excitation of luminescence of scintillator materials in the 7–22 keV region. *Nuclear Instruments and Methods in Physics Res. A*. 1995. Vol. 361. P. 384—387.
80. Gurvich A.M., Katomina R.V., Tombak M.I. Energy yield of X-ray luminescence of polycrystalline luminophors. *Zhurnal Prikladnoi Spektroskopii*. 1977. Vol. 26, No. 1. P. 75—81 [in Russian].
81. Gundiah G. et al. Structure and scintillation of Eu^{2+}-activated BaBrCl and solid solutions in the $BaCl_2$–$BaBr_2$ system. *J. of Luminescence*. 2013. Vol. 138. P. 143—149.
82. Bourret-Courchesne E.D. et al. Crystal growth and characterization of alkali-earth halide scintillators. *J. of Crystal Growth*. 2012. Vol. 352. P. 78—83.
83. Bourret-Courchesne E.D. et al. Scintillation Properties of Eu^{2+}-Activated Barium Fluoroiodide. *IEEE Transactions on Nuclear Science*. 2010. Vol. 57. P. 1702—1705.
84. Wu Y. et al. Quaternary Iodide $K(Ca,Sr)I_3$:Eu^{2+} Single-Crystal Scintillators for Radiation Detection: Crystal Structure, Electronic Structure, and Optical and Scintillation Properties. *Advanced Optical Materials*. 2016. Vol. 4. P. 1518—1532.
85. Giaz A. et al. Preliminary investigation of scintillator materials properties: SrI_2:Eu, $CeBr_3$ and GYGAG:Ce for gamma rays up to 9 MeV. *Nuclear Instruments and Methods in Physics Res. A*. 2015. Vol. 804. P. 212—220.
86. Kapusta M. et al. A high-energy resolution observed from a YAP:Ce scintillator. *Nuclear Instruments and Methods in Physics Res. A*. 1999. Vol. 421. P. 610—613.
87. Dorenbos P. Light output and energy resolution of Ce^{3+}-doped scintillators. *Nuclear Instruments and Methods in Physics Res. A*. 2002. Vol. 486. P. 208—213.
88. Sidletskiy O. Trends in Search for Bright Mixed Scintillators. *Physica Status Solidi (A) Applications and Materials Science*. 2018. Vol. 215. P. 1701034.
89. Villora E.G., Kazuyuki I., Inomata D., Shimamura K. Single-crystal phosphors for high-brightness white LEDs/LDs. *SPIE Conf. Proceed*. Vol. 9768 (Mar, 2016). P. 976805.
90. Rodriguez E., Munoz J.A., Tocho J.O., Cusso F. The luminescent quantum efficiency of Eu^{2+} ions in alkali halides determined by simultaneous multiwavelength photoacoustic and luminescence experiments. *J. of Physics: Condensed Matter.* 1994. Vol. 6. P. 10625.
91. Dorenbos P. Electronic structure and optical properties of the lanthanide activated $RE_3(Al_{1-x}Ga_x)_5O_{12}$ (RE=Gd,Y, Lu) garnet compounds. *J. of Luminescence.* 2013. Vol. 134. P. 310—318.
92. Birowosuto M.D., Dorenbos P., Krämer K.W., Güdel H.U. Ce^{3+} activated $LaBr_{3-x}I_x$: High-light-yield and fast-response mixed halide scintillators. *J. of Applied Physics.* 2008. Vol. 103. P. 103517.
93. Nikl M. et al. Defect Engineering in Ce-Doped Aluminum Garnet Single Crystal Scintillators. *Crystal Growth & Design*. 2014. Vol. 14, No. 9. P. 4827—4833.

94. Kamada K. et al. Alkali earth co-doping effects on luminescence and scintillation properties of Ce doped $Gd_3Al_2Ga_3O_{12}$ scintillator. *Optical Materials*. 2015. Vol. 41. P. 63—66.
95. Hansel A., Allison S. W., Walker D. G. Temperature-dependent luminescence of Ce^{3+} in gallium-substituted garnets. *Applied Physics Letters*. 2009. Vol. 95. P. 114102.
96. Tyagi M. et al. Improvement of the scintillation properties of $Gd_3Ga_3Al_2O_{12}$:Ce, B single crystals having tailored defect structure. *Physica Status Solidi RRL*. 2015. Vol. 9. P. 530.
97. Wu Y. et al. The influence of Sc/Lu ratio on the phase transformation and luminescence of cerium-doped lutetium scandium orthoborate solid solutions. *J. of Alloys and Compounds*. 2011. Vol. 509. P. 366.
98. Wu Y. et al. Effects of scandium on the bandgap and location of Ce^{3+} levels in $Lu_{1-x}Sc_xBO_3$:Ce scintillators. *Applied Physics Letters*. 2012. Vol. 100. P. 021904.
99. Jary V. et al. Influence of yttrium content on the $CeLu_1$ and $CeLu_2$ luminescence characteristics in $(Lu_{1-x}Y_x)_2SiO_5$:Ce single crystals. *Optical Materials*. 2011. Vol. 34. P. 428—432.
100. Belsky A., Gektin A., Gridin S., Vasiliev A.N. Electronic and optical properties of scintillators based on mixed ionic crystals. *Engineer. of Scintillation Materials and Radiation Technologies*: proceed. of ISMART (26—30 Sept., 2016, Minsk). Springer, 2017. 339 p.
101. Belsky A. et al. Estimation of the Electron Thermalization Length in Ionic Materials. *J. of Physical Chemistry Letters*. 2013. Vol. 4. P. 3534—3538.
102. Vasiliev A.N., Mikhailin V.V. Introduction to spectroscopy of dielectrics. Part II. Secondary processes. 2010. 238 p. [in Russian].
103. Katsnelson A.A. Short range order in metal alloys. *Sorosovskiy obrazovatelnyi zhurnal*. 1999. No. 11. P.110—116.
104. Order-Disorder Transformations in Alloys. Berlin; Heidelberg; New York: Springer, 1974. P. 550.
105. Sidletskiy O. et al. Structure and scintillation yield of Ce-doped Al–Ga substituted yttrium garnet. *Materials Res. Bull.* 2012. Vol. 47. P. 3249—3252.
106. Ungaretti L., Leona M., Merli M., Obert R. Non-ideal solid-solution in garnet: crystal-structure evidence and modelling. *Eur. J. Mineral.* 1995. Vol. 7. P. 1299—1312.
107. Nakatsuka A., Yoshiasa A., Yamanaka T. Cation distribution and crystal chemistry of $Y_3Al_{5-x}Ga_xO_{12}$ ($0 \le x \le 5$) garnet solid solutions. *Acta Crystallographica B.* 1999. Vol. 55. P. 266.
108. Marezio M., Remeika J. P., Jayaraman A. High-Pressure Decomposition of Synthetic Garnets. *J. of Chemical Physics*. 1966. Vol. 45. P. 1821.
109. Geller S. Crystal chemistry of the garnets. *Zeitschrift für Kristallographie.* 1967. Vol. 125. P. 1—47.
110. Ashurov M. et al. Spectroscopic study of stoichiometry deviation in crystals with garnet structure. *Physica Status Solidi A*. 1977. Vol. 2. P. 101—110.
111. Sidletskiy O. et al. Impact of Lu/Gd ratio and activator concentration on structure and scintillation properties of LGSO:Ce crystals. *J. of Crystal Growth.* 2010. Vol. 312. P. 601—606.
112. Glowacki M. et al. Growth conditions, structure, Raman characterization and optical properties of Sm-doped $(Lu_xGd_{1-x})_2SiO_5$ single crystals grown by the Czochralski method. *J. of Solid State Chemistry*. 2012. Vol. 186. P. 268—277.
113. Shannon R.D. Revised effective ionic radii and systematic studies of interatomic distances in halides and chalcogenides. *Acta Crystallographica A*. 1976. Vol. 32, No. 5. P. 751—767.

114. Brandle C.D., Valentino A.J., Berkstresser G.W. Czochralski growth of rare-earth orthosilicates (Ln_2SiO_5). *J. of Crystal Growth*. 1986. Vol. 79. P. 308—315.
115. Usui T. et al. Impact of Ce concentration on scintillation properties of $Lu_{2x}Gd_{2(1-x)}SiO_5$:Ce (LGSO, x=0.2) single crystals. *IEEE Nuclear Science Sympos. Conf. Record,* (28 Oct. — 3 Nov., 2007, Honolulu, USA). 2007. P. 1412—1416.
116. Ferroni F. The L3 BGO electromagnetic calorimeter at LEP. *Nuclear Physics B - Proceed. SuPlements*. 1991. Vol. 23A. P. 100—106.
117. Vaithianathan V. et al. Czochralski growth of bismuth germanium silicon oxide (BGSO) single crystal and its characterization. *J. of Crystal Growth*. 2002. Vol. 235. P. 212—216.
118. Hua Jiang et al. Czochralski growth and scintillation properties of bismuth germanium silicon oxide (BGSO) single crystals. *2011 IEEE Nuclear Science Sympos. Conf. Record* (23—29 Oct., 2011, Valencia, Spain). 2011. P. 1580—1582.
119. Zhang Y., Xu J., He Q., Lu B.L. Bridgman growth and characterization of $Bi_4(Ge_xSi_{1-x})_3O_{12}$ mixed crystals. *J. of Crystal Growth*. 2013. Vol. 362. P. 121—124.
120. Hua J. et al. Study on Scintillation Characteristics of BGSO Single Crystals. *IEEE Transactions on Nuclear Science.* 2014. Vol. 61. P. 323—327.
121. Mao R., Zhang L., Zhu R.Y. Crystals for the HHCAL Detector Concept. *IEEE Transactions on Nuclear Science.* 2012. Vol. 59. P. 2229—2236.
122. Galenin E. et al. Engineering of mixed $Bi_4(Ge_xSi_{1-x})_3O_{12}$ scintillation crystals. *Functional Materials*. 2015. Vol. 22(4). P. 423—428.
123. Takagi K., Oi T., Fukazawa T. Improvement in the scintillation conversion efficiency of $Bi_4Ge_3O_{12}$ single crystals. *J. of Crystal Growth.* 1981. Vol. 52. P. 584—587.
124. Choubey A., Bhagavannarayana G., Shubin Yu.V. Study of effect of thermal annealing on crystalline perfection of bismuth germanate single crystals grown by low thermal gradient Czochralski method. *Zeitschrift für Kristallographie — Crystalline Materials*. 2002. Vol. 217. P. 515—521.
125. Choubey A., Bhagavannarayana G., Shubin Yu. V. Study of point defects in as-grown and annealed bismuth germanate single crystals. *J. of Applied Crystallography.* 2005. Vol. 38. P. 448—454.
126. Batarin V.A. et al. Comparison of radiation damage in lead tungstate crystals under pion and gamma irradiation. *Nuclear Instruments and Methods in Physics Res. A.* 2004. Vol. 530, No. 3. P. 286—292.
127. LHC Injectors Upgrade, Technical Design Report. 2014. Vol. 1: Protons.
128. The Int. Linear Collider Technical Design Report. 2013. Vol. 4: Detectors. 384 p.
129. Mavromanolakis G., Auffray E., Lecoq P. Studies of sampling and homogenious dual readout calorimetry with meta-crystals. *J. of Instrumentation*. 2011. Vol. 6. P. 10012.
130. Lucchini M. et al. Test beam results with LuAG fibers for next-generation calorimeters. *J. of Instrumentation*. 2013. Vol. 8. P. 10017.
131. Fukuda T., Chani V. Shaped crystals: growth by micro-pulling-down technique. *Springer Science & Business Media*. 2007. Vol. 8. 341 p.
132. Rudolph P., Fukuda T. Fiber crystal growth from the melt. *Crystal Res. and Tech.* 1999. Vol. 34, No. 1. P. 3—40.
133. Sanglaa D. et al. Yb-doped $Lu_3Al_5O_{12}$ fibers single crystals grown under stationary stable state for laser application. *J. of Crystal Growth*. 2009. Vol. 312, No. 1. P. 125—130.
134. Simura R., Yoshikawa A., Uda S. The radial distribution of dopant (Cr, Nd, Yb, or Ce) in yttrium aluminum garnet ($Y_3Al_5O_{12}$) single crystals grown by the micro-pulling-down method. *J. of Crystal Growth*. 2009. Vol. 311, No. 23. P. 4763—4769.

135. Maier D. et al. Dopant segregations in oxide single-crystal fibers grown by the micro-pulling-down method. *Optical Materials*. 2007. Vol. 30, No. 1. P. 11—14.
136. Hautefeuille B. et al. Shaped crystal growth of Ce^{3+}-doped $Lu_{2(1-x)}Y_{2x}SiO_5$ oxyorthosilicate for scintillator applications by pulling-down technique. *J. of Crystal Growth.* 2006. Vol. 289, No. 1. P. 172—177.
137. Chani V. et al. Evaporation induced diameter control in fiber crystal growth by micro-pulling-down technique: $Bi_4Ge_3O_{12}$. *Res. and Tech.* 2006. Vol. 41, No. 10. P. 972—978.
138. Koroleva T.S. et al. Ce-doped $Li_6Ln(BO_3)_3$(Ln= Y,Gd) single crystals fibers grown by micro-pulling down method and luminescence properties. *Optical Materials.* 2013. Vol. 35, No. 5. P. 868—874.
139. Lecoq P. New crystal technologies for novel calorimeter concepts. *J. of Physics: Conf. Series*. 2009. Vol. 160, No. 1. P. 012016.
140. Pauwels K. et al. Single crystalline LuAG fibers for homogeneous dual-readout calorimeters. *J. of Instrumentation*. 2013. Vol. 8, No. 9. P. 09019.
141. Xu X. et al. Ce-doped LuAG single-crystal fibers grown from the melt for high-energy physics. *Acta Materialia*. 2014. Vol. 67. P. 232—238.
142. Lebbou K. Single crystals fiber technology design. Where we are today? *Optical Materials.* 2017. Vol. 63. P. 13—18.
143. Kononets V. et al. Development of YAG:Ce, Mg and YAGG:Ce Scintillation Fibers. *Engineer. of Scintillation Materials and Radiation Tech.* Proceedings of ISMART (26—30 Sept., 2016, Minsk). Springer, 2017. P.114128.
144. Kononets V. et al. Growth of long undoped and Ce-doped LuAG single crystal fibers for dual readout calorimetry. *J. of Crystal Growth*. 2016. Vol. 435. P. 31—36.
145. Sidletskiy O., Lebbou K., Kononets V. Micro-pulling-down growth of long YAG- and LuAG-based garnet fibres: advances and bottlenecks. *CrystEngComm.* 2021. Vol. 23. P. 2633—2643.
146. Kononets V. et al. Growth of Ce-doped LGSO fiber-shaped crystals by the micro pulling down technique. *J. of Crystal Growth*. 2015. Vol. 412. P. 95102.
147. Kononets V. Growth from melt by micro-pulling down (μ-PD) and Czochralski (Cz) techniques and characterization of LGSO and garnet scintillator crystals: Doctoral dissertation. Université Claude Bernard. Lyon, 1, France, 2014.
148. Carruthers J., Kokta M., Barns R., Grasso M. Nonstoichiometry and crystal growth of gadolinium gallium garnet. *J. of Crystal Growth*. 1973. Vol. 19. P.204—208.
149. Patent 5112524 USA, C09K 11/78. Unactivated yttrium tantalate phosphor. V.B. Reddy, H. K. Cheung. Applicant and patent owner Gte Products Corporation. Appl. № 732,886; filed 19.07.1991; date of patent 12.05.1992.
150. Patent 5762827 USA, C09K 11/78. Yttrium tantalate X-ray phosphors with increased luminance and particle size. V.B. Reddy. Applicant and patent owner Osram Sylvania Inc. Appl. No. 904,496; filed 01.09.1997; date of patent 09.06.1998.
151. Patent 5009807 USA, C09K 11/78. Niobium-activated yttrium tantalate X-ray phosphor with improved brightness and method of making same.V.B. Reddy. Applicant and patent owner Gte Products Corporation. Appl. № 563,133; filed 06.09.1990; date of patent 23.04.1991.
152. Patent 4225653 USA, C09K 11/46, G01T 1/00. X-ray intensifying screen based on rare earth tantalate. L.H. Brixner. Applicant and patent owner E.I. Du Pont De Nemours And Company. Appl. № 23,966; filed 26.03.1979; date of patent 30.09.1980.

153. Blasse G., Brill A. Luminescence in some tantalate host lattices. *J. of Solid State Chemistry.* 1971. Vol. 3, No. 1. P. 69—74.

154. Cava R.J., Roth R. S. The Structure of $LaTaO_4$ at 300° C by Neutron Powder Profile Analysis. *J. of Solid State Chemistry*. 1981. Vol. 36, No. 2. P. 139—147.

155. Levin E.M., Robbins C., McMurdie H.F. Phase Diagrams for Ceramists. Columbus, 1985. 590 p.

156. Zafrir M., Aladjem A., Zilber R., Ben-Dor L. Preparation of a continuous series of solid solutions in the Ta_2O_5-Nb_2O_5 system. *J. of Solid State Chemistry.* 1976. Vol. 18, No. 4. P. 377—380.

157. Vegard L. Die Konstitution der Mischkristalle und die Raumfüllung der Atome. *Zeitschrift für Physik*. 1921. Vol. 5, No. 1. P. 17—26.

158. Chemical Bonds and Bond Energy. New York; London: Academic Press, 1976. 218 p.

159. West A.R. Solid state chemistry and its application. 1985.

160. Waychunas G.A., Dollase W.A., Ross C.R. Short-range order measurements in MgO-FeO and MgO-LiFeO, solid solutions by DLS simulation-assisted EXAFS analysis. *American Mineralogist*. 1995. Vol. 79. P. 274—288.

161. Silva M. A. P. et al. Structural studies on leadecadmium fluoride solid solution. *Solid State Ionics*. 2002. Vol. 147. P. 135—139.

162. Shimizu S. et al. Characteristics of LuGdSiO:Ce (LGSO) for APD-based PET detector. *IEEE Transactions on Nuclear Science*. 2010. Vol. 57, No.1. P. 55—61.

163. Loutts G.B. et al. Czochralski growth and characterization of $(Lu_{1-x}Gd_x)_2SiO_5$ single crystals for scintillator. *J. of Crystal Growth*. 1997. Vol. 174. P. 331—336.

164. Suzuki H., Tombrello T. A., Schweitzer J. S., Melcher C.L. UV and gamma-ray excited luminescence of cerium-doped rare-earth oxyorthosilicates. *Nuclear Instruments and Methods in Physics Res. A*. 1992. Vol. 320. P. 263—272.

165. Pidol L. et al. EPR study of Ce^{3+} ions in lutetium silicate scintillators $Lu_2Si_2O_7$ and Lu_2SiO_5. *J. of Physics and Chemistry of Solids*. 2006. Vol. 67, No. 4. P. 643—650.

166. Ricci C. et al. Ce^{3+}-doped lutetium yttrium orthosilicate crystals: Structural characterization. *Materials Science and Engineer. B*. 2008. Vol. 146. P. 2—6.

167. Usui T. et al. Improvement of scintillation properties and weakening of afterglow of $Lu_{2x}Gd_{2(1-x)}$ SiO_5:Ce (LGSO, x=0.2) single crystals. *IEEE Nuclear Science Sympos. Conf. Record* (29 Oct. —4 Nov., 2006, San Diego, USA). 2007. P. 1166—1169.

168. Kurtsev D.O. Obtaining of efficient scintillators based on $Lu_{2x}Gd_{2-2x}SiO_5$:Ce (LGSO:Ce) crystals: Thesis of candidate of technical sciences: 05.02.01. Institute for Single Crystals NAS of Ukraine. Kharkiv, 2016 [in Russian].

169. Yawai N. et al. Luminescence and scintillation timing characteristics of (Lu_xGd_{2-x}) SiO_5:Ce single crystals. *Nuclear Instruments and Methods in Physics Res. A*. 2017. Vol. 844. P. 116—120.

170. Grodzicka M. et al. Characterization of LFS-3 scintillator in comparison with LSO. *Nuclear Instruments and Methods in Physics Res. A*. 2011. Vol. 652. P. 226—230.

171. Rogers J.G., Batty C.J. Afterglow in LSO and its possible effect on energy resolution. *IEEE Transactions on Nuclear Science*. 2000. Vol. 47. P. 438—445.

172. Mihóková E. et al. Quantum tunneling and low temperature delayed recombination in scintillating materials. *Chemical Physics Letters*. 2013. Vol. 578. P. 66—69.

173. Gerward L., Guilbert N., Jensen K. B., Levring H. Gerward L. et al. WinXCom — a program for calculating x-ray attenuation coefficients. *Radiation Physics and Chemistry.* 2004. Vol. 71. P. 653—654.

174. Zavartsev Yu.D., Koutovoi S.A., Zagumennyi A.I. Czochralski growth and characterisation of large Ce^{3+}:Lu_2SiO_5 single crystals co-doped with Mg^{2+} or Ca^{2+} or Tb^{3+} for scintillators. *J. of Crystal Growth*. 2005. Vol. 275. P.e2167—e2171.
175. Rothfuss H., Melcher C.L., Eriksson L.A., Spurrier M.A., Koschan M.A. The Effect of Ca^{2+} Codoping on Shallow Traps in YSO:Ce Scintillators. *IEEE Transactions on Nuclear Science*. 2009. Vol. 56, No. 3. P. 958—961.
176. Yang K., Melcher Ch., Zhuravleva M., Koschan M.A. Effect of Ca Co-Doping on the Luminescence Centers in LSO:Ce Single Crystals. *IEEE Transactions on Nuclear Science*. 2011. Vol. 58, No. 3. P.1394—1399.
177. Blahuta S. et al. Evidence and Consequences of Ce^{4+} in LYSO:Ce,Ca and LYSO:Ce,Mg Single Crystals for Medical Imaging Applications. *IEEE Transactions on Nuclear Science*. 2013. Vol. 60, No. 4. P. 3134—3141.
178. Zimmerer G. SUPERLUMI: a unique setup for luminescence spectroscopy with synchrotron radiation. *Radiation Measurements*. 2007. Vol. 42. P. 859—864.
179. Kamenskikh I. Energy Relaxation in LSO and LGSO Crystals Studied in the VUV Range. *IEEE Transactions on Nuclear Science*. 2014. Vol. 61, No. 4. P. 290—292.
180. Melcher C.L., Schweitzer J.S. Cerium-doped lutetium oxyorthosilicate: a fast, efficient new scintillator. *IEEE Transactions on Nuclear Science*. 1992. Vol. 39. P. 502—505.
181. Suzuki H. et al. The role of gadolinium in the scintillation processes of cerium-doped gadolinium oxyorthosilicate. *Nuclear Instruments and Methods in Physics Res. A*. 1994. Vol. 346. P. 510—521.
182. Mori K., Nishimura H., Nakayama M., Ishibashi H. Dynamical aspects of the core excitons formed by the 4f-4f transitions of Gd^{3+} in Gd_2SiO_5. *J. of Luminescence*. 2000. Vol. 87—89. P. 266—268.
183. Mori K., Nishimura H., Nakayama M. Role of the core excitons formed by 4f-4f transitions of Gd^{3+} on Ce^{3+} scintillation in Gd_2SiO_5:Ce^{3+}. *Physical Rev. B*. 2003. Vol. 67. P. 165206.
184. Voloshina O.V. Obtaining and characteristics of $REAO_4$ compounds (RE – rare earth element, A – V, Nb, Ta) for applications in scintillators: thesis of candidate of technical sciences: 05.02.01. Institute for Single Crystals NAS of Ukraine. Khakiv, 2017 [in Russsian].
185. Liu W. et al. Growth and and Luminescence of M-Type $GdTaO_4$ and Tb:$GdTaO_4$ Scintillation Single Crystals. *IEEE Transactions on nuclear science*. 2010. Vol. 57, No. 3. P. 1287—1290.
186. Yang H. et al. A promising high-density scintillator of $GdTaO_4$ single crystal. *CrystEngComm*. 2014. Vol. 16. P. 2480—2485.
187. Hristea A. et al. Morpho-structural and luminescent investigations of niobium activated yttrium tantalate powders. *J. of Alloys and Compounds*. 2009. Vol. 471. P. 524—529.
188. Xiao X., Yan B. Photoluminescent properties of Eu^{3+}(Dy^{3+})-activated $YNb_xTa_{1-x}O_4$ and $REVTa_2O_9$ (RE = Y, La, Gd) phosphors from the hybrid precursors. *Applied Physics A. Materials Science* & *Processing*. 2007. Vol. 88, No. 1. P. 333—339.
189. Hristea A. et al. Yttrium tantalate – based phosphors for x-ray intensifying screen. *ROMOPTO-2003 Seventh Conf. on Optics: The Int. Society for Optical Engineer.*: proceed. of SPIE (8—11 Sept., 2003, Constanta, Romania). 2004. Vol. 5581. P. 781—787.

190. Blasse G., Dirksen G.J., Crawford M.K., Brixner L.H. Luminescence of materials based on $LuTaO_4$. *J. of Alloys and Compounds*. 1994. Vol. 209. P. 1—6.

191. Voloshyna O.V. et al. New, dense, and fast scintillators based on rare-earth tantalo-niobates. *Nuclear Instruments and Methods in Physics Res. A*. 2014. Vol. 764. P. 227—231.

192. Spassky D. et al. Composition effect in luminescence properties of $Y(Nb_xTa_{1-x})O_4$ mixed crystals. *Optical Materials*. 2018. Vol. 80. P. 247—252.

193. Voloshyna O., Boiaryntseva Ia., Spassky D., Sidletskiy O. Luminescence properties of the yttrium and gadolinium tantalo-niobates. *Solid State Phenomena*. 2015. Vol. 230. P. 172—177.

194. Voloshyna O.V. et al. Nonlinear behavior of structural and luminescent properties in $Gd(Nb_xTa_{1-x})O_4$ mixed crystals. *Optical Materials*. 2018. Vol. 76. P. 382—387.

195. Blasse G., Bril A. Photoluminescent Efficiency of Phosphors with Electronic Transitions in Localized Centers. *J. of the Electrochemical Society*. 1968. Vol. 115. P. 1067—1075.

196. Qiao X., Seo H.J. Energy transfer and luminescence dynamics in $Ca_3Gd_2(BO_3)_4$:Eu^{3+}. *J. of Luminescence*. 2014. Vol. 145. P. 312—317.

197. Qiao X., Seo H.J. Vacuum ultraviolet and ultraviolet (VUV–UV) spectroscopy and relaxation dynamics of Eu^{3+} ions doped in $Ca_3Gd_2(BO_3)_4$ phosphor. *Materials Res. Bull.* 2014. Vol. 49. P. 76—82.

198. Jamalaiah B.C. et al. Luminescence, energy transfer and color perception studies of $Na_3Gd(PO_4)_2$:Dy^{3+}:Tm^{3+} phosphors. *Optical Materials*. 2014. Vol. 36, No. 10. P. 1688—1693.

199. Baryshevsky V.G. et al. Mechanism of scintillations in cerium-doped gadolinium orthosilicate Gd_2SiO_5:Ce crystals. *J. of Luminescence*. 1994. Vol. 60&61. P. 956—959.

200. Voloshyna O. et al. Fast ultradense $GdTa_{1-x}Nb_xO_4$ scintillator crystals. *Optical Materials*. 2017. Vol. 66. P. 332—337.

201. ET Enterprises 9954 B series electron tubes data sheet. URL: https://et-enterprises.com/images/data_sheets/9954B.pdf (Last accessed: 02.09.2024)

202. Blasse G., Bril A. A New Phosphor for Flying-Spot Cathode-Ray Tubes for Color Television: Yellow-Emitting $Y_3Al_5O_{12}$-Ce^{3+}. *Applied Physics Letters*. 1967. Vol. 11, No. 2. P. 53—55.

203. Baryshevsky V.G. et al. $YAlO_3$:Ce — fast-acting scintillators for detection of ionizing radiation. *Nuclear Instruments and Methods in Physics Res. B*. 1991. Vol. 58. P. 291—293.

204. Minkov B.I. Promising new lutetium based single crystals for fast scintillators. *Functional materials*. 1994. Vol. 1. P. 103—105.

205. Cooke D.W. et al. Crystal growth and optical characterization of cerium-doped $Lu_{1.8}Y_{0.2}SiO_5$. *J. of Applied Physics*. 2000. Vol. 88. P. 7360—7362.

206. Wang C. et al. Optical and scintillation properties of Ce-doped $(Gd_2Y_1)Ga_{2.7}Al_{2.3}O_{12}$ single crystal grown by Czochralski method. *Nuclear Instruments and Methods in Physics Res. A*. 2016. Vol. 820. P. 8—12.

207. Auffray E. et al. Radiation damage of LSO crystals under γ-and 24GeV protons irradiation. *Nuclear Instruments and Methods in Physics Res. A*. 2013. Vol. 721. P. 76—82.

208. Auffray E. et al. Radiation damage effects in Y_2SiO_5:Ce scintillation crystals under γ-quanta and 24 GeV protons. *Nuclear Instruments and Methods in Physics Res. A*. 2015. Vol. 783. P. 117—120.

209. Zorenko Y. Luminescence of isoelectronic impurities and antisite defects in garnets. *Physica Status Solidi C*. 2005. Vol. 2. P. 375—379.

210. Nikl M. et al. The antisite LuAl defect-related trap in $Lu_3Al_5O_{12}$:Ce single crystal. *Physica Status Solidi B*. 2005. Vol. 242. P. 119—121.

211. Zorenko Y. et al. Single-crystalline films of Ce-doped YAG and LuAG phosphors: advantages over bulk crystals analogues. *J. of Luminescence*. 2005. Vol. 114. P. 85—94.

212. Benaglia A. et al. Test beam results of a high granularity LuAG fibre calorimeter prototype. *J. of Instrumentation*. 2016. Vol. 11. P. 05004.

213. Zorenko Y. et al. Luminescent properties of $Y_3Al_{5-x}Ga_xO_{12}$:Ce crystals. *J. of Luminescence.* 2014. Vol. 156. P. 102—107.

214. Zorenko Y. et al. Luminescence and scintillation properties of $Y_3Al_5O_{12}$:Ce single crystals and single-crystal films. *Physics of the Solid State*. 2011. Vol. 53. P. 1542—1547.

215. Zorenko Y. et al. Peculiarities of luminescent and scintillation properties of YAG:Ce phosphor prepared in different crystalline forms. *Optical Materials*. 2012. Vol. 34. P. 1314—1319.

216. Zorenko Y. et al. Time-resolved spectroscopy of intrinsic luminescence of $Y_3Ga_5O_{12}$ and $(LaLu)_3Lu_2Ga_3O_{12}$ single crystals. *Optical Materials*. 2009. Vol. 31. P. 1835—1838.

217. Sidletskiy O. et al. Engineering of bulk and fiber-shaped YAGG: Ce scintillator crystals. *Crystal Engineer. Communications*. 2017. Vol. 19. P. 1001—1007.

218. Zorenko Y. et al. Luminescence of excitons and antisite defects in the phosphors based on garnet compounds. *Radiation Measurements*. 2004. Vol. 38. P. 677—680.

219. Zorenko Yu. et al. Exciton and antisite defect-related luminescence in $Lu_3Al_5O_{12}$ and $Y_3Al_5O_{12}$ garnets. *Physica Status Solidi B*. 2007. Vol. 244. P. 2180—2189.

220. Nikl M. et al. Development of LuAG-based scintillator crystals — A review. *Progress in Crystal Growth and Characterization*. 2013. Vol. 59. P. 47—72.

221. Kamada K. et al. Scintillator-oriented combinatorial search in Ce-doped $(Y,Gd)_3(Ga,Al)_5O_{12}$ multicomponent garnet compounds. *J. of Physics D: Applied Physics.* 2011. Vol. 44, No. 50. P. 505104.

222. Wu Y. et al. Single crystal and optical ceramic multicomponent garnet scintillators: A comparative study. *Nuclear Instruments and Methods in Physics Res. A*. 2015. Vol. 780. P. 45—50.

223. Chewpraditkul W. et al. Comparison of absorption, luminescence and scintillation characteristics in $Lu_{1.95}Y_{0.05}SiO_5$:Ce,Ca and Y_2SiO_5:Ce scintillators. *Optical Materials*. 2013. Vol. 35, No. 9. P. 1679—1684.

224. Tyagi M. et al. Effect of codoping on scintillation and optical properties of a Ce-doped $Gd_3Ga_3Al_2O_{12}$ scintillator. *J. of Physics D: Applied Physics*. 2013. Vol. 46, No. 47. P. 475302.

225. Moretti F. et al. Consequences of Ca codoping in $YAlO_3$:Ce single crystals. *Chem PhysChem*. 2016. Vol. 18, No. 5. P. 493—499.

226. Wu Y., Luo J., Ren G., Nikl M. Origin of improved scintillation efficiency in $(Lu,Gd)_3(Ga,Al)_5O_{12}$:Ce multicomponent garnets: An X-ray absorption near edge spectroscopy study. *APL Materials*. 2014. Vol. 2, No. 1. P. 012101.

227. Lima A.F., Souza S.O., Lalić M.V. Electronic structure and optical absorption of the $Bi_4Ge_3O_{12}$ and the $Bi_4Si_3O_{12}$ scintillators in ultraviolet region: An ab initio study. *J. of Applied Physics*. 2009. Vol. 106. P. 013715.

228. Galenin E. et al. Characterization of bismuth germanate crystals grown by EFG method. *Crystal Res. and Technology*. 2015. Vol. 50, No. 2. P. 150—154.
229. Jiang H. et al. Scintillation properties of $Bi_4(Ge_{1-x}Si_x)_3O_{12}$ single crystals grown by Czochralski method. *J. of Crystal Growth*. 2013. Vol. 367. P. 73—76.
230. Xu. J. Growth and properties of BGO, BSO and BGSO scintillation crystals. *Oral presentaion at ICCGE-17* (11—16 August, 2013, Warsaw, Poland). 2013.
231. Sidletskiy O., Gektin A., Belsky A. Light-yield improvement trends in mixed scintillation crystals. *Physica Status Solidi A*. 2014. Vol. 211. P. 2384—2387.
232. Nikitin A., Bliven S. Needs of well logging industry in new nuclear detectors. *IEEE Nuclear Science Sympos. Conf. Record*. (30 Oct. — 6 Nov. 2010, Knoxville, USA). 2010. P. 1214—1219.
233. Nikl M. et al. Shallow traps and radiative recombination processes in $Lu_3Al_5O_{12}$:Ce single crystal scintillator. *Physical Rev. B*. 2007. Vol. 76. P. 195121.
234. Vedda A. et al. Trap-center recombination processes by rare earth activators in $YAlO_3$ single crystal host. *Physical Rev. B*. 2009. Vol. 80. P. 045113.
235. Visser R. et al. Photostimulated Luminescence and Thermoluminescence of LSO Scintillators. *IEEE Transactions on Nuclear Science*. 1995. Vol. 41, No. 4. P. 689—693.
236. Dorenbos P., van Eijk C.W.W., Melcher C. L., Bos J. J. A. Afterglow and Thermoluminescence properties of Lu_2SiO_5 scintillation crystals. *J. of Physics: Condensed Matter.* 1994. Vol. 6. P. 4167.
237. Vedda A. et al. Thermally stimulated tunneling in rare-earth doped Lu-Y oxyorthosilicates. *Physical Rev. B*. 2008. Vol. 78. P. 195123.
238. Sidletskiy O. et al. Crystal Composition and Afterglow in Mixed Silicates: The Role of Melting Temperature. *Physical Rev. Applied*. 2015. Vol. 4. P. 024009.
239. Vedda A. et al. Tunneling process in Thermally Stimulated Luminescence of mixed $Lu_xY_{1-x}AlO_3$:Ce crystals. *Physical Rev. B*. 2000. Vol. 61. P. 8081.
240. Laguta V.V. et al. Electron traps related to oxygen vacancies in PbWO4. *Physical Rev. B*. 2003. Vol. 67. P. 205102.
241. Antoine C. Tensions des vapeurs; nouvelle relation entre les tensions et les temperatures. Comptes Rendus des Séances de l'Académie des Sciences. 1888. Vol. 107. P. 681—684, 778—780, 836—837.
242. Kulikov I.S. Thermodynamics of oxides. 1986. 344 p. [in Russian].
243. Melcher C.L. et al. Crystal growth and scintillation properties of the rare earth oxyorthosilicates. *Inorganic Scintillators and their Applications*: Proceed. of SCINT'95 (28 August — 1 Sept. 1995, Delft, The Netherlands), 1996. 309 p.
244. Bondar V. et al. Optico-luminescent properties and mechanical strength of G(Y) SO:Ce crystals. *Inorganic Scintillators and their Applications*: Proceed. of SCINT'2005 (19—23 Sept., 2005, Alushta, Crimea, Ukraine). 2006. P. 98.
245. McKeever S.W.S. Thermoluminescence of Solids. *Cambridge University Press, Solid State Science Series*, 1985. 392 p.
246. Curie D. Luminescence in crystals. Wiley, New York. 1963. 332 p.
247. Greskovich C., Duclos S. Ceramic Scintillators. *Annual Rev. of Materials Science*. 1997. Vol. 27. P. 69—88.
248. Derenzo S. et al. Scintillation Properties. URL: https:// http://scintillator.lbl.gov/ (Last accessed: 02.09.2024)
249. Parameters of LYSO:Ce https://www.epic-crystal.com/scintillation-crystals/lysoce-crystal.html (Last accessed: 02.09.2024)

250. Ishii M. et al. Development of BSO ($Bi_4Si_3O_{12}$) crystal for radiation detector. *Optical Materials*. 2002. Vol. 19. P. 201.
251. Cherepy N.J. et al. Strontium and barium iodide high light yield scintillators. *Applied Physics Letters*. 2008. Vol. 92. P. 083508.
252. Zorenko Yu.V. Mechanism of dissipation of the excitation energy in garnet oxides doped with rare-earth ions with 4f-5d transitions. *Optics and Spectroscopy*. 2000. Vol. 88. P. 551.
253. Zhang S. et al. Long-lasting phosphorescence study on $Y_3Al_5O_{12}$ doped with different concentrations of Ce^{3+}. *Journal of Rare Earths*. 2011. Vol. 29. P. 426—430.
254. Selim F.A., Solodovnikov D., Weber M.H., Lynn K.G. Identification of defects in $Y_3Al_5O_{12}$ crystals by positron annihilation spectroscopy. *Applied Physics Letters*. 2007. Vol. 91. P. 104105.
255. Kitaura M. et al. Probing shallow electron traps in cerium-doped $Gd_3Al_2Ga_3O_{12}$ scintillators by UV-induced absorption spectroscopy. *Applied Physics Express*. 2016. Vol. 9. P. 072602.
256. Yang J.-K., Park H.-H. Incorporation of SiO_2 for the band alignment control of Gd_2O_3/n-GaAs(0 0 1) structure. *Applied Surface Science*. 2005. Vol. 244. P. 293—296.
257. Chen Y. et al. Luminescent properties of Gd_2SiO_5 powder doped with Eu^{3+} under VUV–UV excitation. *J. of Physics: Condensed Matter.* 2005. Vol. 17. P. 1217—1224.
258. Znamenskii N. et al. The nature and mechanism of charging of electron traps in $Lu_2SiO_5:Ce^{3+}$ crystals. *J. of Experimental and Theoretical Physics*. 2004. Vol. 99. P. 386—393.
259. Spassky D.A. et al. Luminescence of borates with yttrium and lutetium cations. *Physics of the Solid State*. 2013. Vol. 55, No. 1. P. 150—159.
260. Dorenbos P. Determining binding energies of valence-band electrons in insulators and semiconductors via lanthanide spectroscopy. *Phys. Rev. B*. 2013. Vol. 87. P. 035118.
261. Li Q. et al. Search for improved-performance scintillator candidates among the electronic structures of mixed halides. *Proc. of SPIE*. 2014. Vol. 9213.
262. Dorenbos P. 5d-level energies of Ce^{3+} and the crystalline environment. IV. Aluminates and «simple» oxides. *J. of Luminescence*. 2002. Vol. 99, No. 3. P. 283—299.
263. Dorenbos P. The electronic level structure of lanthanide impurities in $REPO_4$, $REBO_3$, $REAlO_3$, and RE_2O_3 (RE = La, Gd, Y, Lu, Sc) compounds. *J. of Physics: Condensed Matter*. 2013. Vol. 25, No. 22. P. 225501.
264. Canning A. et al. Electronic structure studies and predictions for new Ce-doped gamma detector materials. *IEEE Nuclear Sci. Sympos. Conf. Record,* (28 Oct. — 3 Nov., 2007, Honolulu, USA) 2007. P. 2466—2468.
265. Cowley J.M. An AProximate Theory of Order in Alloys. *Physical Review*. 1950. Vol. 77, No. 5. P. 669.
266. Cowley J.M. Short- and Long-Range Order Parameters in Disordered Solid Solutions. *Physical Review*. 1960. Vol. 120, No. 5. P. 648.
267. Batirev I.G., Leiro J.A., Nikiforova L.A., Katsnelson A.A. Electronic structure and short-range order of amorphous and crystalline alloys in the coherent locator aProximation. *J. of Physics and Chemistry of Solids*. 1993. Vol. 54, No. 7. P. 779—872.
268. Kuznetsov A.Yu., Sobolev A.B., Velichko A.N., Makarov A.S. First-Principles Calculations of the Electronic Structure and Plastic Properties of CsCl, CsBr, and CsI Crystals. *Physics of the Solid State*. 2005. Vol. 47, No. 11. P. 2030—2034.

269. Mengucci P. et al. Structural, mechanical and light yield characterisation of heat treated LYSO:Ce single crystals for medical imaging applications. *Nuclear Instruments and Methods in Physics Res. A*. 2015. Vol. 785. P. 110—116.
270. Ozawa T.C., Kang S.J. Balls&Sticks: easy-to-use structure visualization and animation program. *J.l of Applied Crystallography*. 2004. Vol. 37, No. 4. P. 679.
271. Suzuki H. et al. Scintillation properties of some Ce $^{3+}$ and Pr $^{3+}$ doped inorganic crystals. *IEEE Transactions on Nuclear Science*. 1993. Vol. 40, No. 4. P. 380.
272. Szczesniak T. et al. Timing resolution and decay time of LSO crystals co-doped with calcium. *IEEE Transactions on Nuclear Science*. 2010. Vol. 57, No. 3. P. 1329—1334.
273. Gautier N., Gervais M., Coutures J.-P. Aluminium and gallium substitution in yttrium garnets investigated by NMR and X-ray absorption. *Physica Status Solidi A*. 1998. Vol. 165. P. 329—336.
274. Laguta V. et al. Aluminum and Gallium Substitution in Yttrium and Lutetium Aluminum-Gallium Garnets: Investigation by the Single-Crystal NMR and TSL Methods. *J. of Physical Chemistry C*. Vol. 120. P. 24400—24408.
275. Xu J., Ueda J., Tanabe S. Novel persistent phosphors of lanthanide—chromium co-doped yttrium aluminum gallium garnet: design concept with vacuum referred binding energy diagram. *J. of Materials Chemistry C*. 2016. Vol. 4. P. 4380—4386.
276. Kaufmann U. et al. Single chip white LEDs. *Physica Status Solidi A*. 2002. Vol. 192. P. 246—253.
277. Marezio M., Remeika J.P., Dernier P.D. Cation distribution in $Y_3Al_{5-c}Ga_cO_{12}$. *Acta Crystallographica Section B*. 1986. Vol. 24. P. 1670—1674.
278. Gautier N. et al. Aluminium-gallium substitution in yttrium garnets investigated by NMR. *J. de Chimie Physique*. 1995. Vol. 92. P. 1843—1846.
279. Stanek C.R. et al. The effect of Ga-doping on the defect chemistry of $RE_3Al_5O_{12}$ garnets. *Physica Status Solidi B*. 2013. Vol. 250. P. 244—248.
280. Tien T.Y. et al. Ce^{3+} activated $Y_3Al_5O_{12}$ and some of its solid solutions. *Journal of The Electrochemical Society*. 1973. Vol. 120. P. 278—281.
281. Robertson J.M., van Tol M.W., Smits W.A., Heynen, J.P.H. Colour shift of the Ce^{3+} emission in monocrystalline epitaxially grown garnet layers. *Journal of Research*. 1981. Vol. 36. P. 15—30.
282. Munoz-Garcia A. B., Seijo L. Structural, electronic and spectroscopic effects of Ga codoping in Ce-doped yttrium aluminum garnet: first-principles study. *Physical Review B*. 2010. Vol. 82. P. 184118.
283. Vosegaard T., Massiot D., Gautier N., Jakobsen H.J. ^{71}Ga Chemical Shielding and Quadrupole Coupling Tensors of the Garnet $Y_3Ga_5O_{12}$ from Single-Crystal ^{71}Ga NMR. *Inorganic Chemistry*. 1997. Vol. 36, No. 11. P. 2446—2450.
284. Vosegaard Th. et al. Crystal Structure Studies on the Garnet $Y_3Al_5O_{12}$ by ^{27}Al Single-Crystal NMR Spectroscopy. *J. of the American Chemical Society*. 1998. Vol. 120, No. 31. P. 7900—7904.
285. Kononets V. et al. Confocal Microscopy of Luminescence Inhomogeneity in LGSO:Ce Scintillator Crystal. *IEEE Transactions on Nuclear Science*. 2014. Vol. 61(1). P. 343—347.
286. Patent application WO 2011/093176 A3. Scintillator crystal body, method for manufacturing the same, and radiation detector. Canon Kabushiki Kaisha. Priority date 28.01.2010.

287. Ohashi Y., Yasui N., Den T. Submicron-diameter phase-separated scintillator fibers for high-resolution X-ray imaging. *Applied Physics Letters*. 2013. Vol. 102, No. 5. P. 051907.
288. Hishimura K. et al. LiF/CaF_2/$LiBaF_3$ ternary fluoride eutectic scintillator. *Japanese J. of Applied Physics*. 2015. Vol. 54. P. 04DH04.
289. Greenwood N.N., Earnshaw E. Chemistry of the elements. 2nd edition. 1997. 979 p.
290. Kamada K. et al. 2 inch diameter single crystal growth and scintillation properties of Ce:$Gd_3Al_2Ga_3O_{12}$. *J. of Crystal Growth*. 2012. Vol. 352, No. 1. P. 88.
291. Sidletskiy O. et al. Evaluation of LGSO:Ce scintillator for high energy physics experiments. *Nuclear Instruments & Methods in Physics Res. A*. 2014. Vol. 735. P. 620—623.
292. Hillis R. et al. Coiled tubing drilling and real-time sensing-enabling prospecting drilling in the 21st century. *Society of Economic Geologists Special Publication*. 2014. No. 18. P. 243—259.
293. Nikl M. et al. $Lu_3Al_5O_{12}$-based materials for high 2D-resolution scintillation detectors. *Proc. SPIE. 2009*. Vol. 7310. P. 731008.
294. Riva F. et al. Epitaxial growth of gadolinium and lutetium-based aluminum perovskite thin films for X-ray micro-imaging applications. *CrystEngComm*. 2016. Vol. 18. P. 608—615.
295. Zorenko Yu. et al. High-perfomance Ce-doped multicomponent garnet single crystalline film scintillators. *Physica Status Solidi RRL*. 2015. Vol. 9, No. 8. P. 489—493.
296. Mares J. et al. Scintillation and optical properties of YAG:Ce films grown by liquid phase epitaxy. *Radiation Measurements*. 2007. Vol. 42. P. 533—536.
297. Zorenko Yu. et al. Scintillating screens based on the single crystalline films of multicomponent garnets: new achievements and possibilities. *IEEE Transactions on Nuclear Science*. 2016. Vol. 63. P. 497—502.
298. Zorenko Yu. et al. Growth and luminescent properties of scintillators based on the single crystalline films of $(Lu,Gd)_3(Al,Ga)_5O_{12}$:Ce garnets. *J. of Luminescence*. 2016. Vol. 169. P. 828—837.
299. Prusa P. et al. The α-particle excited scintillation response of the liquid phase epitaxy grown LuAG:Ce thin films. *Applied Physics Letters*. 2008. Vol. 2. P. 1—3.

Книгу присвячено розробці науково-технічних основ створення високоефективних неорганічних сцинтиляційних кристалів на основі твердих розчинів заміщення. Досліджено структурні, люмінесцентні та сцинтиляційні властивості отриманих оксидних кристалів. Визначено умови вирощування великорозмірних оксидних кристалів твердих розчинів методом Чохральського та кристалічних волокон твердих розчинів методом мікровитягування (μ-PD). Визначено загальний феноменологічний підхід до цілеспрямованого отримання кристалів з покращеним світловим виходом, зокрема тенденцію до збільшення світлового виходу твердого розчину в змішаних системах.

Видання може бути корисним фахівцям з матеріалознавства у сфері сцинтиляційних та люмінесцентних середовищ, а також розробникам технологій і нанотехнологій одержання сцинтиляційних матеріалів та виробів з них.

Наукове видання

НАЦІОНАЛЬНА АКАДЕМІЯ НАУК УКРАЇНИ
ІНСТИТУТ СЦИНТИЛЯЦІЙНИХ МАТЕРІАЛІВ
НАН УКРАЇНИ

СІДЛЕЦЬКИЙ Олег Цезарович
ГРИНЬОВ Борис Вікторович

СЦИНТИЛЯЦІЙНІ КРИСТАЛИ НА ОСНОВІ ТВЕРДИХ РОЗЧИНІВ ЗАМІЩЕННЯ

Англійською мовою

Редактор *Вадим Рего*

Коректор *Олеся Чадюк*
Художнє оформлення *Євгена Ільницького*
Технічне редагування *Тетяни Шендерович*
Виготовлення ілюстрацій *Сергія Горбаненка*
Комп’ютерна верстка *Ніни Кучеренко*

Підписано до друку 19.11.2025. Формат 70×100/16. Гарн. Minion Pro.
Ум. друк. арк. 13,48. Обл.-вид. арк. 14,99. Тираж 100 прим. Зам. № 7859

Видавець і виготовлювач Видавничий дім «Академперіодика» НАН України
вул. Терещенківська, 4, Київ, 01024, Україна

Свідоцтво про внесення до Державного реєстру суб’єктів
видавничої справи серії ДК № 544 від 27.07.2001

ВИДАВНИЧИЙ ДІМ
АКАДЕМПЕРІОДИКА